

Vol. 16 • No. 2 • October 2022

# JOURNAL OF GEOMATICS

ISSN: 0976 - 1330



An official publication of Indian Society of  
Geomatics



## Journal of Geomatics

(A publication of the Indian Society of Geomatics)

### Editorial Board

#### Chief Editor: Dr. R.P. Singh

(Address for Correspondence: Director, Indian Institute of Remote Sensing, ISRO, Dehradun - 248001, India)

Phone: +91-135-2744583, 2524101 (O), Email: [rpsingh@iirs.gov.in](mailto:rpsingh@iirs.gov.in), [editorjogisg@gmail.com](mailto:editorjogisg@gmail.com)

#### Associate Editors:

<b>Harish Chandra Karnatak</b>	Dehradun, Email: <a href="mailto:harish.karnatak@gmail.com">harish.karnatak@gmail.com</a>
<b>Bijoy K. Handique</b>	Shillong, Email: <a href="mailto:bkhandique@gmail.com">bkhandique@gmail.com</a>
<b>D. Giri Babu</b>	Jodhpur, Email: <a href="mailto:giribabu.d@nrsc.gov.in">giribabu.d@nrsc.gov.in</a>
<b>R. Ratheesh</b>	Ahmedabad, Email: <a href="mailto:ratheeshr@sac.isro.gov.in">ratheeshr@sac.isro.gov.in</a>
<b>S.V.V. Arun Kumar</b>	Ahmedabad, Email: <a href="mailto:arunkumar@sac.isro.gov.in">arunkumar@sac.isro.gov.in</a>
<b>R. Agrawal</b>	Ahmedabad, Email: <a href="mailto:ritesh_agrawal@sac.isro.gov.in">ritesh_agrawal@sac.isro.gov.in</a>

#### Members:

<b>A.R. Dasgupta</b>	Ahmedabad, Email: <a href="mailto:arup@ieee.org">arup@ieee.org</a>
<b>P.K. Garg</b>	Dehradun, Email: <a href="mailto:gargpfce@iitr.ernet.in">gargpfce@iitr.ernet.in</a>
<b>P.K. Verma</b>	Bhopal, Email: <a href="mailto:drpkverma@rediffmail.com">drpkverma@rediffmail.com</a>
<b>Ashok Kaushal</b>	Pune, Email: <a href="mailto:akaushal1960@yahoo.co.in">akaushal1960@yahoo.co.in</a>
<b>T.T. Medhavy</b>	Australia, Email: <a href="mailto:medhavy.thankappan@ga.gov.in">medhavy.thankappan@ga.gov.in</a>
<b>I.V. Murali Krishna</b>	Hyderabad, Email: <a href="mailto:ivm@ieee.org">ivm@ieee.org</a>
<b>S.M. Ramasamy</b>	Tiruchirapalli, Email: <a href="mailto:grucc@ruraluniv.ac.in">grucc@ruraluniv.ac.in</a>
<b>P.S. Roy</b>	Hyderabad, Email: <a href="mailto:psroy1952@yahoo.in">psroy1952@yahoo.in</a>
<b>Milap Chand Sharma</b>	New Delhi, Email: <a href="mailto:milap@mail.jnu.ac.in">milap@mail.jnu.ac.in</a>
<b>Tara Sharma</b>	Canada, Email: <a href="mailto:sharmatara@yahoo.com">sharmatara@yahoo.com</a>
<b>P. Venkatachalam</b>	Mumbai, Email: <a href="mailto:pvenk@csre.iitb.ac.in">pvenk@csre.iitb.ac.in</a>
<b>Claudio Zucca</b>	Morocco Email: <a href="mailto:c.zucca@cgiar.org">c.zucca@cgiar.org</a>

### Advisory Board

<b>Paul J. Curran</b>	Vice-Chancellor, Bournemouth University, Poole, <b>UK</b>
<b>V. Jayaraman</b>	Bengaluru, <b>India</b>
<b>R. Krishnan</b>	Thiruvananthapuram, <b>India</b>
<b>P. Nag</b>	Varanasi, <b>India</b>
<b>M.P. Narayanan</b>	President, CSDMS, NOIDA, U.P., <b>India</b>
<b>R.R. Navalgund</b>	Bengaluru, <b>India</b>
<b>Y.S. Rajan</b>	Bengaluru, <b>India</b>
<b>Josef Strobl</b>	Interfaculty Dept. of Geoinformatics, University of Salzburg, <b>Austria</b>

## **Indian Society of Geomatics Executive Council 2020-2023**

- President**            **Raj Kumar**, Space Applications Centre, ISRO, Ahmedabad- 380058
- Vice-President**    **Y.V.N. Krishna Murthy**, Indian Institute of Space Science and Technology, Thiruvananthapuram – 695547  
**Sarvesh Palria** (Retd.), M.D.S. University, Ajmer – 305009
- Secretary**            **Shashikant A. Sharma**, Space Applications Centre, ISRO, Ahmedabad - 380058
- Joint Secretary**    **P.L.N. Raju**, North Eastern Space Applications Centre, DOS, Umiam - 793103
- Treasurer**            **P. Jayaprasad**, Space Applications Centre, ISRO, Ahmedabad - 380015
- Members**            **Alpana Shukla**, M.G. Science Institute, Ahmedabad - 380009  
**Anil Sood**, Punjab Remote Sensing Centre, Ludhiana - 141004  
**Sandeep Goyal**, M.P. Agency for Promotion of Information Technology, Bhopal - 462003  
**R.J. Bhanderi**, Space Applications Centre, ISRO, Ahmedabad - 380015  
**Sujata Ghosh**, Advanced Data Processing Research Institute, DOS, Hyderabad - 500009

**Ex-Officio (Immediate Past President) Tapan Misra**, Space Applications Centre, ISRO, Ahmedabad – 380015

**Secretary: (address for correspondence)**

6202, Space Applications Centre, ISRO, Bopal Campus, Ahmedabad-380058, India

Email: [secretary@isgindia.org](mailto:secretary@isgindia.org); [sasharma@sac.isro.gov.in](mailto:sasharma@sac.isro.gov.in)

## Journal of Geomatics

(A Publication of the Indian Society of Geomatics)

Vol. 16. No. 2

Research articles

October 2022

1	<p><b>Appraising Malaria Incidence with Spatial-Oriented Decision Support System in Parts of Zaria, Kaduna State-Nigeria</b> Azua, S., Youngu, T.T., Aliyu, Y.A., Akomolafe, E.A., Ahmadu, A.A., Abubakar, A.Z and Q. O. Majekodunmi</p>	103
2	<p><b>A framework to Georeference Point Cloud in GPS Shadowed Urban Environment by Integrating Computer Vision Algorithms and Photogrammetric Techniques</b> Mayank Sharma, Raghavendra Sara and Shefali Agrawal</p>	114
3	<p><b>Determination of radii of curvature for high resolution geoid models using the harmonic synthesis algorithm</b> Raaed Mohamed Kamel Hassouna</p>	123
4	<p><b>Web-GIS based Dashboard for Real-Time Data Visualization &amp; Analysis using Open Source Technologies</b> Kusum Lata, Anil Sood, Kawaldeep Kaur, Amanpreet Kaur Benipal and Brijendra Pateriya</p>	134
5	<p><b>Assessment of forest fragmentation in greater Gir landscape area, Gujarat using geospatial techniques</b> Abhinav Mehta, Shital Shukla and Shrey Rakholia</p>	146
6	<p><b>Characterisation of Fixed-Wing Versus Multirotors UAVs/Drones</b> P. K. Garg</p>	152
7	<p><b>Impact of various Vegetation Indices on Mango orchard mapping using Object-Based Image Analysis</b> Steena Stephen, Dipanwita Haldar, N.R. Patel</p>	159
8	<p><b>Study of CNN deep learning model for temporal remote sensing data processing to map rabi crops</b> Mragank Snighal, Ashish Payal and Anil Kumar</p>	167
9	<p><b>Geospatial Analysis of Spatial Variability of Groundwater Quality Using Ordinary Kriging: A Case Study of Dungarpur Tehsil, Rajasthan, India</b> Seema Jalan, Devendra Singh Chouhan, and Shailesh Chaure</p>	176
10	<p><b>A geospatial study of the layout and extent of the eighteenth-century walled city of Hyderabad</b> Gaurav Kumar Pal and M.B. Rajani</p>	187
11	<p><b>Monitoring Road maintenance using video-geotagging in geographical information system: an innovative approach</b> Ajay Mathur, Nishant Tiwari, Vipin Kumar and Brijendra Pateriya</p>	196
12	<p><b>Paleo-topographic Reconstruction of Cultural Landscapes using Remote Sensing and GIS: A case study of the ancient port of Tamralipti</b> Arya S Pradeep and M B Rajani</p>	201
13	<p><b>Analysis of Urban Growth and Its Impact on Agriculture Land around the Chalisgaon City in Jalgaon District of Maharashtra, India: A Remote Sensing and GIS Based Approach</b> Patil Nilesh, Patil Vilas, Patil Sanjaykumar, Patil Bhavesh, Suryawanshi Arvind and Jadhav Kavita</p>	213

14	<b>A spatio-temporal analysis of changing trends in rainfall patter: A case study of Kutch District</b> Lakhan Jain and Bindu Bhatt	223
15	<b>Understanding the Vegetation Dynamics of NCT- Delhi Using Remote Sensing</b> Parul Singh, Sudha Ravindranath, Vidya A, K Ganesha Raj	234
	Author Index	v
	Indian Society of Geomatics: Awards	vii
	Indian Society of Geomatics: Fellows	xii
	Instruction for Authors	xiii
	Journal of Geomatics: Advertisement Rates	xv
	Indian Society of Geomatics: ISG Membership Form	xvi
	Indian Society of Geomatics: Membership Fees	xvii

## Appraising Malaria Incidence with Spatial-Oriented Decision Support System in Parts of Zaria, Kaduna State-Nigeria

Azua, S.\*, Youngu, T.T., Aliyu, Y.A., Akomolafe, E.A., Ahmadu, A.A., Abubakar, A.Z and Q. O. Majekodunmi  
Department of Geomatics, Faculty of Environmental Design,  
Ahmadu Bello University, Zaria, Nigeria  
\*Email: adzuasamuel@yahoo.com/sazua@abu.edu.ng

(Received: Apr 16, 2022; in final form: Aug 19, 2022)

**Abstract:** Prevalence of malaria in certain parts of the world without adequate planning and monitoring based on ill-informed decisions has wreaked havoc on the health system and economy of many developing nations. The purpose of this study is to create a functional Spatial Decision Support System (SDSS) for malaria monitoring in parts of Zaria, Kaduna State. A Geographic Information Systems (GIS) SDSS was created using ArcGIS 10.5 software for the 2019 Malaria data obtained from the Ministry of Health, Kaduna State Roll Back Malaria (RBM) Programme for collation and analysis across 13 political wards in Zaria Local Government Area (LGA) of Kaduna State. The results revealed that a total of 443,852 cases of malaria were reported across the 13 political wards of the study area. The reported cases had predominant occurrences at the Gyellesu ward, followed by the Kwarbai A ward. The spatial incidence was displayed via vector control maps, malaria burden maps, malaria prevalence in Zaria maps, and service area maps. The map of demography indicated a higher prevalence of malaria of 73.35% for the male gender compared to the female (26.65%). However, the independent t-test revealed no significant difference between males' and females' malaria prevalence. It was also revealed that the adult population had the highest malaria prevalence followed by children less than 5 years while pregnant women were the least infected. The study further indicated that 38.5% of the existing political wards recorded a shortfall of at least two (2) healthcare facilities. This study identified areas that required the establishment of health facilities to offset the existing shortfall. The SDSS was able to effectively monitor and appraise malaria incidence for proper surveillance and management that will be required for malaria prevention and elimination activities. The study recommends that policymakers invest in the deployment of an SDSS for better and robust planning, monitoring and execution of their malaria intervention programmes as this aligns with the sustainable development goal (SDG) target 3.3.

**Keywords:** Geographic Information System, Health Facility, Malaria Monitoring, Malaria Prevalence, Spatial Decision Support Systems.

### 1. Introduction

Malaria is one of the major causes of mortality in different parts of the world (Idowu et al., 2009). It is caused by the plasmodium parasite and transmitted by an infected female anopheles' mosquito when it bites a person (Besansky et al., 2004; Awosolu et al., 2021). Malaria has wrecked the economy and health system of many nations particularly in developing nations where it is more prevalent (Ahuru and Omon, 2018). Africa has been reported to be the worst hit by malaria as 80% of the 90% of global cases come from Africa (WHO, 2017). The WHO (2021) further reported that about 95% of all malaria cases and 96% of deaths were recorded in the African Region in 2020. The impact was mostly observed in children below the age of 5 years as over 80% of malaria deaths were reported in the Region. Hence, to achieve meaningful success in the fight against malaria globally, Africa needs to be given maximum attention.

In Nigeria, malaria remains one of the major causes of death (Bamidele et al., 2012). WHO (2021) reported that Nigeria accounted for 31.9% of malaria deaths globally in 2020. These results have pushed Nigeria to intensify the use of Long-Lasting Insecticidal Nets (LLIN) over the initial treatment approach adopted for the control of malaria (Omitola et al., 2021). Despite this, malaria continues to spread because the mosquitos still bite when people are not under the LLINs. This situation suggests the need for renewed research efforts into new tools and

approaches to support malaria surveillance, control and elimination for the well-being of the populace (Idowu et al., 2009).

In line with this, many research efforts have been made to curtail the effect of malaria in Nigeria. In a community-based study, Dawaki et al. (2016) designed and investigated the prevalence and risk factors of malaria, and evaluated the knowledge, attitudes and practices (KAP) regarding malaria among rural Hausa communities in Kano State, Nigeria. The study revealed that malaria was still highly prevalent among rural Hausa communities in Kano State as significant gaps persisted in inappropriate preventive practices.

Sturrock (2013) and Wangdi et al. (2016) opined that for malaria to be eliminated in any location, sustained effort is very fundamental. In the light of the foregoing statistics and trends, it is obvious that the steps taken towards malaria prevention and elimination in Nigeria, and in particular, Zaria are not completely effective. This gives room for further research that will enhance planning and coordination for effective malaria prevention and elimination.

This research aims to create a functional SDSS for malaria monitoring in parts of Zaria, Kaduna State, with the view of providing an effective system for planning and management of malaria. This was achieved through the following objectives; to carry out Geographical

Reconnaissance (GR) survey to map, define and quantify target population and household structures; and to develop a simple GIS-based SDSS to serve as the framework for adequate planning and coordination of improved malaria prevention and elimination in parts of Zaria.

**2. Study Area**

The study area is Zaria in Kaduna State (Figure 1). It is located approximately between Latitudes 11° 08' 11.7" and 11° 57' 43.0" North of the Equator and between Longitudes 7° 36' 33.9" and 7° 48' 08.1" East of the Greenwich Meridian. The city has a height of about 660m above mean sea level (Yusuf and Shuaib, 2012) covering an area of about 411.18 km<sup>2</sup>. It is zoned to Kaduna North Senatorial District alongside Kubau, Ikara, Makarfi, Soba, Lere and Kudan Local Government Areas (LGAs). Zaria is bounded by Sabon Gari LGA to the North, Igabi LGA

to the South, Soba LGA to the East and Giwa LGA to the west. The population of Zaria is about 565,571 people making it the second-largest city in Kaduna State.

The climatic condition of Zaria is a tropical savanna climate, with distinct wet and dry seasons each season lasting about six (6) months (Aliyu and Botai, 2018; Azua et al., 2020). The region falls within the Guinea Savannah vegetation. The climax vegetation of the area ought to be northern Guinea Savannah, but because nearly all vegetation within the stream system has been degraded due to human activities, the real climax vegetation is almost absent. What is seen presently are a few scattered trees interspaced with tall tree grasses about 1-15m and 2-5m, respectively (Nyagba, 1986).

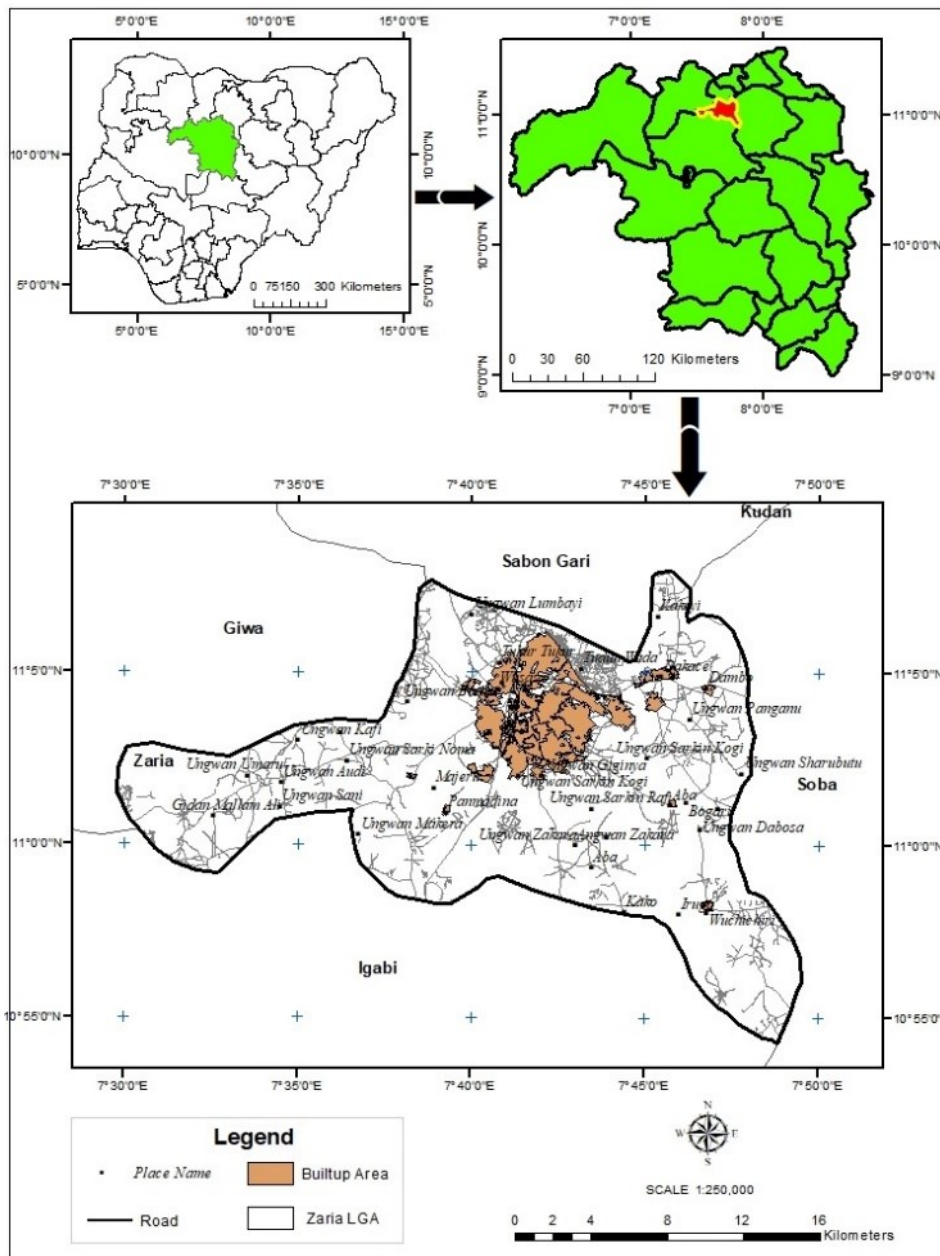


**Figure 1. Map of the Study Area: Top left; Map of Nigeria: Top right; Map of Kaduna State: Bottom; The Study Location**

**3. Methodology Flow Diagram**

The workflow diagram adopted in this study is shown in Figure 2. It entails the data capture, processing, analysis and presentation of reports.

**4. Materials and Methods**

**4.1 Materials**

The Data types used in this study include the primary and secondary datasets, which were obtained from reliable sources as shown in Table 1.

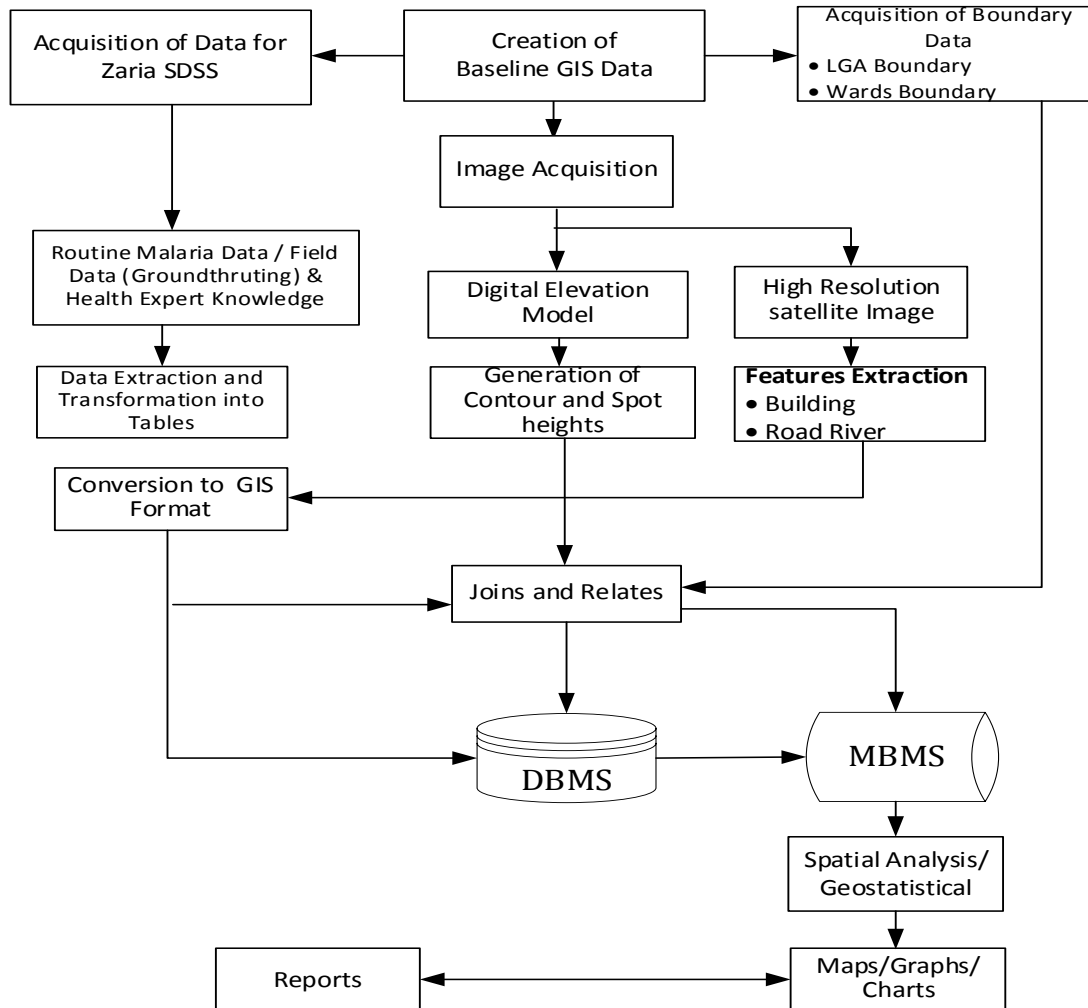


**Figure 2. Workflow Diagram**

**Table 1. Datasets Used**

S/N	Dataset Type	Name	Source/Year	Resolution
1.	Secondary	Google Earth Satellite Imagery/SPOT	Google Earth	2.5m × 2.5m
2.	Secondary	LGA Boundary	UN-OCHA Nigeria	N/A
3.	Secondary	Ward Boundary	GRID3	N/A
4.	Secondary	Malaria Intervention Data Elements	RBM M&E Kaduna State/2019	N/A
5.	Secondary	List of Primary Health Care	KSPHCDA	N/A
6.	Secondary	The population of study wards	GEOPODE (2019)	N/A
7.	Secondary	SRTM Elevation Data	USGS Earth Explorer/2016	30m × 30m
8.	Primary	Geographic Reconnaissance	Ground-Truthing/Field work	N/A

UN-OCHA – United Nations Office for the Coordination of Humanitarian Affairs, Nigeria.  
 GRID 3 – Geo-Referenced Infrastructure and Demographic Data for Development  
 RBM M&E- Roll Back Malaria Monitoring & Evaluation, Ministry of Health, Kaduna State  
 KSPHCDA - Kaduna State Primary Health Care Development Agency  
 GEOPODE (2019). Geographic Population and Demographic Data  
 N/A – Not Applicable

## 4.2 Methods

First, the extent of the satellite imagery covering the study area was determined using the administrative boundary map of Zaria LGA. This was followed by the creation of spatial layers such as roads, railways, water bodies and buildings from the satellite imagery using the ArcMap version 10.5 software.

Second, Geographic Reconnaissance (GR) was carried out to verify spatial locations. This method has been used successfully by Kelly (2010) and Ojo et al. (2016). A random selection of about seven (7) health facilities was visited for field verification and to acquire the spatial locations of these facilities. During the capture of the spatial locations of the facilities, the location serial number generated by the GPS receiver was recorded against the facility names in the field book to ensure easy tracking. The data was then downloaded and filtered using the Garmin MapSource Software V.5 and Microsoft Excel spreadsheet. All points were plotted on the satellite imagery and checked to be okay.

Third, the malaria datasets acquired contained about Seventeen (17) key malaria data elements and indicators, categorised as General attendance, Pregnant women got Intermittent Preventive Treatment (IPT) & Long-Lasting Insecticidal Nets (LLIN), Children who got LLIN, Persons with uncomplicated malaria, Persons with severe malaria etc. All the data were accounted for at the various health facilities throughout 2019. Generally, the data was figure based, with spatial references.

The data was extracted by collating certain data elements (such as attendance to health facilities and persons with malaria) into monthly, quarterly and annual since each of the data elements is facility-based, each having a coordinate and a primary key of Zar1 to Zar48 to easily transform the data into usable and acceptable GIS format. The datasets were then loaded into the DBMS and linked to WGS 1984 UTM Zone 32N as a spatial reference.

## 4.3 Data analysis and interpretation

The maps of people with malaria for the year 2019 were created from the Zaria wards layer. Five (5) maps were created, four (4) of them were prepared for each quarter (Q) of the year namely; Q1, Q2, Q3 and Q4 and the fifth one showed the annual malaria. During the map creation, the Z values used were the aggregate of persons presented with malaria in 2019 and a different colour ramp was employed. Other maps created include malaria prevalence maps, malaria burden maps and service area maps amongst others. The malaria Prevalence map combined a 3D stacked bar chart using the aggregate data values of children under five years, pregnant women and adults with confirmed malaria cases as input. Both maps had health facilities as the reference point.

The Service area map was produced using the Network Analyst tool where the roads, buildings and health facility locations layers were employed as inputs data. Firstly, a new network dataset was built to create network elements, establish connectivity and assign values to defined attributes, using the roads layer as a source feature. Then, the health facility feature was loaded as reference locations where the service area emerged from the predefined distances of 500 metres. This measurement was adopted from Masoodi and Rahimzadeh (2015) who stated that the maximum distance a patient is expected to travel to the health centre is 500m. However, different polygon colour codes were used to signify varying distances from a given health facility as used by Abduselam et al. (2020). Further analysis was carried out on the health centres and the required serviced population. This was done based on the guidelines provided by the WHO (2012) in Eta et al. (2021) which stated that each health centre should service a maximum population of 10,000.

## 5. Results and Discussion

### 5.1 Persons with malaria

Malaria is a deadly disease with a huge burden that affects the health system and growth of many nations. Therefore, providing valuable information to decision-makers on the level of malaria prevalence in Zaria is very vital for its management and control. Figure 3 shows the first, second, third and fourth quarter cases of malaria in the study area while Table 2 summarised all the results for the first, second, third and fourth quarters. The malaria prevalence in the first quarter (Figure 3a) appears to be higher at Dutsen Abba indicating 2,206 which represents 18.95% of the total cases reported, Wuciciri had 1,566 which represents 16.45%, Kufena had 1,447 which represents 12.43% and Kwarbai B had 1,557 which represents 13.38%, while Kaura had the least cases of malaria with 238 which represent 2.10%.

In the second, third and fourth quarters (Figure 3b, c and d), it was observed that Dutsen Abba had the highest number of cases of about 4567 (22.83%), 5646 (18.60%) and 4488 (13.45%), respectively. This was equally followed by Gyellesu with 3063 (15.31%), 4819 (15.87%) and 4176 (12.52%) for the second, third and fourth quarters, respectively. It was, however, observed that Unguwar Fatika had the least number of cases of about 329 (1.64%) and 1366 (4.09%) for the second and fourth quarters, while Dambo had the least malaria prevalence of 659 (2.17%) in the third quarter.

The annual persons with malaria show that Dutsen Abba had the highest number of cases of 16907 which represents 17.74%, followed by Gyellesu with 12454 which represents 13.06%, Unguwar Fatika had the least number of cases of about 3320 which represents 3.48% of the total number of cases in the study area (Figure 4).

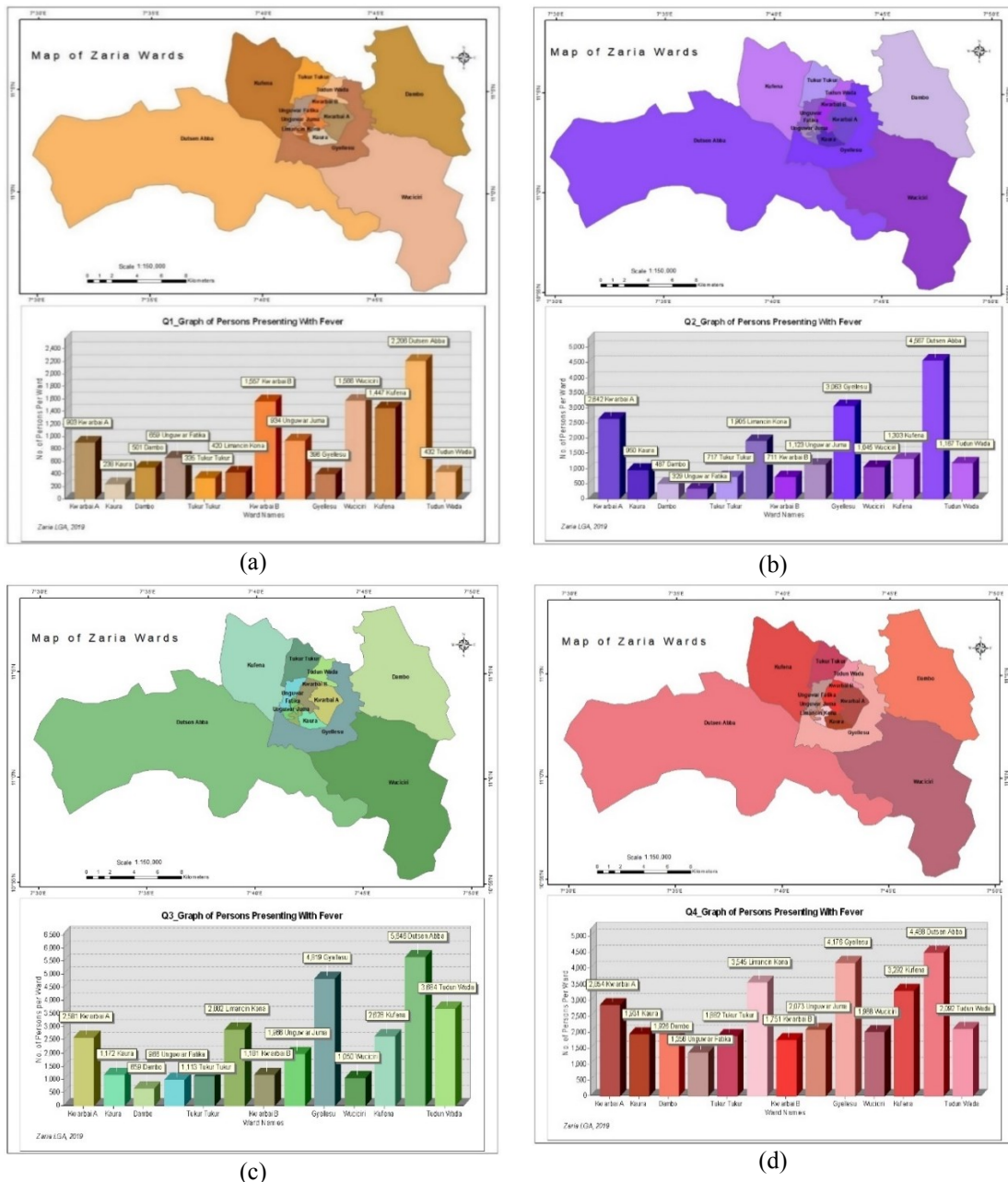


Figure 3. Persons with malaria; (a) First quarter; (b) Second quarter; (c) Third quarter; (d) Fourth quarter

Table 2. Summary of persons with confirmed cases of malaria in the study area

S/N	Name of location	First Quarter	Second Quarter	Third Quarter	Fourth Quarter	Annual cases of malaria
1	Kwarbai A	903	2642	2581	2854	8980
2	Kaura	238	950	1172	1931	4291
3	Dambo	501	487	659	1926	3573
4	Ungwar Fatika	659	329	966	1366	3320
5	Tukur-Tukur	335	717	1113	1882	4047
6	Limancin Kona	420	1905	2882	3545	8752
7	Kwabai B	1557	711	1181	1751	5200
8	Ungwar Juma	934	1123	1966	2073	6096
9	Gyellesu	396	3063	4819	4176	12454
10	Wuciciri	1566	1045	1060	1988	5659
11	Kufena	1447	1303	2628	3292	8670
12	Dutsen Abba	2206	4567	5646	4488	16907
13	Tudun Wada	432	1167	3684	2092	7375
<b>Total</b>		<b>11594</b>	<b>20009</b>	<b>30357</b>	<b>33364</b>	<b>95324</b>

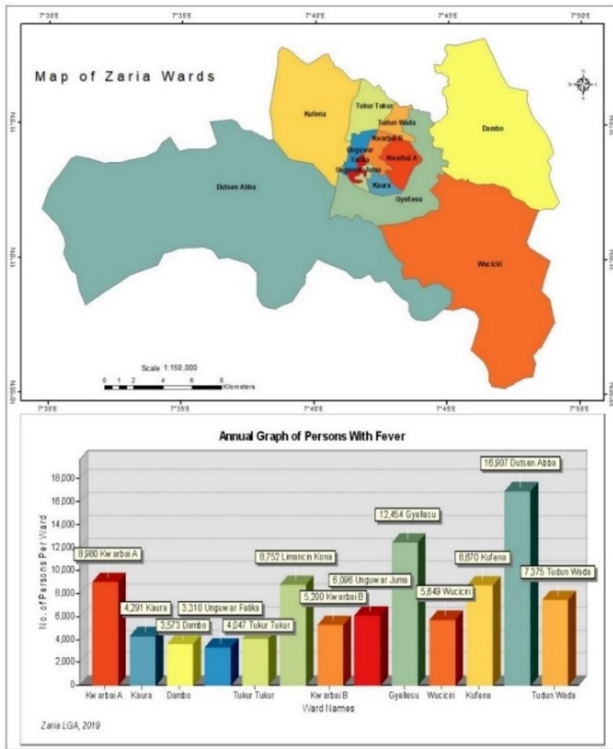


Figure 4. Annual Persons with Malaria

The results of the ANOVA one way test conducted on the persons confirmed with malaria showed that the prevalence of malaria incidences is significantly different

between the various hospital locations. A Tukey posthoc test showed that the prevalence of malaria at Dutsen Abba is significantly different from Kaura ( $p = 0.001$ ), Dambo ( $p = 0.004$ ), Ungwar Fatika ( $p = 0.003$ ), Tukur-Tukur ( $p = 0.006$ ), Kwarbai B ( $p = 0.02$ ), Ungwar Juma ( $p = 0.05$ ) and Wuciciri ( $p = 0.032$ ), respectively. This means that the incidences of malaria reported at Kwarbai A, Limancin Kona, Gyellesu, Kufena and Tudun Wada are not significantly different from Dutsen Abba.

5.3 Malaria burden maps

The malaria burden maps show how the malaria disease affects the most susceptible population. According to WHO (2018) and Awosolu et al. (2021), malaria affects children below five years and pregnant women more than other adults. Figure 5 (a) and (b) shows the prevalence of malaria disease amongst pregnant women and children under age 5, respectively. In Figure 5(a), it was observed that Zaria PHC, Tundun Wada at location 42, was the highest hit by malaria, followed by locations 9, 10, 48 and 35. In Figure 5(b), about four malaria hotspots at locations 2, 15, 42 and 47 were observed. This was followed by locations 12, 18, 19, 24, 36 and 44.

Generally, the incidence rate for children was observed to be higher than that of pregnant women. However, an independent t-test analysis conducted revealed that there was no significant difference between children below five years and pregnant women ( $p=0.066$ ).

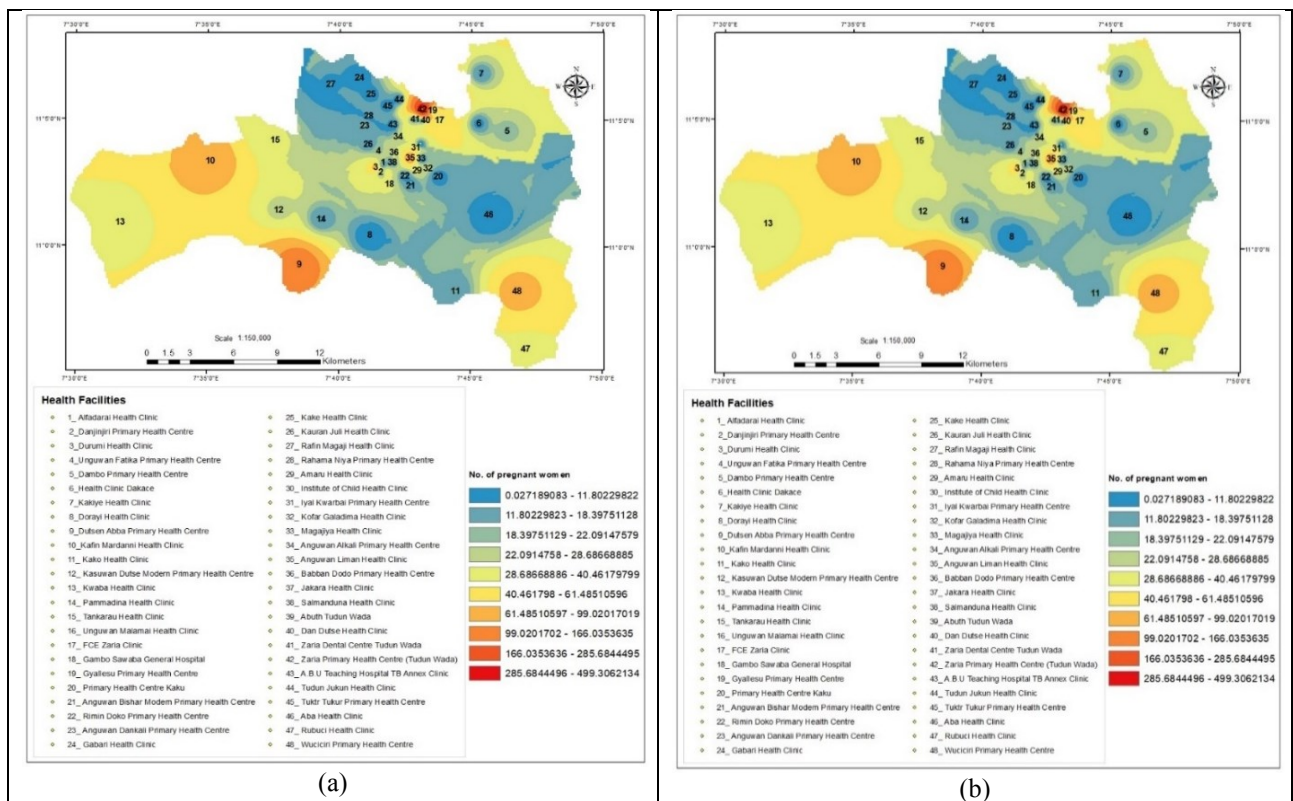


Figure 5. Distribution of malaria cases in 2019 amongst; (a) Women; (b) children less than 5 years

### 5.4 Malaria prevalence in Zaria

Mapping of the malaria prevalence provides information about the level of infection amongst the different strata of the population. Figure 6 shows how the infection rate varies from one place to another amongst children, pregnant women and adults. Each location on the map is represented by a graduated colour bar where yellow indicates children, red indicates pregnant women and green indicates adults. It was observed that pregnant women were the least affected as the red bar could only be seen at locations 3, 9, 1 and 42. This was followed by the children as the yellow bar could be seen across all the locations, however high malaria prevalence was observed at locations 15, 18, 19, 22, 24, 29, 42 and 47. Finally, the adult population (i.e., the entire population excluding children less than 5 and pregnant women) had the highest malaria prevalence in the study area as a high level of green is seen in all the locations. The highest values were observed at locations 19, 23, 31, 40, 42, 44 and 46 amongst others. Generally, the least infected population strata were the pregnant women while the most infected were the adult population.

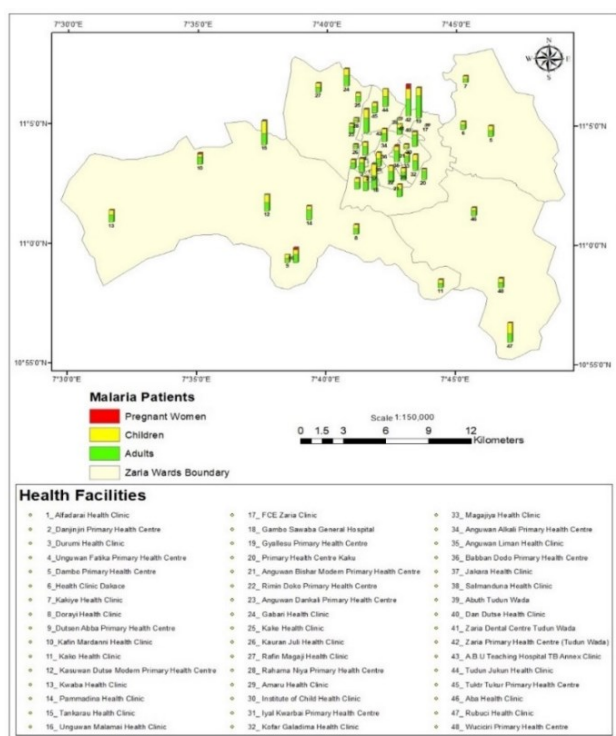


Figure 6. Malaria prevalence in Zari

Further comparison was carried out on the prevalence of malaria in the males and females in the study area. A higher prevalence of malaria of 73.35% was observed in the male compared to the female counterpart with a malaria prevalence of 26.65%. However, the independent t-test showed no significant difference between males and females ( $p=0.447$ ).

### 5.5 Malaria vector control maps

Vector control is a major prevention method and a continuous update of these maps provides a means to

follow up to the elimination stage. Figure 7 shows the distribution of LLIN to pregnant women and children in 2019. These maps visually present the level of the spatial coverage of the distributed LLIN. The serial numbers on the maps correspond to the numbers and names of health facilities in the legend. Distribution of LLIN is carried out by each of the health facilities and the colour gradient represents the number of recipients as shown in the legend. The red and blue shades on the map indicate areas of high and low distribution, respectively. Based on these distribution results, it was observed that other health facilities that had high malaria prevalence such as Alfadarari H. C. (1), Durumi H.C. (3), Rimi Doko H.C. (22), Angwan Dakari H.C. (23), Gabari H.C. (24) and Dan Dutse H.C. (40) did not receive adequate numbers of LLIN for their communities. This information provides the health workers in the LGA, the relevant details to take adequate measures to ensure adequate distribution of the LLIN to attenuate the spread of malaria in the area.

### 5.6 Service area map

Figure 8 shows the service area map used to define the catchment areas of each health facility based on the accessibility of the surrounding buildings. Buffers were created around the health facilities based on the travel distance (by footpath and road). The 0 – 3000m buffers were generated at 500m intervals. A width of 500m was specified as the optimal radius as used by Masoodi and Rahimzadeh (2015). This means that the maximum distance a patient is expected to travel to the health centre is 500m. Different polygon colour codes were used to signify varying distances from a given health facility. The result shows that none of the health facilities meets the requirement of accessibility of less than 500m. This means that most residents in the study area will have to travel more than 500m to receive medical services. Further, 28 health centres which represent 57.14% had accessibility of less than 1000m, while the remaining 21 which represented 42.86% had accessibility above 2000m. This implies that, the identified healthcare centers did not meet the 500m requirement. However, based on the study by Palaniyandi (2008), the 57.14% of clinical centers within the 1km buffer indicate that there is optimum healthcare services in the study area.

Analysis of the health centre to population ratio (1:10,000) stipulated by WHO (2012) in Eta et al. (2021) showed that some of the health centres did not meet the requirement as shown in Table 3. Based on these results, Kwarbai B with a population of 64,710 and currently having only 2 health centres, will require an additional 5 if adequate malaria services are to be provided. Kaura, Turkur-Turkur and Anguwar Fatika will require additional 3 health centres each, while Kwarbai A will require additional 2 health centres. It was also observed that, while some wards did not have adequate health centres, some wards had more than they require. Hence, Dutsen Abba had an excess of 4 while Kufena and Wuciciri both had 1 each.

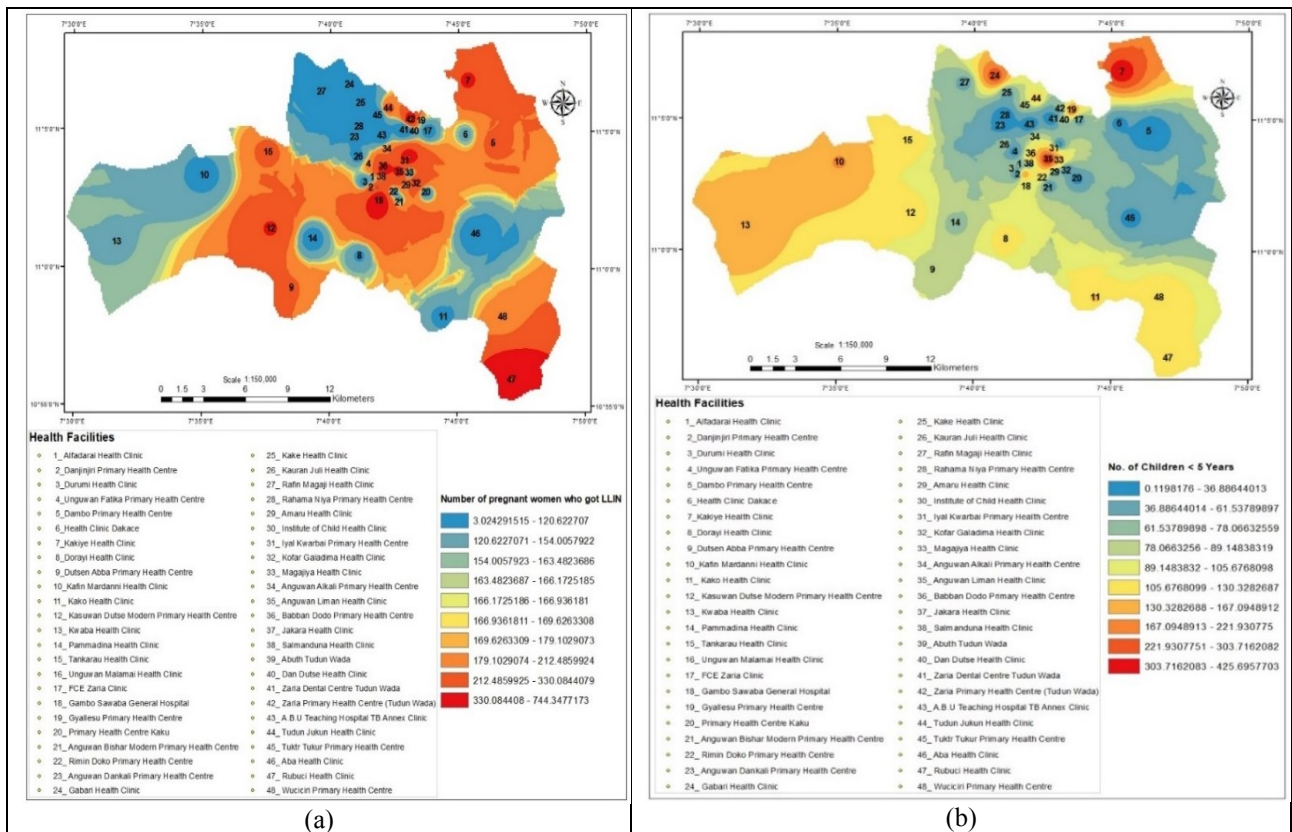


Figure 7. Distribution of LLIN in 2019; (a) Pregnant women; (b) children less than 5 years

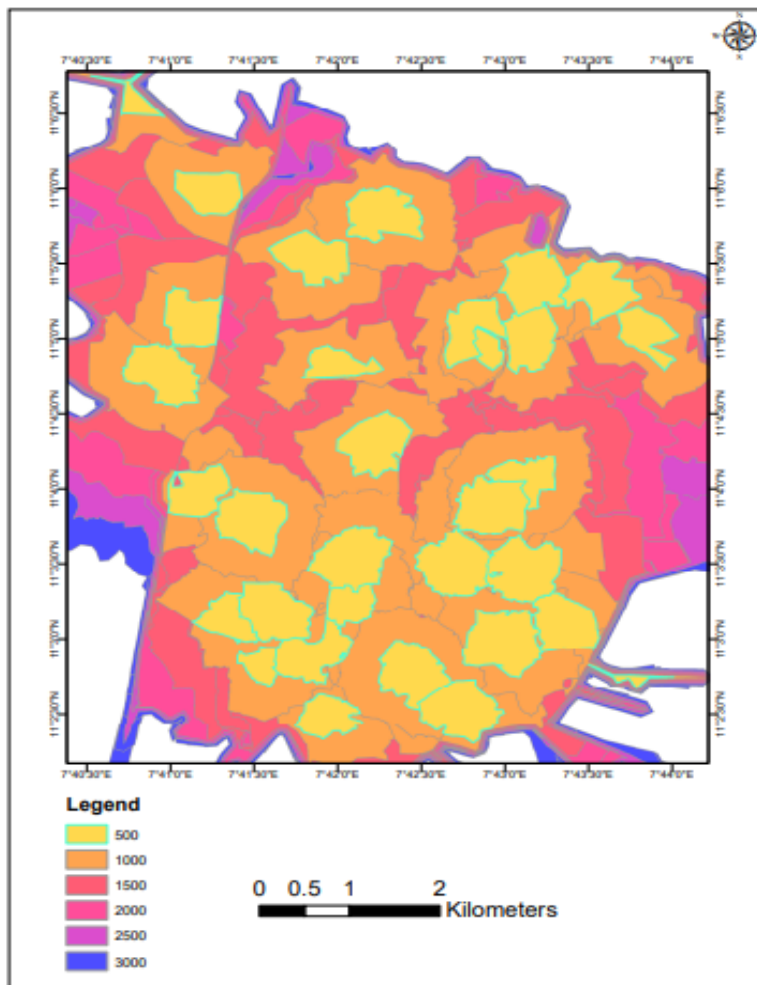


Figure 8. Service Area Coverage

**Table 3. Wards population in Zaria Local Government**

Wards	2019 Population Projection	Required by WHO 2012	Available ward	Shortfall	Excess
Dutsen Abba	46,383	5	9	-	4
Dambo	24,598	3	3	-	-
Gyellesu	42,041	4	4	-	-
Kaura	45,958	5	2	3	-
Kufena	49,791	5	6	-	1
Kwarbai A	69,943	7	5	2	-
Kwarbai B	64,710	7	2	5	-
Limancin Kona	33,733	3	3	-	-
Tukur Tukur	56,334	6	3	3	-
Tudun Wada	37,532	4	4	-	-
Unguwar Fatika	38,643	4	1	3	-
Unguwar Juma	31,956	3	3	-	-
Wuciciri	23,949	2	3	-	1
<b>Total</b>	<b>565,571</b>				

The overall ratio of the health centre to the population was computed using equation 1 (Mansour, 2016; Eta et al., 2021):

$$\frac{10,000 \times (\text{number of health centre})}{\text{population in each district}} \text{ ----- } 1$$

Based on equation 1, it was observed that Zaria LGA with an overall population of about 565,571 people had a ratio of 1.768. This indicates that the result meets the acceptable standard of 1:10,000 as recommended by Eta et al., (2021).

### 5.7 Discussion

The results of the annual persons with malaria show variation across the wards with Dutsen Abba and Gyellesu recording the highest prevalence of malaria in the study area. The results of the ANOVA one way test showed that the prevalence of malaria incidences is significantly different between the various hospital locations. A Tukey posthoc test showed that the prevalence of malaria at Dutsen Abba is significantly different from Kaura, Dambo, Ungwar Fatika, Tukur-Tukur, Kwabai B, Ungwar Juma and Wuciciri. These results corroborate the findings of Jimoh et al. (2019) who showed significant differences in the prevalence of malaria by hospital locations in Kaduna State. The result, however, disagrees with the findings of Awosolu et al. (2021), who reported lower cases of malaria in urban areas. The high reported cases of malaria in urban areas observed in this study may be due to the level of awareness of the consequences of malaria which encouraged the residents to report any symptoms related to malaria. It may also be due to the facilities available in the various health centres and the high population in some of these areas that lead to high malaria cases reported.

The highest prevalence of malaria (17.74%), observed in the study area is lower than the highest prevalence observed in some of the studies that reported above 50% in the southern part of Nigeria (Kalu et al., 2012; Nmor, 2015; Awosolu et al., 2021). This may be due to the difference in environmental condition of the area as there

is more rain in the south leading to favourable environmental conditions for mosquitoes to breed.

Our findings on the incidence rate of malaria for children less than five years old ( $\leq 5$  years) were observed to be higher than that of pregnant women. However, the independent t-test showed no significant difference ( $p = 0.066$ ). This result agrees with the findings of Nmor (2015) and Ocheje and Dogara (2016), who obtained similar results in southern Nigeria and Jigawa, respectively. The result is, however, different from the findings of Dawaki et al. (2016) and Jimoh et al. (2019) who reported that the effect on children below five years is significantly different from that of pregnant women in Kano and Kaduna States, respectively. The result is also at variance with the findings of Bajoga et al. (2019) and Awosolu et al. (2021) who reported that children are more affected than pregnant women in Kaduna State and Ibadan, in Oyo State, respectively. The low prevalence of malaria in children less than 5 years may be due to the improvement in the use of preventive measures such as the LLINs and insecticides by parents in the study area. These results provide health authorities with relevant information by which to scale up interventions in high hit areas which can be easily tracked by the serial numbers on the maps.

The comparison of the effect of malaria amongst the various groups revealed that the adult population were the most infected followed by children, while pregnant women were the least infected across the study population. This result is contrary to Awosolu et al. (2021), who reported that malaria infection decreased with increased age in Ibadan, Nigeria. This may be due to the involvement of adults in outdoor activities that keeps them late outside the home until night time which exposes them to mosquito bites more than others.

Concerning gender, the result showed that females were more affected by malaria than their male counterparts. However, the independent t-test revealed no significant difference in malaria prevalence between males and females ( $p = 0.447$ ). This result is contrary to other studies

that reported differences between males and females (Ocheje and Dogara 2016; Awosolu *et al.*, 2021).

Our findings also revealed that the distribution of LLIN in the study area is not based on the prevalence of malaria in the area as some health centres with high cases of malaria prevalence (1, 3, 22, 23, 24 and 40) did not receive adequate numbers of LLINs. The information provided in this study informs the health authorities saddled with the responsibility of malaria control in the area, with the necessary details to ensure fair distribution of the LLIN to the wards.

The service area map showed that none of the health centres meets the minimum requirement of 500m for residents for easy accessibility. This is contrary to the findings of Masoodi and Rahimzadeh (2015) who reported some health facilities to have an accessibility of less than 500m. Most of the health centres were concentrated in the urban areas where there is a high population. This left some of the areas such as Dakace, Panmadina, and Unguwar Malamai, amongst others, underserved. The implication of this is that, residents in such areas will have to travel long distances to access health facilities. This might lead to health complications as many residents find it difficult to transport themselves to the health centres. This report corroborates the result of Aliyu *et al.* (2020) who observed a similar situation in Borno State, Nigeria. One way to cushion this effect is to provide more health care centres, especially in highly populated areas. Thus, Alfararai, Jakara, Salmanduna and Rimi Doko health centres may need additional health centres to attenuate the pressure on the health workers and to enhance service delivery.

Finally, our findings also show that the health centre to population ratio (1:10,000) provided by WHO (2012) in Eta *et al.* (2021) did not meet the requirement in some of the wards. However, the overall health centre to population ratio was 1.768 which shows agreement. This result corroborates the findings of Eta *et al.* (2021) who obtained a similar result in the Kaduna metropolis. The results also show that some wards had more health centres than the required number despite the limited number in some wards. This means that the location of the health centres in the area was not entirely based on population. This agrees with the findings of Ujoh and Kwaghsende (2014) who reported similar findings in Benue State. The implication of this is that the wards with limited health centres will be overstretched and residents will have to travel several kilometres to access health services. It is important, therefore, to consider wards with limited health centres for addition to enhance service delivery in the area.

## 6. Conclusion

This study set out to create an SDSS for malaria monitoring in parts of Zaria using GIS techniques. By integrating the existing malaria data with other secondary data in a GIS environment, it was possible to identify malaria prevalence and also appraise the spatial variability of malaria as it affects pregnant women, children and adults. After several data analyses, the resulting maps were

presented to convey different types of information, one at a time while showing the various patterns of malaria incidence in Zaria. The maps produced can be used effectively as a means of monitoring, evaluation and surveillance to reduce the spread of malaria in Zaria. Based on the findings of this study, it is recommended that the Kaduna State Ministry of Health should invest in the deployment of a GIS-based SDSS for effective planning and management of malaria incidences in the Zaria metropolis as this aligns with the sustainable development goal (SDG) target 3.3.

## References

- Abduselam A., W. Abdo, A. Mohammedreha and M. Ferhan (2020). Malaria Hazard and Risk Analysis Using GIS and Remote Sensing in Korahey Zone of Somali Regional State, Eastern Ethiopia. *American Scientific Research Journal for Engineering, Technology, and Sciences* (ASRJETS), 68(1), 20-39.
- Ahuru D. R. and I. J. Omon (2018). The Economic Burden of Malaria: Evidence from Nigeria's Data. *Amity Journal of Healthcare Management*, 3 (1), 28–39.
- Aliyu Y. A. and J. O. Botai, (2018). An exposure appraisal of outdoor air pollution on the respiratory well-being of a developing city population. *Journal of Epidemiology and Global Health*, 8(1-2), 91-100.
- Aliyu U. A., M. A. Kolo and M. Chutiya (2020). Analysis of distribution, capacity and utilization of public health facilities in Borno, North-Eastern Nigeria. *Pan African Medical Journal*. 35: 39.
- Awosolu O. B., Z. S. Yahaya, M. T. F. Haziqah, I. A. Simon-Oke and C. Fakunle (2021). A cross-sectional study of the prevalence, density, and risk factors associated with malaria transmission in urban communities of Ibadan, Southwestern Nigeria. *Heliyon* 7(1), e05975.
- Azua S., S. I. Nnah and H. U. Ikwueze (2020). Spatio-temporal Variability of Landuse Landcover and its Impact on Land Surface Temperature in Zaria Metropolis, Nigeria. *FUTY Journal of the Environment*, 14(1), 1-11.
- Bajoga U. A., S. B. Hadiza, A. O. Abayomi, M. D. Mahmood, B. S. Ibrahim, S. I. Muhammed, S. A. Ayo, O. A. Babatunde, Y. Mohammed, O. A. IkeOluwapo, M. N. Patrick and O. A. Olufemi (2019). Trend of malaria cases in Kaduna State using Routine Surveillance Data, 2011-2015. *The Pan African Medical Journal*, 32 (Supp 1):8.
- Bamidele J. O., M. I. Ntaji, E. A. Oladele and O. K. Bamimore (2012). Community Participation in Malaria Control in Olorunda Local Government Area, Osun State, Southwestern Nigeria. *African Journal of Infectious Diseases*, 6(2), 24 – 28.
- Besansky N. J., C. A. Hill and C. Constantini (2004). No Accounting for Taste: Host Preference in Malaria Vector. *Trends Parasitol*, 20, 249-251

- Dawaki S., M. A. Hesham, I. Init, I. Jamaiah, M. A. Wahib, M. A. Awatif, S. Hany, N. E. Fatin, U. A. Ado, I. Y. Saadatu, A. Abdulhamid, A.A. Mona, R. S. Lahvanya, A. N. Nabil and L. Yee- Ling (2016). Is Nigeria winning the battle against malaria? Prevalence, risk factors and KAP assessment among Hausa communities in Kano State. *Malaria Journal*, 15, 1-14.
- Eta J. B., M. Aliyu, N. M. Ihenacho, A. I. J. O. Ibrahim, and D. A. Egbunu (2021). Assessment of Spatial Distribution of Health Facilities in Kaduna Metropolis. *International Journal of Scientific & Engineering Research*, 12(4), 803-810.
- Idowu A. P., N. Okoronkwo and R. E. Adagunodo (2009). Spatial Predictive Model for Malaria in Nigeria [Electronic Version]. *Journal of Health Informatics in Developing Countries*, 3(2), 30-36.
- Jimoh A. A., Z. Abdullahi and S. H. Dogo (2019). Comparative Study of Prevalence, Control and Treatment of Malaria in Urban and Rural Hospitals of Kaduna State, Nigeria. *Nigerian Journal of Pharmaceutical Sciences*, 18(1), 16-25.
- Kalu M. K., N. A. Obasi, F. O. Nduka and G. Otuchristian (2012). A comparative study of the Prevalence of malaria in Aba and Umuahia urban areas of Abia State, Nigeria. *Research Journal of Parasitology*, 7, 17-24.
- Kelly G. C. (2010). Modern geographical reconnaissance of target populations in malaria elimination zones. *Malaria Journal*. 9, 289.
- Masoodi M. and M. Rahimzadeh (2015). Measuring access to urban health services using Geographical Information System (GIS): a case study of health service management in Bandar Abbas, Iran. *International Journal of Health Policy Management*, 4(7): 439–445.
- Mansour S. (2016). Spatial analysis of public health facilities in Riyadh governorate, Saudi Arabia: A GIS-based study to assess geographic variations of service provision and accessibility. *Geo-spatial Information Science*, 19, 26-38.
- Nmor J. C. (2015). Health care-seeking behaviour for malaria among laboratory-confirmed out-patients in a rural community, Southern Nigeria. *International Journal of Tropical Disease and Health*, 6(1), 8-13.
- Nyagba L. (1986). Soils, Climate and Vegetation. Institute of Education Press, A.B.U. Zaria. Accessed 10 February 2020.
- Ocheje A. J and M. M. Dogara (2016). Prevalence and risk factor of malaria, Jigawa. *International Research Journal of Public and Environmental Health*, 3(11), 270-277.
- Ojo W., M. Onazi and O. Olaniyi (2016) Geographical Reconnaissance of Household in Northern Nigeria towards Optimizing Indoor Residual Spraying Method for Malaria Elimination. *Journal of Geographic Information System*, 8, 737-748. doi: 10.4236/jgis.2016.86057.
- Omitola O. O., C. U. Umunnakwe, A. A. Bayegun, S. A. Anifowose, H. O. Mogaji, A. S. Oluwole, S. N. doemene, T. S. Awolola, A. A. Osipitan, S. O. Sammy Olufemi Sam-Wobo and U. F. Uwem Friday Ekpo (2021). Impacts of ivermectin mass drug administration for onchocerciasis on mosquito populations of Ogun state, Nigeria. *Parasites Vectors*, 14(1), 1-12.
- Palaniyandi M. (2008). GIS for lymphatic filariasis morbidity management and control *Coordinates*, 5(5), 24-28.
- Sturrock H. J. W., M. S. Hsiang, J. M. Cohen, D. L. Smith, B. Greenhouse, T. Bousema and R. D. Gosling (2013). Targeting Asymptomatic Malaria Infections: Active Surveillance in Control and Elimination. *PLoS Med*, 10:e1001467.
- Ujoh F. and F. Kwaghsende (2014). Analysis of the Spatial Distribution of Health Facilities in Benue State, Nigeria. *Public Health Research*, 4(5), 210-218.
- Wangdi, K., C. Banwell, M. L. Gatton, G. C. Kelly, R. Namgay and A. C. Clements (2016). Development and evaluation of a spatial decision support system for malaria elimination in Bhutan. *Malaria Journal*, 15(1), 1-13.
- WHO, (2017). *World Health Organization – World malaria report 2017*. Geneva, Switzerland: WHO. Available at <https://www.who.int/malaria/en/>. Accessed 6 August 2018.
- WHO, (2018). *World Health Organization - World malaria report 2018*. Geneva, Switzerland: WHO. Available at: <https://www.who.int/news-room/q-a-detail/world-malaria-report-2018>. Accessed 12<sup>th</sup> February 2020.
- WHO, (2021). *World Health Organization – Malaria Fact Sheet*. Available at <https://www.who.int/news-room/fact-sheets/detail/malaria>
- Yusuf, Y.O. and M. I. Shuaib (2012). The Effect of Wastes Discharge on the Quality of Samaru Stream, Zaria, Nigeria, Ecological Water Quality - Water Treatment and Reuse, Dr. Voudouris (Ed.), ISBN: 978-953-51-0508- 4, InTech, Available at: <http://www.intechopen.com/books/ecological-water-quality-water-treatment-andreuse/the-effect-of-wastes-discharge-on-the-quality-of-samaru-stream-zaria-Nigeria>. Accessed 10 February 2022

# A framework to Georeference Point Cloud in GPS Shadowed Urban Environment by Integrating Computer Vision Algorithms and Photogrammetric Techniques

Mayank Sharma<sup>1,2,\*</sup>, Raghavendra Sara<sup>1</sup> and Shefali Agrawal<sup>1</sup>

<sup>1</sup> Photogrammetry and Remote Sensing Department, Indian Institute of Remote Sensing, Dehradun, Uttarakhand

<sup>2</sup> Indian Institute of Technology Roorkee, Uttarakhand

\*Email: mayanksharma.iirs@gmail.com

(Received: Jan 4, 2022; in final form Sep 13, 2022)

**Abstract:** The integration of computer vision algorithms and photogrammetric techniques has become an alternative to the high-cost Mobile Mapping Systems (MMS) and point cloud generation through Structure from Motion (SfM) algorithm is the best example of it. The point cloud generated using SfM is an arbitrary coordinate system and for its georeferencing known global coordinates of the camera exposure stations, rotational and translational parameters are required. The global coordinates of exposure stations are obtained through GNSS (Global Navigation Satellite System). GPS (Global Positioning System) is widely used for getting the positional information of a point. The problem in georeferencing the point cloud arises if the coordinates of a few camera exposure stations are unknown due to GPS shadowing or poor GDOP (Geometric Dilution of Precision). This issue is common in MMS that use laser scanners, GNSS and IMU (inertial measurement unit). In this paper, efforts are made to develop a methodology for handling GPS shadowing or poor accuracy for the georeferencing of arbitrary point clouds generated through SfM. The adopted method uses a blend of photogrammetric techniques of space resection and space intersection to determine the unknown camera exposure stations' coordinates. Bundle adjustment is applied to improve the accuracy of the results obtained. The developed methodology is well analyzed in different cases, and the results show good accuracy in respective cases.

**Keywords:** Computer Vision, space resection, space intersection, collinearity equations, GPS shadowing

## 1. Introduction

Computer vision and photogrammetry are different fields; however, their integration provides much easier 3D reconstruction from images. Computer vision algorithms are mathematical techniques for image-based reconstruction (Szeliski 2010). Computer vision algorithms are finding their applications both in photogrammetry and mobile mapping. The ability of computer vision algorithms to provide camera information (exterior orientation) has become an alternative to high-cost IMU (Inertial Measurement Unit)/INS (Inertial Navigation Sensors) and thus offer a cost-effective solution to high-cost Mobile Mapping technology for geospatial data collection with the rapid and easy acquisition of the data as the significant advantages (Li 1997).

The recent developments in digital photogrammetry and computer vision-based image processing techniques have formed a new milestone for image-based three-dimensional (3D) reconstruction (Mugnai and Tucci 2022). Both digital photogrammetry and computer vision are different fields, but their integration has numerous applications (Granshaw and Fraser 2015). The role of computer vision technology in Close range photogrammetric applications and mobile mapping technology is increasing at a high pace. Close range photogrammetry provides a low-cost solution for generating georeferenced 3D models, point cloud and digital elevation models (DEMs), etc., with good accuracy. A plethora of literature is available that reports good achievable accuracy through close-range photogrammetric applications. The integration of Computer Vision algorithms with photogrammetric processes is in high demand as this integration results in a cost-effective solution to mobile mapping systems (MMS).

A typical MMS consists of a mobile or moving platform, navigation, and mapping sensor. Mapping sensors may be metric and non-metric cameras, laser scanners, or RADARs. They are used for collecting information about the objects to be surveyed. Navigational sensors such as Global Positioning System (GPS)/IMU are used for obtaining positional and orientation information of the mapping sensors (Li 1997). Navigational sensors play a vital role in geocoding the data acquired from camera and Laser scanners. However, these sensors are expensive, due to which the MMS has been a costly geospatial mapping tool (Warnasch and Killen 2002). Despite this, IMU accumulates bias with time if not corrected by coupling it with GPS. Further, GPS unavailability or lower accuracy of GPS signals affect MMS working in GPS shadowed environments. GPS shadowed environments are the regions where GPS signals are not available or the satellite visibility is poor (Spilker 1996). Thus, Computer vision algorithms, along with photogrammetric techniques, are in high demand. The most widely used computer vision algorithm for point cloud generation is the structure from motion (SfM). It is used for image-based reconstruction and generates a point cloud in an arbitrary coordinate system. The integration of SfM with the photogrammetric techniques enables the estimation of camera parameters and generation of point clouds with reasonable accuracy (Yang et al. 2013). Further, if the coordinates of exposure stations are known, then the point cloud's georeferencing can be done using the direct georeferencing approach, in which the ground control points (GCPs) are not required (Gabrlik 2015; Rizaldy and Firdaus 2012). However, the unavailability or poor GDOP (Geometric Dilution of Precision) of GPS signal affects the point cloud's georeferencing accuracy (Liu et al. 2022). The possible reasons for GPS unavailability or poor accuracy are poor GDOP, high-rise buildings in urban areas and dense forest canopy, etc. Both photogrammetric and mobile mapping

technologies suffer from GNSS (Global Navigation Satellite System) signal unavailability and poor accuracy in GNSS shadowed regions.

This paper introduces an approach to handle the problem of GPS unavailability or lower accuracy in the GNSS shadowed regions for the georeferencing of an arbitrary point cloud generated using SfM. OSM (Open Street Map) Bundler software is a free software that works on SfM. The OSM Bundler software (Lourakis and Argyros 2009; Snavely et al. 2006, 2008) uses the Structure from Motion algorithm for the point cloud generation. PMVS (Furukawa and Ponce 2010) and CMVS packages are also available with Bundler to convert sparse point cloud to dense point cloud. The generated point cloud is in a local coordinate system. To georeference it, global coordinates of each camera exposure station are required. The technique to georeference the point cloud with the help of camera station coordinates is known as direct georeferencing. It does not require ground control points (GCPs) on the surface or target (Liu et al. 2022). Again, the requirement of GNSS availability with proper accuracy is mandatory to achieve better georeferencing accuracy.

## 2. Related works

Highly advanced real-time kinematic (RTK) GNSS receivers used in MMS are available nowadays. These RTK receivers are also used in drones or UAVs (Unmanned Aerial Vehicles) and capture the location of the camera exposure station. Although the accuracy of these instruments is high; however, the speed of drones in aerial surveys and vehicles' high speed in MMS may distort the positional accuracy of these instruments (Liu et al. 2022; Sanz-Ablanedo et al. 2018). Several researchers have highlighted that the accuracy of GNSS receivers plays a crucial role in the accurate georeferencing of the acquired datasets (McMahon et al., 2021). This study also focusses on the georeferencing accuracy of the point cloud data generated using SfM. SfM is a widely used algorithm for photogrammetric point cloud generation and is now more common in UAV photogrammetric processing (Martínez-Carricondo et al. 2018). However, the direct georeferencing of the products of SfM becomes challenging in case the accurate GPS locations of the camera exposure stations are unavailable or inaccurate.

A lot of work has already been done to improve GPS accuracy and handle GNSS unavailability. The capabilities of GPS receivers have already improved a lot to provide better accuracy in complex environments. Specific models are also developed to address the unavailability of GPS signals in dense urban and forest areas. Most of the studies to handle GNSS unavailability are in the field of intelligent driverless transportation. Architecture based on the integration of GNSS/INS instruments to update the position of a vehicle in the absence of GNSS signals is used by (Li et al. 2022). Hassan et al. (2006) present the photogrammetric approach to georeference the overlapping sequence of images captured through MMS in the absence of GPS signals or if weak signals are available. Even the proposed method produces good results;

however, the use of VISAT MMS makes it an expensive approach because of its complex setup and high-cost instruments. Scarmana (2007) also explains developing a prototype to support mobile mapping in GPS unavailable areas using photogrammetric concepts, land surveying, and dead-reckoning techniques. Digital compass, laser range finder, and smartphone supporting GPS are used to configure a portable unit. Thus it requires several external instruments, which again becomes an expensive approach. Choi and Chang (2019) also used these external instruments (IMU and GPS) for accurately estimating the vehicular position in the shadowed regions. Their simulative study provided good accuracy in the shadowed areas. One of the studies presented by Nguyen et al. (2019) combines two range-based non-GPS localization methods by assigning different weights and performing the analysis of the combinations. The simulative study uses AOA (Angle of Arrival) and RSSI (Received Signal Strength Indicator) with different weights to analyze the effects of shadowing. It shows that accuracy and precision have significantly improved by increasing and decreasing the weight of AOA and RSSI, respectively.

The problem of GPS unavailability or poor performance of GPS receivers is commonly seen in dense urban areas and is well explained by Groves (2011). High-rise buildings in urban areas interrupt the proper reception of GPS signals and thus act as an obstruction for obtaining the appropriate positioning information in dense urban areas. Groves (2011) also explains the limitation of GPS in cross-street positioning and presents a shadow matching technique to achieve accurate positioning information in dense urban areas. In this technique, 3D city models are used to predict the availability of GPS signals. GPS, along with other GNSS satellites, is modelled to enhance signal availability in narrow streets or urban areas with high-rise buildings. Clark and Bevely (2008) presented a GPS/INS integrated approach to detect the signal attenuation and boost the GPS positioning accuracy in a shadowed environment. Several high-quality GPS receivers are also developed that support the efficient reception of weak GPS signals. Huang et al. (2009) explain the implementation of chaotic oscillators to enhance weak GPS signal reception. The application of non-linear dynamics has resulted in less acquisition time.

Images acquired from different static locations covering an object with proper successive overlap were used by Jariwala et al. (2014) to generate the three-dimensional point cloud by applying the SfM algorithm. Georeferencing of the generated three-dimensional point cloud was done using the space intersection technique. For georeferencing the generated point cloud, exposure station coordinates corresponding to the images used for point cloud generation are required and are obtained through DGPS (Differential GPS) survey. Thus, the impact of GPS unavailability or poor accuracy directly affects the georeferencing accuracy of the generated point cloud. Computer vision algorithms are widely used for image-based 3D reconstruction. Yang et al. (2013) used the SfM algorithm, Clustering Views for Multi-view Stereo (CMVS), Patch-based Multi-view Stereo (PMVS) and Poisson surface reconstruction techniques for 3D generation from the images taken from conventional

cameras. The benefit of using a computer vision algorithm (SfM) of not requiring any prior information of the camera's internal and exterior orientation parameters is highlighted in this study (Arévalo-Verjel et al. 2022). The research works highlighted in this section clearly indicate the need to handle the problem of GNSS shadowing and thus help boost the potential of this study.

### 2.1 Collinearity equations

As per the collinearity equations, the camera exposure station, an object point, and its image point in a 3D space lie along a straight line (DeWitt and Wolf 2000). Collinearity equations for space intersection are used to determine the coordinates of the unknown camera stations, and then bundle adjustment is applied to improve the results and achieve high accuracy. This approach can be utilized in Mobile Mapping Systems to overcome GPS unavailability or GPS shadowing. Figure 1 describes the existence of the collinearity condition among camera exposure station, object point on the ground, and its image point. This basic principle is utilized in the space intersection technique to determine an unknown camera station's coordinate.

To determine global coordinates of the points that are available on two or more overlapping images, interior and exterior orientation parameters are required. These orientation parameters are obtained using the Structure from Motion algorithm.

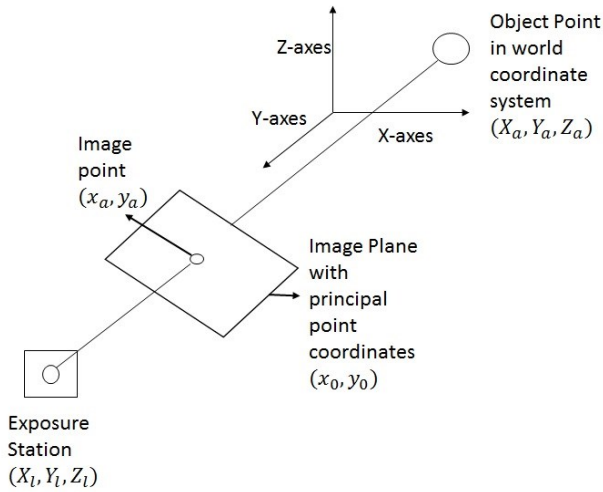


**Figure 1. Illustration of Collinearity Equation**

The collinearity conditions are generally expressed as:

$$x_a = x_0 - f * \left[ \frac{m_{11}(X_A - X_L) + m_{12}(Z_A - Z_L) + m_{13}(Y_L - Y_A)}{m_{31}(X_A - X_L) + m_{32}(Z_A - Z_L) + m_{33}(Y_L - Y_A)} \right] \quad (1)$$

$$y_a = y_0 - f * \left[ \frac{m_{21}(X_A - X_L) + m_{22}(Z_A - Z_L) + m_{23}(Y_L - Y_A)}{m_{31}(X_A - X_L) + m_{32}(Z_A - Z_L) + m_{33}(Y_L - Y_A)} \right] \quad (2)$$

Here,  $(x_a, y_a)$  are image coordinates of the object points,  $(x_0, y_0)$  are the principal point locations,  $f$  is the focal length of the camera,  $X_L, Y_L, Z_L$  are exposure station coordinates,  $(X_A, Y_A, Z_A)$  are ground control points,  $(m_{11}, m_{12} \dots m_{33})$  are rotation parameters and are the functions of rotation angles (omega, phi, and kappa). The principal point location and focal length of the camera are intrinsic camera parameters. These parameters can be

obtained by performing camera calibration. These camera parameters are required to handle the positional shift of a projected point onto an image plane (Scarmana, 2007).

### 3. Study area and dataset

The study area to conduct this study includes two buildings. The description of the selected buildings is given below:

**Building 1:** The first building chosen for this study is the main building of IIRS (Indian Institute of Remote Sensing), Dehradun, Uttarakhand. It has a simple architecture. Figure 2(a) shows the structure of Building 1.

**Building 2:** The second building chosen to validate the developed methodology is the building of the Godavari Hostel of IIRS, Dehradun, Uttarakhand. This building has comparatively complex architecture. Figure 2(b) shows the structure of Building 2.

The dataset used in this study includes the images acquired through the NIKON D60 camera without any zoom. The global coordinates of the image acquisition locations were measured along with the images, using the Trimble R7 GNSS (Global Navigation Satellite System) receivers. The GNSS data was post-processed in the Trimble Business Centre (TBC) software.

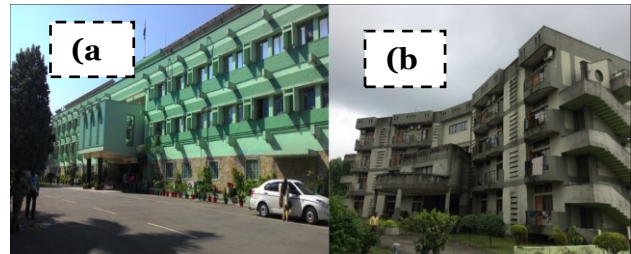


**Figure 2. (a) Building 1 and (b) Building 2**

### 4. Methodology for handling GNSS shadowed regions

The framework to carry out this study starts with the data collection task. The overlapped images of the study area are acquired sequentially using NIKON D60 camera mounted over a tripod. A total of 19 images are captured to cover the complete building façade. Along with image acquisition, the position of the camera exposure station is also measured using the Trimble R7 GNSS receiver. The global coordinates of the camera exposure station are required to georeference the point cloud data. To avoid the issue of time synchronization among sensors, the study is carried out in static conditions. The coordinates of camera exposure stations are obtained by the post-processing of DGPS data in Trimble Business Centre software. The developed methodology is tested on Building 1. In this case, the location of a few camera exposure stations assumed to be unknown, as shown in Figure 3. Thus, it requires that the unknown locations of camera exposure stations should be determined for georeferencing the point cloud generated from images using the SfM technique. The methodology to handle the GPS unavailability problem is shown in Figure 4. The images captured using the digital camera are processed

using OSM Bundler software (Snavely et al. 2006, 2008) to generate the sparse point cloud. Bundler uses the SfM computer vision algorithm for 3D sparse reconstruction. SfM is a highly robust computer vision algorithm that generates the sparse point cloud from overlapping images. It is the robustness of SfM that makes it suitable to apply it on disordered images.

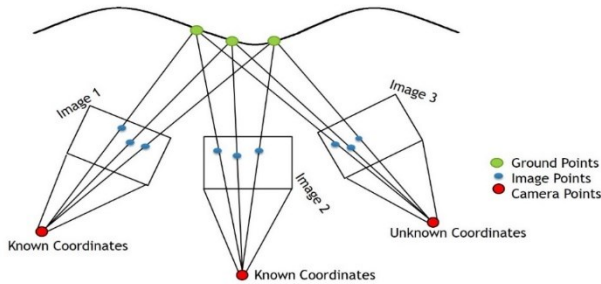


Figure 3. GPS unavailability problem

The point cloud generation through SfM include SIFT (Scale Invariant Feature Transform), ANN (Approximate Nearest Neighbour) (Mount and Arya 2010), RANSAC (Random Sample Consensus) algorithm (Fischler and Bolles 1981) and SBA (Sparse Bundle Adjustment) (Lourakis and Argyros 2009). The SIFT algorithm was developed by (Lowe, 1999) and is used for detecting the features in an image and matching them on other images using the Euclidean distance measurement. SIFT is a robust algorithm, independent of the image scale and orientation. It localizes the detected features and preserves their orientation information obtained through gradient analysis. In SIFT, multiple views are generated using the Gaussian scale space function as shown in equation (3) (Lowe 2004).

$$L(x, y, \sigma) = G(x, y, \sigma) * I(x, y) \quad (3)$$

Here \* is representing the convolution of variable Gaussian scaling function ( $G(x, y, \sigma)$ ) and the input image ( $I(x, y)$ ). As given in equation (4), the DoG (Difference of Gaussian) method where the difference of two images are taken is implemented for getting the extrema of scale space.

$$D(x, y, \sigma) = L(x, y, k\sigma) - L(x, y, \sigma) \quad (4)$$

In equation (4),  $D(x, y, \sigma)$  represents the difference between a scaled image and its unscaled version. To detect the stable features on the difference image ( $D(x, y, \sigma)$ ), extremas are found by identifying the local maxima and minima by comparing every pixel to its 26 neighbours, in which eight neighbours belong to the same scale image and nine each in upscaled and downscaled images. Then, to remove the insignificant features, localizing the keypoints is done by computing the Laplacian on the difference images. It is computed by taking the second derivative of the difference image as given in equation (5). In this process, keypoints having poor contrast or are present on the edges are removed (Lowe 2004).

$$z = -\frac{\partial^2 D^{-1}}{\partial x^2} \frac{\partial D}{\partial x} \quad (5)$$

The value of  $z$  signifies the stability of a key point. A key point is discarded, if its value is below a given threshold as it is considered to be the keypoint with lower contrast. A Hessian Matrix of order  $2 \times 2$  is formed for the location of the keypoint. The ratio of this matrix's highest and lowest eigen vectors is compared to the curvature difference in the horizontal and vertical direction on the difference image. This comparison results in the removal of the keypoints present on the edges. Further, the selected keypoints are assigned an orientation. This orientation assignment of the keypoints makes the algorithm orientation independent. Magnitude gradient and the orientation angles are estimated on the Gaussian smoothed image as per equations (6) and (7).

$$m(x, y) = \frac{1}{\sqrt{(L(x+1, y) - L(x-1, y))^2 + (L(x, y+1) - L(x, y-1))^2}} \quad (6)$$

$$\theta(x, y) = \tan^{-1} \left( \frac{L(x, y+1) - L(x, y-1)}{L(x+1, y) - L(x-1, y)} \right) \quad (7)$$

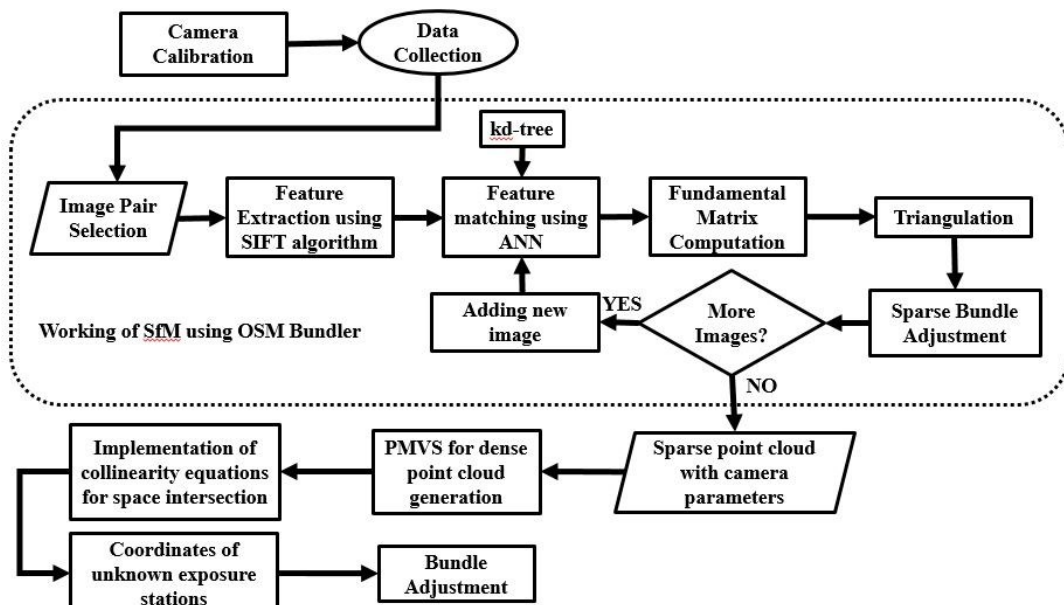


Figure 4. Approach to handle GPS unavailability

Estimated gradient of the orientation is then used to construct a histogram of orientation. The global maxima of the peaks in the histogram is used along with the other local maxima with height up to 80% of the highest peak, to assign the orientation to a keypoint. After orientation assignment, the image gradient data is further used for the creation of keypoint descriptors. The rotation in gradient data is made to align it with the keypoint's orientation and further assigned a weight by Gaussian window. The generated output is subsequently utilized for creating histograms with keypoint at the centre. The keypoint descriptors are arranged in grids of order  $4 \times 4$ . Each grid cell has a further 8 bin orientation histogram representing major directions as per the compass and their midpoints. This generated an output vector which is known as SIFT keys. Each feature vector or SIFT key contains 128 elements. These feature vectors or SIFT keys are further used for the feature matching task. For feature matching, firstly the SIFT feature descriptors are computed for an image and the corresponding SIFT keys are stored in a database. These feature vectors or SIFT keys are matched with the feature vectors of a new image. The matching depends on the Euclidean distance estimation among the feature vectors (Lowe 1999; Lowe 2004). The task of feature matching consumes a lot of time. Thus, ANN is used to optimize the feature matching process by identifying the closest neighbours. It uses kd-tree which is generated with every keypoints of an image (Mount and Arya 2010) so that any queried point could be easily matched with the keypoints of the other image. It uses Minkowski metrics that comprises of Manhattan, Euclidean and max distance. Feature matching also results in a few outliers, and removal of these outliers is necessary. RANSAC is used here to remove the outliers. RANSAC, an iterative algorithm, implements the least squares method to identify the outliers present in the dataset. Then the fundamental matrix is computed that preserves the information about the epipolar geometry and keep a track of relationship of matched feature points. The best matched image pairs are identified through fundamental matrix and a new image is taken further to find the matches again. Finally, the bundle adjustment is applied for parameters optimization and reconstruction of the sparse point cloud.

Along with the point cloud, Bundler generates a camera parameter file that contains the interior and exterior orientation parameters of each exposure station. These parameters are further used to solve the collinearity equations. Before data acquisition, the camera's intrinsic parameters like focal length, principal point location, and lens distortion parameters are estimated by performing camera calibration. To obtain the coordinates of an unknown camera station, global coordinates of at least two common points on the adjacent image (whose camera station coordinates are known) are required. These consecutive images should have proper overlap so that a single point is visible in at most two images. Since the coordinates of the exposure station of the adjacent image are known, so, the global coordinates of the common points can be calculated using collinearity equations. In this case, there are three unknowns ( $X_A, Y_A, Z_A$ ) so at least three equations are required to solve these equations. Since

a point is available in at least two images, so four equations are obtained for a point (two from each image). Then the least square adjustment is applied to obtain the solution. Further to obtain the global coordinates of the unknown exposure station are calculated by using these known points as GCPs to solve equations 1 and 2. In this case, the unknowns are ( $X_l, Y_l, Z_l$ ). Therefore, two points are sufficient to obtain the solution of collinearity equations. Here more number of common points can increase the accuracy; however, two points are enough to get the solution of collinearity equations. A code to determine the coordinates of an unknown camera station is developed in Matlab as well as in Python for the implementation of collinearity equations. These obtained coordinates are used as initial values to perform bundle adjustment in Leica Photogrammetry Suite (LPS) to improve the accuracy of the obtained results.

## 5. Results and discussion

To handle the GPS shadowing or poor accuracy problem, a methodology is developed and is analyzed in different cases based upon the no. of photographs as well as control points. Different cases investigated are listed in Table 1. A program is developed in Python as well as in MATLAB to determine the coordinates of an unknown camera station by implementing the collinearity equations. As mentioned previously, the coordinates of camera exposure stations are obtained by processing the GPS data in Trimble Business Centre software. The horizontal and vertical accuracies obtained in the post-processing of GPS data are 0.6 cm and 0.9 cm, respectively. As mentioned in the methodology, control points are taken from the images whose camera exposure station coordinates are known. More number of control points provides better results. For this study, two buildings are chosen, one for developing the framework and another to verify it. A total of 19 images of Building 1 were taken for this study. The results obtained for different cases are explained in the following sections:

### 5.1 Case 1

Out of 19 images, the location of the camera station corresponding to image number 8 is assumed to be unknown. Inputs used to solve the collinearity equations and obtained coordinates for image number 8 are shown in Table 2.

Figure 5 shows the georeferenced point cloud of Building 1 and Building 2. The locations of all 19 camera exposure stations are shown in Figure 6.

An error of 12.65 m, 11.12 m and 9.54 m in easting, northing and height are obtained by solving the collinearity equations with the help of only two control points. These two control points were taken from the left adjacent image. To improve the solution, triangulation and bundle adjustment were applied using the Leica Photogrammetric Suite (LPS) of Erdas Imagine. The coordinates obtained by solving the collinearity equations were taken as initial coordinates during triangulation in LPS. The obtained error in coordinates with a different number of GCPs used in triangulation is shown in Table 3. The ground control points that are listed in the table are those points that were

used to adjust the block in LPS. From Table 3, it is clear that bundle adjustment improves accuracy and also with more ground control points accuracy improves. It is also clear that with 30 ground control points, errors in easting, northing and height are 3.01 m, 3.98 m and 2.07 m, respectively. This shows that with more GCPs, the accuracy improves. However, there is no significant change in the accuracy.

The collinearity equations are again solved with six control points and corresponding errors in easting, northing and height are obtained as 2.73 m, 2.98 m, and 2.12 m. In this case, three control points were taken from the left image

and the other three from the right image adjacent to the image whose exposure station coordinates are unknown. After processing the block in LPS, the error obtained in the coordinates of the unknown camera station were 0.86 m, 0.92 m, and 0.81 m respectively in easting, northing and height with 25 GCPs. It was found that the control point locations used for solving the collinearity equations play a significant role in the calculation of unknown camera exposure station coordinates. In case 1a, two almost collinear points were used and the error obtained was significant, whereas, in case 3 control points on adjacent images were well distributed and the error obtained was comparatively much less.

**Table 1. Description of different cases used for analysis**

Cases	Number of images	No. of unknown camera stations	No. of control points used for solving collinearity equations
1a	19	1	2
1b	19	1	6
2a	4	1 (Last image)	6
2b	4	1(3rd image)	6
2c	4	2	6

**Table 2. Inputs used to solve collinearity equations and obtained coordinates of unknown camera station**

Image coordinates of two points used (mm)	$\begin{bmatrix} 534.2467 & -239.4600 \\ -318.0120 & -239.7760 \end{bmatrix}$
Principal Point coordinates (mm)	$[11.930593 \quad 8.037962]$
Rotation Parameters (rad)	$\begin{bmatrix} 0.9957 & 0.0768 & 0.0520 \\ -0.0747 & 0.9964 & -0.0396 \\ -0.0548 & 0.0355 & 0.9979 \end{bmatrix}$
GCPs (m)	$\begin{bmatrix} 215814.288539 & 3360261.242831 & 655.161734 \\ 215814.032010 & 3360262.015736 & 655.103009 \end{bmatrix}$
Calculated coordinates of exposure station (m)	$\begin{bmatrix} 215804.785031 \\ 3360262.42872 \\ 654.86307229 \end{bmatrix}$



**Figure 5. Georeferenced point cloud of Building 1 and Building 2**

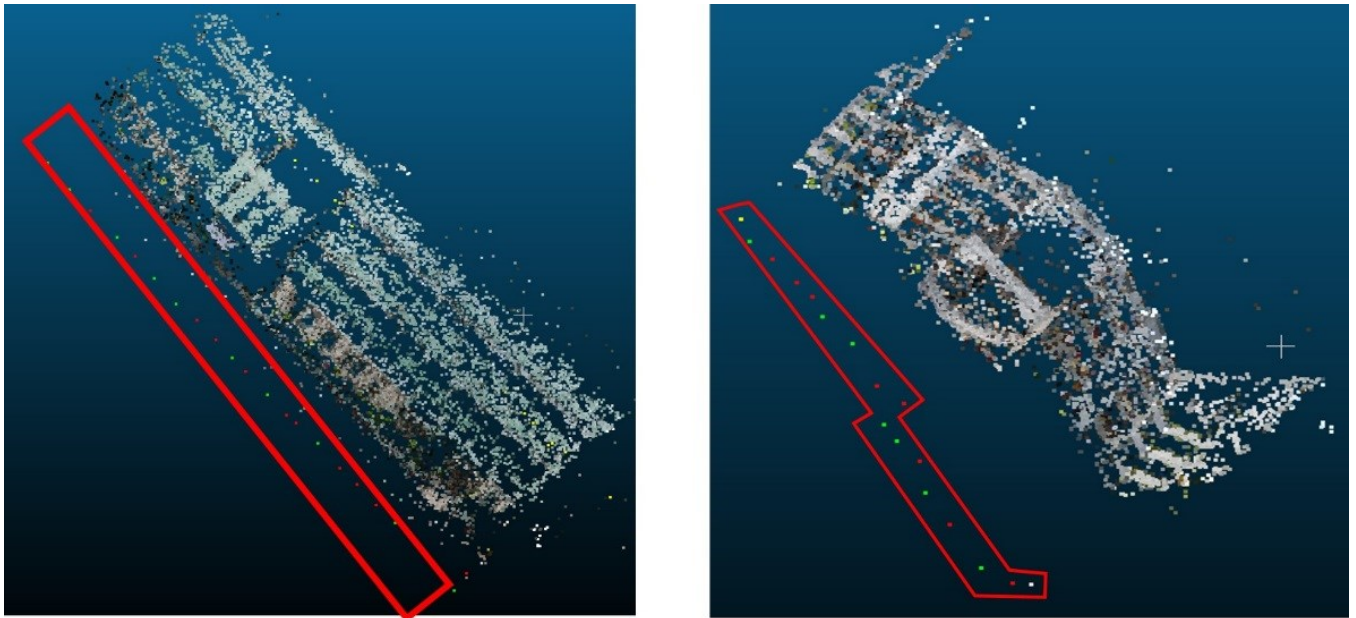


Figure 6. Location of camera exposure stations Building 1 (left) and Building 2 (right)

Table 3. Error in Coordinates

No. of Ground Control Points	Frame No.	Easting(m)	Northing(m)	Height(m)
25	8	3.25	4.66	2.18
30	8	3.01	3.98	2.07

5.2 Case 2

The developed methodology is also analyzed by reducing the number of Images. This case is further divided into three subcases. In this case, the total number of control points used is six and a total of 4 images are taken.

5.2.1 Case 2a

Out of 4 images, the exposure station coordinates of last (4th) image frame are assumed as unknown. Error in Easting, Northing, and Height is shown in Table 4.

Table 4. Error in coordinates of the 4th frame

Frame No.	Easting(m)	Northing(m)	Height(m)
4	0.90	1.65	1.19

5.2.2 Case 2b

Now, the approach is applied when the coordinates of a middle camera station (3rd image frame) are unknown. Here, it is assumed that the third camera station is unknown, and the obtained error is shown in Table 5.

Table 5. Error in coordinates of the 3rd image frame

Frame No.	Easting(m)	Northing(m)	Height(m)
3	0.91	0.99	0.50

It is clear from Table 5 that the accuracy improves if the coordinates of the adjacent (left and right both) camera stations are known.

5.2.3 Case 2c

Considering the case when the coordinates of the two camera stations are unknown. It is assumed that the

coordinates of the third and fourth camera stations are unknown. The error obtained in the coordinates of the 3rd and 4th camera stations is shown in Table 6.

Table 6. Error in coordinates of 3rd and 4th camera station

Frame No.	Easting(m)	Northing(m)	Height(m)
3	0.84	1.95	0.50
4	1.14	2.24	1.72

It is clear from Table 6 that as the number of unknown camera stations increases, the accuracy reduces. The error in the coordinates of the fourth camera station indicates that the error increases if the adjacent camera stations are unknown.

The developed methodology is verified on the captured images of Building 2. The developed framework works well and produces similar results.

6. Conclusions

Even highly efficient MMS suffers from the tracing through GNSS shadowed regions and handling such constraints becomes essential to build up a low-cost MMS. The methodology developed in this research work to address GPS unavailability problems for the georeferencing of an arbitrary point cloud generated using SfM is well analyzed in different cases. It provides a cost-effective solution to handle GPS unavailability in shadowed regions. A collinearity-based solution is suggested treating the global transformed local points as GCPs for obtaining the position of an unknown camera station. Various cases analyzed in this research show that

more distributed GCPs improve the estimation of locations by performing bundle adjustment. The error increases if a large number of consecutive camera stations are unknown. Known adjacent camera stations produce good results. This study integrates computer vision algorithms and photogrammetric-based approaches to handle GPS unavailability in shadowed areas. It can be utilized in MMS and to supplement IMU corrections.

### Acknowledgment

We thank the Director, Indian Institute of Remote Sensing, Dehradun, for providing us with the necessary hardware and infrastructure to conduct this study.

### References

- Arévalo-Verjel A. N., J. L. Lerma, J. F. Prieto, J. P. Carbonell-Rivera and J. Fernández (2022). Estimation of the Block Adjustment Error in UAV Photogrammetric Flights in Flat Areas. *Remote Sensing* 2022, Vol. 14, Page 2877, 14(12), 2877. <https://doi.org/10.3390/RS14122877>
- Choi E. and S. Chang (2019). An Adaptive Tracking Estimator for Robust Vehicular Localization in Shadowing Areas. *IEEE Access*, 7, 42436–42444. <https://doi.org/10.1109/ACCESS.2019.2907647>
- Clark B. J. and D. M. Bevely (2008). GPS/INS integration with fault detection and exclusion in shadowed environments. In *Record - IEEE PLANS, Position Location and Navigation Symposium* (pp. 1–8). <https://doi.org/10.1109/PLANS.2008.4569963>
- DeWitt B. A. and P. R. Wolf (2000). *Elements of Photogrammetry (with Applications in GIS)* (3rd ed.). New York: McGraw-Hill Higher Education.
- Fischler M. A. and R. C. Bolles (1981). Random sample consensus: a paradigm for model fitting with applications to image analysis and automated cartography. *Communications of the ACM*, 24(6), 381–395. <https://doi.org/10.1145/358669.358692>
- Furukawa Y. and J. Ponce (2010). Accurate, dense, and robust multiview stereopsis. *IEEE transactions on pattern analysis and machine intelligence*, 32(8), 1362–1376.
- Gabrlík P. (2015). The use of direct georeferencing in aerial photogrammetry with micro UAV. *IFAC-PapersOnLine*, 28(4), 380–385. <https://doi.org/10.1016/j.ifacol.2015.07.064>
- Granshaw S. I. and C. S. Fraser (2015). Editorial: Computer Vision and Photogrammetry: Interaction or Introspection? *The Photogrammetric Record*, 30(149), 3–7. <https://doi.org/10.1111/phor.12092>
- Groves P. (2011). Shadow Matching: A New GNSS Positioning Technique for Urban Canyons, 417–430. <https://doi.org/10.1017/S0373463311000087>
- Hassan T., C. Ellum and N. El-Sheimy (2006). Bridging land-based mobile mapping using photogrammetric adjustments. In *Proceedings of the ISPRS Commission I Symposium “From Sensors to Imagery*. Citeseer.
- Huang P., Y. Pi and Z. Zhao (2009). Weak GPS signal acquisition algorithm based on chaotic oscillator. *Eurasip Journal on Advances in Signal Processing*, 2009. <https://doi.org/10.1155/2009/862618>
- Jariwala J. J., A. Bhardwaj, S. Raghavendra, and K. Khoshelham (2014). Feasibility of Mobile Mapping System by Integrating Structure from Motion (SfM) approach with Global Navigation Satellite System. In *Proceedings of AGSE 2013: The Geospatial Momentum for Society and Environment* (Vol. 6, pp. 116–132).
- Li B., G. Chen, Y. Si, X. Zhou, P. Li, P. Li and T. Fadiji (2022). GNSS/INS Integration Based on Machine Learning LightGBM Model for Vehicle Navigation. *Applied Sciences* 2022, Vol. 12, Page 5565, 12(11), 5565. <https://doi.org/10.3390/APP12115565>
- Li R. (1997). Mobile mapping: An emerging technology for spatial data acquisition. *Photogrammetric Engineering and Remote Sensing*, 63(9), 1085–1092.
- Liu X., X. Lian, W. Yang, F. Wang, Y. Han and Y. Zhang (2022). Accuracy Assessment of a UAV Direct Georeferencing Method and Impact of the Configuration of Ground Control Points. *Drones* 2022, Vol. 6, Page 30, 6(2), 30. <https://doi.org/10.3390/DRONES6020030>
- Lourakis M. I. A. and A. A. Argyros (2009). SBA: A software package for generic sparse bundle adjustment. *ACM Transactions on Mathematical Software*, 36(1), 1–30. <https://doi.org/10.1145/1486525.1486527>
- Lowe D. G. (1999). Object Recognition from Local Scale-Invariant Features. *IEEE International Conference on Computer Vision*.
- Lowe D. G. (2004). Distinctive Image Features from Scale-Invariant Keypoints. *International Journal of Computer Vision* 2004 60:2, 60, 91–110. <https://doi.org/10.1023/B:VISI.0000029664.99615.94>
- Martínez-Carricondo P., F. Agüera-Vega, F. Carvajal-Ramírez, F. J. Mesas-Carrascosa, A. García-Ferrer and F. J. Pérez-Porras (2018). Assessment of UAV-photogrammetric mapping accuracy based on variation of ground control points. *International Journal of Applied Earth Observation and Geoinformation*, 72, 1–10. <https://doi.org/10.1016/J.JAG.2018.05.015>
- McMahon C., O. E. Mora and M. J. Starek (2021). Evaluating the Performance of sUAS Photogrammetry with PPK Positioning for Infrastructure Mapping. *Drones* 2021, Vol. 5, Page 50, 5(2), 50. <https://doi.org/10.3390/DRONES5020050>
- Mount D. M. and S. Arya (2010, January 27). ANN - Approximate Nearest Neighbor Library. <http://www.cs.umd.edu/~mount/ANN/>. Accessed 5 August 2022
- Mugnai F. and G. Tucci (2022). A Comparative Analysis of Unmanned Aircraft Systems in Low Altitude Photogrammetric Surveys. *Remote Sensing* 2022, 4(3), 726.
- Nguyen N. M., L. C. Tran, F. Safaei, S. L. Phung, P. Vial, N. Huynh., et al. (2019). Performance evaluation of non-GPS based localization techniques under shadowing

- effects. *Sensors* (Switzerland), 19(11), 1–21. <https://doi.org/10.3390/s19112633>
- Rizaldy A. and W. Firdaus (2012). Direct georeferencing: A new standard in photogrammetry for high accuracy mapping. In *International Archives of the Photogrammetry, Remote Sensing and Spatial Information Sciences - ISPRS Archives* (Vol. 39, pp. 5–9). <https://doi.org/10.5194/isprsarchives-XXXIX-B1-5-2012>
- Sanz-Ablanedo E., J. H. Chandler, J. R. Rodríguez-Pérez and C. Ordóñez (2018). Accuracy of Unmanned Aerial Vehicle (UAV) and SfM Photogrammetry Survey as a Function of the Number and Location of Ground Control Points Used. *Remote Sensing* 2018, Vol. 10, Page 1606, 10(10), 1606. <https://doi.org/10.3390/RS10101606>
- Scarmata G. (2007). Mobile mapping in gps-denied areas: a hybrid prototype. In A. Vettore & N. El-Sheimy (Eds.), *The 5th International Symposium on Mobile Mapping Technology*. Padua, Italy.
- Snaveley N., S. M. Seitz and R. Szeliski (2006). Photo tourism: exploring photo collections in 3D. In *ACM transactions on graphics (TOG)* (Vol. 25, pp. 835–846). ACM.
- Snaveley N., S. M. Seitz and R. Szeliski (2008). Modeling the World from Internet Photo Collections. *International Journal of Computer Vision*, 80(2), 189–210. <https://doi.org/10.1007/s11263-007-0107-3>
- Spilker J. J. J. (1996). Foliage Attenuation For Land Mobile Users. In *Global Positioning System: Theory and Applications, Volume I* (pp. 569–583). American Institute of Aeronautics and Astronautics. <https://doi.org/doi:10.2514/5.9781600866388.0569.0583>
- Szeliski R. (2010). *Computer vision: algorithms and applications*. Springer Science & Business Media.
- Warnasch A. and A. Killen (2002). Low cost, high G, micro electro-mechanical systems (MEMS), inertial measurements unit (IMU) program. *Position Location and Navigation Symposium, 2002* IEEE. <https://doi.org/10.1109/PLANS.2002.998922>
- Yang M.-D., C.F. Chao, K. S. Huang, L. Y. Lu and Y. P. Chen (2013). Image-based 3D scene reconstruction and exploration in augmented reality. *Automation in Construction*, 33, 48–60. <https://doi.org/10.1016/j.autcon.2012.09.017>

## Determination of radii of curvature for high resolution geoid models using the harmonic synthesis algorithm

Raaed Mohamed Kamel Hassouna

Department of Civil Engineering, Faculty of Engineering in Shebin El-Kom, Menoufia University,

Shebin El-Kom, Postal code: 32511 Egypt

Email: [raaed.hassona@sh-eng.menofia.edu.eg](mailto:raaed.hassona@sh-eng.menofia.edu.eg)

(Received: Dec 28, 2021; in final form: July 19, 2022)

**Abstract:** Different types of radii of curvature were assessed for the geoid based on the GECO geopotential model, up to degree and order 2190. The route values of gravity and the three horizontal gravity gradients were computed based on such geopotential model and the angular velocity of the Earth. The investigation was performed on coarse global grids and finer grids covering the Egyptian territory. Respective latitudinal and longitudinal profiles for the geoidal radii were extracted. Comparisons were held with the radii of curvature on the WGS-84 ellipsoid, and with the geoidal radii derived from other models of lower resolutions. Unlike the ellipsoid, the values of the geoidal radii exhibited a rather irregular behaviour that is far from any geographical symmetry. The principal radii of the geoid do not generally occur along the meridian and prime-vertical directions. Such irregularities were found to be more exaggerated with higher degrees. At all investigated resolution levels, the signs of the principal radii assured the convexity of the geoid surface. This enabled to define, compute and compare the Gaussian mean radii for the geoid. The local residual geoidal radii showed a decaying spectral tendency. Also, the results implied that the utilized algorithm proved to be convergent.

**Keywords:** Geopotential, level surfaces, geoid, differential geometry, radii of curvature, convexity

### 1. Introduction

According to Gauss, the geoid represents the original mathematical figure of the Earth. In many geodetic applications, the radii of curvature of the geoid have been traditionally assigned a constant value representing the “mean radius of the Earth” (e.g. Bhattacharji 1969). Such spherical approximations have been followed either in a global or regional scale. For example, the determination of geoidal heights as well as the associated topographic reductions necessitate the accurate radius of curvature of the geoid (de Graaff-Hunter 1951; Hirvonen 1954; Müller et al. 1963; Livieratos and Tziavos 1991). This radius significantly differs by about 10 % from that of the ellipsoid (Hirvonen 1954). Also, the geoid is the natural reference system for heights. So, the everywhere convexity of the geoidal surface is an essential property that guarantees its validity as a vertical datum (Vaniček and Santos 2019).

The differential geometry concept was the key for investigating the curvature characteristics of the equipotential surfaces. Over several decades, many works concerning the curvature of level surfaces have been conducted (Burša 1973a, b; Cevallos et al. 2012; Sansò and Sacerdote 2012; Cevallos et al. 2013 and Li 2015).

Almost all of the prescribed investigations have addressed the level surface radii of curvature as a reciprocal measure. Also, some of them have numerically determined the curvatures of the level surfaces. Burša (1973c) has computed the geoidal radii of curvature based on smooth satellite data, up to degree and order 21. However, no study has evaluated updated high degree radii of curvatures of the level surfaces, including the geoid. Furthermore, the convexity of such surfaces has never been computationally judged (Meyer et al. 2004; Vaniček and Santos 2019).

The objectives of the current study are to:

- investigate the geometry of the geoidal surface in terms of its different radii,
- test the convexity of the geoid, and
- investigate the smoothing behaviour of the residual geoidal radii.

The first two tasks are accomplished in both a global and local sense, whereas the third one is performed on a local scheme. The local investigation encounters the Egyptian territory. In all situations, parallel comparisons are held with the radii of the WGS-84 reference ellipsoid. Besides the ultra-high degree GECO (Gilardoni et al. 2016), other geopotential models with different resolutions are used model as a data tool,

Section (2) represents a theoretical overview of the different radii of curvature and shape for level surfaces. In Section (3), the methodology and data, which are used for the current work, are outlined. The results and discussion are presented in Section (4). Finally, in Section (5), the appropriate concluding remarks and recommendations are drawn.

### 2. Level surface radii of curvature: theoretical concept

Figure 1 depicts the alignment of the right-handed local astronomic system at a given point  $P$  on the level surface. In this system, the  $x$ -axis points towards the north, the  $y$ -axis is taken along the east direction and the  $z$ -axis is reckoned towards the zenith.

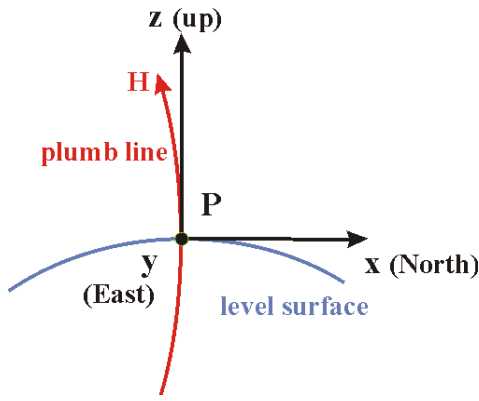


Figure 1. The local astronomic system

The magnitude of gravity at  $P$  within this system is given by (Smith 1998; Barthelmes 2013)

$$g = \sqrt{W_x^2 + W_y^2 + W_z^2}. \quad (1)$$

The corresponding Eötvös tensor is composed of the spatial second derivatives of the potential  $W$ , as follows (Torge 2001)

$$\|W_{ij}\| = \begin{vmatrix} W_{xx} & W_{xy} & W_{xz} \\ W_{yx} & W_{yy} & W_{yz} \\ W_{zx} & W_{zy} & W_{zz} \end{vmatrix}. \quad (2)$$

The curvature of any planar normal section, with azimuth  $\alpha$ , of the level surface through point  $P$  is defined by (Torge 2001)

$$\kappa_\alpha = - \frac{(W_{xx} \cos^2 \alpha + 2W_{xy} \sin \alpha \cos \alpha + W_{yy} \sin^2 \alpha)}{g}, \quad (3)$$

The minus sign is a convention, such that a resulting positive curvature implies an upward convexity of the normal section of concern (Sharipov 2004; Tu 2017).

Based on Equation (3), the radii of curvature of the level surface in the north and east directions are respectively given by (Torge 2001)

$$R_m = - \frac{g}{W_{xx}}, \quad (4a)$$

$$R_n = - \frac{g}{W_{yy}}. \quad (4b)$$

The principal curvatures of a level surface,  $\kappa_{\min}$  and  $\kappa_{\max}$ , occur at two mutually perpendicular directions. Namely, considering the extrema of Equation (3), such principal azimuths are expressed as follows (Torge 2001)

$$\alpha_{\kappa_{\min}} = \frac{1}{2} \tan^{-1} \left( 2 \frac{W_{xy}}{W_{xx} - W_{yy}} \right), \quad (5)$$

$$\alpha_{\kappa_{\max}} = \alpha_{\kappa_{\min}} \pm 90^\circ.$$

So, based on Equations (5) and (3), the respective maximal and minimal radii of curvature are given by (Torge 2001; Li 2015)

$$R_{\max} = \frac{1}{\kappa_{\min}} = - \frac{g}{W_{xx} + W_{yy} \tan \alpha_{\kappa_{\min}}}, \quad (6a)$$

$$R_{\min} = \frac{1}{\kappa_{\max}} = - \frac{g}{W_{xx} + W_{yy} \tan \alpha_{\kappa_{\max}}}. \quad (6b)$$

Such principal radii are of a pure geometric nature, since they are invariant with respect to any change of the adopted coordinate system (Tu 2017). So, another invariant quantity is the average radius of curvature of the level surface (Sharipov 2004),

$$R_{\text{avg}} = \frac{1}{\kappa_{\text{avg}}} = \frac{1}{\frac{1}{2}(\kappa_{\min} + \kappa_{\max})} = - \frac{2g}{(W_{xx} + W_{yy})}, \quad (6c)$$

where  $\kappa_{\text{avg}}$  is the average curvature.

Another important invariant feature is the Gaussian (or total) curvature, which is given by (Raussen 2008; Li 2015)

$$\kappa_{\text{Gauss}} = \kappa_{\min} \kappa_{\max} = \frac{W_{xx}W_{yy} - W_{xy}^2}{g^2} \cdot \left[ \frac{1}{\text{length}^2} \right] \quad (7)$$

Specifically, a surface that is elliptic at a given point could be either convex or concave, depending on the common (positive or negative) sign of the principal curvatures (Raussen 2008). In such case, it is possible to define the Gaussian mean radius of curvature as follows

$$R_{\text{mean}} = \sqrt{R_{\min} R_{\max}} = \frac{1}{\sqrt{\kappa_{\text{Gauss}}}}. \quad (8)$$

So, if existing,  $R_{\text{mean}}$  would be rather efficient in judging the geometry of level surfaces.

### 3. Methodology and data

The gravity potential of the Earth,  $W$ , is composed of the harmonic gravitational potential and the non-harmonic rotational potential,

$$W = \frac{kM}{r} \sum_{n=0}^L \sum_{m=0}^n \left( \frac{a}{r} \right)^n \left[ (\bar{C}_{nm} \cos m\lambda + \bar{S}_{nm} \sin m\lambda) \bar{P}_{nm}(\cos \theta) \right] + \frac{1}{2} \omega^2 r^2 \sin^2 \theta, \quad (9)$$

where

- $L$  maximal harmonic degree of the geopotential model,
- $kM$  product of the universal gravitational constant by the Earth's mass,
- $a$  equatorial radius,
- $r$  geocentric radius,
- $\theta$  geocentric co-latitude,
- $\lambda$  geodetic longitude,
- $\bar{C}_{nm}$  fully normalized spherical harmonic  $C$  -coefficients of degree  $n$  and order  $m$ ,
- $\bar{S}_{nm}$  fully normalized spherical harmonic  $S$  -coefficients of degree  $n$  and order  $m$ ,
- $\bar{P}_{nm}(\cos\theta)$  fully normalized associated Legendre function of degree  $n$  and order  $m$ .
- $\omega$  mean angular velocity of the Earth ( $7.292115 \times 10^{-5}$  radian/second).

So, based on Equation (9), the local Cartesian components of gravity can be evaluated as follows (Reed 1973; Tscherning 1976; Tscherning and Poder 1982; Rummel 1997; Barthelmes 2013)

$$W_x = -\frac{kM}{r^2} \left[ \sum_{n=0}^L \sum_{m=0}^n \left(\frac{a}{r}\right)^n (\bar{C}_{nm} \cos m\lambda + \bar{S}_{nm} \sin m\lambda) \frac{d\bar{P}_{nm}(\cos\theta)}{d\theta} \right] - \omega^2 r \sin\theta \cos\theta \quad (10a)$$

$$W_y = -\frac{kM}{r^2 \sin\theta} \left[ \sum_{n=0}^L \sum_{m=0}^n m \left(\frac{a}{r}\right)^n \left[ \bar{C}_{nm} \sin m\lambda - \bar{S}_{nm} \cos m\lambda \right] \bar{P}_{nm}(\cos\theta) \right] + 0 \quad (10b)$$

$$W_z = -\frac{kM}{r^2} \left[ \sum_{n=0}^L (n+1) \sum_{m=0}^n \left(\frac{a}{r}\right)^n \left[ \bar{C}_{nm} \cos m\lambda + \bar{S}_{nm} \sin m\lambda \right] \bar{P}_{nm}(\cos\theta) \right] + \omega^2 r \sin^2\theta \quad (10c)$$

Also, it can be proved that (Tscherning 1976; Tscherning and Poder 1982; Rummel 1997; Deakin 1998; Zhu 2007; Barthelmes 2013)

$$W_{xx} = -\frac{kM}{r^3} \left[ \sum_{n=0}^L (n+1) \sum_{m=0}^n \left(\frac{a}{r}\right)^n (\bar{C}_{nm} \cos m\lambda + \bar{S}_{nm} \sin m\lambda) \bar{P}_{nm}(\cos\theta) \right] - \left[ \sum_{n=0}^L \sum_{m=0}^n \left(\frac{a}{r}\right)^n (\bar{C}_{nm} \cos m\lambda + \bar{S}_{nm} \sin m\lambda) \frac{d^2 \bar{P}_{nm}(\cos\theta)}{d\theta^2} \right] + \omega^2 \cos^2\theta \quad (11a)$$

$$W_{xy} = -\frac{kM}{r^3 \sin\theta} \left[ \left[ \cot\theta \sum_{n=0}^L \sum_{m=0}^n \left(\frac{a}{r}\right)^n m (\bar{C}_{nm} \sin m\lambda - \bar{S}_{nm} \cos m\lambda) \bar{P}_{nm}(\cos\theta) \right] + \left[ \sum_{n=0}^L \sum_{m=0}^n \left(\frac{a}{r}\right)^n m (\bar{C}_{nm} \sin m\lambda - \bar{S}_{nm} \cos m\lambda) \frac{d\bar{P}_{nm}(\cos\theta)}{d\theta} \right] \right] + 0 \quad (11b)$$

$$W_{yy} = -\frac{kM}{r^3} \left[ -\left[ \cot\theta \sum_{n=0}^L \sum_{m=0}^n \left(\frac{a}{r}\right)^n (\bar{C}_{nm} \cos m\lambda + \bar{S}_{nm} \sin m\lambda) \frac{d\bar{P}_{nm}(\cos\theta)}{d\theta} \right] + \left[ \sum_{n=0}^L (n+1) \sum_{m=0}^n \left(\frac{a}{r}\right)^n (\bar{C}_{nm} \cos m\lambda + \bar{S}_{nm} \sin m\lambda) \bar{P}_{nm}(\cos\theta) \right] + \left[ \frac{1}{\sin^2\theta} \sum_{n=0}^L \sum_{m=0}^n \left(\frac{a}{r}\right)^n m^2 (\bar{C}_{nm} \cos m\lambda + \bar{S}_{nm} \sin m\lambda) \bar{P}_{nm}(\cos\theta) \right] \right] + \omega^2 \quad (11c)$$

A subtle point is that the geoid is one of the level surfaces that extend partially inside the Earth's masses. So, it would be expected to exhibit discontinuities in the second derivatives where density jumps occur (Torge 2001). However, according to Krarup-Runge's theorem, the analytical continuation of the external potential down to the geoid is possible with sufficient practical accuracy (Bjerhammar 1973; Tscherning 1981). Particularly, for points lying on the geoid, the spherical harmonic expansion achieves the harmonic downward continuation of the potential and its derivatives in a natural way simply by amplifying the signal, by using  $r_{geoid} < r_{terrain}$  (Barthelmes 2013).

Equations (10), (1) and (11) are used in Section (4) to determine the different radii of curvature for the geoid. This is performed, based on the ultra-high degree GECO model (Gilardoni et al. 2016), the low-degree satellite only model GOCO03S (d/o 250) (Mayer-Gürr et al. 2012), the ultra-high degree models EIGEN-6C2 (d/o 1949) and SGG-UGM-1 (d/o 2159) (Förste et al. 2012; Liang 2018). For this purpose, the open-source software geopot07 is used. It is capable of synthesizing up to the second order derivatives of the Earth's potential, within the local Cartesian system at any point (Tscherning 1976; Tscherning and Poder 1982; Tscherning et al. 1983; Forsberg and Tscherning 2008; Smith 2010).

## 4. Results and discussion

### 4.1 Global investigation of the geoidal geometry

Table 1 lists the statistics of the different types of the geoidal radii of curvature, which were computed over a  $5^\circ \times 5^\circ$  global grid, based on GOCO03S model. Table 2 shows the same features, but evaluated from GECO harmonic model. Unlike an ellipsoid of revolution, both tables indicate that the geoidal principal radii do not generally correspond to the meridian and prime-vertical directions. Also, the two tables show that the principal radii possess positive signs, which implies a convexity of the

geoid surface at all computational points. Therefore, as shown in the two tables, it was possible to define and compute the Gaussian mean radius of curvature,  $R_{mean}$ . It is obvious that the differences among such mean radii and the average ones are generally small.

**Table 1. Statistics of the  $5^\circ \times 5^\circ$  global geoidal radii of curvature based on GOCO03S (d/o 250) (km)**

	Min.	Max.	Mean	Std. Dev.
$R_m$	6260.117	6480.521	6368.301	25.886
$R_n$	6299.965	6474.130	6388.995	13.758
$R_{min}$	6248.500	6431.304	6364.758	23.466
$R_{max}$	6324.661	6502.624	6392.553	15.244
$R_{avg}$	6302.701	6448.891	6378.615	18.005
$R_{mean}$	6302.739	6449.112	6378.635	17.995
$R_{mean} - R_{avg}$	0	0.307	0.020	0.026

**Table 2. Statistics of the  $5^\circ \times 5^\circ$  global geoidal radii of curvature based on GECO (d/o 2190) (km)**

	Min.	Max.	Mean	Std. Dev.
$R_m$	5655.826	7462.316	6370.516	66.374
$R_n$	5598.276	7058.731	6389.702	57.622
$R_{min}$	5573.306	6873.800	6349.438	61.147
$R_{max}$	5933.936	8234.726	6411.195	71.759
$R_{avg}$	5747.970	7254.914	6379.890	50.293
$R_{mean}$	5750.795	7266.092	6380.103	50.718
$R_{mean} - R_{avg}$	0	85.745	0.213	1.819

Obviously, the variation of all radii types in Table 2, as expressed in terms of the standard deviation, are more exaggerated than those in Table 1. This in turn reflects the gain in radii details as computed from the ultra-high degree GECO model.

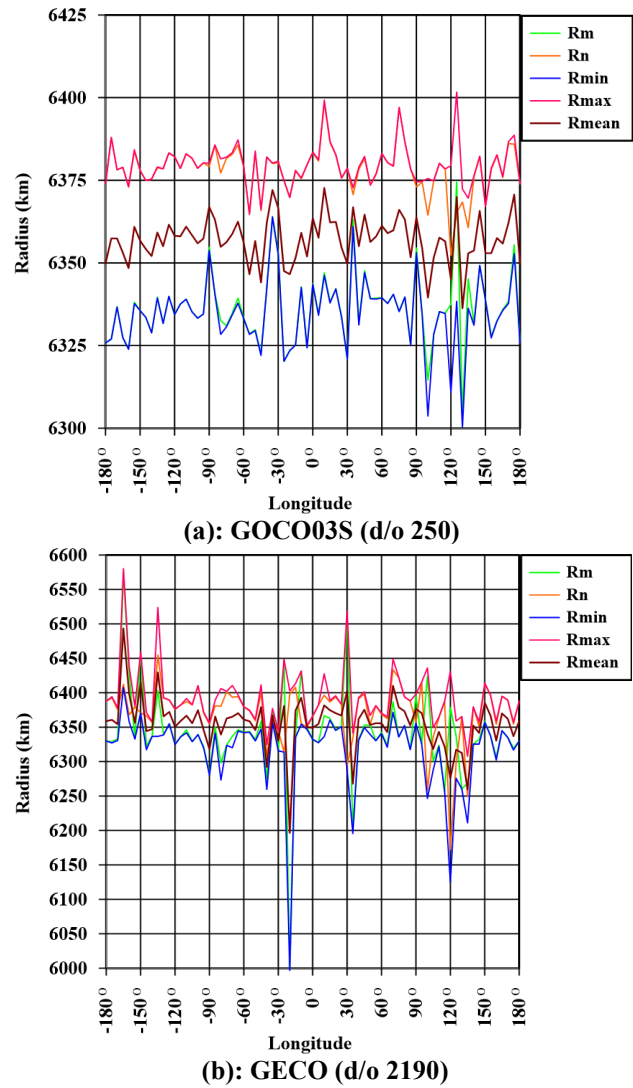


**Figure 2. Equatorial profiles for the geoidal radii of curvature**

In order to have a deeper global insight, two equatorial profiles were extracted from the global two  $5^\circ \times 5^\circ$  sets of meridian, prime-vertical, principal and mean radii of curvatures. Figure (2a) and (2b) depict the details of the two profiles pertaining to GOCO03S and GECO, respectively. Regarding all types of radii of curvature, the rotational symmetry (or the latitude-only dependency) no longer exists. Such rotational anti-symmetry is more pronounced in case of GECO, which exhibits a more oscillatory behaviour.

Tables 3 and 4 show statistical comparisons among the two equatorial profiles depicted in Figure (2a) and (2b), respectively.

**Table 3. Statistics of the geoidal radii along the Equator based on GOCO03S (d/o 250) (km)**

	Min.	Max.	Mean	Std. Dev.
$R_m$	6304.242	6374.468	6336.213	11.054
$R_n$	6352.366	6398.434	6378.160	7.242
$R_{min}$	6300.393	6363.93	6334.713	10.754
$R_{max}$	6364.819	6401.689	6379.679	6.416
$R_m - R_{min}$	0.001	36.091	1.501	5.401
$R_{max} - R_n$	0	36.399	1.519	5.458
$R_{mean}$	6336.269	6372.687	6357.154	7.037

**Table 4. Statistics of the geoidal radii along the Equator based on GECO (d/o 2190) (km)**

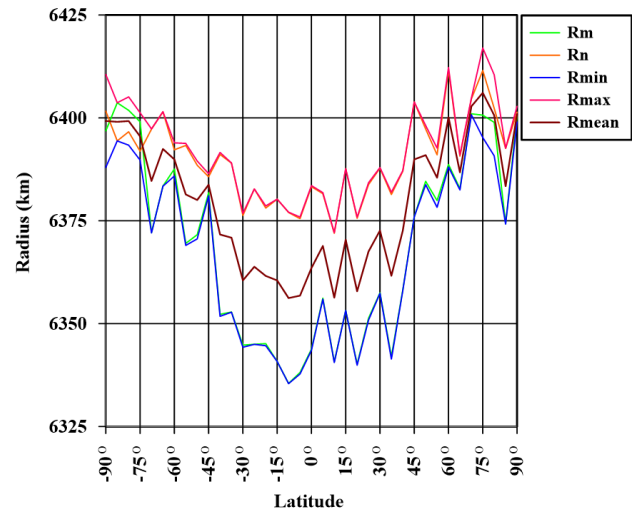
	Min.	Max.	Mean	Std. Dev.
$R_m$	6001.227	6575.318	6340.881	66.462
$R_n$	6172.599	6454.935	6370.694	41.756
$R_{min}$	5996.772	6407.722	6318.095	56.509
$R_{max}$	6307.863	6580.215	6393.674	41.959
$R_m - R_{min}$	0	254.190	22.786	51.406
$R_{max} - R_n$	0	258.260	22.980	51.756
$R_{mean}$	6196.396	6493.396	6355.693	38.572

Likewise, two profiles were extracted from the two global grids of radii of curvatures, but along Greenwich meridian. Figure (3a) and (3b) illustrate these profiles. Both profiles are anti-symmetric with respect to the equatorial plane, a fact which is more exaggerated in Figure (3b) that corresponds to GECO model. Tables 5 and 6 list the corresponding statistics.

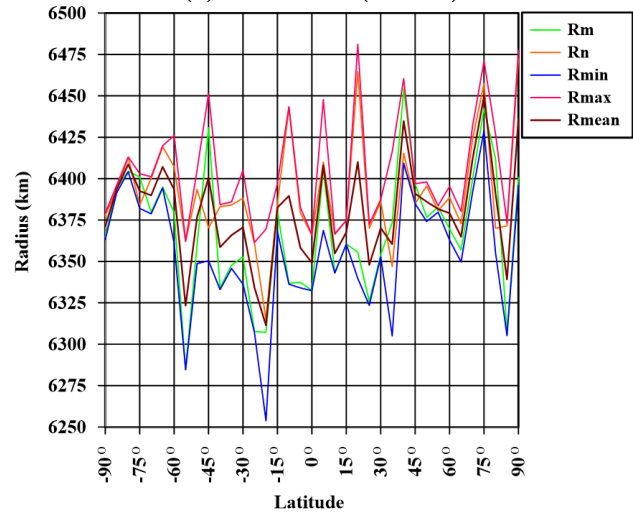
Figure (4a) and (4b) depict the variation of the GECO geoidal radii of curvature with longitude at the poles. The two poles possess different mean and principal radii. Also, it was noticed that the patterns in Figure (4) mirror those pertaining to the western hemisphere, which acted as a validation tool for the computational algorithm.

**Table 5. Statistics of the geoidal radii along Greenwich meridian based on GOCO03S (d/o 250) (km)**

	Min.	Max.	Mean	Std. Dev.
$R_m$	6335.483	6403.669	6368.977	22.814
$R_n$	6371.961	6411.633	6390.273	10.192
$R_{min}$	6335.410	6400.789	6367.279	21.004
$R_{max}$	6372.112	6416.979	6391.976	11.680
$R_m - R_{min}$	0	9.324	1.698	3.001
$R_{max} - R_n$	0	9.330	1.703	3.006
$R_{mean}$	6356.213	6406.098	6379.613	15.951



(a): GOCO03S (d/o 250)



(b): GECO (d/o 2190)

**Figure 3. Greenwich profiles for the geoidal radii**

**Table 6. Statistics of the geoidal radii along Greenwich meridian based on GECO (d/o 2190) (km)**

	Min.	Max.	Mean	Std. Dev.
$R_m$	6284.696	6454.208	6368.891	38.628
$R_n$	6315.068	6472.430	6391.256	31.846
$R_{min}$	6253.770	6429.035	6355.037	35.991
$R_{max}$	6361.470	6481.104	6405.257	33.591
$R_m - R_{min}$	0.043	80.486	13.854	20.823
$R_{max} - R_n$	0.044	80.994	14.000	21.021
$R_{mean}$	6311.386	6449.996	6380.076	30.393

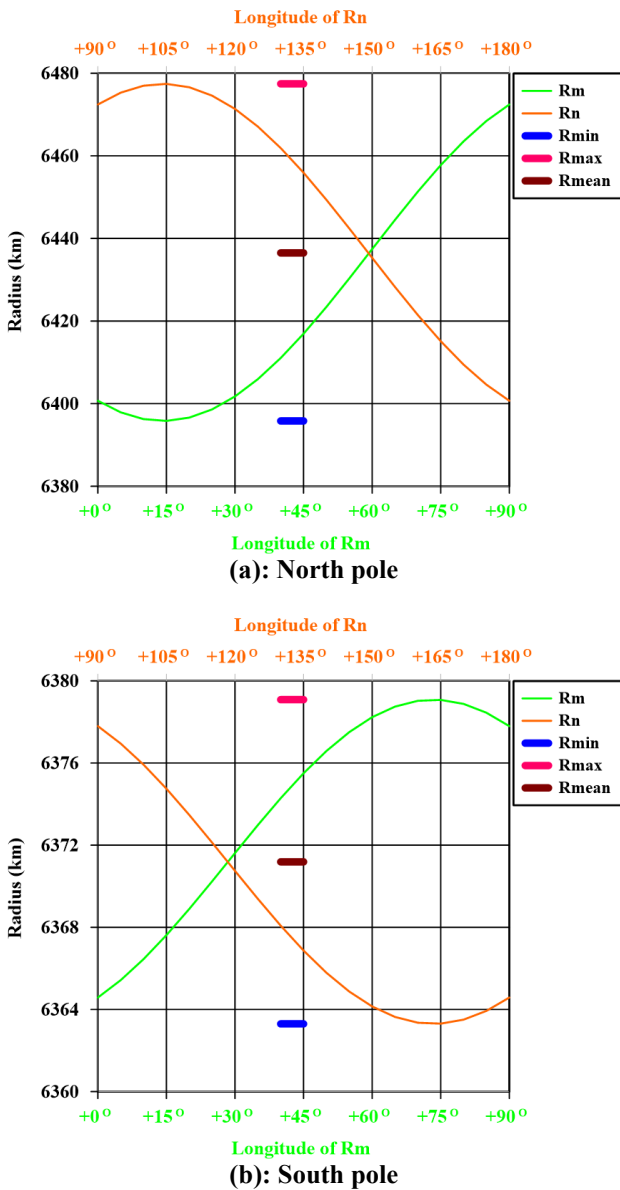


Figure 4. The geoidal radii of curvatures at the poles based on GECO (d/o 2190)

For the sake of comparison,  $5^\circ \times 5^\circ$  global grids for the meridian, prime-vertical and mean radii of curvature were evaluated for the WGS-84 reference ellipsoid (Jekeli, 2006). Tables 7 and 8 list the statistical comparison between the GECO and GOCO03S geoidal radii and those of WGS-84. While the small mean values in the two tables imply a good overall behaviour of the WGS-84 geocentric ellipsoid in approximating the geoid, the associated large ranges and standard deviations could reflect the regional irregularities of the geoidal radii.

Figure 5a shows a global contour map for the differences among the geoidal mean radii from GOCO03S model and those of WGS-84. This map shows significant regional differences, which are neither rotationally nor equatorially symmetric. Such result is more pronounced in Figure (5b), which illustrates another comparative contour map, but regarding GECO model.

Table 7. Statistical comparison among the  $5^\circ \times 5^\circ$  global GOCO03S geoidal radii and those of WGS-84 (km)

	Min.	Max.	Mean	Std. Dev.
$R_m - R_{m_{WGS-84}}$	-104.442	102.153	-0.017	12.861
$R_n - R_{n_{WGS-84}}$	-81.988	89.374	-0.147	11.466
$R_{mean} - R_{mean_{WGS-84}}$	-70.796	60.283	-0.082	9.869

Table 8. Statistical comparison among the  $5^\circ \times 5^\circ$  global GECO geoidal radii and those of WGS-84 (km)

	Min.	Max.	Mean	Std. Dev.
$R_m - R_{m_{WGS-84}}$	-711.556	1110.939	2.199	62.679
$R_n - R_{n_{WGS-84}}$	-786.896	675.250	0.559	57.087
$R_{mean} - R_{mean_{WGS-84}}$	-619.988	898.683	1.386	48.496

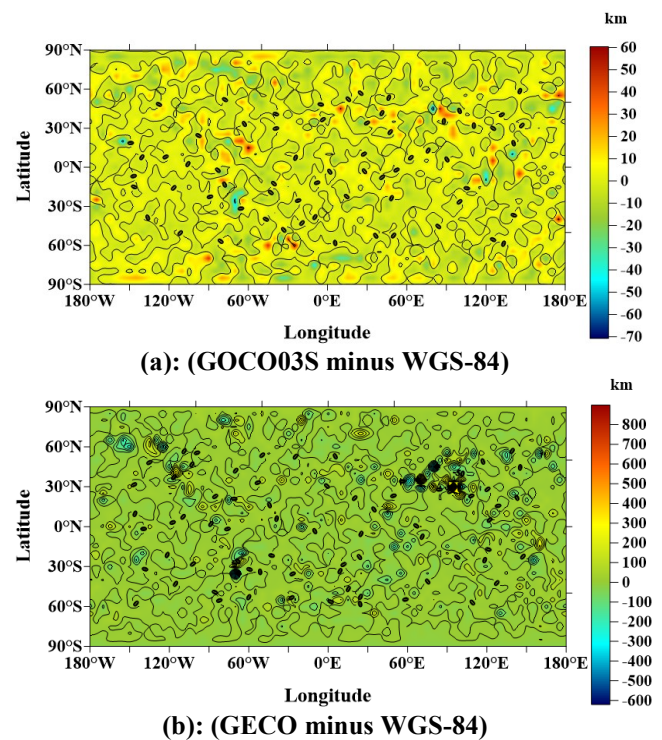


Figure 5. Global contour maps for the differences among the geoidal and WGS-84 mean radii of curvature (Interval: 50 km)

#### 4.2 Local application to the Egyptian territory

Firstly, local  $10' \times 10'$  grids of the geoidal radii of curvature were computed over the Egyptian territory, based on GECO model. These grids cover the window ( $22^\circ N \leq \varphi \leq 32^\circ N$ ;  $25^\circ E \leq \lambda \leq 36^\circ E$ ).

Table 9 shows the corresponding statistics. Again, the principal radii are all positive. This result ascertains the convexity of the geoidal surface at such local scale with a much finer resolution. The large departures of the principal radii from those in the north and east directions are obvious

in Table 9. Each pair of these radii types generally occur at different azimuths. This is easy to infer from Table (10), which lists the statistics of the azimuths of the geoidal maximal radii based on GECO. Obviously, these azimuths exhibit a broad range of values around the east direction.

**Table 9. Statistics of the 10'x10' grids of the geoidal radii for Egypt based on GECO (d/o 2190) (km)**

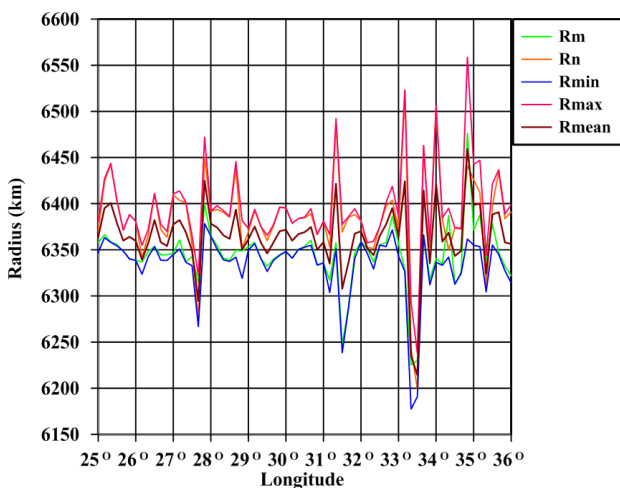
	Min.	Max.	Mean	Std. Dev.
$R_m$	6027.371	6614.634	6347.017	39.104
$R_n$	5863.951	6991.018	6383.203	57.087
$R_{min}$	5835.614	6473.656	6332.606	45.206
$R_{max}$	6136.712	7007.131	6397.845	52.579
$R_{avg}$	5982.377	6656.605	6364.919	38.596
$R_{mean}$	5984.270	6664.949	6365.073	38.706
$R_{mean} - R_{avg}$	0	11.924	0.153	0.503

**Table 10. Statistics of the 10'x10' values of the azimuths of the geoidal maximal radii for Egypt based on GECO (d/o 2190) (arc-degree)**

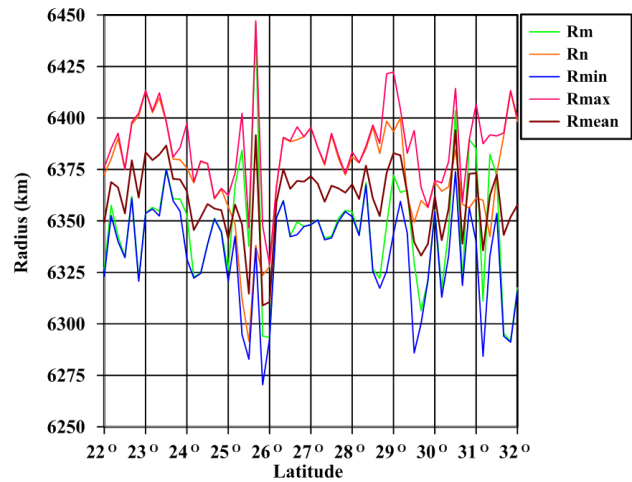
	Min.	Max.	Mean	Std. Dev.
$\alpha_{max}$	0	179.8	90.1	30.9

Figure (6a) and (6b) show the local profiles of the geoidal radii along the 27°N latitude and the 30°E meridian, respectively. These two figures agree with the general observations obtained from the global profiles in Figure (2) and (3), respectively.

Furthermore, it was decided to perform a degree-wise investigation of the residual geoidal radii of curvature. For this purpose, other 10'x10' local grids were established over Egypt, based on WGS-84 ellipsoid; and the GOCO03S (d/o 250), EIGEN-6C2 (d/o 1949) and SGG-UGM-1 (d/o 2159) geopotential models. In order to perform the investigation at appropriate spectral-degree intervals, EIGEN-6C2 model was utilized at two stages: firstly up to d/o 1000 and then up to d/o 1800.



**(a): Profiles along the 27°N latitude**



**(b): Profiles along the 30°E meridian**

**Figure 6. Local profiles for the geoidal radii of curvature from GECO**

Table 11–15 list statistical comparisons for the 10'x10' residual grids of the different geoidal radii types. Such residual values are the result of subtracting the different radii types pertaining to WGS-84, GOCO03S, EIGEN-6C2 (up to d/o 1000), EIGEN-6C2 (up to d/o 1800) and SGG-UGM-1; from those corresponding to GECO model. On one hand, the five tables show that the removal of the contributions of WGS-84 ellipsoid produced remarkably small mean, minimal and maximal residuals, while the corresponding standard deviations are nearly the same as those of GECO model. Again, this reflects the large local irregularity of the geoidal radii with respect to those of a reference ellipsoid. On the other hand, the removal of the radii derived from the remaining three harmonic models lead to an elegantly progressive smoothness of the residuals. Namely, such smoothness increases dramatically with the removal of higher harmonic degrees.

**Table 11. Statistics of the 10'x10' grids of the residual  $R_m$  values (km)**

Residual $R_m$	Min.	Max.	Mean	Std. Dev.
N/A (GECO)	6027.371	6614.634	6347.017	39.104
GECO–WGS-84	–323.367	264.055	–1.656	39.161
GECO–GOCO03S	–313.898	273.407	–0.341	37.990
GECO–d/o 1000	–230.617	202.915	–0.338	28.395
GECO–d/o 1800	–138.883	95.816	–0.379	17.136
GECO–d/o 2159	–24.805	22.797	0.472	5.826

**Table 12. Statistics of the 10' × 10' grids of the residual  $R_n$  values (km)**

Residual $R_n$	Min.	Max.	Mean	Std. Dev.
N/ A (GECO)	5863.951	6991.018	6383.203	57.087
GECO–WGS-84	-519.105	607.645	0.628	57.066
GECO–GOCO03S	-523.772	590.560	0.603	55.936
GECO–d/o 1000	-322.971	441.996	0.201	33.707
GECO–d/o 1800	-123.692	138.350	0.141	18.500
GECO–d/o 2159	-35.872	31.748	0.007	6.387

**Table 13. Statistics of the 10' × 10' grids of the residual  $R_{min}$  values (km)**

Residual $R_{min}$	Min.	Max.	Mean	Std. Dev.
N/ A (GECO)	5835.614	6473.656	6332.606	45.206
GECO–WGS-84	-514.494	120.477	-16.067	45.521
GECO–GOCO03S	-501.491	128.597	-13.786	44.645
GECO–d/o 1000	-300.581	166.759	-4.601	30.241
GECO–d/o 1800	-128.121	134.858	-1.404	17.231
GECO–d/o 2159	-29.964	29.157	0.529	6.085

**Table 14. Statistics of the 10'x10' grids of the residual  $R_{max}$  values (km)**

Residual $R_{max}$	Min.	Max.	Mean	Std. Dev.
N/ A (GECO)	6136.712	7007.131	6397.845	52.579
GECO–WGS-84	-246.344	623.864	15.270	52.477
GECO–GOCO03S	-252.042	601.229	14.270	51.445
GECO–d/o 1000	-272.273	417.436	4.578	32.522
GECO–d/o 1800	-133.447	135.748	1.201	18.135
GECO–d/o 2159	-32.387	33.129	-0.052	6.276

**Table 15. Statistics of the 10' × 10' grids of the residual  $R_{mean}$  values (km)**

Residual $R_{mean}$	Min.	Max.	Mean	Std. Dev.
N/ A (GECO)	5984.270	6664.949	6365.073	38.706
GECO–WGS-84	-382.29	297.968	-0.529	38.694
GECO–GOCO03S	-378.607	288.741	0.118	37.793
GECO–d/o 1000	-219.898	230.075	-0.067	25.240
GECO–d/o 1800	-112.969	95.071	-0.119	14.430
GECO–d/o 2159	-22.250	24.219	0.240	5.023

It should be noted that none of the geoidal radii is harmonic, since not only the harmonic gravitational part, but also the rotational potential contributes to their values. Although this rotational contribution is not a direct additive counterpart of the geoidal radii, it could have been somewhat minimized if not cancelled at all from the residuals in Table 11–15. This speculation could hold true, keeping in mind the larger standard deviations of the residuals relevant to WGS-84 in those five tables and in Table 8. Such large standard deviations could be due to the pure geometrical nature of the ellipsoidal radii.

It is worthy to view the decay of the geoidal radii residuals in Table 11–15 from another perspective. Namely, this attenuation could assure the convergence of the algorithm followed in the current work, in which the geoidal radii are derived based on harmonic models.

Finally, two local profiles for the geoidal mean radii were extracted along the 27°N parallel of latitude and the 30°E meridian. These two profiles are plotted in Figure (7a) and (7b), respectively. Obviously, the mean radii profiles corresponding to GOCO0S possess low resolution smooth trends. Alternatively, those pertaining to the higher resolutions from d/o 1000 to 2159 show irregular rough behaviours. In particular, the coherency of such rough profiles with those of the GECO model agrees with the dramatic decay of their residuals in Table 11–15. Therefore, such coherency again ascertains the convergence of the current algorithm.

**5. Concluding remarks and recommendations**

The computation of the geoidal radii based on ultra-high degree geopotential harmonic models proved to be an efficient and convergent algorithm. Both the global and local investigations indicated that the geoidal radii of curvature exhibit strongly rapid variations. These radii possess neither a longitudinal symmetry nor a latitudinal dependency. Unlike the ellipsoid, the geoidal principal radii do not generally occur along the north and east directions.

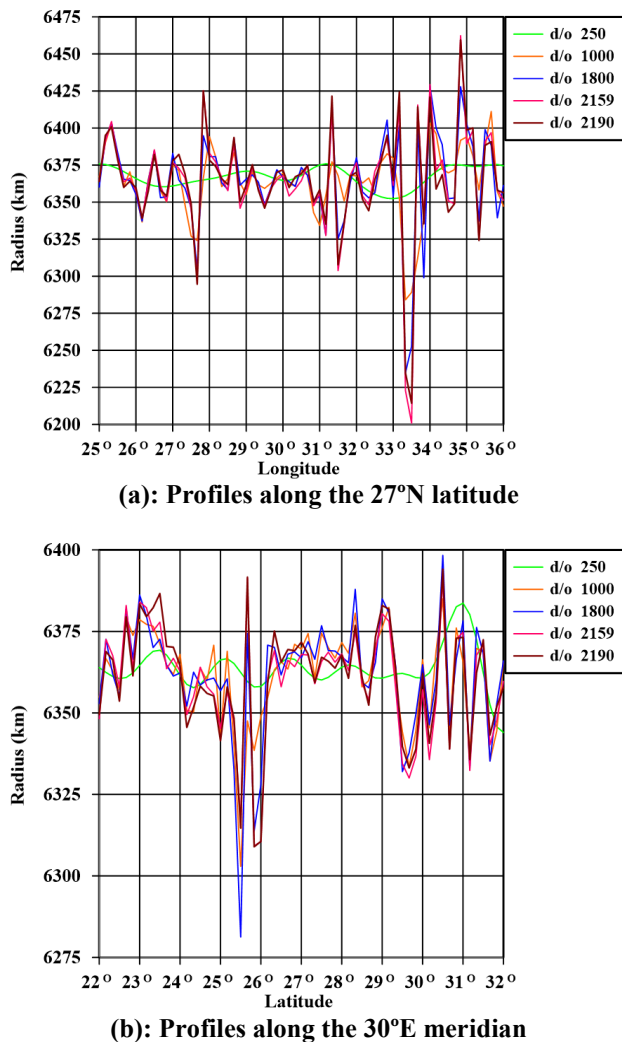


**Figure 7. Local profiles for the geoidal mean radii based on different harmonic degrees**

In general, at any point, there could be remarkable differences among the meridian and prime-vertical radii and the corresponding principal values.

The geoid is a smooth surface that is convex everywhere at seas and on land (Meyer et al. 2004; Vaníček and Santos 2019). Such pioneered opinions were verified in the current work, provided the positive principal radii of the geoid at all encountered evaluation points. Based on this property, it was possible to define and assess the Gaussian radius of curvature for the geoid.

It is recommended to further apply the algorithm presented in the current work to assess the geoidal radii of curvature over any desired geographical window. Obviously, the target resolution of the application in question would judge the maximal degree of the geopotential model of choice. Particularly, some simple surveying tasks might necessitate a realistic value for the geoidal radius along any direction, for example, the reduction of long slope distances to mean sea level.

Also, it is well known that the torsion balance devices are an efficient tool for determining the terrestrial components of the curvature tensor (e.g. Völgyesi 2015). So, co-locating torsion balance devices with gravimeters, mixed

gravity and gravity gradient observations can be collected. After the reduction of these data down to the geoid, detailed (or full-resolution) local geoidal radii of curvature can be assessed, based on the first principles given in Section (2). Furthermore, in view of the smooth behaviour of the residual geoidal radii, the remove-restore strategy might be tried to compute robust local geoidal radii at points with no data. Namely, ultra-high degree model-based radii may be removed from those evaluated from scattered dense co-located and gravity and torsion balance data. Then, the resulting residual radii of the geoid are interpolated into the target new points, and added back to the respective values that are derived from the same harmonic model. This stands in analogy with the remove-restore technique for local gravity field modelling.

The Gaussian radius of the geoid may be used for defining the solid spherical harmonics during the solutions for global harmonic models. This proposal stems from the validity of the Gaussian curvature for such task. This harmonic analysis strategy may be tried and compared with the spherical and ellipsoidal harmonic analysis schemes. These comparisons might be extended to check the efficiency of the corresponding subsequent harmonic synthesis results, regarding their fit to the observed gravitational data. Accordingly, a further future application may be to investigate the use of accurate mean geoidal radii in local geoid determination; and the associated topographic reductions.

Finally, the current algorithm may be generalized to evaluate the different types of radii of curvature for level surfaces through surface terrain points. In this circumstance, a digital terrain model, or the elevations of the scattered points of concern, would be an additional requirement. When applicable, this future outlook could be extended to the above outlined recommendations. In such cases, no doubt would exist regarding the convergence of the harmonic series.

#### Acknowledgments

Dr. D.A. Smith is acknowledged for releasing program Geopot07 as public domain. Also, three anonymous reviewers are thanked for their effort.

#### References

- Barthelmes F. (2013). Definition of Functionals of the Geopotential and Their Calculation from Spherical Harmonic Models: Theory and formulas used by the calculation service of the International Centre for Global Earth Models (ICGEM). GFZ Scientific Technical Report STR09/0. DOI: 10.2312/GFZ.b103-0902-26.
- Bhattacharji J.C. (1969). Modified Earth Model Free-air Gravity Anomaly for Use in Vening Meinesz's Formula, *Studia geoph. et geod.*,13(1969), pp. 373–389.
- Bjerhammar A. (1973). On the Discrete Boundary Value Problem. Symposium on Earth's Gravitational Field & Secular Variations in Position, pp. 475–488.

- Burša M (1973a). Gaussian curvature of smoothed equipotential surfaces from satellite orbit dynamics, *Studia geoph. et geod.*, (17), pp. 1–6.
- Burša M. (1973b). The mean curvature of the external equipotential surface and the vertical gravity gradient as functions of Stokes's constants, *Studia geoph. et geod.*, (17), pp. 74–80.
- Burša M. (1973c). Geoidal curvature radii from satellite data for different degrees of smoothing, *Studia geoph. et geod.*, (17), pp. 193–198.
- Cevallos C., M. Dransfield, J. Hope and H. Carey (2012). Application of curvatures to airborne gravity gradients, *ASEG Extended Abstracts*, 2012, (1), pp. 1–6. DOI: 10.1071/ASEG2012ab270.
- Cevallos C., P. Kovac and S.J. Lowe (2013). Application of curvatures and Poisson's relation to airborne gravity gradient data in oil exploration, *ASEG Extended Abstracts*, 2013, (1), pp. 1–4. DOI: 10.1071/ASEG2013ab112.
- de Graaff-Hunter J. (1951). The Geodetic Uses of Gravity Measurements and their Appropriate Reduction. *Proceedings of the Royal Society of London, Series A, Mathematical and Physical Sciences*, 206 (1084), pp. 1–17.
- Deakin R.E., (1998). Derivatives of the Earth's potentials, *Geom Res Aust*, 68, pp. 31–60.
- Forsberg R. and C.C. Tscherning (2008). An overview manual for the GRAVSOFT Geodetic Gravity Field Modelling Programs. 2<sup>nd</sup> edn., National Space Institute (DTU–Space), Denmark, August, 2008.
- Förste C., S.L. Bruinsma, F. Flechtner, J-C. Marty, J-M. Lemoine, C. Dahle, O. Abrikosov, H. Neumayer, R. Biancale, F. Barthelmes and G. Balmino (2012). A preliminary update of the Direct approach GOCE Processing and a new release of EIGEN-6C. Abstract No. G31B-0923, AGU Fall Meeting, San Francisco, December 3–7, 2012.
- Gilardoni M., M. Reguzzoni and D. Sampietro (2016). GECO: a global gravity model by locally combining GOCE data and EGM2008, *Studia geoph. et geod.*, 60 (2016), pp. 228–247. DOI: 10.1007/s11200-015-1114-14.
- Hirvonen R.A. (1954). The Gravimetric Method for Determination of the Form of the Geoid, *Tellus*, VI (1954), 1, pp. 84–88.
- Jekeli C. (2006). Geometric Reference Systems in Geodesy. *Lecture Notes, Division of Geodesy and Geospatial Science, School of Earth Sciences, the Ohio State University*.
- Li X. (2015). Curvature of a geometric surface and curvature of gravity and magnetic anomalies, *GEOPHYSICS*, 80 (1), pp. 15–26. DOI: 10.1190/GEO2014-0108.1.
- Liang W. (2018). SGG-UGM-1: the high resolution gravity field model based on the EGM2008 derived gravity anomalies and the SGG and SST data of GOCE satellite. *GFZ Data Services*. DOI: <http://doi.org/10.5880/icgem.2018.001>.
- Livieratos E. and I. N. Tziavos (1991). Correlation of strain representations of the potential anomalies with the geoid. In Rapp, R.H. and F. Sansò (eds.), *IAG Symposium 106, Determination of the Geoid: Present and Future*, Milan, Italy, June 11–13, 1990.
- Mayer-Gürr T., D. Rieser, E. Höck, J. M. Brockmann, W. D. Schuh, I. Krasbutter, J. Kusche, A. Maier, S. Krauss, W. Hausleitner, O. Baur, A. Jäggi, U. Meyer, L. Prange, R. Pail, T. Fecher and T. Gruber (2012). The new combined satellite only model GOCO03S. Abstract presented at the International Symposium on Gravity, Geoid and Height Systems GGHS 2012, Venice, October 9–12, 2012.
- Meyer T.H., D.R. Roman and D.B. Zilkoski (2004). What Does Height Really Mean? Part I: Introduction, *Surveying and Land Information Science*, 64(4), pp. 223–233.
- Müller I., O. Holway and R. King (1963). Geodetic Experiment by Means of a Torsion Balance. Report No. 3, Institute of Geodesy, Photogrammetry and Cartography, the Ohio State University Research Foundation.
- Raussen M. (2008). *Elementary Differential Geometry: Curves and Surfaces*. Department of Mathematical Sciences, Aalborg University, Denmark.
- Reed G.B. (1973). Application of Kinematical Geodesy for Determining the Short Wave Length Components of the Gravity Field by Satellite Gradiometry. Report No. 201, Department of Geodetic Science, the Ohio State University.
- Rummel, R. (1997). Spherical Spectral Properties of the Earth's Gravitational Potential and its First and Second Derivatives. In Sansò F. and R. Rummel (eds.), *Geodetic Boundary Value Problems in View of the One Centimeter Geoid*, *Lecture Notes in Earth Sciences*, 65, pp. 359–404.
- Sansò F. and F. Sacerdote (2012). Marussi and the First Formulation of Physical Geodesy as a Fixed-Boundary-Value Problem. In Sneeuw N., P. Novák, M. Crespi and F. Sansò (eds.), *VII Hotine-Marussi Symposium on Mathematical Geodesy*, Rome, June 6–10, 2009, pp. 25–29.
- Sharipov R.A. (2004). *Course of Differential Geometry*. Russian Federal Committee for Higher Education, Bashkir State University, Ufa, Russia.
- Smith D.A. (1998). There is no such thing as “The EGM96 geoid”: subtle points on the use of a global geopotential model, *IGeS Bulletin*, 8, pp. 17–28.

- Smith D.A. (2010). Program geopot07. National Geodetic Survey. Available: <http://ngs.noaa.gov>. Accessed 12 February 2020.
- Torge W. (2001). Geodesy, 3<sup>rd</sup> Edition. Walter de Gruyter Berlin.
- Tscherning C.C., R.H. Rapp and C. Goad (1983). A comparison of methods for computing gravimetric quantities from high degree spherical harmonic expansions, *Manuscr Geod*, 8, pp. 249–272.
- Tscherning C.C. (1976). On the chain-rule method for computing potential derivatives, *Manuscr Geod*, 1, pp. 125–141.
- Tscherning C.C. (1981). Comparison of Some Methods for the Detailed Representation of the Earth's Gravity Field, *Reviews of Geophysics and Space Physics*, 19 (1), pp. 213–221.
- Tscherning C.C. and K. Pöder (1982). Some geodetic applications of Clenshaw summation, *Boll Geofis Sci Aff*, 4, pp. 351–364.
- Tu L.W. (2017). *Differential Geometry: Connections, Curvature, and Characteristic Classes*. Springer International Publishing AG.346.
- Vaniček P. and M. Santos (2019). What Height System Should be Used in Geomatics?, *Int J Earth Environ Sci* 4: 160. DOI: <https://doi.org/10.15344/2456-351X/2019/160>.
- Völgyesi L. (2015). Renaissance of Torsion Balance Measurements in Hungary, *Period. Polytech. Civil Eng.*, 59(4), pp. 459–464. DOI: 10.3311/PPci.7990.
- Zhu L. (2007). *Gradient Modeling with Gravity and DEM*. Report No. 483, Department of Geodetic Science and Surveying, the Ohio State University.

## Web-GIS based Dashboard for Real-Time Data Visualization & Analysis using Open Source Technologies

Kusum Lata\*, Anil Sood, Kawaldeep Kaur, Amanpreet Kaur Benipal, Brijendra Pateriya  
Punjab Remote Sensing Centre, Ludhiana  
\*Email: [verma.kusum91@gmail.com](mailto:verma.kusum91@gmail.com)

(Received: Mar 10, 2021; in final form: June 22, 2022)

**Abstract:** Real-time visualization is the requirement for immediacy of decision making, which tends to be role-based. Using maps to visualize data can enable quicker interpretation of complex geographical phenomena, identify patterns, and aid in planning, resource allocations for policy and decision making. In present study, an interactive Web GIS Dashboard is developed with the objectives to display the work progress of Department of Soil & Water Conservation. The data includes activities and schemes undergoing in the department which was validated and geo-tagged with district & block boundary. For real-time data visualization, the graphs for different year, activities and schemes are developed for number of beneficiaries and area benefitted in ha. Various filters i.e. Year, Scheme and District are provided for viewing map. Different levels of User Authentication are provided for uploading new data and updating data.

**Keywords:** Dashboard, Data Visualization, Web-GIS, Geo-tagging, Spatial Data, Decision.

### 1. Introduction

Data in excel format is bulky which makes it bit difficult for the user to view details in less time. Therefore, there is a need to develop a web application in order to show data in systematic manner. An interactive dashboard is a data management tool that tracks, analyses, monitors, and visually displays key information while allowing users to interact with data, enabling them to make well-informed, data-driven, and healthy decisions. The point of such dashboards is not only to simplify the working environment but also to analysis processes since there are massive volumes of data collected at various levels, need solutions that will bring them to the right answer at the right time.

Dashboards are popular information system elements that provide advantages in terms of managing data. Using a dashboard for providing meaningful information in graphical and other forms of visualization has been increasingly used. Web dashboards can be configured in three different ways, as operational, tactical, and strategic dashboards (Bovkir & Aydinoglu, 2021). The field of geographic information science and its associated technologies have undergone rapid technological advancement and geographic information systems (GIS) now have functional capabilities which include geo-statistical analysis, network analysis and geographic modelling (Visner et al., 2021). The field is characterised by specific expertise, one with a longstanding history of forward thinking and a track record for ongoing innovation. Over the past few decades, in line with the increasingly expansive presence of the internet in daily activity, both personal and commercial, the availability of spatial information online has grown exponentially and has led to the rapid transition of GIS technologies from stand-alone GIS systems for the GIS expert to networked systems supported by distributed client-server applications (Lemmens et al., 2006). These distributed applications, also known as web mapping applications or web GIS in the Cloud, are defined by Esri (Rowland et al., 2020), the leading commercial provider of GIS technologies, as any GIS interface which makes use of web technology to

communicate between a client and server and is available as a web browser, desktop application or mobile application (Rowland et al., 2020). In the past decade Web-GIS tools have become increasingly popular as a result of advances in computer technologies, improved and established geographic standards (e.g. OGC standards) which have helped the dissemination of spatial data to different audiences and the shift from expert tools to community-based tools that are accessible to a wider range of users (Kienberger et al., 2013). Web-based GIS tools are spatial decision support systems (SDSS) that are interactive GIS-based platforms, including integrated database management systems designed to support place-based decision making at the various stages of a planning process (Duncombe et al., 2012; Amiruddin, 2016).

#### 1.1 Web-GIS architecture

The basic architecture of a web GIS application is the client-server architecture as described in Figure 1; this is because the standard of geo-data is very specific in the sense that it requires a Map server on top of the web server and a database server compliant with geo-data, while most other websites do not require these extra technologies to function properly (Ismanto et al., 2016). GIS engine is installed in application server which will exposes certain services. Open Geospatial Consortium (OGC) defined a set of standards for distributing geographic data and make layers of information more accessible. GIS engine take input in the form of Georeferenced data and converts into compressed formats like PNG (Portable Network Graphics), JPG (Joint Photographic Experts Group) or GIF (Graphics Interchange Format). Output can be of XML (Extensible Markup Language) based like yielding as a vector format e.g. KML (Keyhole Markup Language), GML (Generalized Markup Language).

WebGIS applications have web browser as a client for sending the request and a web server for responding to the request. The non-spatial web applications usually contain only web server, but in case of WebGIS, there is an additional server called data or map server for spatial data. This server handles the geospatial data, provides geospatial data compatible services like WMS and WFS,

and is able to perform GIS functionalities like editing, routing, and object tracking. The client can make the request to the server located at any place using middleware technologies like Remote Procedure Calls (RPC) or Open Database Connectivity (ODBC) (Tsou & Buttenfield, 2002). In 'thin client' approach, most of the processing is done at the server side after a simple request from the client. And in 'thick client' approach the client is more powerful by augmenting its capabilities with the help of plug-ins, applets or some additional modules (Agrawal & Gupta, 2017) as . The WebGIS architecture grows from multi-tier approach to plug-and-play to SOA (Service oriented Architecture) to cloud computing (Yang et al., 2010). Spatial cloud computing architecture is described in Figure 2. Virtual pool of resources is provided to users in cloud by Internet. Users can easily access the data uploaded on the cloud by Internet, which provides more flexibility and availability of resources at a lower cost.

The GIS Based open source dashboards had been created for many purposes. The dashboard for big urban data visualization approaches within the smart city is developed by BOVKIR (Bovkir & Aydinoglu, 2021) and Michael Visner created dashboard for Monitoring Spatio-Temporal Changes of Hotspots of Bushfires over 100 Years in New

South Wales, Australia (Visner et al., 2021). Tsou developed Smart dashboard for Social Media Analytics (Tsou et al., 2015). Geospatial dashboards have been created to determine the performance of smart cities (Achachlouei & Hilty, 2016; Batty, 2015; Jing et al., 2019; Kitchin, 2016b), which have attracted extensive interest from industry, academia and government due to the geospatial nature of city development, function, and management, the need for sustainable urban development, and the interest in new managerialism systems. The geospatial dashboard supports smart city sustainability goals by tracking city performance measurements (Achachlouei & Hilty, 2016; Diaz-Sarachaga et al., 2018; Kitchin, 2016b; Miola & Schiltz, 2019). Most of the WebGIS based dashboards have been developed to support urban management but little work has been carried out for conservation of soil and water. The new managerialism involves citizens who generate geospatial data, interact collaboratively with the government (Spyratos et al., 2014), and look for evidence-based decision-making (Kitchin, 2016a; Stoddart & Godfrey, 2020). Therefore, these characteristics of new managerialism result in the need for geospatial dashboards to support soil and water management.

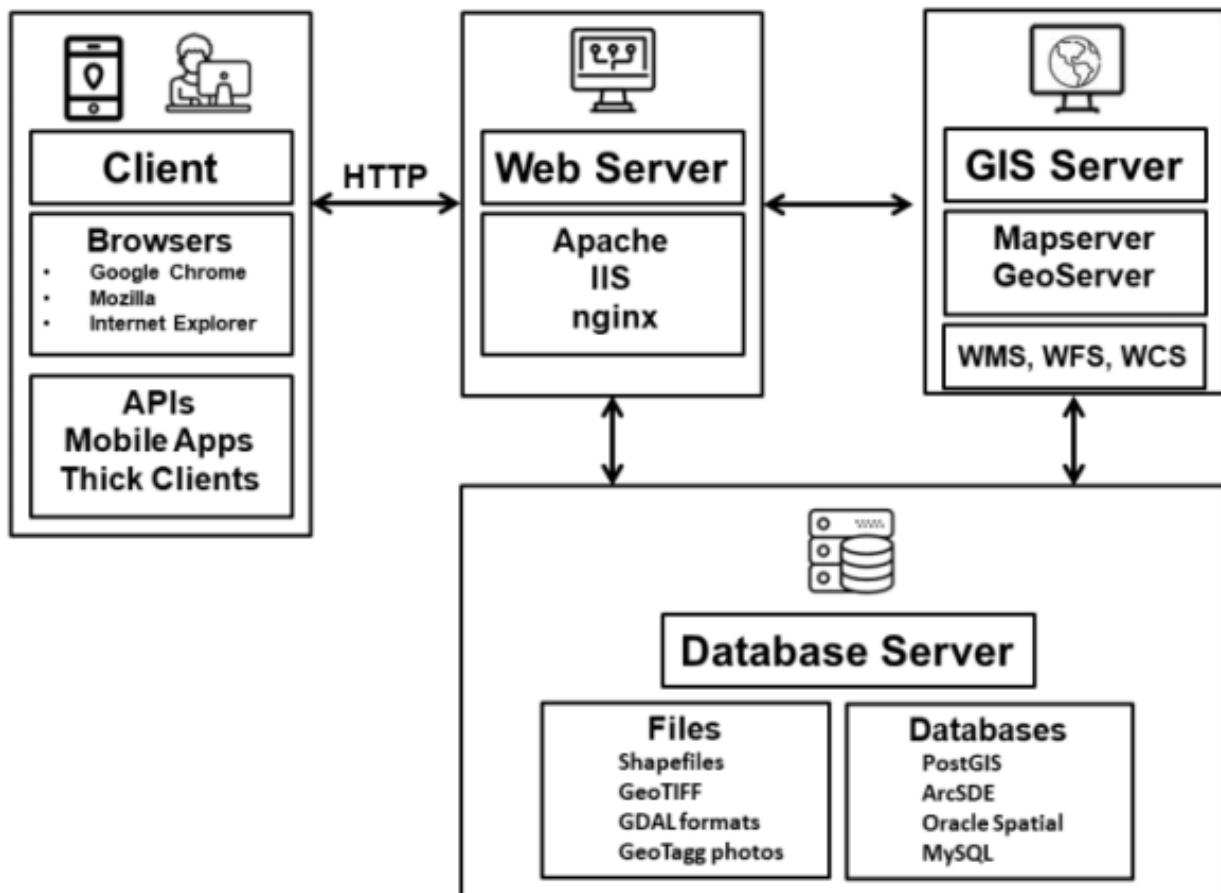


Figure 1. WebGIS Architecture (Giribabu et al. 2018)

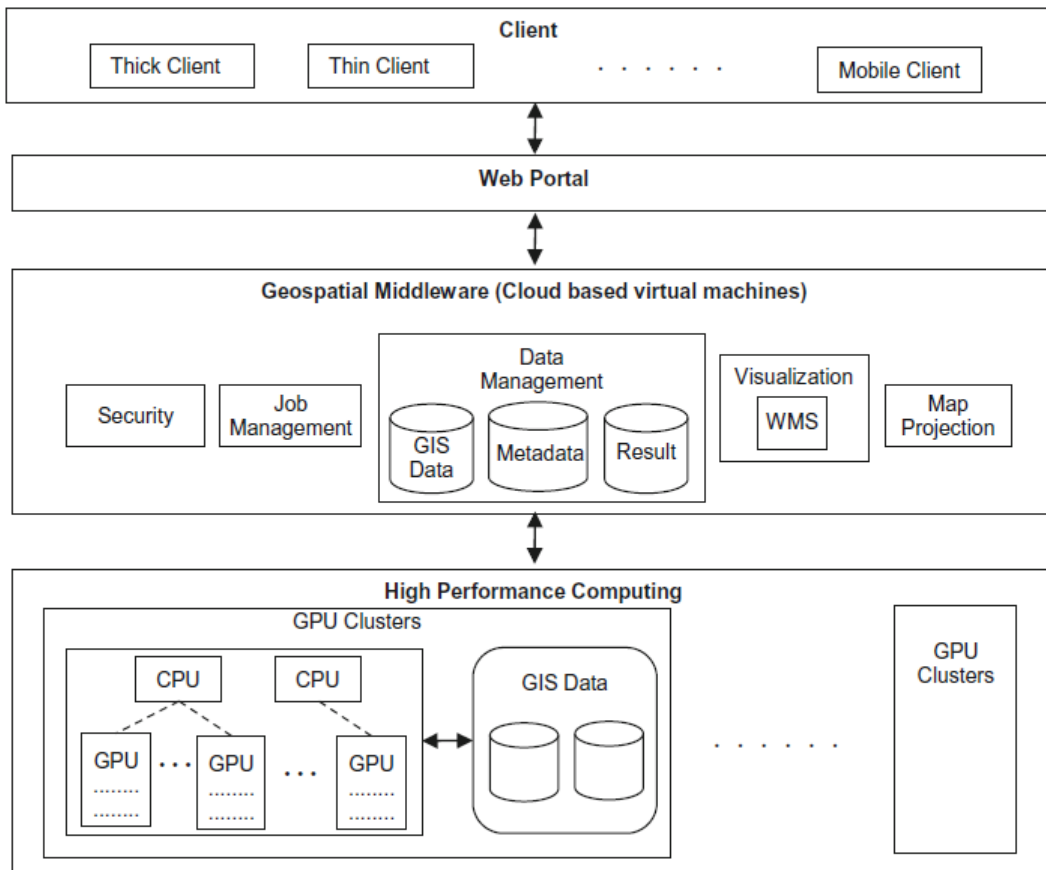


Figure 2. Spatial cloud computing architecture (Agrawal & Gupta, 2017)

**1.2 Open Source Technologies**

The design of open source technology is publicly accessible to modify and share among other users. Free and open-source software (FOSS) libraries grant the four basic freedoms of running, studying and adapting, redistributing, and releasing improvements to the public (Steiniger & Hunter, 2013). Traditional GIS software was robustly platform-dependent as they were generally written in programming languages which has to be recompiled between different hardware architectures and operating systems (e.g., C, C++) (Farkas, 2017). A platform independent client is needed to use server resources on place of local geoprocessing which can be done through browsers. Web processing Service can be used to make the product used on different Operating Systems and Devices.

Open-source web mapping libraries are helpful for the development of Web-GIS Applications. Many APIs and Web Mapping libraries are available, out of which Leaflet is the lightweight solution for creating web mapping applications which is highly capable due to its extensibility, and huge amount of third-party extensions developed. This library is used to develop the dashboard in present work due to rich vector format support and has the

capability to write features in GeoJSON format natively, and WFS transactions with an extension (Farkas, 2017). The tools for zoom in, zoom out, searching, measuring distance between points are available in the web page by using this library.

**2. Study Area**

The state of Punjab can be broadly divided into three socio-cultural regions, viz. Majha, the land between the Ravi and Beas rivers (8660 sq. km); Doaba, the land between rivers Satluj and Beas (8892 sq. km) and Malwa, encompassing area south of river Satluj (32,810 sq. km), out of which South-West zone (cotton belt) covers 14923 sq. km area. The state of Punjab is divided into 23 districts, which are further divided into 152 development blocks. Study area covers the whole state of Punjab (Figure 3), a part of Indus plain, covers a geographical area of 50362 sq. km. It lies between 29° 32' & 32° 31' N latitude and 73° 52' & 76° 52' E longitude. It shares the International border with Pakistan in western side while in the north it is bounded by Jammu and Kashmir, in the north-east by Himachal Pradesh, in east, south-east and south by Haryana and in south-west by Rajasthan.

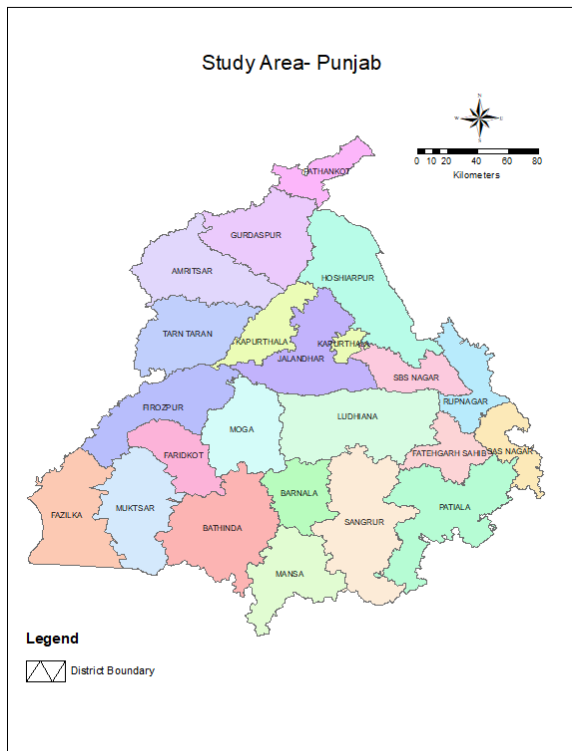


Figure 3. Study area – Punjab State

3. Data visualization approaches

Data visualization techniques consist of a combination of many disciplines such as computer graphics, image processing, computer vision, and user interface design (Balzer et al., 2020). Visualization techniques vary according to the processed data types.

- a) **One-Dimensional data:** One-dimensional data has only one variable. Temporal data can be an example to one-dimensional data(Keim, 2002).
- b) **Two-Dimensional data:** Two-dimensional data has two different dimensions. Geographic data with two different dimensions (latitude and longitude) is a typical example of two-dimensional data. Maps with X-Y plots are a typical method for displaying two-dimensional data(Keim, 2002).

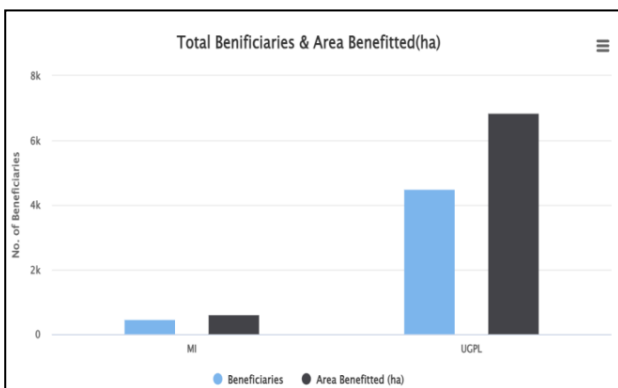


Figure 4. Example of 2D Graph

c) **Multidimensional data:** Many datasets contain more than three dimensions, so they cannot be observed with simple visualization techniques such as 2D or 3D graphs. Sophisticated visualization techniques are used in order to represent this type of data(Keim, 2002).

d) **Text and hypertext:** It is not possible to demonstrate all data types in sizing terms. Multimedia sources like web pages consist of text and hypertexts. Principle component analysis (PCA) and multi-dimensional scaling (MDS) are two of the leading methods applied for dimensional reduction of this data type.

e) **Hierarchies and graphs:** Data records are often associated with other pieces of information and graphs are often preferred to show these types of ordered, hierarchical or arbitrary relationships. A graph composes of a set of objects, called “node”s, and connections between these nodes, called “edge”. File structures in computers, e-mail relations between people or shopping behaviours can be given as examples(Keim, 2002).

f) **Algorithms and software:** The purpose of software visualization is to enable the development of the software by helping to understand algorithms. Graphical techniques can be classified according to the graphical possibilities of the software(Keim, 2002). In the present study, Two-Dimensional data is used for creating graphs & Plotting Maps. 2D graph example is shown in Figure 4.

4. Methodology

Web-GIS Dashboard is created using Open source technology. The Open source tools used for implementing Geospatial Dashboard are QGIS, HTML (Hypertext Markup Language), CSS (Cascading Style Sheets), JavaScript, jQuery, PHP (Hypertext Preprocessor) and PostgreSQL. HTML and CSS are used for designing the different elements on web pages in the dashboard. PostgreSQL is object-relational database which stores the spatial data to visualize on the Map. The spatial data of the present study is stoted in the PostgreSQL Database Version 9.4.PHP is used for database connectivity to visualize the real-time data i.e. connectivity of PostgreSQL database with web page.2D charts are implemented on the dashboard for real time data visualization. The flowchart (Figure 6) given below represents the methodology for creating dashboard, which follows System Development Life Cycle.

4.1 System development life cycle

There are many Software Development Life Cycle (SDLC) models. A project’s quality, timeframes, budget, and ability to meet the stakeholders’ expectations largely depend on the chosen model. Today, there are more than 50 recognized SDLC models in use. None of them is perfect, and each brings its favourable aspects and disadvantages for a specific software development project or a team (Purwonegoro & Setiawan, n.d.).

In the present study, waterfall model is used to develop the application as given in Figure 5. The waterfall model is

Sequential Development Model. A schedule can be set with deadlines for each stage of development and a product can proceed through the development process model phases one by one (Adel & Abdullah, 2015). The advantages of waterfall development are that it allows for departmentalization and control. Development moves from concept, through design, implementation, testing, installation, troubleshooting, and ends up at operation and maintenance (Balaji, 2012). Each phase of development proceeds in strict order as given in the requirement phase by the Department of Soil & Water Conservation.

#### 4.2 Steps for development of dashboard:

As described in Figure 6, the steps for development of dashboard are:

1. In requirement analysis phase, the data is collected in CSV format from the department of Soil and Water Conservation, Punjab and validated by geo-tagging with district and block boundary for each activity and scheme implement by them.
2. It is converted to spatial data in shape file format and then stored in the PostgreSQL database.
3. In System Design Phase, Layouts, Data Flow Diagram, UML Diagram and flowcharts for design of the web pages are created.
4. In Implementation phase, Frontend or Web pages are designed by using HTML, CSS and JavaScript etc and Database connectivity is done by PHP language built in functions. User authentication is implemented for security of the information and different types of users are created.
5. Open source scripts and Ajax is used to create the 2-D graphs.
6. In System Testing Phase, Guidelines are followed for creating Government department's Websites and testing of the dashboard is done.
7. In System Deployment Phase, System is deployed to the department of Soil & Water Conservation.
8. In System maintenance phase, new data will be added to the dashboard.

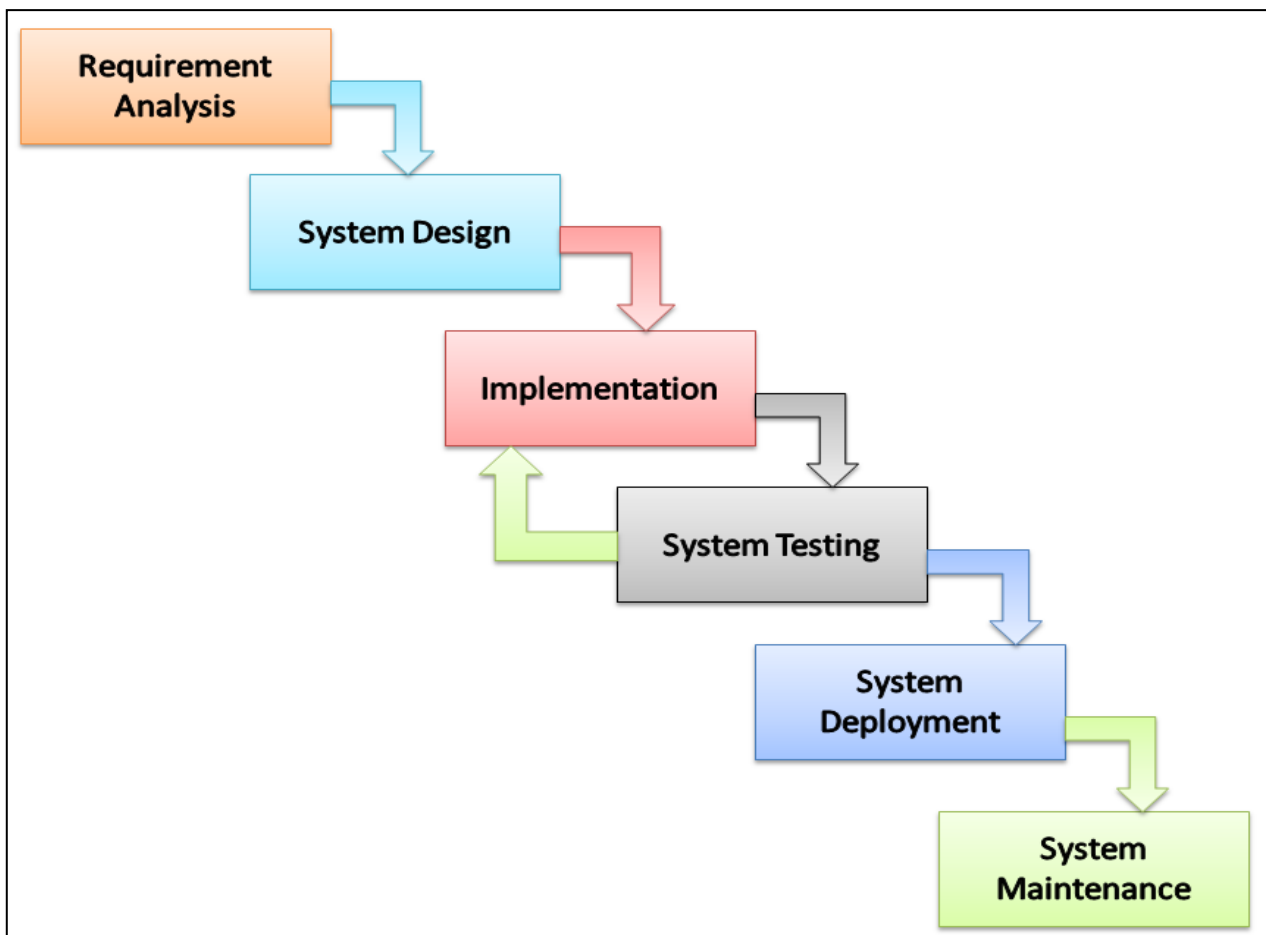


Figure 5. Waterfall Model (Boris, 2018)

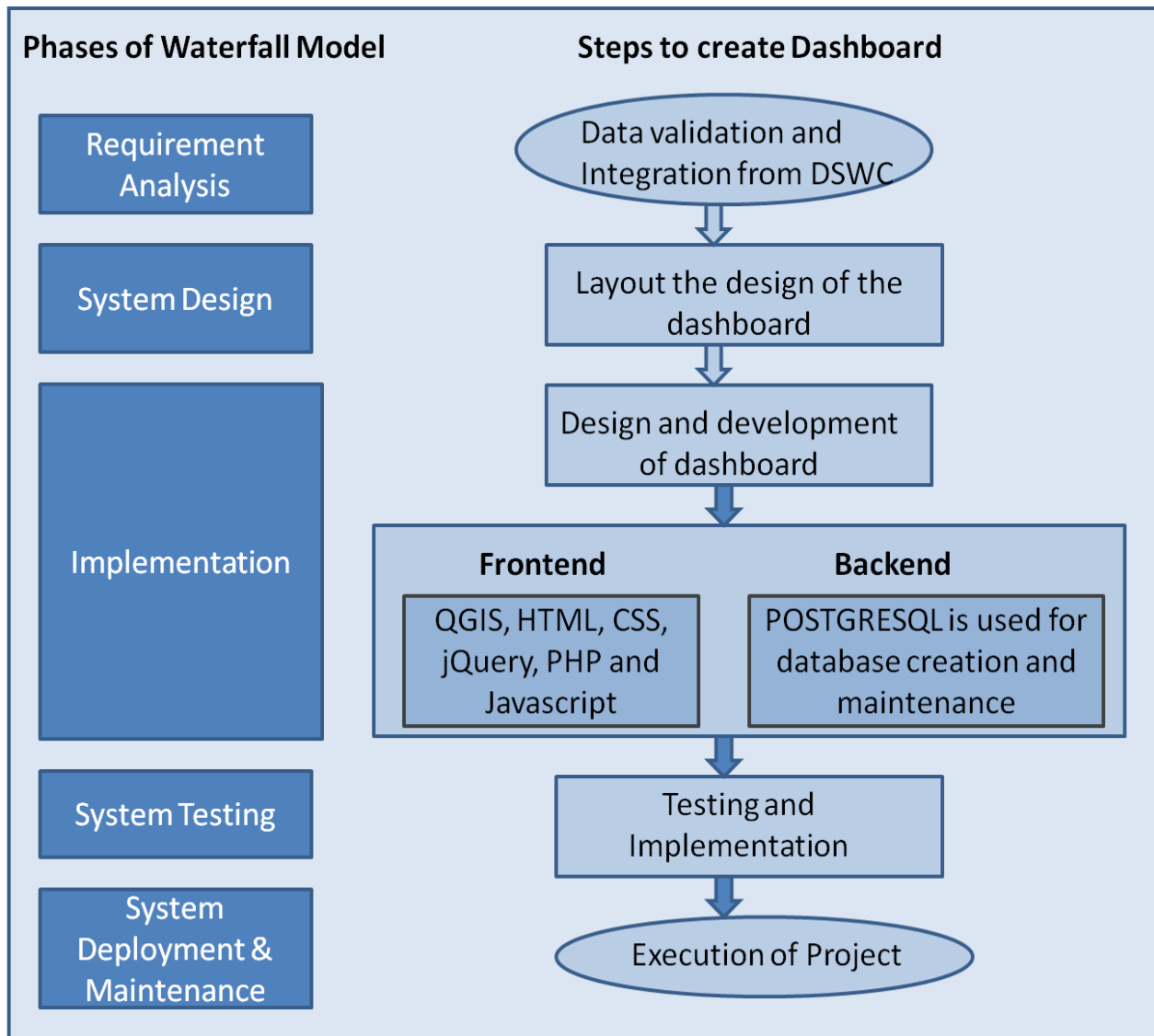


Figure 6. Methodology for developing Dashboard

5. Results and discussion

In present study, web-GIS based interactive dashboard is created for real time data visualization and analysis for the various schemes running under the department of Soil & Water Conservation, Punjab. The data for dashboard is collected and provided by department of Soil & Water Conservation, Punjab in excel format which includes various activities i.e. Underground Pipeline Systems, Micro-Irrigation Systems, Rainwater Harvesting cum Recharging Projects, Sewerage Treatment Plants & Watershed Based Projects and various schemes under these activities as shown in Figure 7. The data for different activities as given in table 1. is validated and geo-tagged with district & Block Boundary. Field images of the same have been geo-tagged. For real-time data visualization, the graphs for different year, activities and schemes are

developed for number of beneficiaries and area benefitted in ha. Various filters i.e. Year, Scheme and District are provided for viewing map.

Different levels of User Authentication are provided for Uploading new data and Updating data. Soil Conservation officers can only view the data and upload new data. The nodal officers can upload the new data and also update existing data (Figure 8). The Open-Source dashboard shows different activities under department of Soil & Water Conservation as shown in the homepage of the Dashboard in Figure 7. The work is done under 5 activities i.e. Underground Pipeline System, Micro-Irrigation Systems, Sewerage Treatment Plants, Rainwater Harvesting cum Recharging and Watershed Based Projects under different schemes. i.e. RKVY, PMKSY, PIDB etc. in different years.

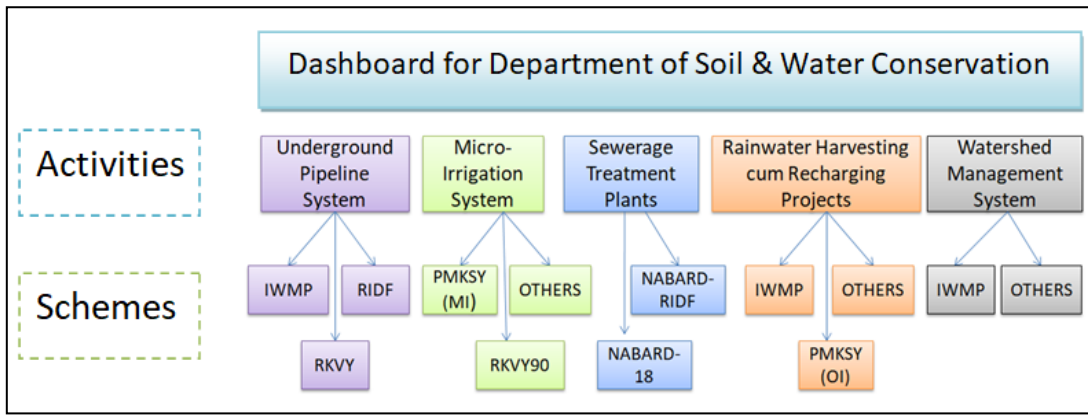


Figure 7. Activities and Schemes for Dashboard of Soil & Water Conservation

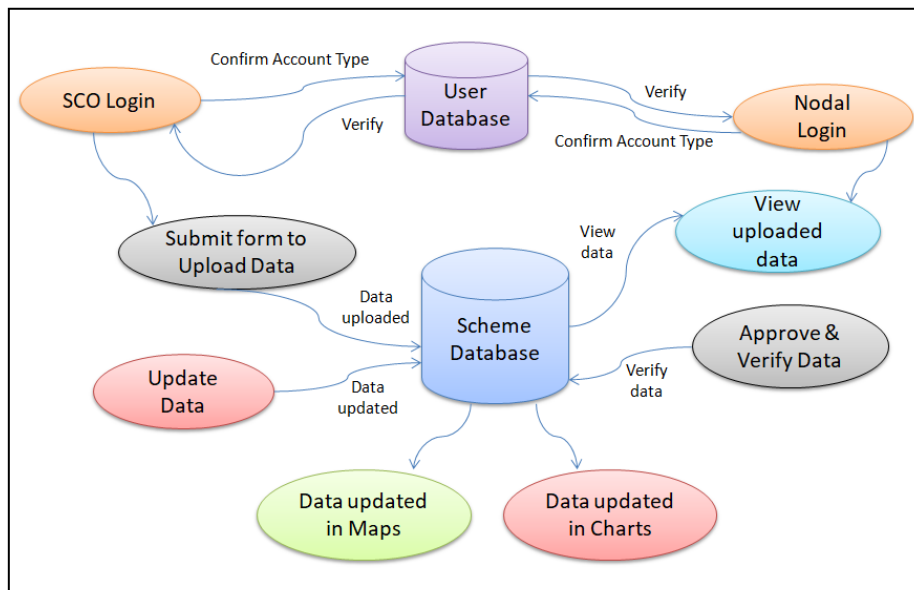


Figure 8. Data Flow Diagram of real-time Data Visualization

Homepage is designed by following the Guidelines for Indian Government Websites (GIGW) and Rights of persons with disabilities act, 2016 so that it is made accessible to persons with disabilities. Any user can view the information by the link [http://202.164.39.172:2345/test/acm/schemes\\_Dashboard/index.php](http://202.164.39.172:2345/test/acm/schemes_Dashboard/index.php).

Certain information is not made available publicly; user authentication is required for the security of information. Different types of User Logins are provided on the online dashboard for authenticity of data. First type of users is Soil Conservation officers. They can upload new data by filling form along with location and field image and view the existing data in form of maps and graphs. Second types of users are nodal officers. They can verify the data uploaded by Soil Conservation officers and make modifications. Also view the existing data and graphs and Upload the verified data in CSV Format. Third type of user is Admin, which has full privileges for storing, editing and updating the database, which is depicted in the Use Case Diagram (Figure 9). Use case is used in system analysis to identify, clarify and organize system requirements. It includes the graphs for area benefitted and number of

beneficiaries for the all activities and schemes under that activities as well as map for each activity, which can be filtered year-wise, scheme-wise and district-wise. Different utilities are provided in map view i.e. to zoom a particular area, measuring distance, searching particular place etc. Info window on click of any point gives information about all attributes i.e. Name of Beneficiary, Number of Beneficiaries, District, Tehsil, Block, Village, Type of Activity, Type of Scheme, Area Benefitted, Subsidy Disbursed, Type of Pipeline or Micro Irrigation, Type, Date of commencement of project, Financial Year, Date of completion of Project and field image of that location. On homepage (Figure 10), total subsidy, number of beneficiaries and area benefitted is displayed till the date which is real time information. Facility for zooming of image is also provided which is shown in Figure 11. Figure 12 shows the form for uploading the data, as Soil Conservation Officers can upload the data from the field along with location after login and Figure 13 also shows the form for uploading the new data, which is for nodal officers to upload the data in CSV format and they can also verify the data uploaded by Soil Conservation Officers by using form to view data and give the remarks to them (as given in Figure 14).

**Table 1. List of various Activities and its associated data**

<b>Activity</b>	<b>Underground Pipeline System</b>	<b>Micro Irrigation System</b>	<b>Rainwater Harvesting and Recharging Projects</b>	<b>Sewerage Treatment Plants</b>
<b>Spatial Data</b>	<b>Associated Data</b>	<b>Associated Data</b>	<b>Associated Data</b>	<b>Associated Data</b>
<b>District Boundary</b>	District Name	District Name	District Name	District Name
<b>Block Boundary</b>	Block Name	Block Name	Block Name	Block Name
<b>OpenStreetMap</b>	Google Map with labels	Google Map with labels	Google Map with labels	Google Map with labels
<b>Location of UGPL</b>	Sno	Sno	Sno	Sno
	Financial_year	Financial_year	Financial_year	Financial_year
	Scheme	Scheme	Scheme	Scheme
	No_of_Beneficiary	No_of_Beneficiary	Division	Division
	Beneficiary_Name	Beneficiary_Name	SubDivision	SubDivision
	Beneficiary_Father_Name	Beneficiary_Father_Name	Section	Section
	Beneficiary_Contact	Beneficiary_Contact	District	District
	Beneficiary_Aadhar	Beneficiary_Aadhar	Block	Block
	Division	Division	Village	Town where STP Located
	SubDivision	SubDivision	Latitude	No. of Beneficiary Villages
	Section	Section	Longitude	Village Name
	District	District	Type_of_Structure	Latitude
	Block	Block	Benefitted_Area	Longitude
	Village	Village	Total_cost	Discharge (MLD)
	Latitude	Latitude	Financial_Assistance	Benefitted_Area
	Longitude	Longitude	Present_Status	Type_of_Pipeline
	Type_of_Crop	Type_of_Crop	Date_start_of_project	Length_of_Pipeline
	Benefitted_Area	Benefitted_Area	Date_completion_of_project	Total cost
	Type_of_Pipeline	Type_of_MI	Photograph	Subsidy Disbursed
	Length_of_Pipeline	Total_cost		Maintenance
	Total_cost	Subsidy Disbursed		Date_start_of_project
	Subsidy Disbursed	Present_Status		Date_completion_of_project
	Present_Status	Date_start_of_project		Photograph
	Date_start_of_project	Date_completion_of_project		
	Date_completion_of_project	Photograph		
	Photograph			

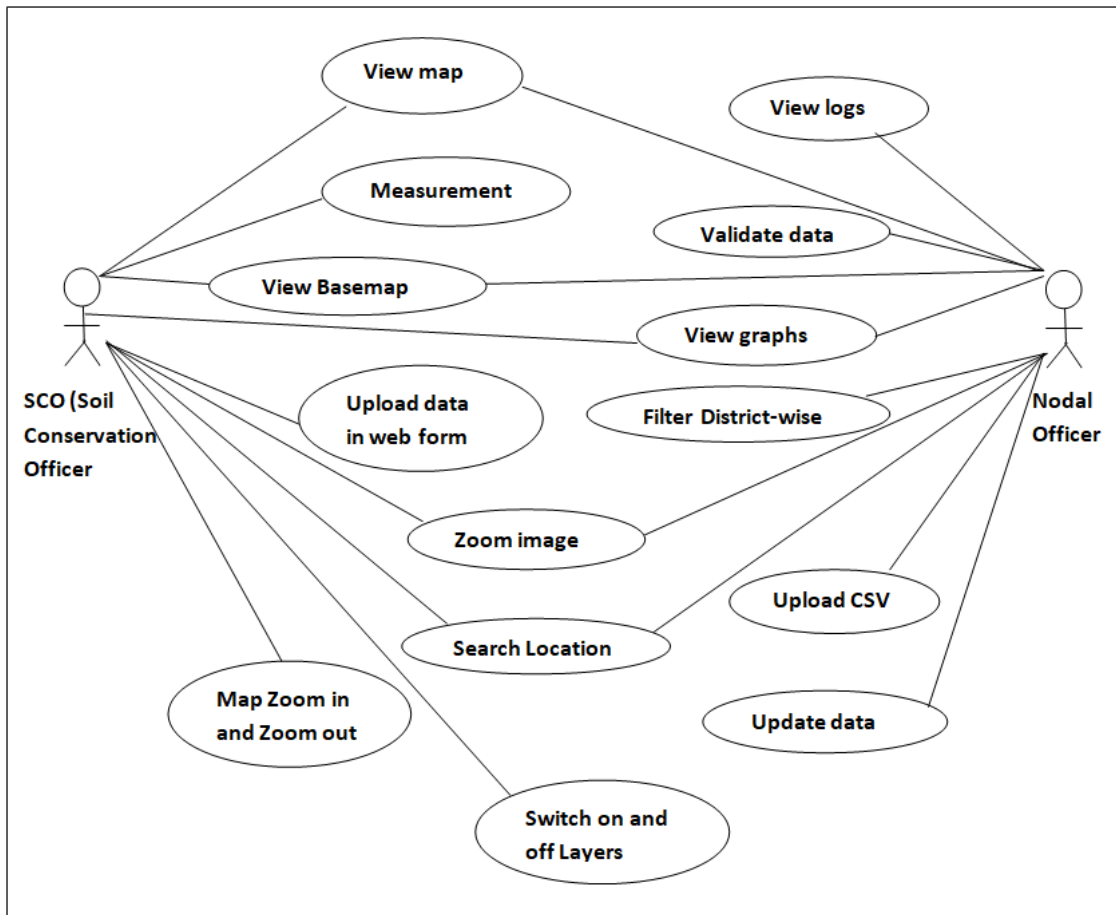


Figure 9. Use Case Diagram

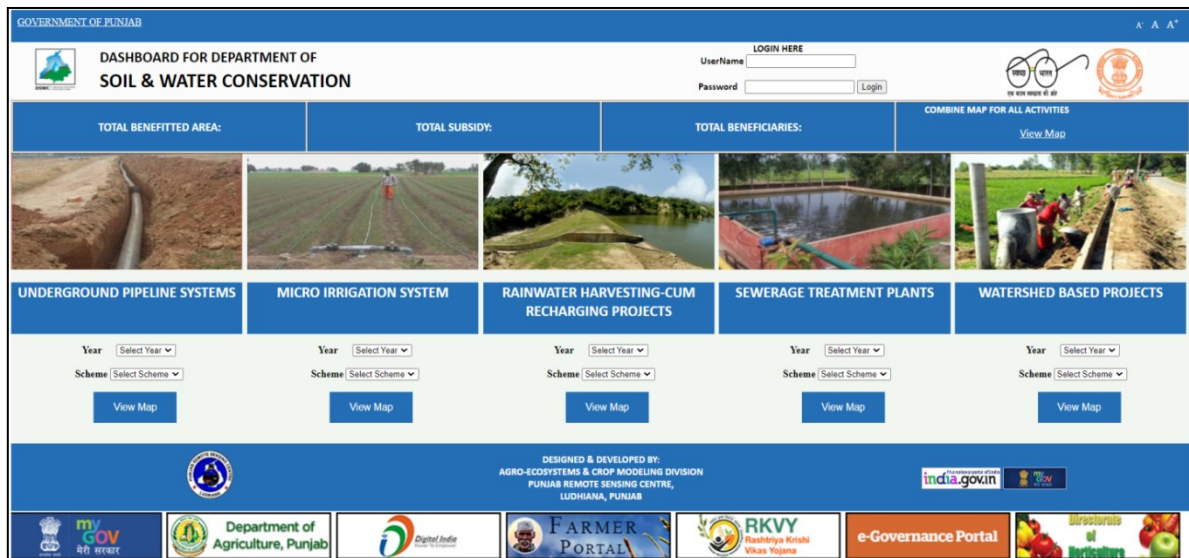


Figure 10. Homepage of Web-GIS Based Interactive Dashboard for Dept of Soil & Water Conservation

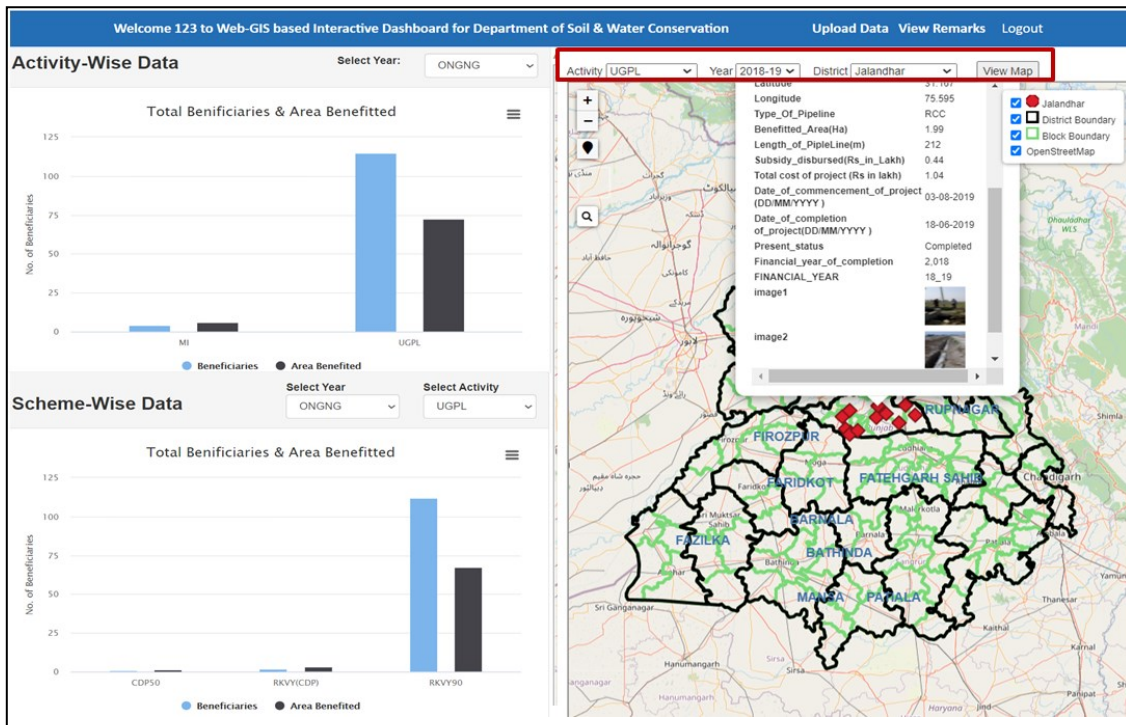


Figure 11. Data Visualization in Web-GIS Based Interactive Dashboard for Department of Soil & Water Conservation

### Upload UGPL Data

Sr.No.	<input type="text"/>	Benefitted Area(HA)	<input type="text"/>
Name of Beneficiary	<input type="text"/>	Length of Pipeline (in m)	<input type="text"/>
No. of Beneficiaries	<input type="text"/>	Subsidy disbursed(Rs in Lakh)	<input type="text"/>
Contact No. of Beneficiary	<input type="text"/>	Total cost of project (Rs in lakh)	<input type="text"/>
Aadhar No. of Beneficiary	<input type="text"/>	Date of commencement of project (DD/MM/YYYY)	<input type="text"/>
Name of Village	<input type="text"/>	Date of completion of project (DD/MM/YYYY)	<input type="text"/>
Name of Block	<input type="text"/>	Present status	<input type="text"/>
Name of District	<input type="text"/>	Financial year of completion	<input type="text"/>
Name of Section	<input type="text"/>	FINANCIAL YEAR	<input type="text"/>
Name of Division	<input type="text"/>	Unicode of Photograph1	<input type="text"/>
Name of Scheme	<input type="text"/>	Upload Photograph1	<input type="button" value="Choose File"/> No file chosen
Latitude	<input type="text"/>	Unicode of Photograph2	<input type="text"/>
Longitude	<input type="text"/>	Upload Photograph2	<input type="button" value="Choose File"/> No file chosen
Type Of Pipeline	<input type="radio"/> RCC <input type="radio"/> PVC <input type="radio"/> HPDE		
<input type="button" value="Submit"/>		<input type="button" value="Clear"/>	
		<input type="button" value="Back"/>	

Figure 12. Form for uploading data in Web-GIS Based Interactive Dashboard for Department of Soil & Water Conservation

[BACK](#)

[Go to Previous Page](#)

**Upload Data for Underground Pipeline Systems (CSV file)**

Select CSV File:  No file chosen

Figure 13. Form for uploading data in CSV format for Nodal Officers in Web-GIS Based Interactive Dashboard for Department of Soil & Water Conservation

Username	Download excel	Remarks	Submit
123	<input type="button" value="Download excel"/>	<input type="text"/>	<input type="button" value="Submit"/>
sco	<input type="button" value="Download excel"/>	<input type="text"/>	<input type="button" value="Submit"/>

**Figure 14. Form for Viewing uploaded data in CSV format in Web-GIS Based Interactive Dashboard for Department of Soil & Water Conservation**

## 6. Conclusion

To visualize data on a dynamic dashboard with charts, maps, and other visual elements that show the status and performance of vital assets and events in real time, user friendly Web GIS dashboard is developed for real-time data visualization and analysis, where, one can visualize the work carried out in any particular block/district/state on the click of the mouse on a particular point. It also helps the officials to take further analysis based on the gap analysis, where less work has been carried out for a particular activity or scheme. Web GIS is a powerful tool for helping management, since it provides the information, geo-located data and capabilities to make the information accessible to everyone and everywhere in the world.

## Acknowledgements

The Authors acknowledge the funds received from the Department of Soil & Water Conservation, Punjab for conducting the study.

## Funding

The work is funded by the Department of Soil & Water Conservation, Punjab.

## References

- Adel A. and B. Abdullah (2015). A Comparison Between Three SDLC Models Waterfall Model, Spiral Model, and Incremental/Iterative Model. *IJCSI International Journal of Computer Science Issues*, 12(1), 106–111. [https://www.academia.edu/10793943/A\\_Comparison\\_Between\\_Three\\_SDLC\\_Models\\_Waterfall\\_Model\\_Spiral\\_Model\\_and\\_Incremental\\_Iterative\\_Model](https://www.academia.edu/10793943/A_Comparison_Between_Three_SDLC_Models_Waterfall_Model_Spiral_Model_and_Incremental_Iterative_Model)
- Agrawal S. and R. D. Gupta (2017). Web GIS and its architecture: a review. *Arabian Journal of Geosciences*, 10(23). <https://doi.org/10.1007/s12517-017-3296-2>
- Amiruddin S. M. (2016). Real-time Web GIS to monitor marine water quality using wave glider. *IOP Conference Series: Earth and Environmental Science*, 37(1). <https://doi.org/10.1088/1755-1315/37/1/012074>
- Balaji S. (2012). Waterfall vs v-model vs agile: A comparative study on SDLC., 2(1), 26–30.
- Balzer C., R. Oktavian, M. Zandi, D. Fairen-Jimenez and P. Z. Moghadam (2020). Wiz: A Web-Based Tool for Interactive Visualization of Big Data. *Patterns*, 1(8). <https://doi.org/10.1016/j.patter.2020.100107>
- Batty M. (2015). A perspective on city dashboards. *Regional Studies, Regional Science*, 2(1), 29–32. <https://doi.org/10.1080/21681376.2014.987540>
- Boris S. (2018). 8 Software Development Models: Sliced, Diced and Organized in Charts. *ScienceSoft*, 1. <https://www.scnsoft.com/blog/software-development-models>
- Bovkir R. and A. C. Aydinoglu (2021). Big urban data visualization approaches within the smart city: Gis-based open-source dashboard example. *International Archives of the Photogrammetry, Remote Sensing and Spatial Information Sciences - ISPRS Archives*, 46(4/W5-2021), 125–130. <https://doi.org/10.5194/isprs-Archives-XLVI-4-W5-2021-125-2021>
- Diaz-Sarachaga J. M., D. Jato-Espino and D. Castro-Fresno (2018). Is the Sustainable Development Goals (SDG) index an adequate framework to measure the progress of the 2030 Agenda? *Sustainable Development*, 26(6), 663–671. <https://doi.org/10.1002/sd.1735>
- Duncombe J., A. Clements, W. Hu, P. Weinstein, S. Ritchie and F. E. Espino (2012). Review: Geographical information systems for dengue surveillance. *American Journal of Tropical Medicine and Hygiene*, 86(5), 753–755. <https://doi.org/10.4269/ajtmh.2012.11-0650>
- Farkas G. (2017). Applicability of open-source web mapping libraries for building massive Web GIS clients. *Journal of Geographical Systems*, 19(3), 273–295. <https://doi.org/10.1007/s10109-017-0248-z>
- Ismanto H., A. Doloksaribu and A. Syafrianto (2016). Webgis-based Irrigation basic Map Model of Merauke Regency Papua. *International Journal of Computer Applications*, 152(3), 21–24. <https://doi.org/10.5120/ijca2016911816>
- Jing C., M. Du, S. Li and S. Liu (2019). Geospatial dashboards for monitoring smart city performance. *Sustainability (Switzerland)*, 11(20). <https://doi.org/10.3390/su11205648>
- Keim D. A. (2002). Information visualization and visual data mining. *IEEE Transactions on Visualization and Computer Graphics*, 8(1), 1–8. <https://doi.org/10.1109/2945.981847>
- Kienberger S., M. Hagenlocher, E. Delmelle and I. Casas (2013). A WebGIS tool for visualizing and exploring socioeconomic vulnerability to dengue fever in Cali, Colombia. *Geospatial Health*, 8(1), 313–316.

<https://doi.org/10.4081/gh.2013.76>

Kitchin R. (2016a). The ethics of smart cities and urban science. *Philosophical Transactions of the Royal Society A: Mathematical, Physical and Engineering Sciences*, 374(2083). <https://doi.org/10.1098/rsta.2016.0115>

Kitchin R. (2016b). *Urban data and city dashboards: Six key issues*. 1–20. <https://doi.org/10.31235/osf.io/k2epn>

Lemmens R., A. Wytzisk, R. de By, C. Granell, M. Gould and P. van Oosterom (2006). Integrating semantic and syntactic descriptions to chain geographic services. *IEEE Internet Computing*, 10(5), 42–52. <https://doi.org/10.1109/MIC.2006.106>

Miola A. and F. Schiltz (2019). Measuring sustainable development goals performance: How to monitor policy action in the 2030 Agenda implementation? *Ecological Economics*, 164(June), 106373. <https://doi.org/10.1016/j.ecolecon.2019.106373>

Rowland A., E. Folmer and W. Beek (2020). Towards self-service gis—combining the best of the semantic web and web gis. *ISPRS International Journal of Geo-Information*, 9(12). <https://doi.org/10.3390/ijgi9120753>

Spyratos S., M. Lutz and F. Pantisano (2014). Characteristics of Citizen - contributed Geographic Information. *Connecting a Digital Europe through Location and Place. Proceedings of the AGILE'2014 International Conference on Geographic Information Science*, 3–6.

Steiniger S. and A. J. S. Hunter (2013). The 2012 free and open source GIS software map - A guide to facilitate

research, development, and adoption. *Computers, Environment and Urban Systems*, 39, 136–150. <https://doi.org/10.1016/j.compenvurbsys.2012.10.003>

Stoddart R. and B. Godfrey (2020). Gathering evidence of learning in library curriculum center spaces with web GIS. *Evidence Based Library and Information Practice*, 15(3), 21–35. <https://doi.org/10.18438/ebliip29721>

Tsou M. H. and B. P. Buttenfield (2002). A dynamic architecture for distributing geographic information services. *Transactions in GIS*, 6(4), 355–381. <https://doi.org/10.1111/1467-9671.00118>

Tsou M. H., J. A. Yang, S. Han, C. Te Jung, J. M. Gawron, C. Allen and B. H. Spitzberg (2015). Social Media Analytics and Research Test-bed (SMART Dashboard). *ACM International Conference Proceeding Series*, 2015-July. <https://doi.org/10.1145/2789187.2789196>

Visner M., S. Shirowzhan and C. Pettit (2021). Spatial analysis, interactive visualisation and gis-based dashboard for monitoring spatio-temporal changes of hotspots of bushfires over 100 years in New South Wales, Australia. *Buildings*, 11(2), 1–27. <https://doi.org/10.3390/buildings11020037>

Yang C., R. Raskin, M. Goodchild and M. Gahegan (2010). Geospatial Cyberinfrastructure: Past, present and future. *Computers, Environment and Urban Systems*, 34(4), 264–277. <https://doi.org/10.1016/j.compenvurbsys.2010.04.001>

## Assessment of forest fragmentation in greater Gir landscape area, Gujarat using geospatial techniques

Abhinav Mehta<sup>1,\*</sup>, Shital Shukla<sup>2</sup> and Shrey Rakholia<sup>3</sup>

<sup>1,2</sup> Department of Earth Sciences, Gujarat University, Ahmedabad 380009, India.

<sup>3</sup>The Geographic Information System (TGIS) Laboratory, 526, ISCON EMPORIO, Jodhpur Cross Road, Satellite, Ahmedabad 380015, India

\*Email: mehta.abhinav01@gmail.com

(Received: May 25, 2022; in final form: Aug 25, 2022)

**Abstract:** Due to the negative consequences of climate change, the fragmentation of forest areas worldwide as a result of increased anthropogenic pressure has become a source of concern. The objective of this research study was to evaluate forest fragmentation analysis around the Greater Gir Landscape, Gujarat. The Fragmentation assessment was performed based on Land-use & Land-cover (LULC) analysis using the Landsat 8 OLI images of 2015 and 2019 as primary datasets for the study. Geographic Information System (GIS) techniques were employed for LULC mapping with seven classes showing increment in the agriculture and vegetation patches with the year 2019 in compare to year 2015 due to accumulative rainfall pattern. The Spatial Metric was performed with the use of FRAGSTATS software, where Landscape Metrics were quantified using Class level, Landscape level and Moving Window Analysis. The trend observed in all the metrics calculated indicates increasing of continuity in Greater Gir Landscape. The forest has not undergone severe degradation but a rise in the natural classes like agriculture, vegetation patches, and waterbodies has led to increase in the level of continuity which is leading to conversion of these land patches in homogeneity of the areas using geospatial techniques. These spatial metrics using FRAGSTATS helps in simplifying quantification of the complex spatial processes and can be used for generating a positive framework for forest conservation.

**Keywords:** LULC, Homogeneity, Landscape Metrics, GIS, FRAGSTATS

### 1. Introduction

Forest plays a vital role in our ecosystem being a habitat to the flora and fauna (Siti Yasmin et al., 2019) and sustaining human lives. Human-induced pressure on the forest ecosystem has risen rapidly in recent years, isolating certain forest sections in the process (Referowska-Chodak, 2019).

Fragmentation being an important factor leads to deprivation of habitat, biodiversity, ecosystem functions including detrimental impact on continuous patches and quality of forest (Sharma et al., 2022). Fragmentation is a non-random process where the conversion of forest area to agricultural, Built-up, road networks and other land use is done knowingly by mankind for developmental purposes (Laurance, 2008). The intensity of fragmentation in the landscape is based on reduction in size, deformation of shape, Isolation, increase in edge effects and reduction of core area (Tolessa et al., 2016). A study revealed that about 20% of the forest around the world is within 100m of an edge to agricultural, urban, or other modified environments where the ecosystem is affected most severely and about 70% is within 1 km radius from the forest edge (Ripperger et al., 2013). Remote sensing is being widely used for the assessment of fragmentation occurring around the world by the means of Landscape metrics (Dutta et al., 2020).

Landscape metrics is an entity which facilitates quantification of land use and understand the pattern of land cover distribution (Singh et al., 2014) i.e., changes in the spatial structure of patches and understanding the relationships between different patches present in the landscape (McGarigal, K. and SA Cushman, 2012).

Landscape heterogeneity, assessed using metrics, is an important feature which can be used for the protection of biodiversity (Syrbe et al., 2012). Comparison of landscape metrics belonging to different temporal periods help in quantifying the changes that has taken place in the landscape, the degree of fragmentation, the spatial isolation of ecosystems, the disappearance or increase of their surface (Badora et al., 2020). The degree of fragmentation can be explained as a function of the varied size, form, spatial distribution, and abundance of patches (David et.al, 1993). In the recent past, Government of Gujarat has taken many initiatives for consolidating the conservation of Asiatic Lions. The concept of Greater Gir Landscape (GGL) has been adopted through which additional suitable habitat for lion is being developed for the habitation of lion. (Pandey et.al, 2014)

According to a study, with timely and stringent protection given by the erstwhile rulers and the subsequent Government, the lions showed a steady increase in their population (Ram, 2022). Dispersal in the areas adjoining the Gir Protected Areas PAs required the rise of the Greater Gir region concept to conserve and manage the lions and their habitat (Bharat Pathak, 2002). Due to the efforts of the Forest Department and local communities, the Kathiawar region contains a number of sanctuaries and National Parks, including Mitiyala, Paniya, and Velavadar (Black Buck National Park), which are the best examples of conservation methods. Due to the pioneering conservation action plan and the cooperation of the local community, threats like grazing, logging, hunting, poaching, etc. are less of a concern here. Study area map with the major State/National highway that passes through the Landscape can posed a great barrier to faunal species of the sanctuary and its movement (Figure 1). A

framework for better management and conservation of the Greater Gir Landscape must be put in place as a result of this anthropogenic strain. The objective of this research study is to identify the factors causing fragmentation in and around the GGL using landscape metrics based on satellite derived landuse datasets. This study can help the planners comprehend how fragmentation has changed the environment and help them develop better GGL conservation policies.

## 2. Materials and methods

### 2.1 Study area

Greater Gir Landscape is situated in Kathiawar region of Amreli, Gir Somnath, Bhavnagar and Botad Districts in the state of Gujarat. The Study area comprises of regular animal movement between two districts of Amreli and Bhavnagar, India with the geographic range between 20°45' and 22°7' N latitude and 71°5' and 72°22'E Longitude (Mehta et al., 2021). GGL has hilly terrain with forest patches, natural vegetation and agricultural land with covering of coastal areas of Rajula, Mahuva etc. The plains are starting from 0mtrs above mean sea level as it is touching the Gulf of Khambhat in Eastern side and Arabian Sea in southern side towards 580mtrs near Palitana hills basically observed and derived Digital Elevation Profile tool using Google Earth Software. The river streams present in the area includes streams of Shetrunji, Kalubhar rivers. GGL falls under the administration of Wildlife Circle-Junagadh covering Forest Division of Amreli, Shetrunjai & Bhavnagar Division. Kamnath, Kalubhar & Shetrunji are the major man-made reservoirs existing in the landscape. The area supports an ecological setting for a range of faunal and floral species because of its unique geographic location. The climate of this region is classified as Hot Semi-arid climate (Bsh) with hot dry summers and mild winters as per Köppen-Geiger climate classification map (Peel et al., 2007). Teak (*Tectona Grandis*) and other species like *Acacia*, *Ziziphus*, etc. make up the majority of the forest cover in the area. The major fauna of the area is displayed by the presence of Asiatic Lions, Jungle cat, Leopard, Wild pigs, Nilgai, Sambar, Chital, Common mongoose, Hyena, and Indian porcupine (MoEFCC, 2019). The Average Yearly Precipitation is 561.8 mm for Amreli and 655.9 mm for Bhavnagar. Average Daily Max. air temp. for Amreli is 34.3°C and for Bhavnagar is 33.9°C whereas Average Daily Min. air temp. is 20.1 °C and 21.7 °C respectively (Indian Meteorological Department, 2010). The annual precipitation for Bhavnagar and Amreli is 556 mm and 782 mm, respectively, according to the 2015 IMD statistics. Also, for 2015 post-monsoon Bhavnagar and Amreli received a meagre 0.4 mm and 6.3 mm rainfall respectively. Whereas, in 2019 Bhavnagar and Amreli received annual precipitation of 813 mm and 886 mm respectively where in post monsoon season Bhavnagar and Amreli 53 mm and 83.2 mm rainfall respectively (IMD 2015 & 2019).

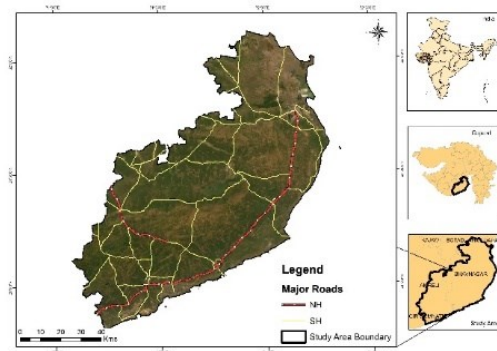


**Figure 1. Study area map of The Greater Gir Landscape (GGL)**

### 2.2 Methodology

The study was performed using two USGS LANDSAT-8 images geometrically and atmospherically corrected to level 2, where sensor OLI (Operational Land Imager) provides 9 Optical bands and 2 Thermal bands from TIRS (Thermal Infrared Sensor). Satellite imagery was acquired from Earth explorer platform which is Free & Open access (FOSS) worldwide. Images with acquisition dates of 16 November 2015 and 3 December 2019 were chosen because they have the lowest cloud cover and are temporally compatible with post-monsoon mapping to achieve most land-use and habitat mapping classes. Additionally, 2015 was used as a reference point for the 2015 Asiatic Lion Census study, which calculates points of occurrence of direct and indirect evidence for lions over the habitats, and 2019 was used as the groundtruthing survey conducted during this time of period. LULC map was prepared using these datasets for 2015 and 2019 classified into 13 classes of supervised classification scheme using Maximum Likelihood Classifier (MLC) algorithm of Semi-automatic Classification (SCP) Plugin under QGIS 3.16 version. SCP Plugin allows to perform the supervised classification of remote sensing satellite images, providing tools for the download, the preprocessing and postprocessing of images (<https://plugins.qgis.org/plugins/SemiAutomaticClassificationPlugin>). Study area boundary was prepared using Block level (Taluka) boundaries contained in the Greater Gir Region as per the movement pattern of Lions using occurrence data. To analyze the fragmentation occurring in the sanctuary, raster files of LULC were assessed using the FRAGSTATS v.4.2 software which is an open-source program for analyzing spatial pattern in the classified maps. FRAGSTATS is a free programme that analyses rasterized maps to characterize spatial patterns of land cover. Quantifying variances and alterations in land cover over time is possible by using FRAGSTATS on two landuse images obtained at different times. After importing the LULC raster files for 2015 and 2019 FRAGSTATS allows to set various parameters like that of Class descriptor file with '.fcd' extension which contains information about the LULC classes used. Apart from that, the edge depth which accounts for the distance from the edge of the patch to the core area was kept fixed at 30m which is approximately 1 pixel as the resolution of satellite image is 30 m.

Landscape level analysis representing spatial pattern for the whole landscape mosaic, which considers different patch types simultaneously was performed (McGarigal, 2014). Class level analysis represents the structure and spatial distribution of patches belonging to same patch type was performed. For cell-level analysis, the moving window method was integrated using 100 m windows. It is calculated at the class level of the forest class and returns the results in raster format.

**Table 1. Detailed description of FRAGSTATS metrics used for the study (after McGarigal et al., 1995)**

Metrics & Analysis Level	Description
Number of patches (NP) <b>Class Level</b>	Total number of patches as per forest class (No Units)
Patch Density (PD) <b>Class Level</b>	Total patches for forest class divided by the total forest area, multiplied by 100 ha. (Number/100ha.)
Edge Density (ED) <b>Class Level</b>	Total lengths (m) of all edge segments (perimeter) of the forest class divided by total area (ha). (Metres/Ha.)
Euclidean nearest neighbor distance (ENN_MN) <b>Class Level</b>	Total distance (m) to the nearest neighboring patch of the same class. (Meters)
Shannon’s Diversity Index (SHDI) <b>Landscape Level</b>	More the number of different patch classes (i.e., patch richness, PR) more the SHDI. (No Units)
Largest Patch Index (LPI) <b>Landscape Level</b>	Area of the largest patch of the forest class, depicted as percentage of total forest cover. (Percent)
Contiguity Index (CONTIG) <b>Cell Level</b>	Analyses patch shape depending on spatial connectedness of pixels inside a single patch. (No Units)
Radius of Gyration <b>Cell Level</b>	The mean distance (m) between each pixel of the patch and the centroid of the patch. (Meters)
Aggregation Index (AI) <b>Class &amp; Cell Level</b>	Expresses the frequency of ambiguous pairs of patches class (including like adjacencies between the same patch type) appearing next to each other. (Percent)
Interspersion and Juxtaposition Index (IJI) <b>Class Level</b>	Provides the interspersion observed over the possibility of highest interspersion for the number of forest class present. (Percent)

### 3. Results and discussion

#### 3.1 LULC Change analysis

The major trends in LULC change includes conversion of Agriculture majorly from Fallowland and barrenland respectively. Additionally, major positive shift can be seen in vegetation patches/plantation from Barrenland. Moreover, Forest patches can be seen as somewhat decreased but due to classification techniques & pixel reflectance there are chances that it is mixed up with vegetation patches class in 2019. Overall landuse shows positive trends towards the good agricultural practices and contiguity between landscape patches. (Figure 2(a)(b)(c)).

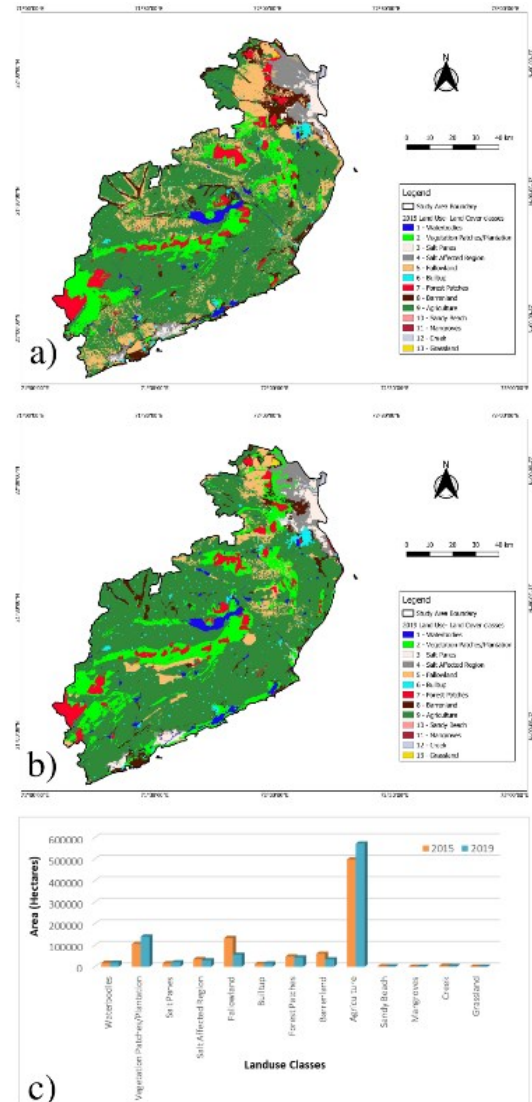


**Figure 2. LULC map of the study area a) 2015 LULC Map & b) 2019 LULC Map c) Graph showing LULC Changes**

#### 3.2 Fragmentation analysis

##### 3.2.1 Landscape Level Metrics

The values for the average contiguity index showed increase in the value from 2015 to 2019 (Table 3) indicating increase in larger contiguous patches and thus more spatial connectedness and less subsequent fragmentation (Lagro, 1991). Additionally, the CAI (Core Area Index) shows growth, indicating that core areas of classes are expanding generally on a landscape level.

However, the Shannon Diversity Index (SHDI) shows a decline in value, indicating that over the study years, the heterogeneity of distinct classes has been declining.

**Table 2. Landuse Statistics (IMD, 2015 & 2019)**

Srno	Landuse Classes	2015	2019
		Area(Ha)	Area(Ha)
1	Waterbodies	17626.95	19819.17
2	Vegetation patches/Plantation	105916.77	140324.94
3	Salt Panes	16388.28	21271.95
4	Salt Affected Region	35526.78	29797.83
5	Fallowland	133747.65	55777.95
6	Builtup	14236.2	15597.29
7	Forest Patches	48148.65	42779.54
8	Barrenland	60727.95	34652.43
9	Agriculture	499155.2	572001.43
10	Sandy Beach	2632.86	2477.25
11	Mangroves	722.88	1249.74
12	Creek	4642.83	3718.53
13	Grassland	855	859.95
	<b>Total</b>	<b>940328</b>	<b>940328</b>

**Table 3. Landscape Metrics summary**

Landscape Metrics	SHDI	CAI	CONTIG
2015	1.58	30.68	0.61
2019	1.41	42.83	0.68

**3.2.2 Class level metrics (for forest & vegetation patches classes)**

In addition, to the landscape metrics the class metrics analysis was also included. The Class level metrics used in this study to infer the results include Euclidean Nearest-Neighbor Distance (ENN), Aggregation Index (AI), Edge Density (ED), Patch Density (PD), Number of Patches (NP), Largest Patch Index (LPI) and Interspersion and Juxtaposition Index (IJI).

It was noted that the NP decreased pretty noticeably between 2015 and 2019, which caused the PD value to fall. In contrast, while ED denotes perimeter, the patches are becoming significantly larger in terms of perimeter in 2019 as compared to 2015.

In addition, ENN and AI also increased simultaneously in the time period (Table 4). Increasing value of ENN in 2019 exhibits overall increases in large patches of forest & vegetation patches (Tolessa et al., 2016) whereas lower value of AI in 2015 compared to 2019 indicates more disaggregation, thus higher the fragmentation in previous year.

LPI comparisons between research years reveal that, as seen in 2019, the area of the largest patches is expanding. Moreover, IJI is slightly higher in 2019 than 2015 which

depicts higher interspersion with other classes thus it shows more intervals. As per the IJI value which is slightly higher than 55% that means it is adjacent with at least 6 classes.

**Table 4. Class metrics for forest class for 2015 and 2019**

Class Metrics	NP	PD	ED	ENN	IJI	AI	LPI
<b>2015</b>	544	0.057	4.373	672.6	55.30	96.39	2.02
<b>2019</b>	232.5	0.024	4.424	874.4	55.44	97.11	2.35

**3.2.3. Moving window analysis**

This technique was used to build a raster file with the findings by computing values for each cell. Analysis was done for obtaining Contiguity Index map at Landscape level and Aggregation Index map at Class level. The classes for Aggregation Index map include Vegetation Patches and Forest patches.

The result for Contiguity Index (Figure 3(a & b)) for year 2019 shows increased values in the area having higher values which implies more interconnections between various classes in 2019 as compared to 2015 indicating less fragmentation. According to the Aggregation Index results (Figure 4(a & b)), there was an increase in the area with a higher fragmentation value in 2015 than in 2019, indicating that over the course of the study period, forest and vegetation patches became more aggregated, resulting in a larger aggregated habitat that is conducive to animal movement.

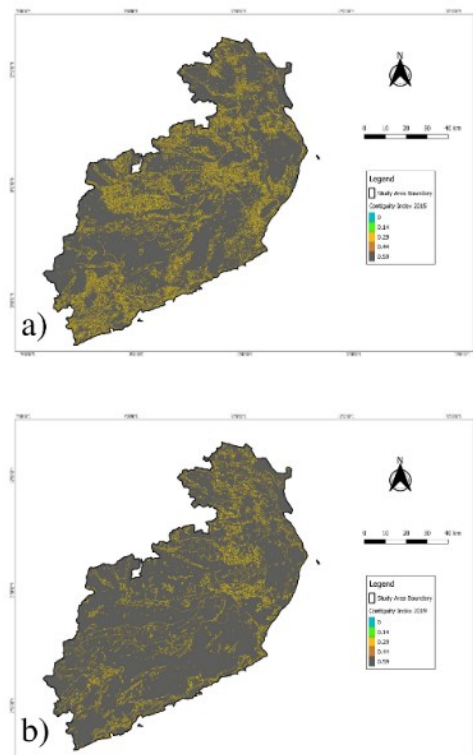


**Figure 3. Contiguity Index of the study area. a) 2015 Contiguity Index Map b) 2019 Contiguity Index Map Note: Lesser value of Contiguity Index means high degree of fragmentation and vice versa.**

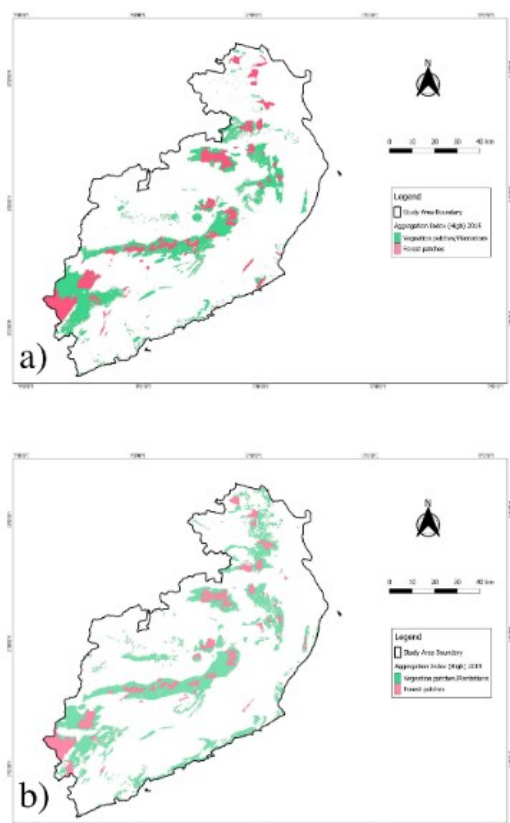


**Figure 4. Aggregation Index of the study area. a) 2015 Aggregation Index Map b) 2019 Aggregation Index Map**

The aggregation index decreased significantly near the canals originating from Shetrunji reservoir in both the study years. Major positive changes can be seen over 2019 in compare to 2015 is due the positive rainfall trend in 2019. Additionally, State Highway 31 and National Highway 351 passes close to the same canal at the Shetrunji reservoir, which is located in the north-western portion of the research area. It also has a low aggregation index, which may indicate that the traffic movements and the effects of the road on the accompanying infrastructure had an effect on the vegetation patches. (Figure 1, 4(a & b)). As roads take up substantial area of forest and plays a detrimental role causing fragmentation (Reed et al., 1996). Increase in number of fragments, leading to isolation of patches and there was further decrease in mean patch size. The increase in the number of patches could be attributed to conversion of the forest to other categories like road construction (Narmada, 2021).

#### 4. Conclusions

Based on study and comparison between 2015 and 2019, the landscape analysis (class level) based on FRAGSTATS metrics reveals that there is little evidence of forest fragmentation in many patches. Additionally, it demonstrates how buffering vegetation patches outside protected forest areas can expand the space available for wildlife to migrate and may even contribute to the genetic diversity of Asiatic Lions.

In addition, larger vegetation patches and forest patches can be brought to focus for conservation which can

increase connectivity between the landuse classes. Increasing interspersion and juxtaposition may be beneficial in wildlife movement since diversity of classes including Agriculture, Fallowland, Grassland etc. are also important to include in study as these classes serve as the potential home for the Asiatic Lions.

Under the SDG (Sustainable Development Goals) 15, For the continued existence of life on Earth and in the fight against climate change, forests are crucial and making investments in land restoration is essential for enhancing livelihoods, lowering vulnerabilities, and lowering economic risks. Moreover, Fragmentation Analysis is an important parameter for any landscape dynamics as it is becoming an important issue towards the gene flow & corridor mapping for the wild species and sustainable land development.

#### Acknowledgements

We are grateful to USGS Earth Explorer Online Platform for Landsat satellite images used in our analysis. Also, we are thankful to the Department of Earth Sciences, Gujarat University-Ahmedabad, and associated staff for provision of lab, software & data facilities.

#### References

- Badora K. and R. Wróbel (2020). Changes in the spatial structure of the landscape of isolated forest complexes in the 19th and 20th centuries and their potential effects on supporting ecosystem services related to the protection of biodiversity using the example of the Niemodlin Forests. *Sustainability (Switzerland)*, 12(10). doi: 10.3390/su12104237
- Bharat Pathak (2002). *Biodiversity Conservation Plan for Gir (A supplementary Management Plan, 2002-03 to 2006-07)*. Wildlife Circle, Junagadh. Gujarat State Forest Department, India.
- David J. M., A. Mark and J. P. White (1993). *Comparing Spatial Pattern in Unaltered Old-Growth and Disturbed Forest Landscapes Authors (s): David J. Mladenoff, Mark A. White, John Pastor and Thomas R. Crow*. Published by: Wiley Stable URL: <http://www.jstor.org/stable/1941832> Accessed: 28-03-2022, 294–306.
- Dutta S., I. Dutta, A. Das and S. K. Guchhait (2020). Quantification and mapping of fragmented forest landscape in dry deciduous forest of Burdwan Forest Division, West Bengal, India. *Trees, Forests and People*, 2(July), 100012. doi: 10.1016/j.tfp.2020.100012
- Indian Meteorological Department (2010). *Climatological Tables of Observations in India, 1981-2010*.
- Indian Meteorological Department (2015 & 2019). *Rainfall Statistics of India – 2015 & 2019*. New Delhi.
- Lagro J. (1991). Assessing patch shape in landscape mosaics. *Photogrammetric Engineering & Remote Sensing*, 57(3), 285–293.

- Laurance W. F. (2008). Theory meets reality: How habitat fragmentation research has transcended island biogeographic theory. *Biological Conservation*, 141(7), 1731–1744. doi: 10.1016/j.biocon.2008.05.011
- McGarigal K. and S. A. Cushman, (2012). *FRAGSTATS v4: Spatial Pattern Analysis Program for Categorical and Continuous Maps*. Retrieved from <http://www.umass.edu/landeco/research/Fragstats/Fragstats.html>
- McGarigal K. (2014). Landscape Pattern Metrics. *Wiley StatsRef: Statistics Reference Online*, 1–13. doi: 10.1002/9781118445112.stat07723
- McGarigal K. and B. J. Marks (1995). *FRAGSTATS: spatial pattern analysis program for quantifying landscape structure*. Retrieved from <https://www.fs.usda.gov/treesearch/pubs/3064>
- Mehta A., S. Shukla and S. Rakholia (2021). Vegetation Change Analysis using Normalized Difference Vegetation Index and Land Surface Temperature in Greater Gir Landscape. *Journal of Scientific Research*, 65(03), 01–06. doi: 10.37398/jsr.2021.650301
- MoEFCC. (2019). *Notification 11th March 2019 - S.O. 1316(E)*.
- Narmada K. (2021). Landscape metrics to analyze the forest fragmentation of Chitteri Hills in Eastern Ghats, Tamil Nadu. *Journal of Civil Engineering and Environmental Sciences*, 7, 001–007. doi: 10.17352/2455-488x.000038
- Pandey C. N., R. L. Meena, S. Kumar and M. S. Alam (2014). *Asiatic the Lion Conservation of the Action Plan of for Gujarat State Forest Department*.
- Peel M. C., B. L. Finlayson and T. A. McMahon (2007). Updated world map of the Köppen-Geiger climate classification. *Hydrology and Earth System Sciences*, 11(5), 1633–1644. doi: 10.5194/hess-11-1633-2007
- Ram M. (2022). *Home ranges of Asiatic lions in the Asiatic Lion Landscape, Gujarat, India. August*.
- Reed R. A., J. Johnson-barnard, W. L. Baker, R. A. Reed, J. Johnson-barnard and W. L. Bakert (1996). *Contribution of Roads to Forest in the Fragmentation Rocky Mountains*. 10(4), 1098–1106.
- Referowska-Chodak E. (2019). Pressures and threats to nature related to human activities in European urban and suburban forests. *Forests*, 10(9). doi: 10.3390/f10090765
- Ripperger S. P., M. Tschapka, E. K. V. Kalko, B. Rodriguez-Herrera and F. Mayer (2013). Life in a mosaic landscape: Anthropogenic habitat fragmentation affects genetic population structure in a frugivorous bat species. *Conservation Genetics*, 14(5), 925–934. doi: 10.1007/s10592-012-0434-y
- Sharma S., M. Bista and M. Li (2022). Characterizing changes in land cover and forest fragmentation from multitemporal Landsat observations (1993–2018) in the Dhorpatan Hunting Reserve, Nepal. *Journal of Forestry Research*, 33(1), 159–170. doi: 10.1007/s11676-021-01325-9
- Singh S. K., A. C. Pandey and D. Singh (2014). *Land Use Fragmentation Analysis Using Remote Sensing and Fragstats BT - Remote Sensing Applications in Environmental Research* (P. K. Srivastava, S. Mukherjee, M. Gupta, & T. Islam (eds.); pp. 151–176). Cham: Springer International Publishing. doi: 10.1007/978-3-319-05906-8\_9
- Siti Yasmin, Y. and M. Muhamad Afizzul (2019). Evaluating spatial patterns among forest types in peninsular Malaysia using fragstats. *Proceedings - 39th Asian Conference on Remote Sensing: Remote Sensing Enabling Prosperity, ACRS 2018*, 2, 683–691.
- Syrbe, R. U. and U. Walz (2012). Spatial indicators for the assessment of ecosystem services: Providing, benefiting and connecting areas and landscape metrics. *Ecological Indicators*, 21, 80–88. doi: 10.1016/j.ecolind.2012.02.013
- Tolessa, T., F. Senbeta and M. Kidane (2016). Landscape composition and configuration in the central highlands of Ethiopia. *Ecology and Evolution*, 6(20), 7409–7421. doi: 10.1002/ece3.2477

# Characterisation of Fixed-Wing Versus Multirotors UAVs/Drones

P. K. Garg

Indian Institute of Technology - Roorkee, Roorkee 247667, Uttarakhand, India

Email: pkgiitr@gmail.com

(Received: Dec 02, 2021; in final form: Sep 15, 2022)

**Abstract:** Drones are Unmanned Aerial Vehicles (UAVs) that do not carry a human operator, fly remotely or autonomously, and carry lethal or non-lethal payloads. Advances in fabrication, navigation, remote control capabilities, and power storage systems have made possible the development of a wide range of drones. The most popular ones are fixed-wing and multirotor drones. They have several advantages and disadvantages and can be deployed quickly to obtain very high resolution imagery/point cloud data. With sophisticated computer vision, robotics and data, and low cost digital cameras, it is possible to get centimeter-level resolution and accuracy. Advances in technology have made the increased uses of drones for various applications. The uses of UAVs/drones are increasing allowing 2D and 3D maps to be created and used for creation of 3D maps and digital elevation models (DEMs). This paper describes in details about the two broad categories of UAVs; fixed-wing and multirotor UAVs. Their salient characteristics along with advantages and disadvantages are also given. It also provides insights to the users for selection of right kind of UAV.

**Keywords:** UAV, Fixed-wing drones, multirotors, Endurance, Selection of UAV

## 1. Introduction

Different types of drones have been around since as early as 1917. Although initially they were used for military applications, but today drone operations have much more use in business industry. Drones are flying robots which include Unmanned Air Vehicles (UAVs). Aerial vehicles that do not carry a human operator, fly remotely or autonomously, and carry lethal or non-lethal payloads are considered as drones. Advances in fabrication, navigation, remote control capabilities, and power storage systems have made possible the development of a wide range of drones/UAVs which can be utilized in various situations where the presence of human is difficult, impossible, or dangerous. The UAV images/data belong to the Big Data category, and are particularly useful to assess large and not easily accessible areas or dangerous sites (Gupta, et.al., 2016). These images can be collected at regular intervals with much lower cost than the traditional photogrammetric images from the aircraft. They have several advantages, such as deployed quickly and repeatedly, flexible in terms of flying height, timing of missions, and very high resolution imagery/point cloud data. With sophisticated computer vision, robotics and data, and low-cost digital cameras and sensors, it is now possible to get centimeter-level resolution and accuracy from drone data (Colomina and Molina, 2014). Providing a swath width of 50–500 m and a spatial resolution of 1-20 cm, UAV platforms are able to provide very high resolution inputs (Garg, 2020). The high spatial resolution and high temporal resolution make the UAV an ideal platform to apply in various fields and conduct a variety of research in remote sensing.

The UAVs/drones are very useful in many applications due to availability of high resolution images and laser data, and thus save time & efforts to collect the field data of a large area. The use of drones for surveying and mapping has expanded in recent years as many organisations realise the benefits of using geospatial data provided by these systems. Drones can provide much more detailed data at high resolution than the traditional surveying and remote sensing methods, allowing 2D and 3D maps to be created

and used for various applications. These images are processed to produce 3D models, like Digital Elevation Models (DEMs) for viewing the terrain or for volume computations. They can provide up to centimeter-level accuracy of a GPS rover. In addition, the UAV derived orthophotos, point clouds and DEMs could significantly enhance the extraction of relevant information from the UAV images (Boon et al., 2017).

The drones are used in a wide range of civil and military applications, and can perform both outdoor and indoor missions in challenging environments. These applications can be categorized in different ways; based on the type of missions (military/civil), the flight zones (outdoor/indoor), and the environments (underwater/water/ground/air/space), as shown in Figure 1.

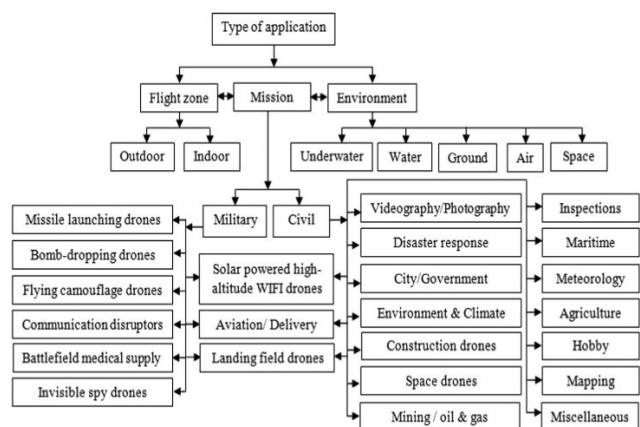


**Figure 1. Various applications of UAVs**

Drones can be used for surveying and mapping, search and rescue missions, agricultural crop mapping, environmental protection, damage assessment, mailing and delivery, performing missions in oceans or other planets, inside buildings, in the battlefield and several other applications. The UAV systems have shown remarkable progress in terms of performance, reliability, increased capabilities, and ease of use. In coming years, the UAVs will establish

themselves as a viable alternative to conventional mapping and surveying.

## 2. Types of UAVs/Drones

Today, there are several types of UAVs available commercially with different configurations and specifications. There is no standard classification system of UAVs available. Defense agencies have their own standard, while civilians have their own categories for UAVs. Generally, UAVs can be categorized by their performance characteristics. Features including weight, wing span, wing loading, range, maximum altitude, speed, endurance, and production costs, are important parameters that distinguish different types of UAVs/drones, and classify them into several categories. Furthermore, UAVs can be classified based on their engine types, size, weight, range and endurance, applications, and also use a tier system that is employed by the military. The UAVs often vary widely in their configurations depending on the platform and mission. The classification according to size includes: Very small UAVs, Micro or Nano UAVs, Small UAVs, Mini UAVs, Medium UAVs, and Large UAVs. They have also been classified according to the ranges they can travel and their endurance in the air: Very low-cost close-range UAVs, Close-range UAVs, Short-range UAVs, Mid-range UAVs, and Endurance UAVs, as given in Table 1. These are mainly used for reconnaissance and surveillance tasks.

**Table 1. Drone types, their ranges and endurance time (Abdullah, 2019)**

Types	Range (km)	Endurance time (min)
Very low-cost, close range UAVs	5	20 to 45 min
Close range UAVs	50	1 to 6 hrs
Short range UAVs	150 km or longer	8 to 12 hours
Mid-range UAVs	650 km working radius	-
Endurance UAVs	300 km working radius	36 hours

The latest innovation in UAV is the Small Unmanned Aerial Vehicle (sUAV) which are light-weight under 55 pounds (lbs), and are designed for commercial and civilian uses (Garg, 2020). Micro-UAVs are even further smaller systems that weigh less than 4.4 lbs. According to the U.S. Department of Defence, UAVs are classified into five categories, as shown in Table 2.

In general, there are two broad categories of UAVs; fixed-wing and multirotor drones. Both the types have their own advantages and disadvantages, including their suitability for some specific applications. Fixed-wing UAVs normally have longer flight endurance capabilities, while multirotors can provide stable image capturing and easy vertical take-off & landing characteristics. Therefore, the main aim of this paper is to assess the capabilities of fixed-wing versus multirotor UAVs for their suitability and applicability.

**Table 2. UAVs Classification according to the US Department of Defense (Fahlstrom and Gleason, 2012)**

Category	Size	Maximum Gross Takeoff Weight (lbs)	Normal Operating Altitude (ft)	Airspeed (knots)
Group 1	Small	0-20	<1,200	<100
Group 2	Medium	21-55	<3,500	<250
Group 3	Large	<1320	<18,000	<250
Group 4	Larger	>1320	<18,000	Any airspeed
Group 5	Largest	>1320	>18,000	Any airspeed

AGL– Above ground level, MSL– Mean sea level

### 2.1 Fixed-wing UAVs

Fixed-wing UAVs use wings like a normal aeroplane to provide the lift as opposed to vertical lift by multirotors. They are available with a number of different configurations, but typically have a fuselage with two wings and a single rotor. Because of this reason, they only need to use energy to move forward and can't hold themselves at a point up in the space. A fixed-wing drone is always moving forward faster than a multirotor drone, and manoeuvring longer times for monitoring the area. They provide greater efficiency, and are able to cover longer distances, thus mapping much larger areas in short time. Due to their superior engine efficiency, most commercial models can fly for an hour or more and cover around 400 hectares. It is also possible to use gas engines as their power source, and with the greater energy density of fuel many fixed-wing drones can work for 16 hours or more. Fixed-wing drones can also carry heavier loads than the multirotor drones. The fixed-wing structure provides exceptional stability that allows the drones to carry loads of up to 50 kg.

Fixed-wing drones are most advantageous in agricultural sector, electricity pylons and oil & gas industries as they can cover large areas at a higher speed. They are less common for surveying applications, where area covered is small. As fixed-wing drones fly much faster than the multirotors, so they work efficiently for large worksites. For certain jobs, flying just one fixed-wing drone over a site is far more efficient than flying multiple quadcopters (multi-rotors), as they can stay in the space much longer on a single battery charge. Other greatest advantage of fixed-wing drones is their ability to recover from a total power failure, whereas the sudden loss of power in a multirotor can result in complete loss of the aircraft. These drones are able to continue flying, and more importantly, can land safely without power. Since, fixed-wing drones are better able to withstand side winds, the windy areas, such as electricity pylons in open countryside can easily be surveyed with these drones.

The disadvantages include the requirement of ground distance for take-off & landing, as well as long sweeping turns, however, the actual distance required will depend on the model and its configuration. For their launching and landing, a runway or catapult launcher is needed to get

them into the space, and either a runway, parachute or net to recover them safely again at the end. Fixed-wing UAV requires a trained pilot to land it smoothly in order to avoid any damage to the UAV and sensors. Only the smallest fixed-wing UAVs are suitable for hand launch and 'belly landing' in an open field. As fixed-wing UAVs fly like normal aircraft, operators need to plan ahead to avoid obstacles, which may be a real challenge for operators to fly them. The airframes of fixed-wing UAVs are significantly larger than a similarly specified multirotor, and thus would require a significant amount of space for transportation. They are usually much more expensive than the multirotor drones; although the prices are coming down as the technology grows.

The fixed-wing UAVs are unable to hover at one spot constantly, which makes them unsuitable for any general aerial photography work. The other disadvantage of these drones is that they are less manoeuvrable than the multirotor UAVs, so they provide a challenge for some surveying applications, especially in confined spaces (small areas, urban environments or construction sites) where the UAV needs to turn quickly. Finally, a big challenge when operating fixed-wing UAVs is big Eagles which are a menace as they can strike to UAVs and cause damages.

## 2.2 Multirotor UAVs

These are the most common types of UAVs used in commercial and consumer market. Several configurations are available but they generally follow the same design principle. The four-propeller multirotor (quadcopter) is the most popular design, as it provides the best balance between lift, control, manoeuvrability and cost. A central frame connects up to eight fixed-pitched propellers that control the speed, direction and height of the drone. The multiple rotors provide power to the propellers, enabling flight and manoeuvrability. By changing the speed of each propeller, varying amount of thrust and torque is produced that controls the speed and height of the drone. It provides the drone a unique capability allowing it to fly with precision in both indoor and outdoor.

Multirotors are easy to fly and control, and can easily perform autonomous flights (Thamm et al., 2015). The main reason of wide-spread use of multirotors is that they are easy to get started, as they are cheaper and easier to fly, with some skills and little practicing, which isn't the case with the fixed-wing drones. They can also operate in headless mode which aligns drone movements relative to the controller, so the drone always moves forward irrespective of the direction it is facing. Multirotors are much more cost-effective than the fixed-wing drones that can cost almost twice. They are the easiest, economical and perfect option for collecting the images with great control over position and framing. If a small camera is to be operated in the air for a short period of time for aerial photography work, then multirotor drones are the best option. Multirotors can carry much more payload than a fixed-wing drone. The eight-rotor drones are capable of lifting more payloads as compared to four-rotor or six-rotor drones. As a general rule of aerodynamics, the larger the rotor blade is and the slower it spins, the more efficient

it is. This is why a quadcopter (four rotors) is more efficient than an octocopter (eight rotors), and special long-endurance quads have a large prop diameter.

They can hover in a stationary position, and provide VTOL (vertical take-off & landing) capability (Garg, 2020). The other advantage of multirotor UAVs is their manoeuvrability as compared to fixed-wing UAVs, as these can easily fly in areas where other types of UAVs can't reach. The ability of UAVs to fly low with appropriate sensors provides the opportunity to collect data at fine spatial resolution (Anderson and Gaston, 2013), and makes them ideal tools for land mapping. Multirotors are compact in design, and therefore easy to transport and carry around as they don't have wings that makes them suitable for surveying professionals who transport them from site to site for various jobs. The multirotor drones provide a number of advantages for surveying work as compared to fixed-wing drones but these should not be used by default in all kind of surveying works.

The multirotor UAVs have disadvantages due to their reduced range and speed as compared to fixed-wing UAVs. The main disadvantage of multirotors is their limited endurance and speed, making them unsuitable for large scale aerial mapping, long endurance monitoring and long distance inspection, such as pipelines, roads and power lines. Since, the multirotors can't take flight for longer time, therefore the area coverage is limited (Cai et al., 2014), whereas the fixed-wing UAVs have very good flight endurance and can cover large areas in one flight. To survey a large area more than 7 km long, a fixed-wing drone may not be used. Multirotors are fundamentally not efficient and require a lot of energy just to fight with gravity and keep them in the air. With current available battery technology, they are limited to fly around 20-30 minutes when carrying a light-weight camera payload. Heavy-weight lift multirotors are although capable of carrying more weight, but they have much shorter flight time. Due to the need for fast and high-precision throttle changes to keep them stabilised, the use of multirotors is restricted to only electric motors, as it is practically not possible to use a gas engine to power them. They use more energy, and are more sensitive to weather conditions. Lastly, this type of UAV requires complex and regular maintenance, due to its elaborate structure.

## 3. Selection of a UAV/Drone

For new users, many times it becomes a difficult task to choose the right type of UAV/drone for the work to be performed. A systematic and efficient approach for the selection of the UAV is necessary to choose the best UAV for the critical tasks under consideration. When selecting the most suitable UAV type, firstly it is necessary to decide what task is going to be performed with it, and consequently what is most important for that task, such as speed and long range, manoeuvring ability, and accuracy. Other selection criteria depend on several basic characteristics of UAVs, for example, the flight duration (endurance) which determines how much area can be covered during a single flight, and hence determines the

economic efficiency. The UAVs with flight endurance of a few minutes to several hours are now available. A UAV's endurance depends on two factors: its wing type (fixed-wing have a higher flight endurance) and weather conditions as some UAVs are very sensitive to it. If a UAV flies against the wind, it is going to consume a lot of energy, which has an impact on its endurance. The flight duration should be considered together with the carrying capacity and take-off weight. Some companies publish flight times for the UAVs without a payload (camera) and under ideal conditions (e.g., no wind, at 68°F/20°C), but when a payload is attached, the operational flight time of UAV can be reduced by over 50% (Kroetsch, 2014).

The UAVs can be equipped with various payloads; cameras and sensors, so selection of a suitable payload is also critical. Changing from one payload to another needs to be seamless for the operator. The UAV must provide the ability to swap payloads in all weather conditions, and includes electronics and software that recognise the different payloads automatically. Without the ability to quickly adapt to the needs of the operation, valuable time can be lost reconfiguring/calibrating the system after each change. The weight of payload and UAV affects the UAV's stability in the air, so the heavier it is, the more stable its trajectory and the higher the image quality. It is essential that a UAV is reliable, portable and easy to fly. It should be light and strong enough to carry loads during flight and, more importantly, during landing. The UAVs of composite materials provide the necessary rigidity and strength, but may not be sufficiently flexible and robust to take heavy impact loads. Polymeric materials are able to withstand impact, do not break in case of deformation, and retain their shape, but are not able to provide structural rigidity. The combined use of polymers and composite materials is considered the best. The UAV's portability is critical which is achieved through solutions, such as a folding frame or modular design. The time needed to prepare a UAV for flight by a single operator should not exceed a few minutes.

The safety of the operator and the people and property over which flights are performed are very important when choosing a UAV. It is best to choose the UAVs with intelligent control of the application having best practice guidelines for safe operations and trouble-shooting procedures, and built-in safety functions, such as warning system for low battery levels and radio communication quality, automatic flight mission, automatic return to the starting point when connection is lost or the battery is critically low, and geofencing. This will ensure the safety of property and people in the areas adjacent to the site as well safety of the UAV, and also enables the operator to focus on the collection of images and data with confidence. The UAVs with network and streaming capabilities can provide additional benefits in surveillance and search & rescue applications.

Price is a key factor when choosing a UAV. A comparison of prices can be done considering their maintainability, availability of spare parts and the service life of their components. Fixed-wing and VTOL UAVs are typically around 2-3.5 times the cost of a multirotor UAV but they

last longer in the air. The capabilities of a UAV to operate in a range of environmental temperatures are also required to be considered while selecting a system (Kroetsch, 2014). With any UAV, the ability to operate safely in windy conditions is a requirement, and many UAVs adjust flying altitude as per existing wind speed.

Hamurcu and Eren (2020) have proposed multicriteria decision-making (MCDM) approaches that are well suited to deal with the intricacy in selection of a UAV for military applications. It also proposes an integrated methodology based on the analytical hierarch process (AHP) and Technique for Order Preference by Similarity to Ideal Solution (TOPSIS) to evaluate UAV alternatives for selection process. Petkovics et. al., (2017) have discussed specific UAV characteristics in order to facilitate the selection of right kind of UAV according to the farmers' heterogeneous requirements regarding the data collection on their crops. Selection of appropriate UAV for specific needs of farmers was carried out by using a MCDM approach. The weighting parameters for the selection, evaluation software parameters and selection of the best conditions were formulated based on data recording, data collection and data processing, supporting software, selective sputtering/fertilization, data collection/recording and data processing in greenhouses.

When choosing a drone for surveying, the first decision is either select a fixed-wing or a multirotor drone, as each one has its own advantages and disadvantages. The right choice of drone, however, depends on the type of surveying and data collection job intended to be carried out, the size of area, the terrain type, and finally the applications for which the spatial data/maps are to be used. There are some hybrid models also available designed specifically for mapping purposes. The VTOL drones represent a blended approach, combining elements from both the multirotor and fixed-wing drones. They take-off and land vertically like a multirotor, but act like a fixed-wing drone in flight to facilitate the high efficiency for large-scale mapping.

Chapman (2016) has presented a comparison between multirotor and fixed-wing drones as well as single rotor and hybrid rotor drones, including their typical uses, as given in Table 3. While a multirotor has many rotors to hold it up, a single rotor has just one, plus a tail rotor to control its heading. A single-rotor helicopter has the benefit of much greater efficiency over a multirotor, and also that it can be powered by a gas motor for longer endurance. It is the best if hovering is to be done with a heavy payload (e.g., an aerial LiDAR laser scanner) or have a mixture of hovering with long endurance or fast forward flight. A single-rotor allows for very long blades which are more like a spinning wing than a propeller, giving greater efficiency.

**Table 3. A comparison between multirotor, fixed-wing drones, single rotor and hybrid rotor drones, including their typical uses**

Types of UAV	Advantages	Disadvantages	Typical uses
Multirotor	Accessibility Ease of use VTOL and hover flight Good camera control Can operate in a confined area	Short flight time Small payload capacity	Aerial photography and Video, Aerial inspection
Fixed-wing	Long endurance Large area coverage Fast flight speed	Launch and recovery needs a lot of space No VTOL/hover Harder to fly, more training needed Expensive	Aerial mapping, Pipeline and Power line inspection
Single-rotor	VTOL and hover flight Long endurance (with gas power) Heavier payload capability	More dangerous Harder to fly, more training needed Expensive	Aerial LiDAR laser scanning
Fixed-wing Hybrid	VTOL and long-endurance flight	Not perfect at either hovering or forward flight Still in development	Drone delivery

The disadvantages of single-rotors are their complexity, cost, vibration, and also the danger of getting hurt from their large spinning blades. In terms of difficulty, single-rotor drones lie somewhere between multi-rotors and fixed-wing aircraft. They can hover over the area, but they aren't as stable as multirotors, and also require a lot of maintenance and care due to their mechanical complexity. The hybrid drones combine the benefits of fixed-wing drones with the ability to hover, and also can take-off and land vertically. With the availability of modern autopilots, gyros and accelerometers, these types of drones are feasible because the autopilot can keep them stable, and human pilot can guide them flying in the space. There are only a handful of hybrid fixed-wing aircraft currently in the market, such as Amazon's Prime Air delivery drone, but more are expected in the future as the technology is refined.

Boon et al., (2017) have evaluated the performance of a Skywalker fixed-wing UAV versus a Raven multirotor UAV for environmental mapping applications. The completely automated computer vision Structure from

Motion (SfM) pipeline provided by Agisoft PhotoScan Professional software package was used for 3D point cloud generation. They found that the cost, maintenance and flight time was lower in case of Skywalker fixed-wing, while the multirotor was found to provide much accurate data, although the quality of data of fixed-wing drone was also found to be satisfactory for most environmental mapping applications. The fixed-wing drone provided the data with elevation of the study area that ranged from 1564.5 to 1545 m above mean sea level (*msl*), which equates to a height difference of 19.5 m with a slope of 1.7%. Whereas, the elevation using the multi-rotor data ranged from 1560.5 to 1543 m above *msl*, providing a height difference of 17.5 m with a slope of 1.59%. The height information differed with exactly 2 m between the two UAVs; this difference is equivalent to height error of data derived from the fixed-wing UAV. Suitability for different attributes for both types of UAVs is also presented by them, as shown in Table 4.

**Table 4. Suitability for different attributes for both types of UAVs**

Attributes	Fixed-wing (Skywalker)	Multi-rotor (Raven)
Payload capacity		√
Flight time	√	
Stabilisation		√
Georeferencing	√	
Cost	√	
Maintenance	√	
Vegetation representation		√
Erosion gully representation		√
Wetland slope mapping	√	√
Contour mapping	√	√

Overall, the multirotor data was found to be more accurate and better represented the environmental features. Nevertheless, the basic identification and estimation of environmental impacts from the fixed-wing data was still satisfactory. For other applications, like close proximity inspections and when more detailed data is required for smaller areas in land surveying, a multirotor will definitely be more suitable. Boon et al., (2017) gave several recommendations, such as (i) data should be collected during mid-day when the position of the sun is higher that results in high amount of the sun's illumination under clear sky conditions, and less shadows in the data, (ii) the GCPs (ground control points) should be placed in a grid format ensuring that they do not merge with the vegetation cover, (iii) a flying altitude of below 150 m is advised for environmental mapping purposes to enhance the features, such as vegetation and erosion gullies in the imagery, (iv) the self-calibration method for calibrating the camera prior to the flight should be done to improve the quality of data, and (v) the camera settings, such as the exposure should be standardised to achieve repeatable and comparable results.

On the basis of various literature review, a brief discussion on comparison between fixed-wing and multirotor UAVs

is given below as well as presented in Table 5. These observations might help the users to make a right selection of drone for their applications.

**Table 5. A comparison between fixed-wing and multirotor UAVs**

Capability	Fixed-wing	Multirotor
Speed	High	Low
Flight time	High	Low
Coverage	Large	Small
Object resolution	Cm/inch per pixel	mm per pixel
Take-off and landing area	Large	Very small
Landing in case of power failure	Can land safely without power	Can result in complete damage of UAV
Wind resistance	High	Low
Skill required to fly	High	Low
Projects	Large area mapping	Small area mapping, Machine and industrial plant monitoring, Indoor inspection
Applications	Land surveying, Agriculture, Mining, Environmental, Humanitarian etc.	Inspection, Urban survey, Construction sites, Emergency response, Law enforcement, Transport of medicines and light goods, Cinematography and videography etc.

1. A multirotor drone is not successful for large area mapping. It is because of its low speed as compared to fixed-wing drone. Obviously, the area covered per day by a fixed-wing drone will be greater than the multirotor. The disadvantage of multirotor drone is their reduced range and speed as compared to the fixed-wing drone. The time that is taken in mapping and the cost incurred is directly proportional to the area that is to be mapped. The rotors of a multirotor drone consume a lot of energy and that is why they are suitable only for small mapping projects. On the other hand, fixed-wing and hybrid drones can stay in the air for a long time, fly faster and map with more efficiency, while maintaining a consistent quality of data captured. This makes fixed-wings and hybrid drones preferable when large land areas have to be mapped.

2. The multirotor drone is not stable in windy areas due to thrust on the drone by the winds, whereas the fixed-wing drone is much more stable due to its smooth aerodynamics and design, like a conventional aircraft. Wind speed can profoundly influence the completeness of a drone dataset. Turbulences lead to adaptive flight manoeuvres. Constant wind increases the power consumption of the engine, and

can reduce the flight time enormously. Side wind affects the orientation of the drone as fixed-wing drones tend to correct their position against the wind.

3. In multirotor drones, aerodynamics is not the highest priority in the design. The vibrations are more in multirotor drone as compared to fixed-wing drone, so it would affect the image quality used for mapping purpose. Comparatively, higher resolution cameras would be needed to generate orthophotos of the same resolution of a fixed-wing adding significantly to the processing time requirements. Vibration from the motors in multirotor drone (at least four motors) during the flight can affect the sharpness and contrast of the images.

4. Fixed-wing drone can fly with a constant cruising speed, however, the data collection from these drones require specialised skills.

5. Fixed-wing drones have more flight time compared to the multirotors. Larger flight time up to one hour or more of fixed-wing drone against multirotor drone whose average flight time is 20-25 minutes, allows mapping of several km during one flight. In addition, they have some advantages from the aspect of durability and flight height. Fixed-wing systems with the ability to fly at high altitude have long durability.

6. Other overlooked advantage of fixed-wing drones is their ability to recover from a total power failure. The sudden loss of power in a multirotor can result in complete loss of the aircraft. But a fixed-wing drone can continue gliding, and more importantly, land safely without power.

#### 4. Conclusions

Drones can be used for surveillance, aerial photography, search & rescue, agriculture, disaster, cinematography, inspections of structures, delivery of goods, etc. There are two broad types of drones: multirotor and fixed-wing types. Each type of drone contributes to the amount of weight they can carry (payload), efficiency, duration of flight and application. Multirotors have four, six or eight rotors; four being the most common for small to regular-sized drones. The more rotors it has, the more it can manoeuvre. However, they are not as efficient as fixed-wing drones. On the other hand, fixed-wing drones need either a catapult or a runway to take-off the ground and landing. These drones are sometimes used for surveillance, like in the military, and are more commonly flown for the purpose of long-distance. Fixed-wing drones require quite a bit more drone flying experience and training, mainly with take-off and landing.

As more UAVs become available, choosing the right type of UAV is important. In most cases, a multirotor has good range, excellent manoeuvrability, easy to fly, cost-effective, and can be fitted with a range of sensors. If a large open tract of land is to be surveyed, a fixed-wing UAV will suit well. The UAVs have a number of key values that define their performance, such as weight, maximum speed, maximum flying height above sea level, maximum flight time, operating temperature, hover

accuracy, dimensions, etc. The multirotor is the preferred choice for most surveying applications, but fixed-wing drones also have some specific advantages, like speed. It is expected that in future, drones would be designed that have the speed and range advantage of a fixed-wing, with the manoeuvrability and practicality of a multirotor drone. This would allow the drones to take-off and land like a multirotor, but fly like a fixed-wing drone. This combination can cover ten times more ground area than a multirotor while collecting two times more data, thus providing efficiency. The future of drones appears to be very promising for spatial data collection as well as deriving results for the applications in hand.

## References

- Abdullah Q. A., (2019), Classification of the unmanned aerial systems, The Pennsylvania State University, <https://www.e-education.psu.edu/geog892/node/5>.
- Anderson K. and J. G. Kavin (2013), Lightweight unmanned aerial vehicles will revolutionize spatial ecology, *Frontiers in Ecology and the Environment*, March
- Boon M A., A.P. Drijfhoutand and S. Tesfamichael (2017), Comparison of a fixed-wing and multi-rotor UAV for environmental mapping applications: a case study, *The International Archives of the Photogrammetry, Remote Sensing and Spatial Information Sciences*, Volume XLII-2/W6, International Conference on Unmanned Aerial Vehicles in Geomatics, 4–7 September 2017, Bonn, Germany.
- Cai G., J. Dias and L. Seneviratne (2014), A survey of small-scale unmanned aerial vehicles: Recent advances and future development trends. *Unmanned Systems*, 2(02), 175-199.
- Chapman A. (2016), Types of drones: multi-rotor vs fixed-wing vs single rotor vs hybrid VTOL, *Australian UAV* (June), <https://www.auav.com/au/articles/drone-types/> [<https://perma.cc/Z7SY-ECCM>].
- Colomina I., and P. Molina (2014). Unmanned Aerial Systems for Photogrammetry and Remote Sensing: A Review.” *ISPRS Journal of Photogrammetry and Remote Sensing* 92 (June): 79– 97. doi:10.1016/j.isprsjprs.2014.02.013.
- Fahlstrom P. and G. Thomas (2012), *Introduction to UAV Systems*, 4<sup>th</sup> Edition, Wiley & Sons, <https://www.wiley.com/en-ax/9781119978664>.
- Garg P. K. (2020), *Introduction to Unmanned Aerial Vehicles*, New Age International Publishers Ltd., New Delhi.
- Gupta L, R. Jain and G. Vaszkun (2016), Survey of important issues in UAV communication networks,” *IEEE Communications Surveys & Tutorials*, Vol. 18, no. 2, pp. 1123–1152
- Hamurcu, M. and E. Tamer (2020), Selection of unmanned aerial vehicles by using multicriteria decision-making for defence, *Journal of Mathematics*, Hindawi, Open access, Volume 2020, <https://doi.org/10.1155/2020/4308756>.
- Kroetsch D. (2014), Choosing the right UAV, *Geospatial World*, 16 Sept 2014, <https://www.geospatialworld.net/article/choosing-the-right-uav/>
- Petkovics I., S. Janos, P. Armins and C. Zlatko (2017), Selection of unmanned aerial vehicle for precision agriculture with multi-criteria decision making algorithm, *IEEE 15<sup>th</sup> International Symposium on Intelligent Systems and Informatics*, September 14-16, Subotica, Serbia.
- Thamm H. P., N. Brieger, K. P. Neitzke, M. Meyera, R. Jansenaand and M. Mönninghof (2015), SONGBIRD- an innovative UAS combining the advantages of fixed wing and multi rotor UAS, *The International Archives of the Photogrammetry, Remote Sensing and Spatial Information Sciences*, Volume XL-1/W4, 2015 International Conference on Unmanned Aerial Vehicles in Geomatics, 30 Aug–02 Sept, Toronto, Canada.

# Impact of various Vegetation Indices on Mango orchard mapping using Object-Based Image Analysis

Steena Stephen\*, Dipanwita Haldar, N.R. Patel  
Indian Institute of Remote Sensing, Dehradun, 248001  
\*Email: [steesaini@gmail.com](mailto:steesaini@gmail.com)

(Received: Dec 30, 2021; in final form: 15 Sep 2022)

**Abstract:** Mango farming is an important part of the Indian agriculture economy. Mapping of mango orchards is essential for monitoring mango plantations as well as its yield assessment. Object-based Image Analysis (OBIA) is a powerful image classification method which uses spatial and spectral information for image classification. This study assesses the impact of three vegetation indices; NDVI (Normalised Difference Vegetation Index), ReNDVI (Red Edge Normalised Difference Vegetation Index) and LSWI (Land Surface Water Index) on the accuracy of classification using object-based image analysis using Sentinel - 2 data. A temporal profile was generated to select the best possible dates for classification based on the maximum and minimum values of the index. LSWI gave the highest overall accuracy of the classification (89%) followed by ReNDVI (87%) and NDVI (86%). The study found that LSWI and ReNDVI have the potential for better mapping of Mango orchards and can be explored further to generate accurate Mango orchard maps.

**Keywords:** OBIA, NDVI, LSWI, ReNDVI, Mango Orchard, Sentinel 2

## 1. Introduction

Mango (*Mangifera indica L.*), the king of fruits is an important part of the Indian agriculture economy. India is the largest exporter of Mangoes in the world and the second-largest producer of fruits after China. Since growing mango is important for commercial farming, it is necessary to monitor the orchard for its yield and health. By assessing mango orchards for their yield, orchard management practices can be altered to get the required output from the trees. Mapping mango orchards is an important part of monitoring.

Studies have been carried out to map mango orchards using satellite and drone imagery. Drone imagery and machine vision have been used to map trees and to estimate yield (Liang et al., 2018). Laser scanning methods like airborne laser scanning (Wu et al., 2020) and terrestrial laser scanning methods have been used to map mango orchard canopies for better yield estimation. High spatial resolution imagery like Worldview 3 have also been explored for mango orchard mapping and yield estimation by using geometric and spectral data through ANN (Artificial Neural Network) (Rahman et al., 2018). A study was conducted in 2014 which used high-resolution data for the generation of an inventory for orchards. For mango orchards, the parameters for classification were obtained through a temporal profile of orchard NDVI. The study identified further need for techniques that help in the delineation of orchards under wide spacing, diverse agro-horticultural systems and very young orchards (Hebbar et al., 2014). Another study conducted on the estimation of the area of orchards using pixel-based classification methods stated that the accuracy of classification reduces due to spectral mixing of Mango, Sapota trees and the presence of young orchards. Thus, a new method needs to be developed to solve the issue of spectral mixing of signatures from Mango trees and other crops (Chaudhari

et al., 2019). Multi-temporal EVI data from MODIS was used to classify different LULC (Land Use Land Cover) features using object-based image analysis (OBIA). The study was performed with a single date image and a combination of multi-date imagery. It was found that the multi-date imagery gave better results compared to single date imagery (Gao et al., 2009).

Various studies indicate that traditional pixel-based classifiers don't use spatial information for classifying imagery making OBIA (Object-based image analysis) more efficient than these methods (Chandra et al., 2019; Blaschke et al., 2014). OBIA groups pixels in the form of image objects based on the spatial relationship with neighbouring pixels. Image segmentation is the most important part of classifying an image by OBIA (Baatz & Schape, 2000). After segmentation, the image is classified according to shape, size, spatial and spectral properties. Vegetation indices are calculated to enhance the contrast between vegetation and other features such as building and soil. This study assesses the impact of three vegetation indices; NDVI (Normalized Difference Vegetation Index), LSWI (Land Surface Water Index) and ReNDVI (Red Edge Normalized Difference Vegetation Index) on the accuracy of classification of mango orchards in level two classification using object-based image analysis.

## 2. Study area

Syana is a sub-district of Bulandshahr in Uttar Pradesh. The study area for the project is located at 28.626871° N, 78.060737° E and occupies an area of 756.237 Km<sup>2</sup> (Figure 1). The region receives a maximum rainfall of 782mm and the temperature ranges from 1.5° C to 44.5° C (Bhartariya, 2012). Syana lies in the mango producing belt of the country and is dominated by large clusters of mango orchards.

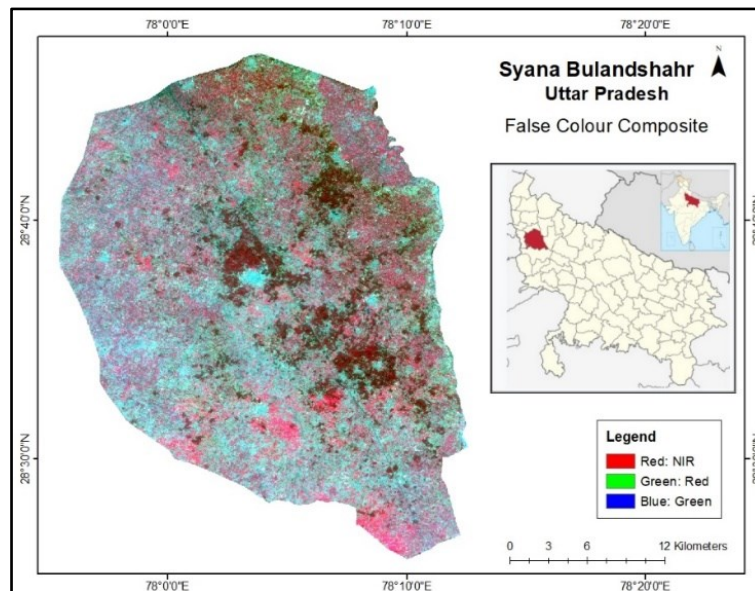


Figure 1. Study Area map

### 3. Methodology

The OBIA based methodology for level 2 classification is as mentioned below (Figure 2).

#### 3.1 Satellite imagery

For the study, Sentinel 2 imagery has been used. Sentinel 2 satellite provides Multispectral data in 13 bands from visible, near-infrared and short-wave infrared through Multispectral Instrument (MSI) and has a temporal resolution of 5 days. The images were processed using google earth engine using 5 bands (Table 1).

#### 3.2 Ground truth collection

The spatial location of Mango orchards was obtained through a survey carried out by Saha & Haldar (2021)

from 2<sup>nd</sup> to 5<sup>th</sup> February 2021 in the study area. During this survey, a total of 96 points were collected corresponding to the satellite pass of 3<sup>rd</sup> February 2021. The mango orchards were found to be in the early inflorescence emergence stage during the survey.

Table 1. Bands used for the study

Band No	Name	Wavelength( $\mu\text{m}$ )
3	Red	0.66
5	Red Edge	0.70
7	NIR	0.78
8A	Red Edge	0.86
11	SWIR	1.61

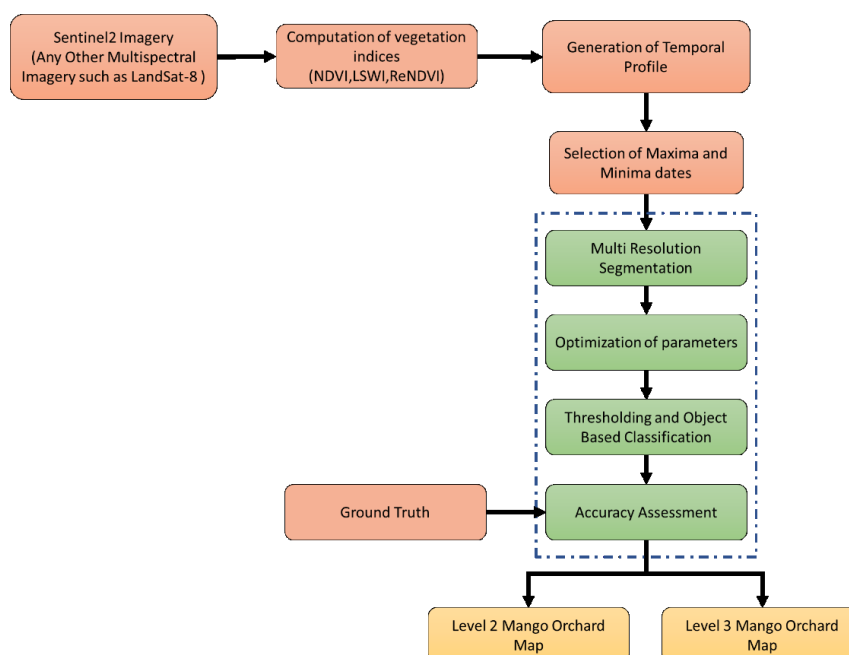


Figure 2. Methodology Flowchart

### 3.3 Vegetation indices generation

Vegetation indices combine the spectral reflectance of two or more wavelengths to highlight a particular property of vegetation. In this study, three indices were used: NDVI, LSWI and ReNDVI (Table 2.).

#### 3.3.1 NDVI

Normalized Difference Vegetation Index is used to quantify vegetation by measuring the difference between NIR and red bands. This index is sensitive to vegetation cover, biomass, crop condition and density. NDVI has been used for classification of images into different land use and land cover classes (Clerici et al., 2012).

#### 3.3.2 ReNDVI

Rededge Normalised Difference Index is the ratio between the red-edge band and the near-infrared band. It is a modification of the traditional NDVI and is used to monitor vegetation stress.

#### 3.3.3 LSWI

Land Surface Water Index is calculated by using the shortwave infrared and near-infrared bands. This index is sensitive to the amount of moisture in vegetation and its soil background (Chandrasekar et al., 2010). This index has been used in the mapping of irrigated croplands and monitoring annual changes in irrigation (Xiang et al., 2020).

### 3.3 Temporal profile

By using the mango orchard and crop location coordinates collected during the ground truth survey and the vegetation indices, a temporal profile was generated from May 2020 to May 2021 using Google Earth Engine (GEE). Two age groups of mango orchards i.e. old (>30yrs) and middle-aged (15 to 30 yrs) (Meena & Asrey, 2018) were chosen for the generation of the temporal profile due to the dominance of these age groups in the study area. Along with the two age groups of mango orchards, two crop types (wheat and sugarcane) grown in the region were also selected. The temporal profile was generated to observe separability between the features and to select the best possible dates for classification. The dates were then stacked for classification (Hebbar et al 2014).

### 3.4 Classification

In OBIA, image segmentation is the first step for classification of an image. For this study, multiresolution segmentation was carried out. After segmentation, the image objects were classified using the threshold obtained

from the temporal profile. Assign class algorithm, a knowledge-based classifier was used for classification. The images were classified into five classes; building, mango orchard, crop, fallow and waterbody.

### 3.5 Accuracy assessment

After classification, accuracy assessment was carried out using the ground truth samples collected from the field. An error matrix was generated and kappa coefficient was calculated.

## 4. Results

Using the Sentinel 2 imagery, vegetation indices were calculated (Table 2). A temporal profile was generated for each index illustrated below.

Temporal profiles were generated using the vegetation index values. The indices consisted of peak and troughs due to changes in seasons and the phenological cycle of the crops and mango orchards. The dips in the curves of mango orchards indicate the dormant and the flowering stages. The peaks in the temporal profiles indicate the vegetative stage.

The temporal profiles of NDVI and ReNDVI (Figure 3&4) have a similar pattern due to the use of similar band ranges (B4, B5, B8) for the computation of NDVI and ReNDVI. The graphs also indicate that the class separability is highest in the temporal profile of LSWI (Figure 5) compared to ReNDVI and NDVI. The maximum value of NDVI for the middle-aged orchard class was obtained on 3<sup>rd</sup> Feb2021 and the minimum value of NDVI was obtained on 5<sup>th</sup> Dec 2020. In case of ReNDVI, the maximum value was obtained on 18<sup>th</sup> June 2020 and minimum value was obtained on 5<sup>th</sup> Dec 2020. The temporal profile of LSWI shows maximum and minimum value on 01<sup>st</sup> Oct20 and 5<sup>th</sup> Dec20 respectively.

In the case of all the three vegetation indices, a combination of images obtained during the dormant stage and the peak vegetative stage have performed the best. After the generation of temporal profile, the images were classified and accuracy assessment was carried out using the ground truth collected. Error matrices for each index was generated to observe the effect of index on the accuracy of classification.

**Table 2. Vegetation Indices used for the study**

Index	Formula	Sentinel2 Bands used	Range
NDVI (Sellers, 2007)	$(\text{NIR}-\text{Red})/(\text{NIR}+\text{Red})$	(B8-B4)/(B8+B4)	-1 to 1
ReNDVI (Gitelson & Merzlyak, 1994)	$(\text{NIR}-\text{Red Edge})/(\text{NIR}+\text{Red Edge})$	(B8-B5)/(B8+B5)	-1 to 1
LSWI (Wong et al., 2019)	$(\text{NIR}-\text{SWIR})/(\text{NIR}+\text{SWIR})$	(B8A-B11)/(B8A+B11)	-1 to 1

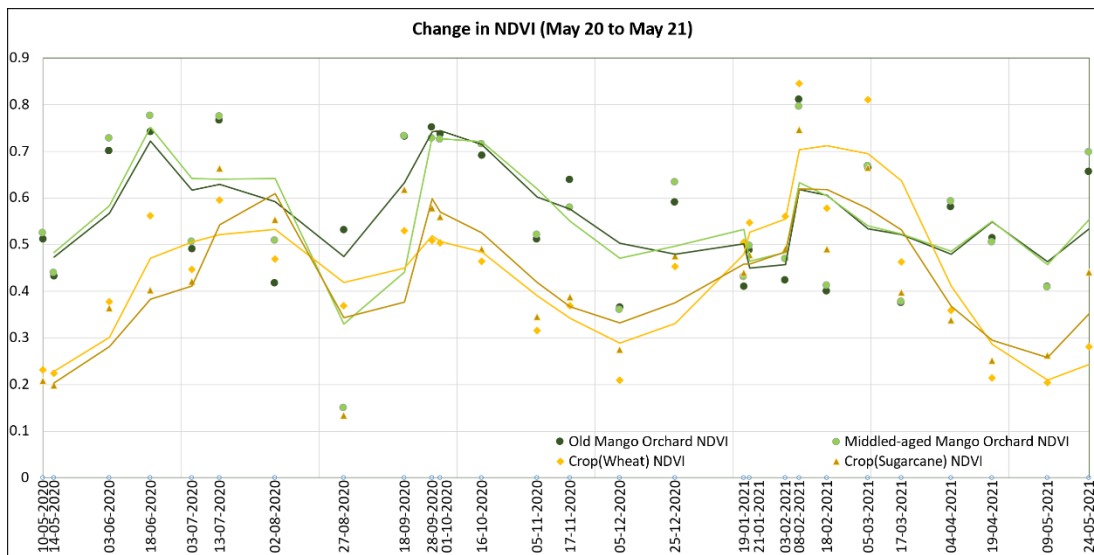


Figure 3. Temporal profile of NDVI from May 2020 to May 2021

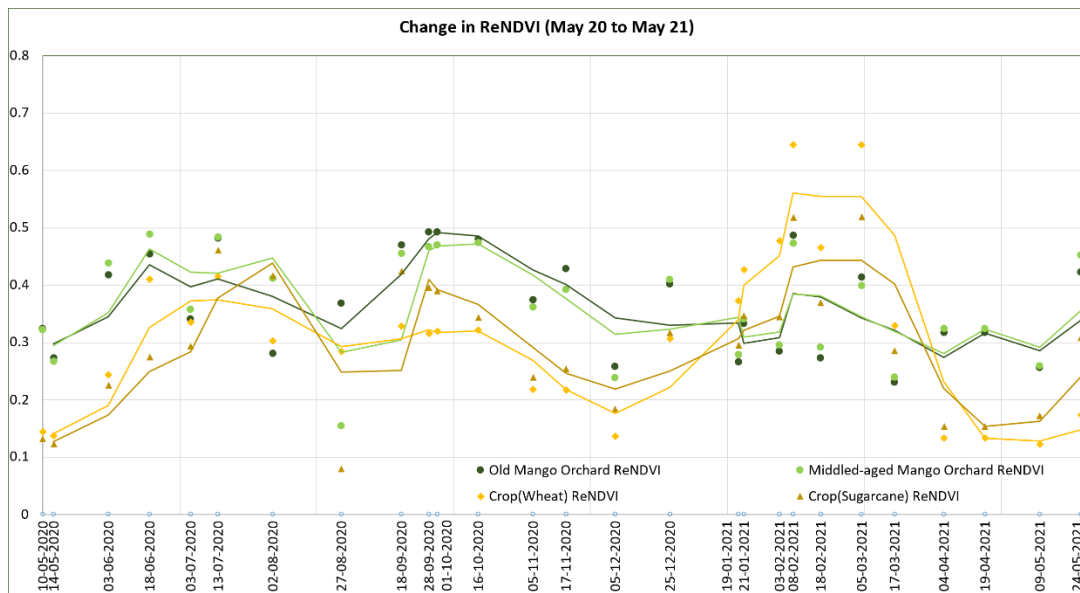


Figure 4. Temporal profile of ReNDVI from May 2020 to May 2021

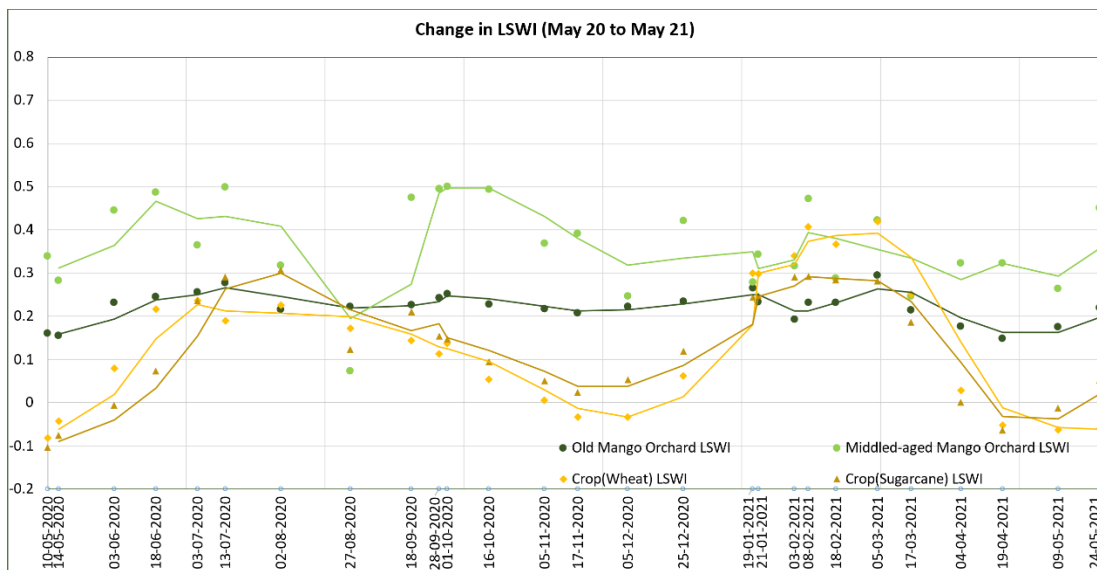


Figure 5. Temporal profile of LSWI from May 2020 to May 2021

Maps were generated (Figure 6, 7 & 8) after carrying out the classification and accuracy assessment. The image was classified into five major classes; building, mango orchard, crop, fallow and waterbody.

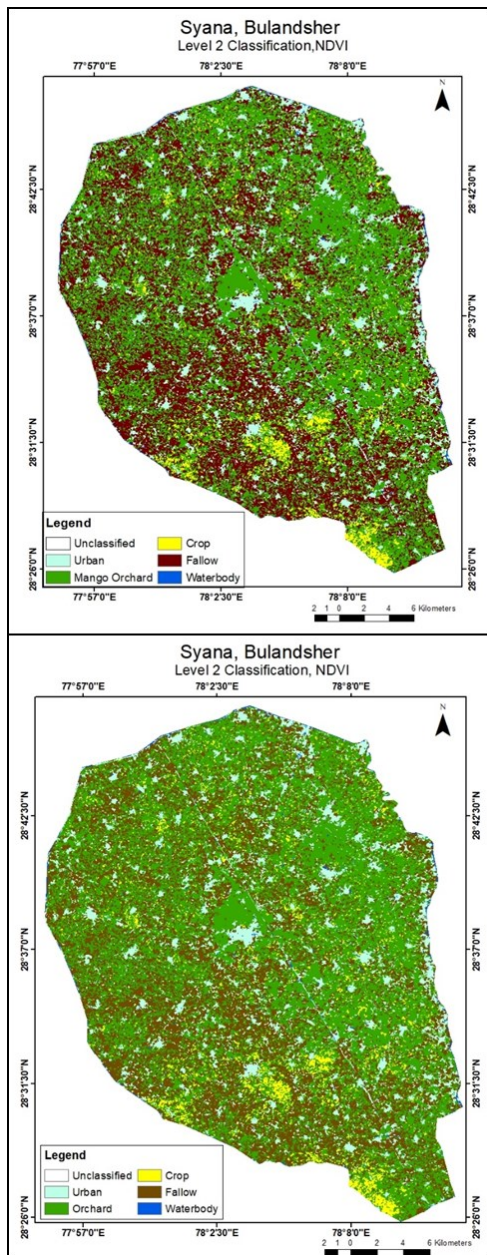


Figure 6. Classified image using NDVI stack of 3<sup>rd</sup> Feb21 and 5<sup>th</sup> Dec20

The accuracy assessment after classification (Table 3) revealed that the LSWI stack (Table 4) performed the best with an overall accuracy of 89% and a kappa coefficient of 0.86. NDVI (Table5) achieved an overall accuracy of 86% and a kappa coefficient of 0.83. This result is almost similar to the result of the Mango orchard classification carried out by Hebbbar et al (2014). ReNDVI (Table 6) gave classification accuracy of 87% and a kappa coefficient of 0.84. The user and producer accuracy for the orchard class was the highest for ReNDVI, followed by LSWI and NDVI.

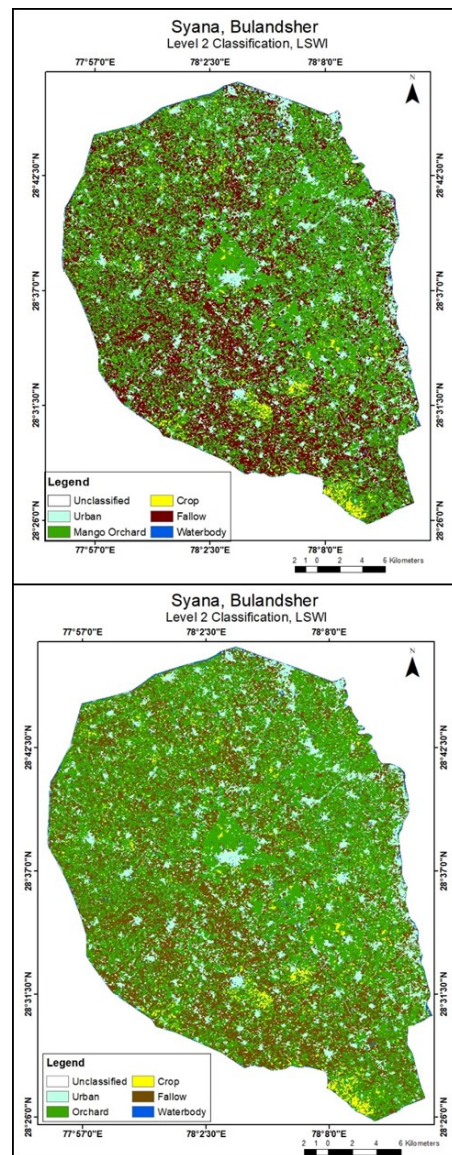


Figure 7. Classified image using LSWI stack of 1<sup>st</sup> Oct20 and 5<sup>th</sup> Dec20

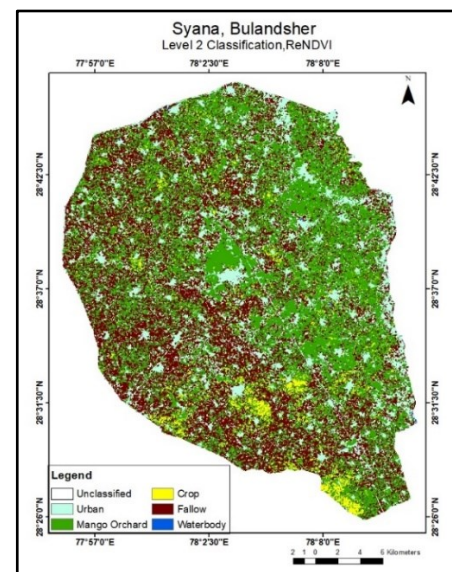


Figure 8. Classified image using ReNDVI stack of 18<sup>th</sup> June 20

**Table 3. Comparison of results obtained of NDVI, ReNDVI and LSWI**

Index	Overall Accuracy (%)	KIA	Mango Orchard User Accuracy	Mango Orchard Producer Accuracy
NDVI	86	0.83	0.65	1
ReNDVI	87	0.84	0.80	0.98
LSWI	89	0.86	0.78	0.96

**Table 4. Classification carried out using LSWI stack; Overall accuracy: 89% Kappa Index Agreement: 0.86**

	Urban	Mango Orchard	Crop	Fallow	Waterbody	Sum	User Accuracy
Urban	101	0	0	10	0	111	0.91
Mango Orchard	2	54	10	1	2	69	0.78
Crop	0	2	84	0	3	89	0.94
Fallow	1	0	1	89	0	91	0.97
Waterbody	2	0	4	2	42	50	0.84
Unclassified	3	0	0	0	0	3	
Sum	109	56	99	102	47		
Producer Accuracy	0.92	0.96	0.84	0.87	0.89		

**Table 5. Classification carried out using NDVI stack; Overall accuracy: 86% Kappa Index Agreement: 0.83**

	Urban	Mango Orchard	Crop	Fallow	Waterbody	Sum	User's Accuracy
Urban	97	0	0	4	7	108	0.89
Mango Orchard	0	42	12	6	4	64	0.65
Crop	0	0	85	0	0	85	1
Fallow	0	0	0	84	18	102	0.82
Waterbody	1	0	0	1	49	51	0.96
Unclassified	1	0	0	0	1	2	
Sum	99	42	97	95	79		
Producer Accuracy	0.97	1	0.87	0.88	0.62		

**Table 6. Classification carried out using ReNDVI stack; Overall accuracy: 87% Kappa Index Agreement: 0.84**

	Urban	Mango Orchard	Crop	Fallow	Waterbody	Sum	User's Accuracy
Urban	93	0	0	14	10	111	0.81
Mango Orchard	1	51	9	2	0	63	0.80
Crop	0	1	81	0	0	81	0.98
Fallow	0	0	0	84	7	91	0.92
Waterbody	0	0	0	0	44	51	0.86
Unclassified	0	0	0	0	0	0	
Sum	94	52	90	100	61		
Producer Accuracy	0.95	0.98	0.8	0.84	0.72		

## 5. Conclusions

In the previous studies, NDVI has been used to map Mango orchards (Hebbar et al., 2014). As NDVI saturates in dense canopy crops, a new approach has been made to study the effect of red edge and SWIR based indices on the accuracy of Mango orchard mapping. The study was carried out to map Mango orchards using three different vegetation indices and object-based classification. Two-day stacks were generated based on the maximum and minimum value of the vegetation index obtained from the temporal profile of the index. Out of the three indices, LSWI gave the best overall accuracy. The best user and producer accuracy for orchard class was given by ReNDVI. Therefore, ReNDVI and LSWI hold the best potential for mapping of mango orchards and can be explored further to improve classification and mapping. One of the possible future applications of this method could be mapping mango orchards based on their age groups. This methodology can be further improved by considering the textural variation amongst the mango orchard class.

### Funding

This study is funded by JECAM (Joint Experiment for Crop Assessment and Monitoring)

### References

- Baatz M. and A. Schape (2000). Multiresolution segmentation-an optimization approach for high quality multiscale image segmentation, *Angewandte Geographische Informationsverarbeitung XII*, Salzburg, July 5 to 7, 2000
- Blaschke T., G. J. Hay, M. Kelly, S. Lang, P. Hofmann, E. Addink, R. F. Queiroz, F. Van der, H. Werff, F. Coillie and D. Tiede (2014). Geographic Object-Based Image Analysis – Towards a new paradigm, *ISPRS Journal of Photogrammetry and Remote Sensing* 87, pp.180. <https://doi.org/10.1016/J.ISPRSJPRS.2013.09.014>
- Chandrasekar K., M. V. R. Sessa Sai, P. S. Roy and R. S. Dwevedi (2010). Land Surface Water Index (LSWI) response to rainfall and NDVI using the MODIS vegetation index product, *International Journal of Remote Sensing* 31(15), pp.3987–4005. <https://doi.org/10.1080/01431160802575653>
- Chaudhari K., N. Nishant, G. Upadhyay, R. More, N. Singh, S. P. Vyas and B. K. Bhattacharya (2019). Crop inventory of orchard crops in India using remotely sensed data, *International Archives of the Photogrammetry, Remote Sensing and Spatial Information Sciences - ISPRS Archives* 42(3/W6), pp. 269–275. <https://doi.org/10.5194/ISPRS-ARCHIVES-XLII-3-W6-269-2019>
- Clerici N., C. J. Weissteiner and F. Gerard (2012). Exploring the Use of MODIS NDVI-Based Phenology Indicators for Classifying Forest General Habitat Categories, *Remote Sensing* 20124(6), pp.1781–1803. <https://doi.org/10.3390/RS4061781>
- Gao Y., J. F. Mas and A. Navarrete (2009). The improvement of an object-oriented classification using multi-temporal MODIS EVI satellite data, *International Journal of Digital Earth* 2(3), pp. 219–236. <https://doi.org/10.1080/17538940902818311>
- Gitelson A. and M. N. Merzlyak (1994). Spectral Reflectance Changes Associated with Autumn Senescence of *Aesculus hippocastanum* L. and *Acer platanoides* L. Leaves Spectral Features and Relation to Chlorophyll Estimation, *Journal of Plant Physiology* 143(3), pp.286–292. [https://doi.org/10.1016/S0176-1617\(11\)81633-0](https://doi.org/10.1016/S0176-1617(11)81633-0)
- Chandra H., Verma and A. Tasneem. (2019). Mapping and Area Estimation of Mango Orchards of Lucknow Region by Applying Knowledge Based Decision Tree to Landsat 8 OLI Satellite Images, *International Journal of Innovative Technology and Exploring Engineering* 9(3), pp.3627–3635. <https://doi.org/10.35940/ijitee.B8109.019320>
- Hebbar R., H. M. Ravishankar, S. Trivedi, S. R. Subramoniam, U. Raj and V. K. Dadhwal (2014). Object oriented classification of high resolution data for inventory of horticultural crops. *International Archives of the Photogrammetry, Remote Sensing and Spatial Information Sciences - ISPRS Archives* 40(8), pp.745–749. <https://doi.org/10.5194/ISPRSARCHIVES-XL-8-745-2014>
- Liang Q., W. Zhu, J. Long, Y. Wang, W. Sun and W. Wu (2018). A Real-Time Detection Framework for On-Tree Mango Based on SSD Network, *Lecture Notes in Computer Science (Including Subseries Lecture Notes in Artificial Intelligence and Lecture Notes in Bioinformatics)* 10985 LNAI, pp. 423–436. [https://doi.org/10.1007/978-3-319-97589-4\\_36](https://doi.org/10.1007/978-3-319-97589-4_36)
- Meena N. K. and R. Asrey (2018). Tree Age Affects Postharvest Attributes and Mineral Content in Amrapali Mango (*Mangifera indica*) Fruits, *Horticultural Plant Journal* 4(2), pp. 55–61. <https://doi.org/10.1016/J.HPJ.2018.01.005>
- Rahman M. M., A. Robson and M. Bristow (2018). Exploring the Potential of High Resolution WorldView-3 Imagery for Estimating Yield of Mango. *Remote Sensing* 10(12), pp.1866. <https://doi.org/10.3390/RS10121866>
- Sellers P. J. (2007). Canopy reflectance, photosynthesis and transpiration, *International Journal of Remote Sensing* 6(8), pp.1335–1372. <https://doi.org/10.1080/01431168508948283>
- Bhartariya S. G.. (2012). District Profile, CGWD, 2012–2025, pp. 1-29
- Saha S. and D. Haldar. (2021). Orchard assessment using time series multi-sensor data, *Indian Institute of Remote Sensing*
- Wong C. Y. S., P. D'Odorico, Y. Bhatena, M. A. Arain and I. Ensminger (2019). Carotenoid based vegetation

indices for accurate monitoring of the phenology of photosynthesis at the leaf-scale in deciduous and evergreen trees, *Remote Sensing of Environment* 233,pp. 1-14.  
<https://doi.org/10.1016/J.RSE.2019.111407>

Wu D., K. Johansen, S. Phinn and A. Robson (2020). Suitability of Airborne and Terrestrial Laser Scanning for Mapping Tree Crop Structural Metrics for Improved

Orchard Management, *Remote Sensing* 202012(10), pp.1647. <https://doi.org/10.3390/RS12101647>

Xiang K., W. Yuan, L. Wang and Y. Deng (2020). An LSWI-Based Method for Mapping Irrigated Areas in China Using Moderate-Resolution Satellite Data, *Remote Sensing* 12(24), pp.4181.  
<https://doi.org/10.3390/RS12244181>

# Study of CNN deep learning model for temporal remote sensing data processing to map rabi crops

Mragank Snighal<sup>1,\*</sup>, Ashish Payal<sup>2</sup> and Anil Kumar<sup>3</sup>

<sup>1,2</sup> USIC&T, Guru Gobind Singh Indraprastha University, New Delhi, India

<sup>3</sup> Indian Institute of Remote Sensing, Dehradun, India

\*Email: mraganksinghal@gmail.com

(Received: Dec 5, 2021; In final form: 25 Sep 2022)

**Abstract:** Convolution Neural Network (CNN) is a deep learning approach that has become an area of interest to the researchers for solving complex problems. With the evaluation of CNN, extraction of deep features for accurate classification of remotely sensed images has gained lot of momentum. This research work uses CNN deep learning model for mapping rabi crops (mustard and wheat) using temporal remote sensing data. The mappings of mustard and wheat crops have been conducted using multispectral temporal images obtained from Sentinel 2A/2B between the dates 1<sup>st</sup> Nov 2019 and 24<sup>th</sup> Feb 2020 of Banasthali, Rajasthan region. The CNN model created in this research work uses several layers along with 5 activation functions (relu, sigmoid, tanh, elu and selu) for finding out which activation function gave the best result for the proposed study. Batch size has been examined from 1 to 50 in the multiple of 5 and epochs have been tested from 1 to 10 for a training data of 200 samples for each class. The optimal value with a batch size of 5 and epochs of 30 has been calculated as best suited in this study as the accuracy was getting constant. The implementation of CNN model for classification shows better results as compared to the traditional approach as the CNN algorithms are learning algorithms. This also helps in handling the heterogeneity within a class. A comparison has been conducted using Modified Possibilistic *c*-Means (MPCM) fuzzy algorithm for the classification of the same set of classes. F-Score, Kappa and Overall Accuracy have been calculated to show how the proposed approach has been outperformed and the level of classification accuracy achieved.

**Keywords:** Convolution Neural Network (CNN), Deep feature extraction, multispectral image classification, Soft Classification

## 1. Introduction

Digital image classification is one of the prominent application domains to map and extract the data of remote areas through satellite imagery. Lillesand and Kiefer (2015) have mentioned digital image classification as a quantitative technique to classify image data into various categories. Supervised and unsupervised image classifications are two broad categories of classification procedure (Campbell, 1996). When training data is available, supervised classification is widely used and when training data is unavailable, unsupervised classification is applied on remote sensing imagery. Higher accuracy can be achieved with the intervention of computers to process a digital image (Richards and Jia, 2013).

Bezdek et al. (1984) presented Fuzzy *c*-Means (FCM) algorithm with a thought of fuzzy sets to solve mixed pixel problem. Later, to overcome the drawbacks of FCM, Krishnapuram et al. (1993) proposed an algorithm based on a possibilistic concept and improvement in the objective function, which was labeled as Possibilistic *c*-means (PCM). Fuzzy based classifiers are generally effective in handling mixed pixels to produce precise and reasonable outcomes from image classification (Chawla, 2010).

Supervised noise clustering (NC) has been opted as the base classifier. Adding nine different kernel functions as the distance functions resulting in a kernel-based classifier, termed KNC (Sengupta et al. 2019). Li et al. (2003) revised the objective function of PCM, and an efficient clustering algorithm, named Modified Possibilistic *c*-Means

(MPCM), was presented by him. This algorithm saves an amount of running time by eliminating the computation of membership parameters in every iteration. Since PCM causes a coincident cluster problem, MPCM was introduced to fit the clusters, closer to one another. As compared to PCM, MPCM is less sensitive to noise and avoids trivial solutions too (Li et al., 2003).

PCM and MPCM algorithms are capable of mapping specific classes of interest from temporal datasets (Misra et al., 2012; Singh et al., 2019). The reflectance from these classes depends upon several factors such as soil type, terrain, moisture content, and atmospheric condition (Rawat et al., 2021). A single date image may have spectral overlap between two or more classes while mapping the second/third classification level. This spectral overlap can effectively be separated by the use of temporal images (Chandola et al., 2010).

Traditional classifiers are not capable to map single class of interest from remote sensing image. ID-CNN model implemented in this research work has been designed to map only wheat or mustard from given temporal remote sensing data. So, this specific single class mapping capabilities of ID-CNN model has been explored in this research work, which is not there with traditional image classifiers. Secondly, the accuracy and reliability of the information gathered by the imagery is dependent on the classification. Although there are some advanced classification methods such as Support Vector Machines, Random Forest, etc., which have been used widely traditionally, but still the researchers have been still working to improve the classification accuracy because the classified images provide important base information for

GIS applications and analysis on decision making process. The gap in the traditional approach was the loss of information and also lack of learning algorithms that were addressed with the help of learning algorithms like CNN (Mustafa et al., 2016).

Many fields of science, remote sensing included, were able to exploit the success of natural image classification by Convolutional Neural Network (CNN) models using a technique commonly called transfer learning (Lima et al., 2019). Hu et al. (2015) remarked that the performance of remote- sensing image classification has only slightly improved in recent years. The main reason remote- sensing image classification only marginally improved is due to the fact that the approaches relying on low- level features are incapable of generating sufficiently powerful feature representations for remote- sensing scenes (Lima et al., 2019). Hu et al. (2015) concluded that the more representative and higher- level features, which are abstractions of the lower- level features, are desirable and play a dominant role in the scene classification task.

Convolutional Neural Networks (CNNs) mostly improve prediction performance using big data and plentiful computing resources and have pushed the boundaries of what was possible. Problems which were assumed to be unsolvable are now being solved with super-human accuracy (Mahony et al., 2019). Current progress in deep-learning models, specifically deep convolutional neural networks (CNN) architectures, have improved the state-of- the- art in visual object recognition and detection, speech recognition and many other fields of study (Cun et al. 2015). Many CNN models use 10 to hundreds of layers. Huang et al. (2016) proposed models with thousands of layers (Huang et al., 2016). Due to the vast number of operations performed in deep CNN models, it is often difficult to discuss the interpretability, or the degree to which a decision taken by a model can be interpreted.

Remote Sensing images have features at many layers which can be extracted using deep feature extraction methods. Many classifiers are designed for classification but at a single layer, there some classifiers which also work on two layers such as decision tree or kernel SVMs (Bengio et al., 2013). Despite CNNs' powerful feature extraction capabilities, Hu et al. (2015) and others found that in practice it is difficult to train CNNs with small datasets. However, Yosinski et al. (2014) and Yin et al. (2017) observed that the parameters learned by the layers in many CNN models trained on images exhibit a very common behavior.

This research work experimented classification with a CNN model which has been applied on temporal remote sensing data to map rabi crops and compared using Modified Possibilistic *c*-Means (MPCM) algorithm. The proposed CNN approach has been compared with Euclidean and variance-covariance parameters in the MPCM classifier. Secondly, spectral overlaps between classes like mustard and wheat have been handled using the temporal indices database. This temporal indices database for each class has been generated during the class-based sensor independent (CBSI)-NDVI approach

and compared with NDVI temporal database. Convolutional Neural Networks (CNNs) do not generate statistical parameters from training samples. In place of generating statistical training parameters, CNN considers all training samples as it is, so that each sample can give equal impact on training the model as well as classify unknown pixel in an image. Due to this, outputs from CNN models are very homogeneous. Due to this factor 1D-CNN model has been tested in this research work.

## 2. Vegetation indices

Many scientists have extracted and modelled various vegetation biophysical variables using remote sensing data since 1960. Various efforts have been taken towards developing vegetation indices, which are defined as dimensionless, radiometric measures that function as indicators of relative abundance and activity of green vegetation. Although there are more than 20 different vegetation indices in use, in this research work, NDVI has been considered. Cohen (1991) suggests that the first true vegetation index was the *Simple Ratio (SR)*, which is the near – infrared (*NIR*) to red reflectance ratio described in Birth and Mc-Vey (1968) as mentioned in Eq. (2.1):

$$SR = \frac{NIR}{Red} \quad (2.1)$$

Rouse et al. (1974) developed the generic *Normalized Difference Vegetation Index (NDVI)* as mentioned in Eq. (2.2):

$$NDVI = \frac{NIR - Red}{NIR + Red} \quad (2.2)$$

Temporal indices datasets can provide spectral change over time for a crop (Upadhyay et al., 2012). Band ratio is used in remote sensing to eliminate the different topography and illumination effects and enhance a class (Sengar et al., 2001). The *NDVI* was widely used and applied to the original Landsat MSS digital remote sensing data. A novel Class-Based Sensor-Independent Indices (*CBSI*) generates a much-enhanced class of interest in indices data (Upadhyay et al., 2013). The advantage of using CSBI approach in indices generation is that, user does not have to provide bands in given indices formula. CBSI have minimum and maximum operators which selects bands such a way that class of interest get maximum enhancement. It has also been used to reduce the spectral dimensionality of temporal remote sensing dataset which has been used in this study as well. The *CBSI-NDVI* formula is mentioned in Eq. (2.3):

$$CBSI - NDVI = \frac{\rho_{max} - \rho_{min}}{\rho_{max} + \rho_{min}} \quad (2.3)$$

where  $\rho_{max}$  and  $\rho_{min}$  represent the band of maximum and minimum reflectance, respectively.

## 3. Mathematical concept of classification algorithm

MPCM has been introduced to resolve the limitations of FCM and PCM. MPCM has fast clustering ability, abilities to resist noise, and trivial solution (Li et al, 2003). Since PCM causes coincident clusters, thus MPCM is proposed to overcome this problem and fit the clusters, which are

close to one another. Li et al. (2003) introduced the main limitation of PCM that it takes more time in implementation, and a large number of parameters need to be determined. This section will present the mathematical concepts of the MPCM algorithm and its objective function formulation. Li et al. (2003) revised the objective function of PCM, presented an efficient clustering algorithm, and discussed how to choose parameters.

*Pseudo code of MPCM Algorithm*

1. Assign mean values of each class from training data.
2. Assign the value of the degree of fuzziness  $\infty > m > 1$ .
3. Compute the regularization parameter ‘ $\eta_i$ ’ as mentioned in Eq. (3.6).
4. Compute the membership matrix, as given in Eq. (3.1):

$$u_{ij} = e^{\left(\frac{-d_{ij}^2}{\eta_i}\right)}, \text{ where } d_{ij}^2 = \|x_i - v_j\| \quad (3.1)$$

5. Assign the final class to each pixel.

To minimize the impact of noise and outlier’s parameter  $\lambda_i$  was introduced for each training sample, and the modification has been done in PCM’s objective function. The objective function of MPCM is mentioned in Eq. (3.2):

$$J_m = \sum_{i=1}^N \sum_{j=1}^C (\mu_{ji})^m \|x_i - v_j\|^2 + \sum_{i=1}^N \eta_i \sum_{j=1}^C (\lambda_i - \mu_{ji})^m \quad (3.2)$$

$\lambda_i$  is taken according to the expression mentioned in (3.3):

$$\lambda_j = \sum_{i=1}^C \exp\{-\alpha \|x_j - \beta_i\|^2\} \quad \lambda_i > 0 \quad (3.3)$$

where  $\alpha$  is a suitably chosen constant, and

$$\beta_i = \sum_{j=1}^N w_{ij} x_j / \sum_{j=1}^N w_{ij}, \text{ where } w_{ij} \text{ is a monotonous decreasing function.}$$

**4. CNN model**

Convolutional neural network is a class of deep learning methods which has become dominant in various computer vision tasks and is attracting interest across a variety of domains, including image classification. CNN is designed to automatically and adaptively learn spatial hierarchies of features through backpropagation by using multiple building blocks, such as convolution layers, pooling layers, and fully connected layers (Yamashita et al., 2018).

A CNN is composed of a stacking of several building blocks: convolution layers, pooling layers (e.g., max pooling), and fully connected (FC) layers. A model’s performance under particular kernels and weights is calculated with a loss function through forward propagation on a training dataset, and learnable parameters, i.e., kernels and weights, are updated according to the loss value through backpropagation with gradient descent optimization algorithm, ReLU, rectified

linear unit. An overview of a convolutional neural network (CNN) architecture and the training process is shown in Figure 1.

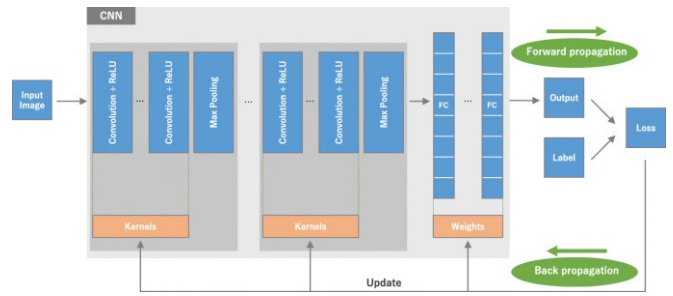


**Figure 1. CNN Architecture**

The CNN architecture includes several building blocks, such as convolution layers, pooling layers, and fully connected layers. A typical architecture consists of repetitions of a stack of several convolution layers and a pooling layer, followed by one or more fully connected layers. In this research work, two 1D convolution layers are used which reduces the in-plane dimensionality of the feature maps in order to introduce a translation invariance to small shifts and distortions, and decrease the number of subsequent learnable parameters. The max pooling layer extracts patches from the input feature maps, outputs the maximum value in each patch, and discards all the other values. Once the features extracted by the convolution layers and down-sampled by the pooling layers are created, they are mapped by a subset of fully connected layers to the final outputs of the network, such as the probabilities for each class in classification tasks. The final fully connected layer has the same number of output nodes as the number of classes. Each fully connected layer is followed by a nonlinear function, ReLU (Rectified Linear Activation Unit). The CNN Model used in this research work is shown in Figure 2.

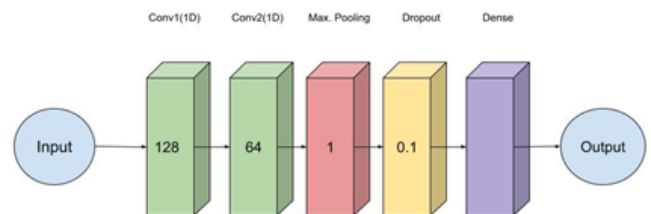


**Figure 2. CNN Model used**

MPCM algorithm has fast clustering abilities and also it can resist noise and trivial solutions. With each layer, the CNN’s complexity in understanding the image increases. This means that layers at the beginning are responsible for detecting low-level features such as edges and colors and the layers at the end are responsible for detecting high-level features such as shapes that we can easily recognize. The main advantage of CNNs compared to a traditional neural network is that they automatically detect important features without any human supervision.

**5. Study area and dataset used**

This section elaborates the details about the study area and the dataset used in this research work.

**5.1. Study area**

Surroundings of the Banasthali Vidyapith area, Rajasthan state, India, have been selected as the study area for this research to identify mustard and wheat fields while testing the proposed approach. Banasthali is located in the district Tonk and is surrounded by agricultural land where mustard covers around 2,99,000 hectares of area, whereas wheat is cultivated in approximately 66,000 hectares. Several other crops such as barley, gram, jowar, bajra, moong and urd can also be found in comparatively less area. The area is located in the north-eastern part in the state of Rajasthan. The study area lies between 26°23' and 26°24' north latitude, 75°51' and 75°54' east longitude. It is surrounded by Jaipur towards the north, Sawai Madhopur towards the east, Kota district on the southeast, Bundi towards the south, Bhilwara district on the southwest, and Ajmer towards the west.

The reasons for selecting this study area were:

- The area is surrounded by small villages where mustard, wheat, and grass fields can be found easily.
- During November (2019) and December (2019) large fields of mustard can be seen here, which later becomes fallow land by the end of March (2020).

The different classes of interest i.e., mustard and wheat ground truth samples were collected from the field visit which has been shown in Figure 3. The location map and different land cover classes identified in the study area are presented in Figure 4.

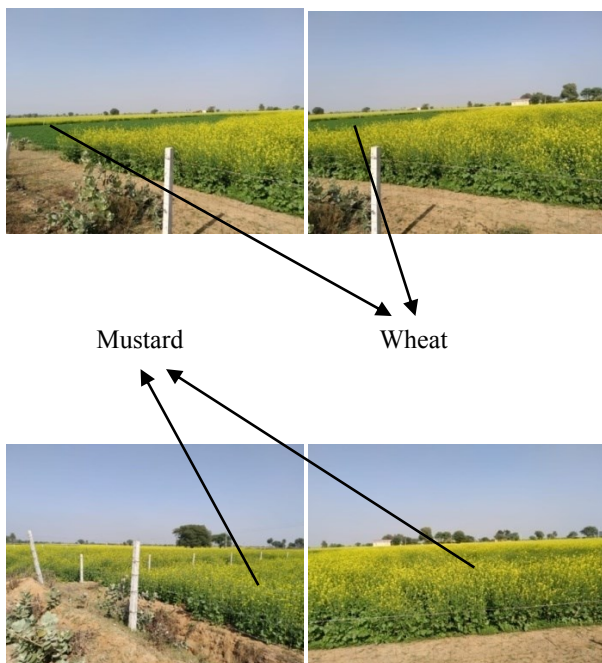


**Figure 3. Photographs taken during the field visit on 11<sup>th</sup> Dec 2019 in the surroundings of Banasthali Vidyapith region**

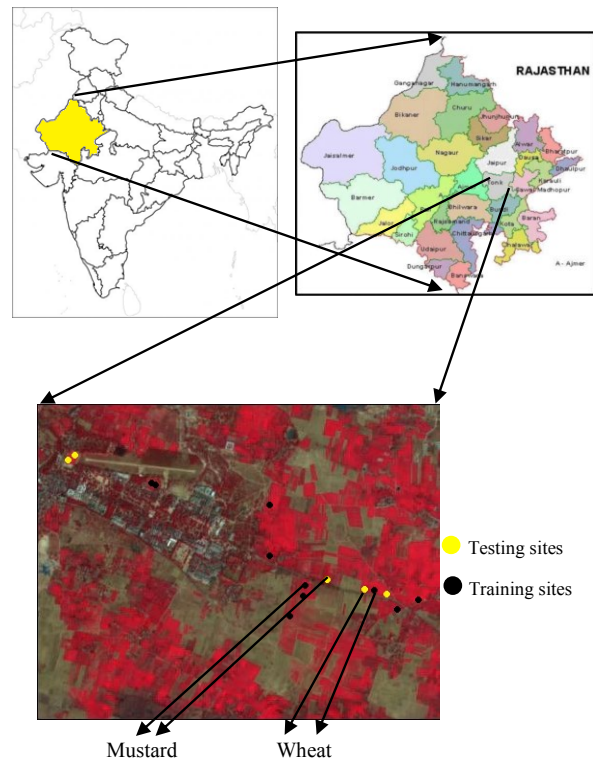


**Figure 4. Location of study, Banasthali Vidyapith area, Rajasthan State, India**

Table 1 shows the latitude and longitude locations of various field samples collected during the field visit done on 11<sup>th</sup> Dec 2019 in the Banasthali Vidyapith region's surroundings. Around the field, 200 samples were identified at different locations for these classes of interest. Ten fields of mustard and wheat classes and a total of twenty field samples have been shown in Table 1, from where training pixels were collected. Table 2 shows ten field samples that have been used for reference data.

**Table 1. Ground Truth Samples Collected during the field visit**

Classes->	Mustard		Wheat	
Samples	Latitude	Longitude	Latitude	Longitude
Sample 1	26°23'49''	75°53'08''	26°23'45''	75°53'36''
Sample 2	26°23'47''	75°53'21''	26°23'45''	75°53'36''
Sample 3	26°23'43''	75°53'34''	26°23'47''	75°53'38''
Sample 4	26°23'44''	75°53'35''	26°23'47''	75°53'38''
Sample 5	26°23'44''	75°53'40''	26°25'51''	75°52'30''
Sample 6	26°23'41''	75°53'45''	26°25'46''	75°52'31''
Sample 7	26°23'43''	75°53'40''	26°25'45''	75°52'32''
Sample 8	26°23'40''	75°53'46''	26°25'21''	75°52'37''
Sample 9	26°23'59''	75°53'13''	26°25'18''	75°52'38''
Sample 10	26°23'44''	75°53'31''	26°25'15''	75°52'38''

**Table 2. Reference Data Collected during the field visit**

Classes->	Mustard		Wheat	
Samples	Latitude	Longitude	Latitude	Longitude
Sample 1	26°25'06''	75°52'08''	26°25'21''	75°52'23''
Sample 2	26°25'03''	75°51'45''	26°25'24''	75°52'36''
Sample 3	26°25'04''	75°51'43''	26°25'02''	75°52'38''
Sample 4	26°25'02''	75°52'38''	26°25'01''	75°52'48''
Sample 5	26°24'58''	75°52'25''	26°24'55''	75°52'51''

## 5.2. Dataset used

In this research work, the multispectral temporal images from twin satellites i.e., Sentinel-2A and Sentinel-2B have been used to discriminate mustard and wheat fields. Seven temporal images have been acquired from 1<sup>st</sup> Nov 2019 to 24<sup>th</sup> Feb 2020 of the same area. These images were then used to study the CNN deep learning model's performance. The multispectral temporal Sentinel 2A/2B dataset and its sensor specification have been given in Table 3.

**Table 3. Sentinel 2A/2B dataset and sensor specification.**

Specifications	Sentinel – 2A/B
Spatial Resolution	10 – 60 meters
Spectral Resolution	13 bands
Scene Size	290 km x 290 km
Image Acquired on	1-Nov-19, 16-Nov-19, 11-Dec-19, 26-Dec-19, 10-Jan-20, 30-Jan-20, 24-Feb-20

## 6. Methodology

Initially, multispectral images have been pre-processed to generate temporal indices database using Sentinel-2A/B satellite images. CBSI-NDVI approach has been applied to generate a temporal indices database parallel to it. The objective of generating temporal indices database was to reduce the spectral dimension of temporal images and maintain temporal dimension to incorporate phenological profile of crop, and represented in the form of vector elements to be used in MPCM classifier. Spectral dimension was reduced, and only the temporal dimension used in a fuzzy-based classifier to have input data representing indices as vector elements. Temporal indices database has been used in separability analysis, using Euclidean separability, to find out the best temporal date combination for separating mustard and wheat fields, as shown in table (4) and (5). Once suitable dates for each class were identified, using these dates, temporal indices database was generated.

The temporal indices database was used as an input to the CNN Model to generate the classified outputs for mustard and wheat fields. The temporal indices database was also used in the supervised Modified Possibilistic *c*-Means (MPCM) algorithm for accuracy assessment. A detailed description of the methodology has been given in Figure 5.

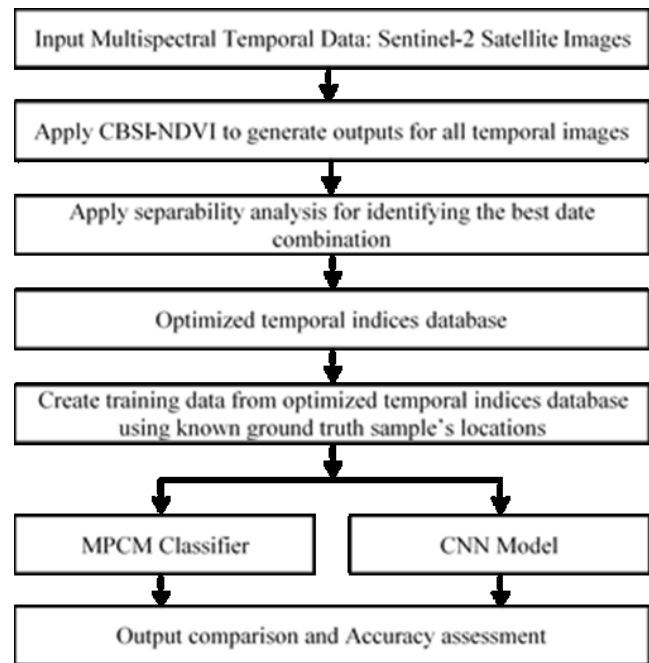


**Figure 5. Methodology Adopted**

Following steps were applied to identify mustard and wheat fields' classes using temporal dataset of 1<sup>st</sup> Nov 2019, 16<sup>th</sup> Nov 2019, 11<sup>th</sup> Dec 2019, 26<sup>th</sup> Dec 2019, 10<sup>th</sup> Jan 2020, 30<sup>th</sup> Jan 2020, and 24<sup>th</sup> Feb 2020 images:

- 1) All temporal images were used to generate CBSI-NDVI outputs using seed training data for mustard and wheat fields separately, with the help of the CBSI-NDVI formula mentioned in Eq. (2.3).
- 2) Outputs from step (1) were used in separability analysis to identify temporal images suitable to be used for any specific class.
- 3) Temporal images identified in step (2) were then used to generate CBSI-NDVI outputs using seed training data for mustard, wheat, and grass fields separately in a similar way as done in step (1).
- 4) The outputs generated in step (3) were used to create an optimized temporal indices database.
- 5) Training data was created from the optimized temporal indices database generated from step (4) using the ground truth samples locations.
- 6) The optimized temporal indices database (generated from step 4) was then classified using training data created in step (5), by applying CNN Model and MPCM classifier.
- 7) The classified outputs from step (6) were then compared, and an accuracy assessment was conducted.
- 8) The same steps were applied to generate classified outputs for other classes of interest.

As discussed in the methodology, Table 4 and Table 5 gives information about bands and optimized temporal dates used for mustard, wheat, and grass classes as identified from step (2).

**Table 4. Selected Bands for Mustard using CBSI-NDVI approach**

Dates	Mustard		
	CBSI-NDVI value	$\rho_{max}$	$\rho_{min}$
1-Nov-19	0.57	SWIR	Blue
16-Nov-19	0.4	VNIR	Blue
11-Dec-19	0.62	VNIR	SWIR
30-Jan-20	0.86	VNIR	Blue
24-Feb-20	0.52	VNIR	SWIR

**Table 5. Selected Bands for Wheat using CBSI-NDVI approach**

Dates	Wheat		
	CBSI-NDVI value	$\rho_{max}$	$\rho_{min}$
11-Dec-19	0.52	VNIR	Blue
26-Dec-19	0.81	VNIR	Blue
10-Jan-20	0.89	VNIR	Red
30-Jan-20	0.91	VNIR	Blue
24-Feb-20	0.72	VNIR	SWIR

The graph in Figure 6 represents the CBSI-NDVI values of mustard for the suitable temporal dates using CBSI-NDVI as shown in Table 4. Similarly, the graph in Figure 7 represents the CBSI-NDVI values of wheat for the suitable temporal dates using CBSI-NDVI as shown in Table 5. Since the suitable dates of mustard are different from wheat, therefore, CBSI-NDVI values have been shown in two graphs.

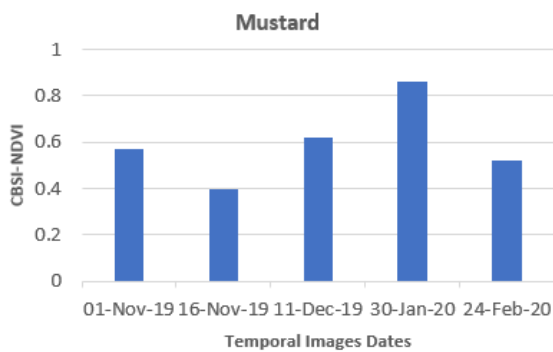


**Figure 6. Graphical representations of CBSI-NDVI values for mustard**

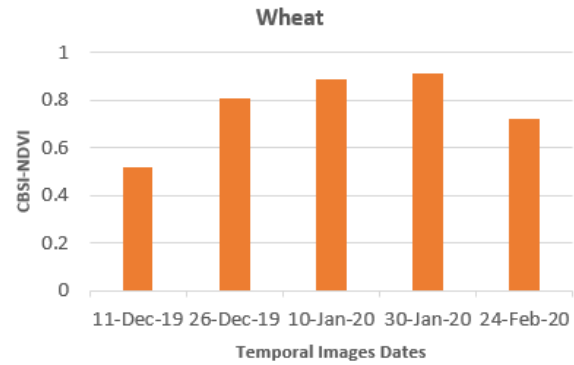


**Figure 7. Graphical representations of CBSI-NDVI values for wheat**

**7. Results and discussion**

To identify the mustard and wheat fields in the Banasthali area of Rajasthan state, temporal remote sensing data for seven different dates have been available. The seed training samples of temporal datasets were collected, which were applied on 1<sup>st</sup> Nov 2019, 16<sup>th</sup> Nov 2019, 11<sup>th</sup> Dec 2019, 26<sup>th</sup> Dec 2019, 10<sup>th</sup> Jan 2020, 30<sup>th</sup> Jan 2020 and 24<sup>th</sup> Feb 2020 temporal images. Separability analysis has been conducted for mustard, wheat, and grass fields to identify suitable optimum temporal images for classification.

For model generalization training data was used to train the model, validation ground samples were used to validate the 1D-CNN model. Testing samples as unknown pixels were used to classify the temporal indices data. Classified output was assessed through collecting testing samples from classified outputs while comparing it with training sample outputs, to find out generalization performance of 1D-CNN model.

Figure 8 shows the mustard fields' output by using MPCM classifier and CNN Model using the selected temporal images. Figure 9 shows the wheat fields' output by using MPCM classifier and CNN Model using the selected temporal images.

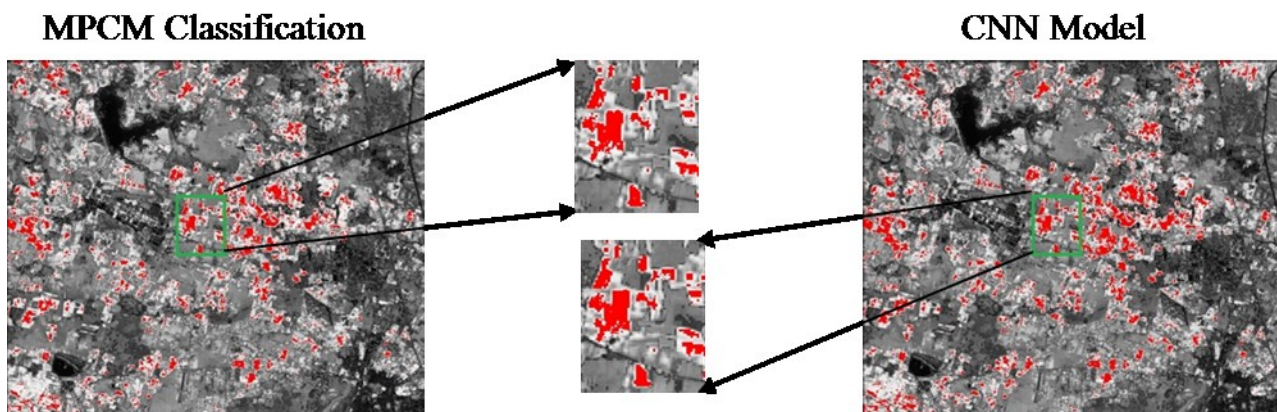


**Figure 8. Mustard class output using MPCM and CNN model**

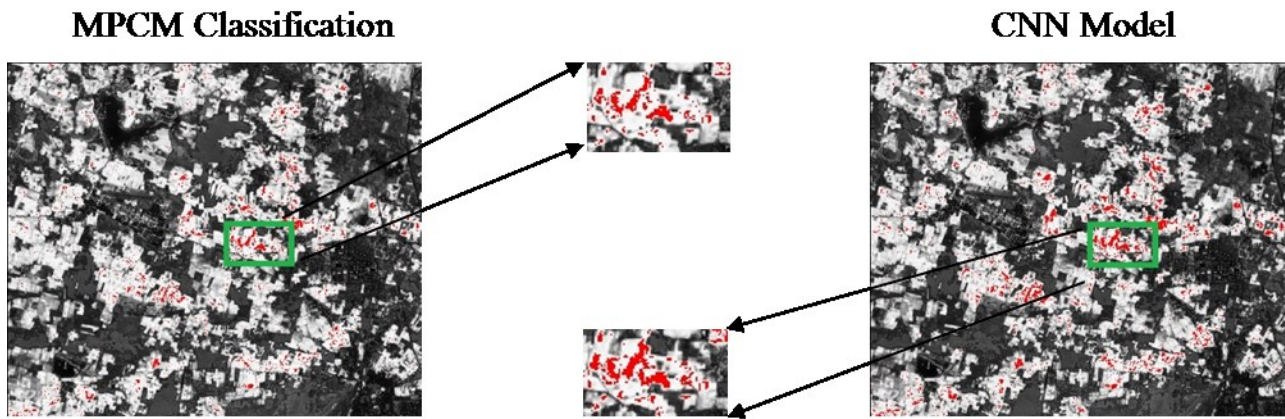


Figure 9. Wheat class output using MPCM and CNN model

Figure 10 shows the optimized CNN model for performance. Batch size has been examined from 1 to 50 in the multiple of 5 and epochs have been tested from 1 to 10 for a training data of 200 samples for each class. The optimal value with a batch size of 5 and epochs of 30 has been calculated as best suited in this study as the accuracy was getting constant.

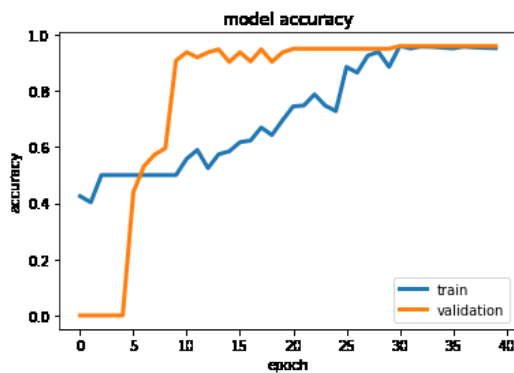


Figure 10. Optimized CNN performance model

Table 6 shows the mean-membership difference (MMD) between favorable and non-favorable classes using different methodologies for quantitative comparison between traditional and proposed approaches. MMD is an independent approach for the stability of the concerned class by calculating the mean difference of membership value of the concerned class and other classes of pure pixel (Singh et al., 2021).

Table 6. Mean-Membership Difference (MMD) between favorable and non-favorable classes

MMD using MPCM Classifier			
Favourable Classes		Non-Favourable Classes	
Mustard-Mustard	0.03	Mustard-Wheat	0.27
Wheat-Wheat	0.02	Wheat-Mustard	0.22
MMD using CNN Model			
Favourable Classes		Non-Favourable Classes	
Mustard-Mustard	0.01	Mustard-Wheat	0.42
Wheat-Wheat	0.01	Wheat-Mustard	0.74

Using the quantitative comparison from table 6, with the help of mean-membership difference, it can be concluded that the CNN model was capable of yielding better results as compared with MPCM classifier. Table 7 shows the accuracy assessment using F-Score, Kappa, and Overall Accuracy using different methodologies for qualitative comparison between traditional and proposed approaches.

Table 7. Accuracy Assessment through F-Score and Overall accuracy

Using MPCM Classification					
Class	Precision	Recall	F-Score	Kappa	Overall Accuracy
Mustard	0.92	0.90	0.91	0.80	90.0
Wheat	0.91	0.84	0.88	0.74	87.0
Using CNN Model					
Mustard	0.93	0.96	0.94	0.88	94.0
Wheat	0.92	0.92	0.92	0.84	92.0

Overall accuracy which is mentioned in Table 7 also supports the same conclusion of the proposed approach compared to the traditional MPCM classification.

### 8. Conclusions

This study has integrated CNN deep learning model for temporal remote sensing data processing. The proposed approach uses CNN model for the processing of mustard and wheat crops using temporal datasets. Identification of these classes has been carried out using temporal datasets obtained from Sentinel 2A/2B between the dates 1<sup>st</sup> Nov 2019 and 24<sup>th</sup> Feb 2020.

The classification results of optimized temporal indices database with MPCM and CNN model were studied. The CNN model outperformed the traditional MPCM approach. From this research it can be concluded that CNN model gave the best classification results for the mapping of mustard and wheat fields.

### References

Bengio Y, A. Courville and P. Vincent (2013). Representation learning. A review and new perspectives. IEEE Trans. Pattern Anal. Mach. Intell, 35(8), pp 1798–1828.

- Bezdek J. C., R. Ehrlich and W. Full (1984). FCM: The fuzzy c-means clustering algorithm. *Computers & Geosciences*, 10 (2), 191–203. Available: doi:10.1016/0098-3004(84)90020-7
- Birth G. S. and G. R. McVey (1968). Measuring the Color of Growing Turf with a Reflectance Spectrophotometer. *American Society of Agronomy*, 60, 640-643. Available: <https://doi.org/10.2134/agronj1968.00021962006000060016x>
- Campbell J. B. (1996). *Introduction to Remote Sensing*, 2nd ed. Guilford Press, pp 337–349.
- Chandola V. and R. Vatsavai (2010). Multi-temporal remote sensing image classification - A multi-view approach. *Proceedings of the 2010 Conference on Intelligent Data Understanding, CIDU*, pp 258-270.
- Chawla S. (2010). Possibilistic c-means-spatial contextual information based sub-pixel classification approach for multi-spectral data. University of Twente Faculty of Geo-Information and Earth Observation (ITC), Enschede.
- Cohen W. B (1991). Temporal versus spatial variation in leaf reflectance under changing water stress conditions. *International Journal of Remote Sensing*, 12(9), 1865–1876. Available: doi:10.1080/01431169108955215
- Cun L., Y. Bengio G. Hinton (2015). Deep learning. *Nature*. 521, 436–444. Available: doi:10.1038/nature14539
- Hu F., G. Xia, J. Hu and L. Zhang (2015). Transferring Deep Convolutional Neural Networks for the Scene Classification of High-Resolution Remote Sensing Imagery. *Remote Sens.* 7, 14680–14707. Available: doi:10.3390/rs71114680
- Huang G., Y. Sun, Z. Liu, D. Sedra and K. Weinberger (2016). Deep Networks with Stochastic Depth. *Proceedings of the 14th European Conference, Amsterdam, The Netherlands*.
- Krishnapuram R. and J. M. Keller (1993). A possibilistic approach to clustering. *IEEE Transactions on Fuzzy Systems*, 1(2), 98–110. Available: doi:10.1109/91.227387.
- Li K., H. Huang and K. Li (2003). A modified PCM clustering algorithm. *International conference on machine learning and cybernetics*, 2, 1174-1179. Available: doi:10.1109/ICMLC.2003.1259663
- Lillesand T. M. and R. W. Kiefer (2015). *Remote Sensing and Image Interpretation*, 7th ed. Wiley & Sons, NJ, pp 485–608.
- Lima P., Rafael and Marfurt (2019). Convolutional Neural Network for Remote-Sensing Scene Classification: Transfer Learning Analysis. *Remote Sensing*, 12, 86. Available: doi:10.3390/rs12010086
- Mahony N. O., S. Campbell and A. Carvalho (2019). Deep Learning vs. Traditional Computer Vision. *Advances in Computer Vision Proceedings of the 2019 Computer Vision Conference (CVC)*. Springer Nature Switzerland AG, pp. 128-144. Available: doi: <https://doi.org/10.1007/978-3-030-17795-9>
- Misra G., A. Kumar, R. Patel, R., Zurita and A. Singh (2012). Mapping specific crop-A multi sensor temporal approach. *International Geoscience and Remote Sensing Symposium (IGARSS)*, IEEE International, 3034-3037. Available: doi:10.1109/IGARSS.2012.6350786
- Mustafa U., M. Esetlili, S. Balik, Fusun, S. Abdikan and Y. Kurucu (2016). Comparison of crop classification methods for the sustainable agriculture management. *Journal of environmental protection and ecology*, 17, 648–655.
- Rawat A., A. Kumar and P. Upadhyay (2021). A Comparative Study of 1D-Convolutional Neural Networks with Modified Possibilistic c-Mean Algorithm for Mapping Transplanted Paddy Fields Using Temporal Data. *J Indian Soc Remote Sens.* Available: doi: 10.1007/s12524-020-01303-4
- Richards J. A. and X. Jia (2013). *Remote Sensing Digital Image Analysis*, 4th ed. Springer-Verlag Berlin Heidelberg, pp 295-332.
- Rouse J. W., R. H. Haas, J. A. Schell and D.W. Deering (1974). Monitoring vegetation systems in the Great Plains with ERTS. *Third Earth Resources Technology Satellite-1 Symposium*, 1, NASA SP-351, NASA, Washington, D.C., 309-317.
- Sengar S. S., A. Kumar, S. K. Ghosh, H. R. Wason and P. S. Roy (2001). Liquefaction identification using class-based sensor independent approach based on single pixel classification after 2001 Bhuj, India earthquake. *Journal of Applied Remote Sensing*, 6(1):063531-1-063531-13. Available: doi:10.1117/1.JRS.6.063531
- Sengupta I., A. Kumar and R. Dwivedi (2019). Performance Evaluation of Kernel-Based Supervised Noise Clustering Approach. *Journal of the Indian Society of Remote Sensing*, 47. Available: doi:10.1007/s12524-019-00938-2.
- Singh A. and A. Kumar (2019). Fuzzy Based Approach to Incorporate Spatial Constraints in Possibilistic c-Means Algorithm for Remotely Sensed Imagery. *International Conference on Sustainable Computing in Science, Technology & Management, Jaipur*. Available: <http://dx.doi.org/10.2139/ssrn.3354465>
- Singh A., A. Kumar and P. Upadhyay (2021). A novel approach to incorporate local information in Possibilistic c-Means algorithm for an optical remote sensing imagery, *The Egyptian Journal of Remote Sensing and Space Science*, 24 (1), pp 151-161, ISSN 1110-9823. Available: doi: 10.1016/j.ejrs.2020.06.001
- Upadhyay P., A. Kumar, P. S. Roy, S. K. Ghosh and I. Gilbert (2012). Effect on specific crop mapping using WorldView-2 multispectral add-on bands: soft classification approach. *Journal of Applied Remote Sensing*, 6(1):063524-1-063524-15. Available: doi:10.1117/1.jrs.6.063524
- Upadhyay P., S. K. Ghosh and A. Kumar (2013). High resolution temporal normalized difference vegetation indices for specific crop identification. *ISPRS - International Archives of the Photogrammetry, Remote Sensing and Spatial Information Sciences*, XL-1/W1, 351-

355. Available: 10.5194/isprsarchives-XL-1-W1-351-2013

Yamashita R., M. Nishio and R. K. G. Do (2018). Convolutional neural networks: an overview and application in radiology. *Insights Imaging* 9, 611–629. Available: <https://doi.org/10.1007/s13244-018-0639-9>

Yin X., W. Chen, X. Wu and H. Yue (2017). Fine-tuning and visualization of convolutional neural networks.

Proceedings of the 2017 12th IEEE Conference on Industrial Electronics and Applications (ICIEA), Siem Reap, Cambodia, pp. 1310–1315. Available: doi:10.1109/ICIEA.2017.8283041

Yosinski, J., J. Clune, Y. Bengio and H. Lipson (2014). How transferable are features in deep neural networks? Proceedings of the 27th International Conference on Neural Information Processing Systems, Montreal, QC, Canada, Volume 27, pp. 3320–3328.

## Geospatial Analysis of Spatial Variability of Groundwater Quality Using Ordinary Kriging: A Case Study of Dungarpur Tehsil, Rajasthan, India

Seema Jalan<sup>1\*</sup>, Devendra Singh Chouhan<sup>2,\*</sup> and Shailesh Chaure<sup>3</sup>

<sup>1</sup>Professor of Geography, Mohanlal Sukhadia University, Udaipur, Rajasthan

<sup>2</sup> Assistant Professor of Geography, Mohanlal Sukhadia University, Udaipur, Rajasthan

<sup>3</sup> Associate Professor of Geology, Government Holkar Science College, Indore, Madhya Pradesh

\*Email: [seemajalan1@gmail.com](mailto:seemajalan1@gmail.com)

(Received: Dec 21, 2021; in final form: Sep 3, 2022)

**Abstract:** Groundwater is one the major sources of natural water being exploited excessively for various uses in India. Thus, it is very essential to monitor the spatial and temporal variability of groundwater quality. Geo-Statistical Interpolation using GIS has been considered as the best and most advanced method for the interpolation and prediction studies of groundwater pollution and quality, and is adopted universally. In this paper, ordinary Kriging with logarithmic data transformation has been used to interpolate and predict the spatial variation of groundwater quality parameters - EC, TDS, pH, Na<sup>+</sup>, Ca<sup>2+</sup>, Bi-Carbonate, Fluoride, Chloride, Sulphate and Nitrate using data pertaining to 48 well locations in the Dungarpur tehsil. Data was transformed and normalized using Logarithmic Transformation Method and Semivariograms were drawn and analyzed for selecting the suitable model. The best Semivariogram model was obtained based upon cross validation and on the lesser RMSE criterion and Coefficient of Determination. The results show that the best semivariogram model based on RMSE varied for each water quality parameter. For log transformed data Exponential model was found suitable for EC, TDS, Na<sup>+</sup>, TH etc.; Spherical model for Ca<sup>2+</sup>; Chloride Gaussian Model for Chloride. For original or raw for non-transformed data Exponential Model was found suitable for Fluoride, Sulphate and Nitrate; and Gaussian Model for pH and Bi-Carbonates.

**Keywords:** Interpolation, Spatial Distribution, Ground Water Quality, Kriging, Transformation

### I. Introduction

Water is crucial for the existence and propagation of life on earth. However, its reserves are depleting day by day due to either over exploitation and contamination through natural and anthropogenic agents or industrial activities. Groundwater quality is severely affected in the regions with low rainfall, high temperatures, and lithology with high concentration of various contaminants and chemical compounds such as Sodium, Fluoride, Bi-Carbonates, various other metals and their compounds. The extraction of ground water is increasing day by day due to limited amount of good quality potable water resources from which water is available to human beings. Further, the water quality of various surfaces water bodies has deteriorated day by day due to industrialization (Nas, 2009). It is essential now that serious efforts must be made for sustainable development, management, monitoring and preparation of government policies for the development of ground water and its quality. In understanding the spatial and temporal variability in distribution of ground water quality parameters based upon the data known or collected, Geostatistics and Interpolation are universally accepted as most suitable methods.

In the recent past, various researches used advanced methods of Statistics and Geo-Statistical Interpolation, IDW, Spline, Kriging, Global Polynomial Interpolation, Radial Basis Function etc. which proved very promising in the accuracy and prediction of unknown parameters from known parameters at variable levels (Shankar et al, 2018; Ali, 2019; Zeybek et al, 2020; Katipoğlu, 2021) The objectives of the study are to select suitable and appropriate spatial interpolation models and methods for studying the spatial variability of ground water quality

parameters. Most commonly used methods of data transformation have been executed and analysed to predict the general trend of the spatial distribution of selected groundwater quality parameters in Dungarpur tehsil of Dungarpur district in southern Rajasthan, India. The performance and suitability of different Geo-Statistical data processing and semivariogram models has been assessed and ordinary Kriging has been employed for various ground water quality parameters to study their spatial variations and patterns.

### 2. Study area, data used, materials and methods

#### 2.1. Study Area

Dungarpur tehsil is situated in the north-western part of Dungarpur district, one of the southernmost districts of the state of Rajasthan in India (Figure 1) between 23° 20' 1.56" N latitude and 73° 21' 6.70" E longitude to 24° 0' 41.4144" N latitude and 74° 22' 50.484" E longitude. It shares political boundaries with the state of Gujarat in the south as well as in west direction. In 2022, the estimated total population of the district is 15,59,120 persons (as per aadhar uidai.gov.in in December 2020 data).

Dungarpur tehsil is a tribal dominated area being economically, socially and educationally backward. The estimated population of the tehsil in 2022 is 6,34,141 persons. As per Census 2011, the total population of the tehsil was 4,95,423 persons residing in 98,876 households. It is a predominantly rural area with 90.4 percent of population living in 305 villages. In 2011, ST population comprised 77.71 percent of the total population. Main workers comprised only one-third of the population of the tehsil having gainful employment for more than 06 months in a year. The population is mostly dependent on groundwater for drinking requirements.

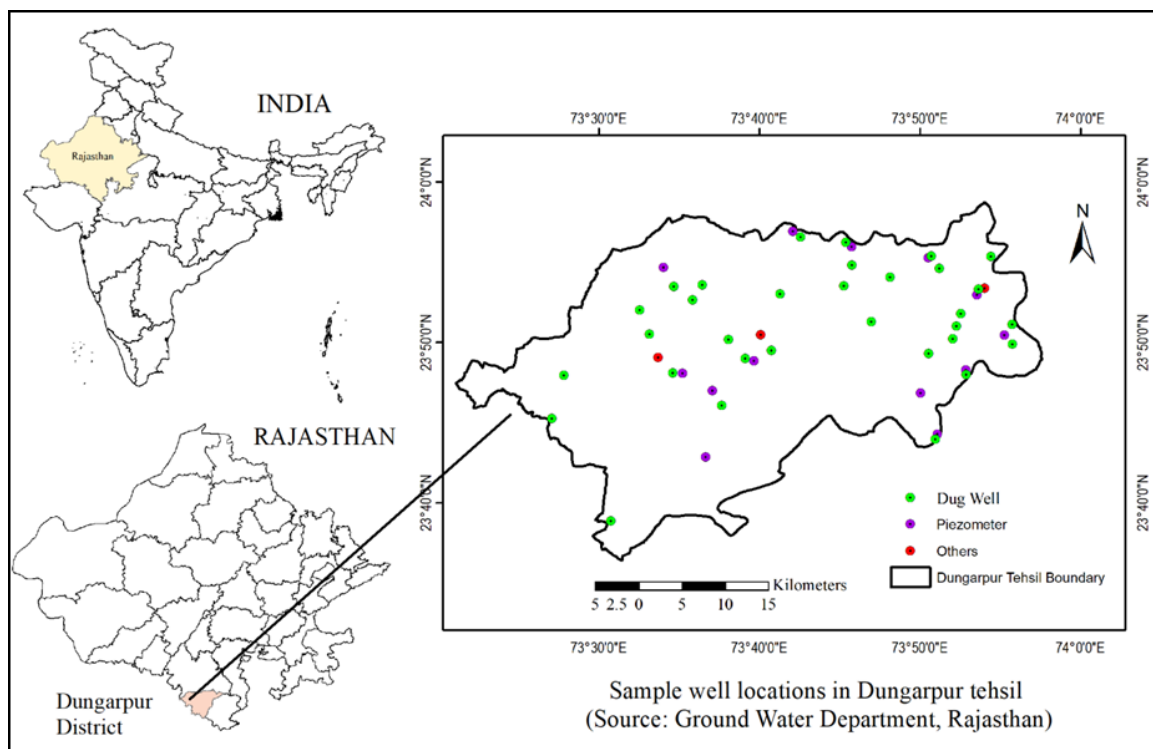


**Figure 1. Location of study area and sample well locations in Dungarpur tehsil.**

Occurrence of high fluoride in ground water is a matter of great concern. Particularly the areas adjoining blocks of Aspur, Dungarpur and Sagwara tehsils are severely affected by Fluoride contamination in groundwater. The high amount of fluoride in the groundwater is reflected in the bone related diseases widely prevalent in the resident population.

The overall geology of the area is highly complex. Dungarpur district is underlain mainly by hard rock formations such as Gneiss, Schists, Phyllites and Slates. The Fluorides in groundwater apparently originate from the rock formations.

**2.2. Data used**

A total number of 48 sites were selected using the water quality observation well locations used by the Ground Water Department (GWD), Rajasthan and mentioned in the ‘Water Quality Report of Pre-Monsoon 2014’, issued by the GWD (Figure 1). The well location sites were identified with help of their names and searching their geographic latitude and longitude values by querying and identify tool on the GWD Assets layer in the ‘Rajdharaa-Ground Water GIS’ Portal of the Government of Rajasthan. The pre-monsoon water quality data of 11 parameters - Electric Conductivity (EC), Total Dissolved Solids (TDS), pH, Sodium (Na<sup>+</sup>), Calcium (Ca<sup>2+</sup>), Bi-Carbonate (HCO<sub>3</sub><sup>-</sup>), Fluoride (F<sup>-</sup>), Total Hardness (TH), Chloride (Cl<sup>-</sup>), Sulphate (SO<sub>4</sub><sup>2-</sup>) and Nitrate (NO<sub>3</sub><sup>-</sup>) - were taken from the above mentioned Water Quality Report.

Since the primary objective of the study is to assess the performance of spatial interpolation models, only representative pre-monsoon data of the region has been used. The spatial variability of some of the physicochemical parameters may be altered due to the precipitation in the post monsoon season.

**3. Method of spatial correlation analysis**

**3.1. Semi-variable function**

In statistics, semi variable function (Equation 1) is used for the calculation and understanding the pattern of spatial correlation, if the sampling data values are normally distributed and the skewness of the sample data value distribution lie within a range of - 1 to +1. (Hu et. al, 2009)

Semivariogram analysis is the main tool to graphically represent the spatial correlation among the neighboring sample data values and observations (Bárdossy, 1997). It shows the relationship between the lag distance on the horizontal axis and the semivariogram value on the vertical axis (Figure 2). Lag distance is the distance between the measurements of a particular property. The semivariogram value increases from low to high values indicating higher spatial autocorrelation at the small lag distance (Nayanaka et al., 2010).

$$\gamma(h) = \frac{1}{2N(h)} \sum_{i=0}^{N(h)} [Z(x_i) - Z(x_i + h)]^2$$

.....Equation (1)

Where,  
 $\gamma(h)$  = Semi-Variable Function,  
 $Z(x_i)$  = Sample or Data Value,  
 $Z(x_i + h)$  = Sample or data value with ‘h’ distance from  $x_i$ ,  
 $N(h)$  = No. of attribute pairs that are separated by distance ‘h’.

Degree of spatial correlation can be evaluated by calculation of nugget effect which is the ratio of nugget to sill

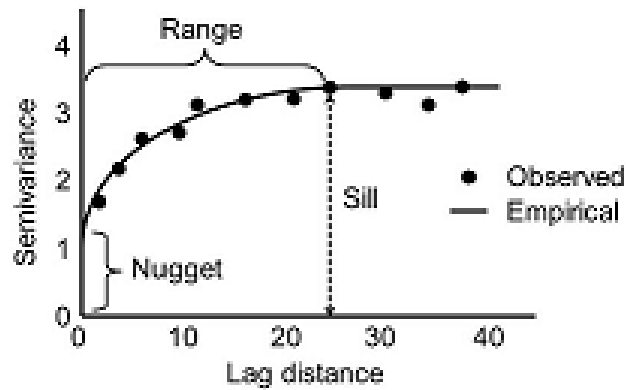


Figure 2. Semi-Variogram

**3.2. Common Semi-Variogram Model Fitting**

**Equations**

The equations of some of the commonly used models for the fitting of semi-variograms are:

**a) Spherical model**

$$\gamma(h) = C \left( \frac{3h}{2a} - \frac{1}{2} \frac{h^3}{a^3} \right), \text{ if } h \leq a$$

$$\gamma(h) = C, \text{ if } h > a$$

.....Equation (2)

Where,

a = Range or distance between correlated and uncorrelated data,

h = Lag distance and

C ≠ 0

If any two points are separated by a distance greater than range ‘a’, then the corresponding points or data locations are independent of each other. The value of the Sill ‘C’ is the value of the variogram for the distances greater than the range. It is equal to C(0), the variance of the random variable (Bárdossy, 1997)

**b) Exponential model**

$$\gamma(h) = C \left( 1 - e^{-\frac{h}{a}} \right)$$

..... Equation (3)

Where,

a = Range or distance between correlated and uncorrelated data,

h = Lag distance and

C ≠ 0

In case of exponential model all the random variables are supposed to be dependent. But there is an effective range ‘3a’ such that random variables related to points more distant than ‘3a’ can be treated as independent. The Sill ‘C’ is equal to ‘C(0)’, the variance of the random variable (Bárdossy, 1997).

**c) Gaussian model**

$$\gamma(h) = C \left( 1 - e^{-\frac{h^2}{a^2}} \right)$$

.....Equation (4)

Where,

a = Range or distance between correlated and uncorrelated data,

h = Lag distance and

C ≠ 0

Again, in Gaussian model the Sill ‘C’ is equal to ‘C(0)’, the variance of the random variable. Parameter ‘a’ is again related to effective range of the variogram. There is a limit to the effective range in Gaussian model which is equal to ‘√3a’ (Bárdossy, 1997).

**4. Interpolation method**

There are two most common categories in which statistical interpolation methods viz. Deterministic and Geostatistical. (Chen et al., 2013) Geo-statistics can be regarded as a collection of numerical techniques that deal with the characterization of spatial attributes employing primarily random models in a manner similar to the way in which time series analysis characterizes temporal data (Olea et al., 2012). It deals with spatially autocorrelated data that have a basic structure or spatial patterns which can be manifested in semivariogram analysis.

Kriging is a Geostatistical interpolation method used to study and predict the values for the locations where no data is available, on the basis of data collected and measured known locations. Kriging also facilitates in the calculation of the uncertainty of error and estimation of accuracy in the surface of values generated. Moreover, various researchers have found that Kriging provides better results as compared to other deterministic and stochastic methods. Therefore, Kriging has been selected for the present study.

**4.1. Kriging**

Kriging method works on the principle of existence of spatial autocorrelation for the application of geostatistics. To study the spatial pattern of the data values and parameters, semivariograms are used as a descriptive tool (Goovaerts, 1999). The spatial dependence between measured points is calculated on the basis of the distance between these points with the help of semivariance (Tatalovich, 2006). Thereafter, the fitting of semivariograms is done using different models such as Gaussian, Spherical and Exponential to check the best suitable model to be adopted for the study and to generate optimum interpolation weights (Burroughs and

McDonnell, 1998). Kriging is a very flexible interpolator that can be exact or smooth. It allows a variety of output surfaces including predictions, prediction standard errors, and probability (Johnston et al., 2004). Kriging technique eases out the optimal, unbiased estimation of the regionalized variables of unsampled sites with the properties of the semivariogram, using initially taken data values. (Mehrijardi et al., 2008).

#### 4.2. Logarithmic transformation

To perform Kriging operation the data value distribution of random variable which is taken must be normally distributed and follow stationarity principle. But it may not be practically necessary. To account for the non-normality, the mathematical process of data transformations are used such as 'Logarithmic' transformation. Logarithmic transformation is basically a class of mathematical operation in which the log values of all the random variable values are taken to make the whole distribution follow normality principle or comes closer to it. In this study natural logarithmic transformation has been used for all different water quality parameters whenever the data distribution for any particular parameter was not found normally distributed by taking the natural logs of all the individual parameter values (after Osbourne, 2002).

#### 4.3 Cross-Validation

Generally, the method used for the validation of interpolation processes is called Cross-Validation (Voltz and Webster, 1990). The key procedure in the process of cross-validation is the temporary removal of one data point and the removed point is estimated with the help of remaining data points, thereafter the difference between the actual and estimated values is calculated. This procedure is repeated for all the remaining set of data points.

In this study, the cross-validation of interpolation has been performed for all the water quality parameters on the basis of least Root Mean Square Error (RMSE).

### 5. Methodology

Suitable hydro geochemical parameters for modeling the ground water quality have been selected based on literature review (after McNeely et al., 1979). Geo-statistical analysis (Ordinary Kriging) has been used for spatial interpolation to model the spatial distribution of groundwater chemistry.

Geostatistical analysis has been implemented in the following three steps:

- Semivariogram creation and analysis.
- Validation of Semivariogram models.
- Generation of the groundwater quality prediction surfaces and maps.

Geostatistical Wizard of ArcGIS 10.5 was used for the exploratory data analysis, data transformation, and semivariogram analysis.

RMSE criterion has been used for comparison between the different semivariogram models and data transformation. The smallest value of RMSE indicates the most suitable model for the data. Figure 3 illustrates the methodological workflow of the study.

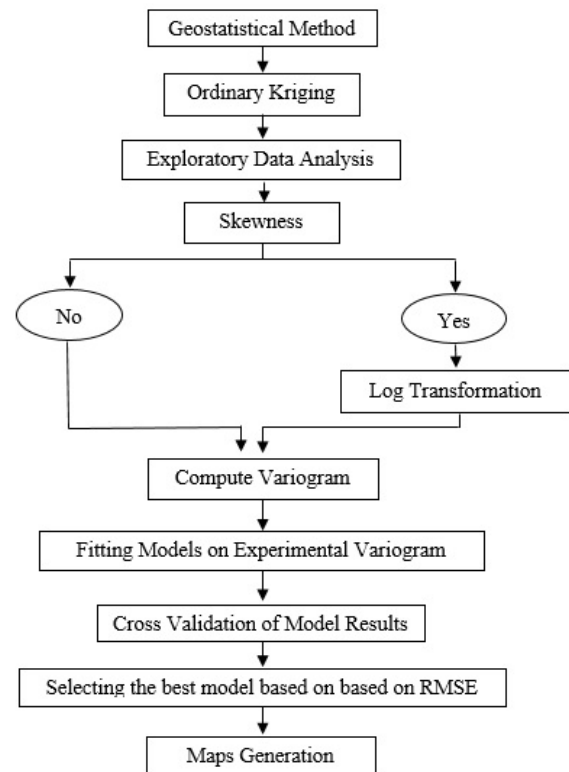


Figure 3. Methodological flowchart

### 6. Result and discussion

#### Distribution Characteristics

The following tables summarize the distribution characteristics of the selected hydro-geochemical parameters based on raw and log transformed data. Descriptive statistics describing distribution based on natural log transformed and raw untransformed values has been given in Tables 1.

Results reveal that the raw data distributions of EC, TDS, TH,  $\text{Na}^+$ ,  $\text{Cl}^-$  and  $\text{NO}_3^-$  were highly positively skewed, whereas those of pH,  $\text{Ca}^{2+}$ ,  $\text{F}^-$ ,  $\text{HCO}_3^-$ ,  $\text{CO}_3^{2-}$  and  $\text{SO}_4^{2-}$  were more or less normally distributed. The natural log transformed distributions of all the parameters obeyed normal distribution. The acceptable range of skewness considered was -2 to + 2 and the acceptable range of kurtosis considered was -3 to +3 (after Garson, 2012).

**Table 1. Descriptive statistics of hydro-geochemical parameters for raw and log transformed distribution.**

Indices	Minimum		Maximum		Average		Standard Deviation		Skewness		Kurtosis	
	lgN	Raw	lgN	Raw	lgN	Raw	lgN	Raw	lgN	Raw	lgN	Raw
EC	2.66	460	3.38	2390	2.9	835.73	0.14	335.59	0.98	2.42	1.35	8.75
TDS	2.40	252	3.12	1315	2.65	472.10	0.15	193.74	0.96	2.21	1.07	6.76
pH	0.89	7.8	0.99	9.7	0.93	8.62	0.02	0.40	0.12	0.35	1.46	1.72
TH	2.0	100	2.83	680	2.36	245.93	0.16	99.44	0.39	1.93	0.59	6.50
Na <sup>+</sup>	1.46	29	2.40	251	1.87	81.19	0.19	37.86	0.06	1.92	0.03	7.31
Ca <sup>2+</sup>	1.30	20	1.95	90	1.61	45.29	0.20	19.83	-0.14	0.44	-1.16	-0.91
F <sup>-</sup>	-0.92	0.12	0.25	1.8	-0.10	0.93	0.26	0.49	-0.72	0.49	0.59	-0.8
Cl <sup>-</sup>	1.63	43	2.72	525	2.04	126.67	0.21	79.85	0.78	2.93	0.85	12.41
HCO <sub>3</sub> <sup>-</sup>	1.38	24	2.58	378	2.20	178.29	0.22	80.90	-0.98	0.75	3.0	0.15
SO <sub>4</sub> <sup>2-</sup>	1.04	11	2.15	141	1.57	46.42	0.29	33.05	0.13	1.39	-0.54	1.25
NO <sub>3</sub> <sup>-</sup>	0	1	2.06	116	1.24	27.35	0.44	29.06	-0.47	2.08	1.29	3.84

The log normal values of EC range between 2.66 to 3.38  $\mu\text{Scm}^{-1}$ ; for TDS range between 2.40 to 3.12 mg/l; for pH range from 0.89 to 0.99; for TH range from 2 to 2.83 mg/l; for Na<sup>+</sup> range from 1.46 to 2.40 mg/l; for Cl<sup>-</sup> range from 1.63 to 2.72 mg/l; and for NO<sub>3</sub><sup>-</sup> range from 0 to 2.06 mg/l.

The log transformed values of Ca<sup>2+</sup> range from 1.30 to 1.95 mg/l; for F<sup>-</sup> range from -0.92 to 0.25 mg/l; for HCO<sub>3</sub><sup>-</sup> range from 1.38 to 2.58 mg/l; and for SO<sub>4</sub><sup>2-</sup> range from 1.04 to 2.15 mg/l. The raw values of EC range from 460 to 2390  $\mu\text{Scm}^{-1}$ ; that of TDS range from 252 to 1315 mg/l; and that of TH range from 100 to 680 mg/l. The raw values of Na<sup>+</sup> range from 29 to 251 mg/l; that of Ca<sup>2+</sup> range from 20 to 90 mg/l; that of F<sup>-</sup> range from 0.12 to 1.8 mg/l and of Cl<sup>-</sup> range from 43 to 525 mg/l. The raw values of HCO<sub>3</sub><sup>-</sup> range from 24 to 378 mg/l, that of SO<sub>4</sub><sup>2-</sup> range from 11 to 141 mg/l and of NO<sub>3</sub><sup>-</sup> range from 1 to 116 mg/l.

Higher spatial variability, with pockets of extremely high concentration, as reflected in the range of raw values, high

standard deviation, high positive skewness and kurtosis, is observed in EC, TDS, TH, Na<sup>+</sup>, Cl<sup>-</sup> and NO<sub>3</sub><sup>-</sup>. However positive skewness and leptokurtic distribution indicates higher concentration of values towards lower end of the scale. The distribution of Ca<sup>2+</sup>, F<sup>-</sup>, HCO<sub>3</sub><sup>-</sup> and SO<sub>4</sub><sup>2-</sup> is normally distributed. However the range and standard deviation values indicate high spatial variability in concentration of these parameters too across the tehsil.

#### Semivariogram creation and validation of models

Attempt has been made to identify the best optimum model by comparing the Spherical, Gaussian and Exponential model for both raw data distributions as well as natural log normalized data distributions for all the twelve indices. The minimum Root Mean Square Error (RMSE) values across different models (Gaussian, Spherical and Exponential variogram models using raw and log transformed data) have been compared for each parameter to identify the most suitable model. The RMSE values obtained for all water quality parameters for different Semivariogram models have been given in Table 2.

**Table 2. Best fit Semivariogram model for the selected water quality parameters (bold and asterisk indicates lowest RMSE).**

Parameters	Angle Tolerance (in°)	Ordinary Kriging					
		Model on Raw Data			Model on Log Transformed Data		
		Spherical	Exponential	Gaussian	Spherical	Exponential	Gaussian
EC	45	329.53	312.91	412.35	321.73	<b>306.19*</b>	378.78
TDS	45	182.14	171.14	222.6	178.02	<b>167.60*</b>	209.53
pH	45	0.3463	0.3426	<b>0.3351*</b>	0.3486	0.3379	0.3381
TH	45	107.2	101.7	134.76	106.3	<b>100.76*</b>	102.46
Na <sup>+</sup>	45	32.89	31.42	36.49	32.66	<b>31.41*</b>	32.16
Ca <sup>2+</sup>	45	18.96	19.26	19.21	<b>18.95*</b>	19.28	19.25
F <sup>-</sup>	45	0.303	<b>0.288*</b>	0.349	0.319	0.309	0.311
Cl <sup>-</sup>	45	89.93	83.66	95.34	87.84	83.46	<b>80.52*</b>
HCO <sub>3</sub> <sup>-</sup>	45	73.75	71.54	<b>71.29*</b>	74.43	72.44	80.71
SO <sub>4</sub> <sup>2-</sup>	45	26.97	<b>26.57*</b>	27.77	28.36	27.23	29.95
NO <sub>3</sub> <sup>-</sup>	45	19.7	<b>18.07*</b>	24.9	22.44	20.05	22.33

The best semivariogram model varies for each water quality parameter. Exponential model of logarithmically transformed data was most suitable method for EC, TDS, Na<sup>+</sup> and TH. For Ca<sup>2+</sup> Spherical model for logarithmically transformed data was found suitable. For Cl<sup>-</sup> Gaussian model of logarithmically transformed data was found suitable. For F<sup>-</sup>, SO<sub>4</sub><sup>2-</sup>, and NO<sub>3</sub><sup>-</sup> the Exponential model with original (raw) data has been found most suitable. The Gaussian model with original data has been found most suitable for pH and HCO<sub>3</sub><sup>-</sup>. The best fit Semivariance models have been illustrated in Figure 4 (a - k).

The spatial structure indices of the best fit Semivariogram model selected for each parameter have been summarized in Tables 3. The EC shows high spatial correlation, and there is no nugget effect, which has a range of 0.947 degrees. TDS also shows high spatial correlation with zero nugget effect and effective range of 0.965 degrees. The pH shows high spatial correlation, 0.09% nugget effect and in effective range of 3.662 degrees. TH also shows high spatial correlation with zero nugget effect, where range is 9.051 degrees.

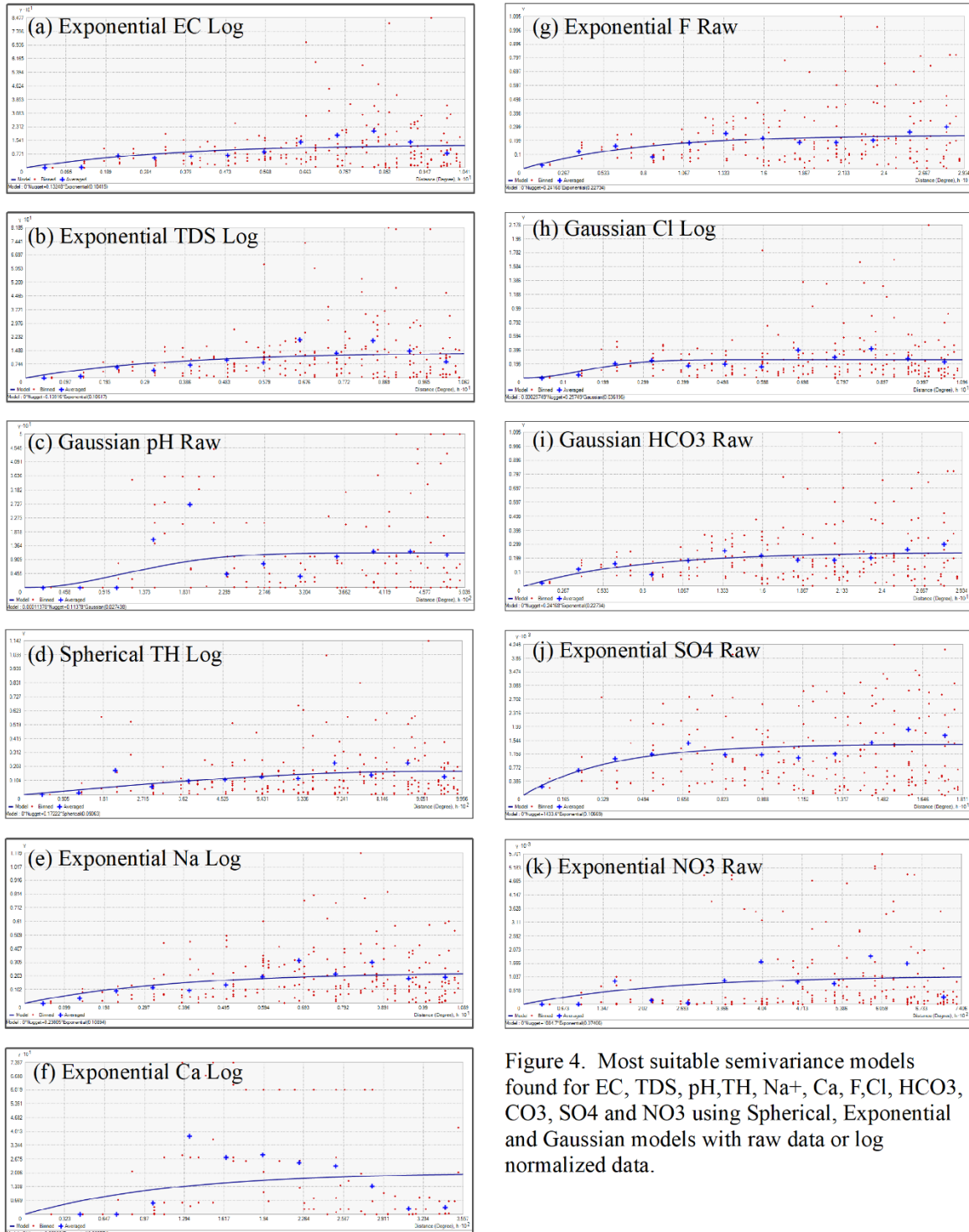


Figure 4. Most suitable semivariance models found for EC, TDS, pH, TH, Na<sup>+</sup>, Ca, F, Cl, HCO<sub>3</sub>, CO<sub>3</sub>, SO<sub>4</sub> and NO<sub>3</sub> using Spherical, Exponential and Gaussian models with raw data or log normalized data.

**Spatial structure analysis**

Na<sup>+</sup> shows high spatial correlation, and there is no nugget effect, which has a range of 1.089 degrees. Values of Ca<sup>2+</sup> also show high spatial correlation with zero nugget effect and effective range of 3.557 degrees. F<sup>-</sup> shows high spatial correlation, zero nugget effect in effective range of 2.667 degrees. The values of Cl<sup>-</sup> also show high spatial correlation with 0.1% nugget effect, where range is 0.498 degrees.

HCO<sub>3</sub><sup>-</sup> data shows high spatial correlation, and there is no nugget effect, which has a range of 5.225 degrees. SO<sub>4</sub><sup>2-</sup> also shows high spatial correlation, zero nugget effect in effective range of 1.482 degrees. NO<sub>3</sub><sup>-</sup> also shows high spatial correlation with zero nugget effect, where range is 6.733 degrees.

The basis for the describing the spatial correlations in the values of different indices as high spatial correlation is that if the nugget effect is less than 25 percent it suggests that a large portion of the variance in data is introduced spatially and thus emphasizes a strong spatial dependence of the data

or variable. A high nugget effect (greater than 75 percent) indicates weak spatial dependency (Mutuma, 2017). Thus all the geochemical parameters are highly spatially correlated.

**Generation of ground water quality prediction surfaces and analysis**

The interpolation surfaces generated by Kriging with optimal parameters models are shown in Figure 5 (a) & (b). The interpolation surfaces are smooth and show regional variation patterns corresponding to the hydrogeological conditions in the region.

Table 4 shows the correlation (r) among various water quality parameters. Table 5 shows the Coefficient of Determination (R<sup>2</sup>) between the raw and predicted or interpolated values of the different water quality parameters. The measured values explain 20% to ~80 percent variability in predicted values.

**Table 3. Spatial structure indices of the selected parameters for the best fit Semivariogram**

Parameters	Model	Transformation	Indices				
			Nugget	Sill	Nugget/Sill	Nugget Effect (%)	Range (Decimal Degrees)
EC	Exponential	lgN	0	0.132	0	0	0.947
TDS	Exponential	lgN	0	0.139	0	0	0.965
pH	Gaussian	Raw	0.0001	0.113	0.0009	0.09	3.662
TH	Exponential	lgN	0	0.169	0	0	9.051
Na <sup>+</sup>	Exponential	lgN	0	0.23	0	0	1.089
Ca <sup>2+</sup>	Spherical	lgN	0	0.184	0	0	3.557
F <sup>-</sup>	Exponential	Raw	0	0.241	0	0	2.667
Cl <sup>-</sup>	Gaussian	lgN	0.0003	0.257	0.001	0.1	0.498
HCO <sub>3</sub> <sup>-</sup>	Gaussian	Raw	7.8063	7814.12	0.001	0.1	5.225
SO <sub>4</sub> <sup>2-</sup>	Exponential	Raw	0	1433.6	0	0	1.482
NO <sub>3</sub> <sup>-</sup>	Exponential	Raw	0	1084.7	0	0	6.733

**Table 4. Correlation matrix of the selected water quality parameters.**

Correlation	EC	TDS	pH	Cl <sup>-</sup>	SO <sub>4</sub> <sup>2-</sup>	HCO <sub>3</sub> <sup>-</sup>	NO <sub>3</sub> <sup>-</sup>	F <sup>-</sup>	TH	Na <sup>+</sup>	Ca <sup>2+</sup>
EC	1										
TDS	<b>0.99</b>	1									
pH	-0.48	-0.43	1								
Cl <sup>-</sup>	<b>0.9</b>	<b>0.87</b>	-0.421	1							
SO <sub>4</sub> <sup>2-</sup>	<b>0.7</b>	<b>0.77</b>	-0.188	0.535	1						
HCO <sub>3</sub> <sup>-</sup>	<b>0.63</b>	<b>0.58</b>	-0.53	0.384	0.186	1					
NO <sub>3</sub> <sup>-</sup>	0.419	0.515	-0.095	0.17	<b>0.61</b>	0.145	1				
F <sup>-</sup>	0.234	0.254	-0.182	0.017	0.391	0.132	<b>0.53</b>	1			
TH	<b>0.91</b>	<b>0.88</b>	<b>-0.6</b>	<b>0.82</b>	<b>0.63</b>	<b>0.603</b>	0.36	0.26	1		
Na <sup>+</sup>	<b>0.86</b>	0.171	-0.238	<b>0.79</b>	<b>0.62</b>	<b>0.548</b>	0.248	0.04	<b>0.6</b>	1	
Ca <sup>2+</sup>	<b>0.65</b>	<b>0.66</b>	-0.255	<b>0.57</b>	<b>0.51</b>	0.355	0.398	0.17	<b>0.71</b>	0.37	1

**Table 5. Coefficient of Determination ( $R^2$ ) between measured and predicted value of various water quality parameters**

Parameters	EC	TDS	pH	TH	Na <sup>+</sup>	Ca <sup>2+</sup>	F <sup>-</sup>	Cl <sup>-</sup>	HCO <sub>3</sub> <sup>-</sup>	SO <sub>4</sub> <sup>2-</sup>	NO <sub>3</sub> <sup>-</sup>
$R^2$	0.4	0.5	0.6	0.2	0.6	0.38	1	0.2	0.47	0.6	0.79

The estimation of EC shows that medium to high levels of EC are found in the southern, north-eastern, northern parts of the Dungarpur tehsil which can be contributed to high levels of salinity and high mineral percentage due to the ionization and solubilization taking place in ground water aquifers in these areas. Strong positive association of EC occurs with TDS ( $r = 0.988$ ), TH ( $r = 0.91$ ), Cl<sup>-</sup> ( $r = 0.898$ ), and Na<sup>+</sup> ( $r = 0.856$ ). EC also moderately positively correlates with levels of SO<sub>4</sub><sup>2-</sup> ( $r = 0.695$ ) Ca<sup>2+</sup> ( $r = 0.646$ ) and HCO<sub>3</sub><sup>-</sup> ( $r = 0.634$ ).

The distribution surface of TDS reveals that the high concentrations are found in the southern, north-eastern and northern parts of the tehsil. High levels of TDS strongly correlate with occurrence of high levels of Cl<sup>-</sup> ( $r = 0.868$ ), SO<sub>4</sub><sup>2-</sup> ( $r = 0.771$ ) and TH ( $r = 0.881$ ). Moderate positive association occurs with Ca<sup>2+</sup> ( $r = 0.662$ ) and HCO<sub>3</sub><sup>-</sup> ( $r = 0.583$ ). The highest occurrences predominantly correspond with barren, rocky wasteland region. Thus lithology may be a significant factor for the observed spatial distribution.

Concentration of pH is higher in a major area of eastern and north-eastern zone of the tehsil. However the entire tehsil has highly alkaline ground water with the minimum being 7.8. The distribution of pH shows moderate to low correlation with all other parameters. Strongest negative association occurs with TH ( $r = -0.599$ ), HCO<sub>3</sub><sup>-</sup> ( $r = -0.53$ ) and Cl<sup>-</sup> ( $r = -0.421$ ).

Distribution of Na<sup>+</sup> and Cl<sup>-</sup> have strong positive association ( $r = 0.786$ ). Distribution of Na<sup>+</sup> is moderately associated with SO<sub>4</sub><sup>2-</sup> ( $r = 0.615$ ), HCO<sub>3</sub><sup>-</sup> ( $r = 0.548$ ) and TH ( $r = 0.595$ ). The concentrations of these parameters are distinctly highest in the north central, north western and north eastern part of the tehsil. Extreme southern part of the tehsil has moderate levels of Na<sup>+</sup>, Cl<sup>-</sup> and TH while high concentration of HCO<sub>3</sub><sup>-</sup> and SO<sub>4</sub><sup>2-</sup>. Entire tehsil, except a small pocket in the south-east has moderate to high levels of Ca<sup>2+</sup> being highest in north-east and western half of the region, and moderate in the central and northern

part. Distribution of Ca<sup>2+</sup> has strongest positive correlation with TH ( $r = -0.71$ ), EC ( $r = 0.646$ ) and TDS ( $r = 0.662$ ), and moderately associated with Cl<sup>-</sup> ( $r = 0.573$ ) and SO<sub>4</sub><sup>2-</sup> ( $r = 0.51$ )

The spatial distribution of F<sup>-</sup> shows a distinctly concentrated pattern. Extreme eastern and south-western parts of the tehsil have notably high levels, while western part is a low concentration region. The central region has moderate F levels. The distinctive concentration is substantiated by the correlation values which are on the lower end of the scale for all parameters except NO<sub>3</sub> ( $r = 0.533$ ), which also shows highest concentration in the eastern half of the tehsil. The southern pocket of high concentration corresponds with the predominantly forest and agricultural area. The eastern part of the tehsil is predominantly agricultural and settlement area. The NO<sub>3</sub> distribution in the tehsil may be accounted for by geological conditions and anthropogenic causes like use of agricultural fertilizers and coal combustion as well.

Broadly it is observed that most of the red patches of the geo-chemical parameters (high predicted values) are falling in the areas occupied by gneisses particularly the extreme east and northern part. Minimum values of EC, TDS and TH (blue) are in an elongated zone falling in areas occupied by phyllites. However, the areas in the extreme west having moderate values (yellow) are also occupied by phyllites. The high values of F<sup>-</sup> are in the extreme east and extreme south-west suggesting relation of fluoride concentration with Gneissic and Schistose rocks.

The observed patterns of various parameters derived as interpolated surfaces relate logically to the probable natural, geological and anthropogenic factors to a significant extent. The  $R^2$  values between the measured and predicted values of various parameters range from approx. 20 percent for TH, Cl<sup>-</sup> to approx. 80 percent for F and NO<sub>3</sub>. Approximately 50 percent variability is explained for distribution of SO<sub>4</sub>, TDS, Na and pH.

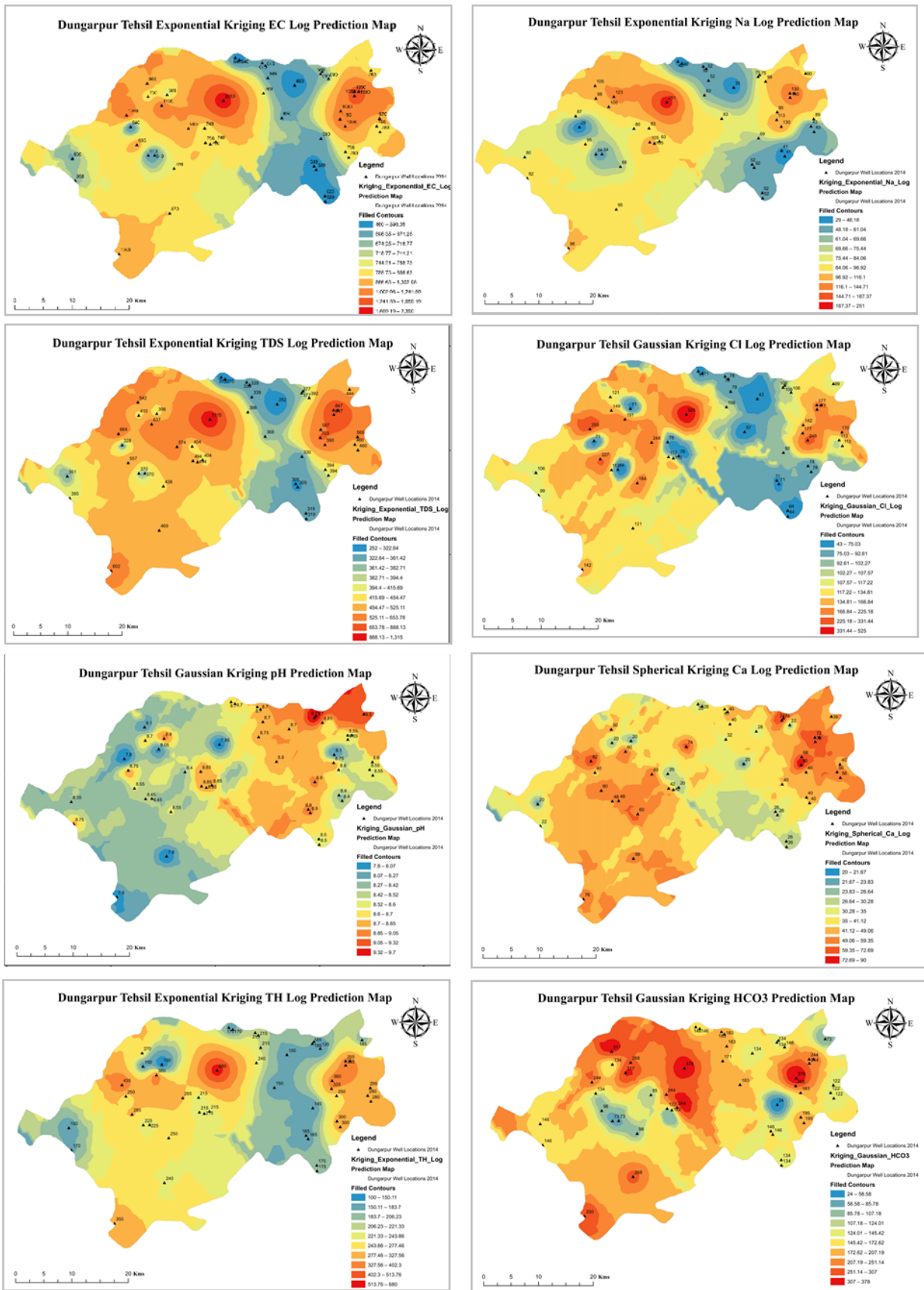


Figure 5a. The interpolation surfaces generated by Kriging with optimal parameters models for EC, TDS, pH, TH, Na, Ca, Cl and HCO<sub>3</sub>.

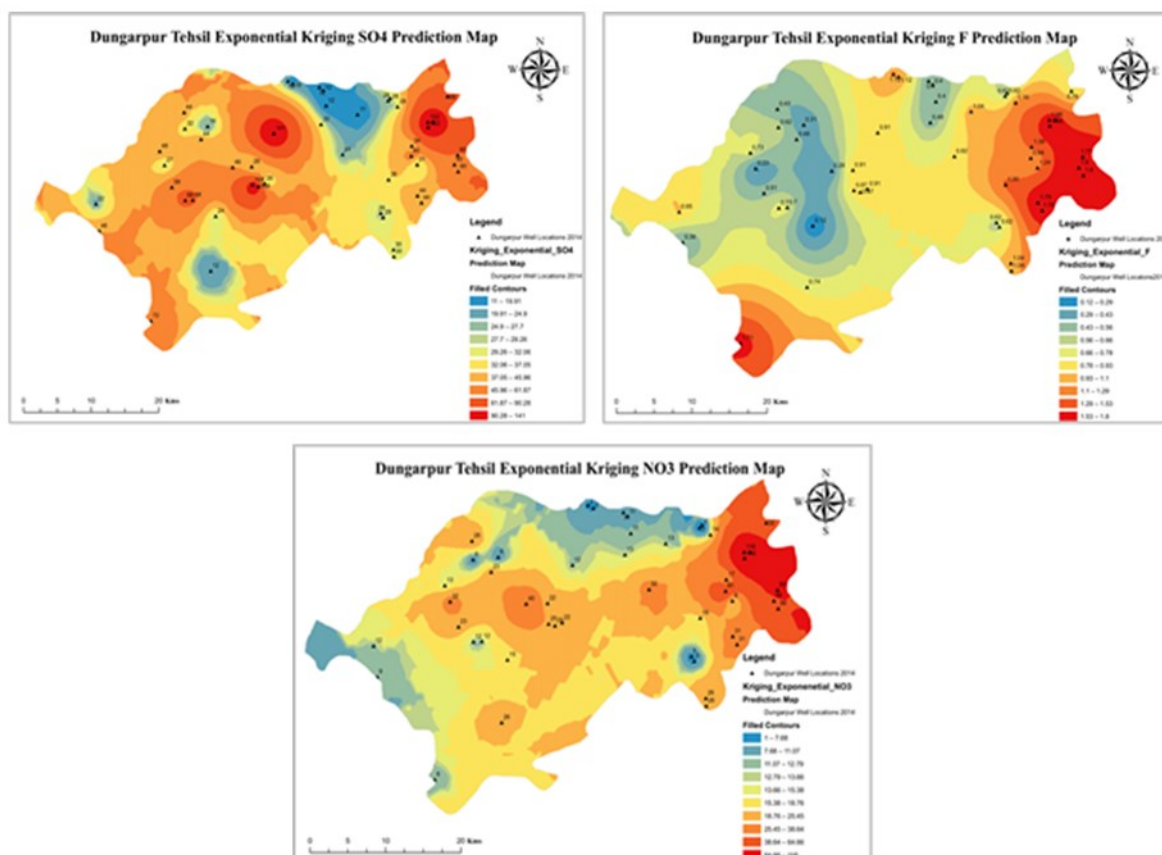


Figure 5b. The interpolation surfaces generated by Kriging with optimal parameters models for F, SO<sub>4</sub> and NO<sub>3</sub>

#### 4. Conclusions

It can be concluded that the most of the northern, north-eastern, central and extreme southern regions of the Dungarpur tehsil are affected by higher concentrations of various chemical parameters such as EC, TDS, pH, TH, Na<sup>+</sup>, Ca<sup>2+</sup>, F<sup>-</sup>, Cl<sup>-</sup>, HCO<sub>3</sub><sup>-</sup>, SO<sub>4</sub><sup>2-</sup> and NO<sub>3</sub><sup>-</sup>. Kriging estimation can be considered as a reliable method for generation of interpolated surfaces of ground water quality based on point sample data and selection of best suitable semi-variance model among Gaussian, Spherical and Exponential over the log normal transformed data of water quality parameters. The nugget effect can be employed as an efficient index to illustrate the degree of spatial correlation based on semi-variable function. The performance of the models varies for different parameters. In the present study the distribution of geochemical parameters like Flouride, Nitrate, Alkalinity, TDS, Sulphate and Sodium has been effectively modelled using the Kriging tool. However, the prediction capability for TH and Chlorine has been relatively low.

#### Acknowledgements

This paper is a part of the study being carried out under major research project funded by Ministry of Human Resource Development, Government of India (MHRD) under Rashtriya Uchhatar Shiksha Abhiyan (RUSA) 2.0 scheme. The authors are thankful to MHRD and State Project Directorate, Government of Rajasthan for funding the project.

#### References

- Ali S.A. and A. Ahmad (2019). Analysing water-borne diseases susceptibility in Kolkata Municipal Corporation using WQI and GIS based Kriging interpolation. *GeoJournal*, 85, 1151-1174.
- Bárdossy A. (1997). Introduction to geostatistics. *Institute of Hydraulic Engineering, University of Stuttgart*, 28-32
- Burrough P. A. and R. A. McDonnell (1998). Creating continuous surfaces from point data. *Principles of Geographic Information Systems*. Oxford University Press, Oxford, UK.
- Garson G. D. (2012). Testing statistical assumptions. *Asheboro, NC: Statistical Associates Publishing*.
- Goovaerts P. (1999). Geostatistics in soil science: state-of-the-art and perspectives. *Geoderma*, 89(1-2), 1-45.
- Hu K., H. Chen, Y. Zhang, B. Li and D. Chen (2009). Spatial distribution of shallow groundwater depth, total dissolved solid and nitrate pollution. *Transactions of the Chinese Society of Agricultural Engineering*, 25(Supp. 1), 21-25.
- Chen J, Z. Hanting, Q. Hui, W. Jianhua and Z. Xuedi (2013, June). Selecting proper method for groundwater interpolation based on spatial correlation. In *2013 Fourth International Conference on Digital Manufacturing & Automation* (pp. 1192-1195). IEEE.

- Johnston K. (2004): ArcGis 9. Using ArcGIS geostatistical analyst. Redlands, California. *Esri Press (GIS by ESRI)*.
- Katipoğlu O.M. (2021). Spatial Analysis of Seasonal Precipitation Using Various Interpolation Methods in the Euphrates Basin, Turkey.
- McNeely R. N., V. P. Neimanis and L. Dwyer (1979). A guide to water quality parameters. *Water quality source book. Ottawa: Inland waters directorate, water quality branch, 88*.
- Mehrdadi R. T., M. Z. Jahromi, S. Mahmodi and A. Heidari (2008). Spatial distribution of groundwater quality with geostatistics (case study Yazd-Ardakan Plain). *World Applied Science Journal* 4(1):9-17.
- Mutuma E. (2017), Innovative approaches of predicting soil properties and soil classes in the eastern slope of Mt. Kenya. *Thesis of Hungarian University of Agriculture and Life Sciences*.
- Nas B. (2009). Geostatistical Approach to Assessment of Spatial Distribution of Groundwater Quality. *Polish Journal of Environmental Studies, 18*, 1073-1082.
- Nayanaka V. G. D., W. A. U. Vitharana, and R. B. Mapa (2010). Geostatistical analysis of soil properties to support spatial sampling in a paddy growing alfisol.
- Olea R. A. (2012). *Geostatistics for engineers and earth scientists*. Springer Science & Business Media.
- Osbourne J. W. (2002). Notes on the Use of Data Transformation. *Practical Assessment, Research & Evaluation, 8*(6), n6.
- Shankar B.S. and Shobha (2018). A Comprehensive Assessment of Spatial Interpolation Method Using IDW Technique for the Groundwater Quality Evaluation of an Industrial Area in Bangalore, India.
- Tatalovich Z., J. P. Wilson and M. Cockburn (2006). A comparison of thiessen polygon, kriging, and spline models of potential UV exposure. *Cartography and Geographic Information Science, 33*(3), 217-231.
- Voltz M. and R. Webster (1990). A comparison of kriging, cubic splines and classification for predicting soil properties from sample information. *Journal of Soil Sciences. Wiley Online Library*.
- Zeybek M. and I. Şanlıoğlu (2020). Investigation of landslide detection using radial basis functions: a case study of the Taşkent landslide, Turkey. *Environmental Monitoring and Assessment, 192*, 1-19.

# A geospatial study of the layout and extent of the eighteenth-century walled city of Hyderabad

Gaurav Kumar Pal\* and M.B. Rajani

National Institute of Advanced Studies, IISc Campus, Bangalore, India

\*Email: [palgaurav1024@gmail.com](mailto:palgaurav1024@gmail.com)

(Received: Dec 30, 2021; in final form: Aug 18, 2022)

**Abstract:** Hyderabad and Golconda are prominent medieval cities in Deccan India, claiming significant roles in shaping the transformation of the region in the 20<sup>th</sup> and 21<sup>st</sup> centuries. This study focuses on defining the contours of Hyderabad's walled settlement, a fortified structure built around Hyderabad city, the capital of Hyderabad State after the fall of Golconda in 1687. The capital shift to Hyderabad occurred gradually even with the construction of Char Minar in 1591. The city became an important factor to understand the growth of Hyderabad in the Nizam and British eras. The core of the study is based on how different maps of the walled city dating from the 18<sup>th</sup> c. to 20<sup>th</sup> c. describe a picture of change in the settlement arena of Hyderabad. These maps signify the areas of development, which can be conjectured in present-day Google Earth. It also compares different maps to bring about the information on built features in the city and georeference them in today's setting so as to understand the spatial change in the arrangement of the city. The findings of the current work are used to conduct a detailed field survey to check and document remains that still exist and also the condition they are in at present. The study focuses on the sustainable development of a burgeoning urban sprawl of Hyderabad considering the cultural heritage of the area

**Keywords:** Hyderabad, Geospatial, Remote sensing, Charminar

## 1. Introduction

The cultural heritage setting of Hyderabad today shows two precincts, Golconda Fort Complex and Char Minar with associated structures. The construction of Char Minar in 1591 by Muhammad Quli Qutb Shah of the Qutb Shahi Dynasty marked the beginning of the shift of the capital from Golkonda to the new city of Hyderabad. Char Minar was constructed as a central point of the new city, built on a new road running north to south intersecting the already running road in the form of a trade route from east of Golkonda to Masulipatnam and other coastal towns of the kingdom (Sherwan, 1967) further east. The city followed a plan of a giant double cross being built on a gridiron system.

As the new capital began to thrive, there was a need to strengthen and consolidate the city of Hyderabad with a fort wall. The fortification wall was built at the end of the Qutb Shahi Dynasty, during the last days of Mubarez Khan in 1712, and completed by the first Nizam in 1740. This wall defined the city's limits as well as provided security to the city (Nayeem, 1987). The stretch of wall from Chadder Gate to Dabirpura gate was originally built with no turret parapets, but Asaf Jah I surmounted turret parapets later (Bilgrami, 1927). The circumference of the wall was 9 miles enclosing an area of 4.5 sq. Miles. The existence of the wall has been recorded till the end of the 19<sup>th</sup> century and there are reference of some remains even post-independence. The focus of this paper is to identify the original extent of the walled city and understand its transformations over time by comparing the maps made in three different centuries i.e. from 18<sup>th</sup> to 20<sup>th</sup>. The study also identifies the locations of the wall remains using satellite imagery and digitizes them using GIS. The present remains of the wall stretch along the areas Nashemannagar, Fateh Darwaza, Aliabad and Lal Darwaza, but with geospatial analysis, the current study identifies and documents the remains of the walls across various settlements of the city. The history of Hyderabad

city is recorded by Nizam and Colonial rulers, each using their own mapping techniques depicting a different shape and orientation of the city wall.

## 2. Origin of Hyderabad (Capital city of Hyderabad State)

The present city of Hyderabad is divided into two: south and north banks by the River Musi. The plain on the southern bank is in the shape of an elongated trapezium bounded by Mir Alam Tank, Koh-i-Tur (Falakhnuma Hill) and Sarurnagar tank in the south-west, south and east distance of 6.3 and 4 miles, respectively, from Charminar (Nayeem, 1987). This study focuses on this area and how it was developed historically with an inclusion of a fort wall at the periphery of Hyderabad City.

Hyderabad became a full-fledged state in the 18th century with the capital first at Aurangabad and then Hyderabad in 1763. The city of Hyderabad was founded in the last decade of the 16th century, later becoming the capital of Qutb Shahi Sultans of Golconda and Nizams of the state of Hyderabad till 1948. Leading up to the foundation of the city of Hyderabad, the plan to construct a new city was made in 1591. Muhammad-Quli Qutb Shah is said to have taken these plans further for the new city, as he was already aware of the large swath of land present at the south of the Musi River as his father had already constructed a bridge in 1578 on the Musi River to access the other side (Sherwani, 1967). Construction of Char Minar was completed in 1592 with four radial roads projecting from it: northern road stretch to Musi River at Afzal Bridge; southern till the present day Falakhnuma Castle (originally called as Koh-i-Tur); eastern towards the coast of the Bay of Bengal and western towards Golkonda.

### 3. Hyderabad city wall through maps

#### 3.1 Map of 1772

The wall completed by the first half of the 18<sup>th</sup> century by which time Hyderabad's population was 2,25,000; highest in India at the time. The first site plan of the new Hyderabad city is depicted in a 1772 map (Figure 1). Although the map is not to scale, it shows the entire walled extent with Char Minar as its central feature. It also shows structures such as Char Khaman, Mecca Masjid, and other religious and civic structures. The map suggests that in 1772 the central area near Charminar was densely populated with residential features, while the north and northeast parts were sparsely populated. The map gives road intersection layouts and street patterns that are identifiable with 20<sup>th</sup>-century maps and even today. It is quite clear that the fort wall was in good condition in 1772 with as many as 13 gates and many windows (Table 1). These gates are numbered on the map by S.P.Shorey, who has analyzed the original map and recorded his impressions (Shorey, 1993). The northwest quadrant shows the city where the Qutb Shahi Palace Complex was destroyed in 1687 and residential structures were built (Shorey, 1993). The new residential quarters were most probably built by reusing construction material from the old Palace. The largest house of the city was Charnahal where the French made their residence (Sarkar 1963).

#### 3.2 Map of 1854

The map (Figure 2) was made by the British, which explains the focus predominantly on structures of the British colony. Along with Hyderabad, the map features Secunderabad and Golconda as well as mentions residential and official places of the British chiefs. The actual area of the Hyderabad fort is only about double that of the Golkonda fort, yet the Hyderabad fort is the central

feature on the map and the size is exaggerated to more than 4 times that of the Golconda fort.

Although it marks the wall boundary of Hyderabad, the shape and profile are different from what we find on the 1772 map. The wall boundary is marked as a neat and almost symmetrical unlike the shape marked 1772 map (Figure 1, for instance, no curves in the fort wall at the eastern boundary adjacent to the Purani Haveli) as well as on the 1914 Survey of India map of Hyderabad (Figure 3) which are closer to its actual asymmetrical shape. The interior settlements are shown as a four-part grid with Char Minar at the center also marking Mecca Masjid, Char Khaman and the Chowk area. The map label mentions 'Burra Durree' at the northernmost part of the map with Meer Alum's Bazar east of the Purani Haveli. The map shows the 'Meerjimplah Tank just outside the southeast corridor of the fort wall with adjacent bazaars and canals emerging from the tank. This map gives the name of gates and their positions with windows as well (Table.1). However, one of the gates seems to be mistaken to be a khirki as the other gates on the map are marked with double curves and khirkis are marked with a single dot. Point 2 is marked as 'Dubbulpoor' which is Dabeerpura gate, while point 3 is marked as 'Kittiky' for khidki with double curves as for other gates. The names of the gates are consistent with what is found in other sources. The map also shows River Musi and the bridge over it on the northeast part making the way towards Golconda. A total of 17 gates and windows were found in the 1854 map. The names of these 17 gates and windows are Chuddergaut, Dubbulpoor, Kittiky, Yakutpoor, Kittiky, Meerjimplah, Gowlepoor, Laul, Alleabad, Kittiky, Gagubunda, Fettez, Oomdabaur, Phool, Charnal, Chumpa and Dhilly

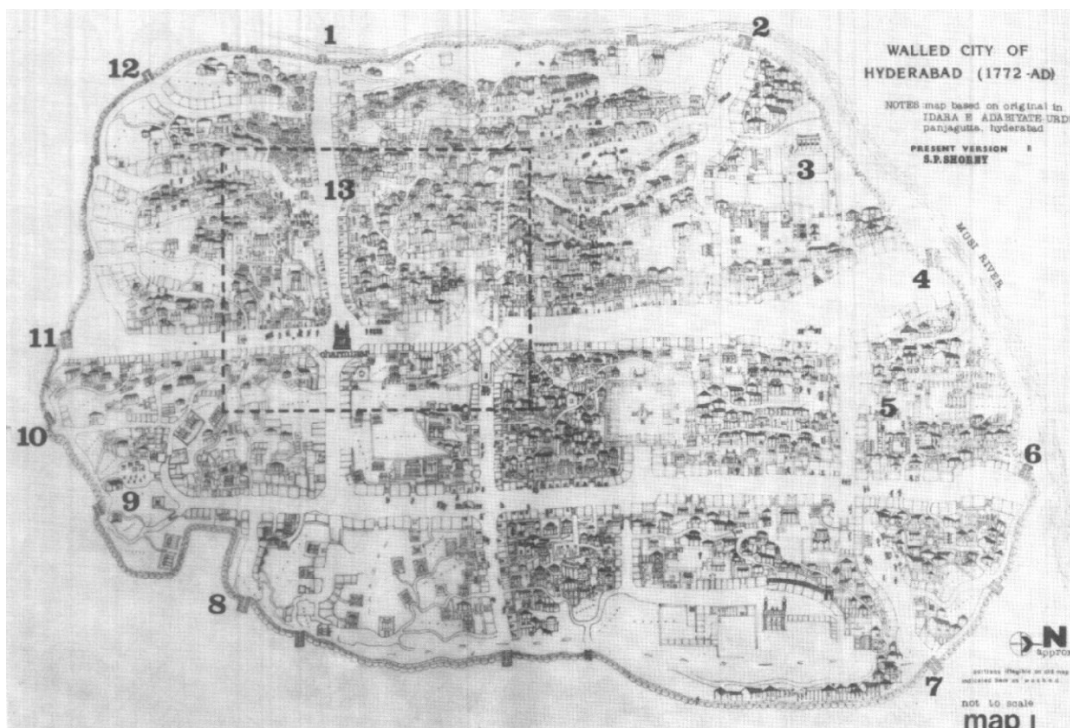


Figure 1. Walled City of Hyderabad (1772)

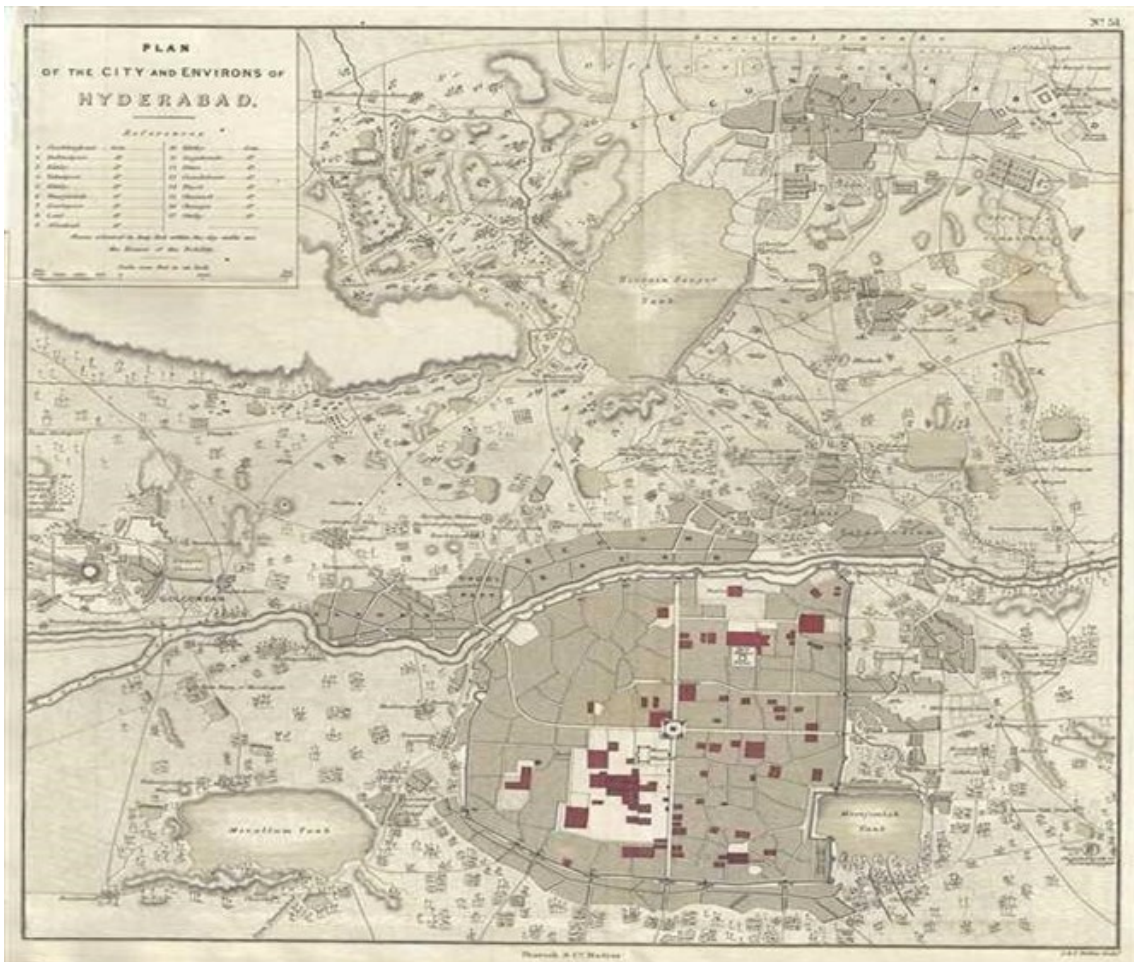


Figure 2. Plan of the City and Environs of Hyderabad; made by Cartographers J.B. Pharoah and J.C. Walkers for Atlas of Southern India, 1854.

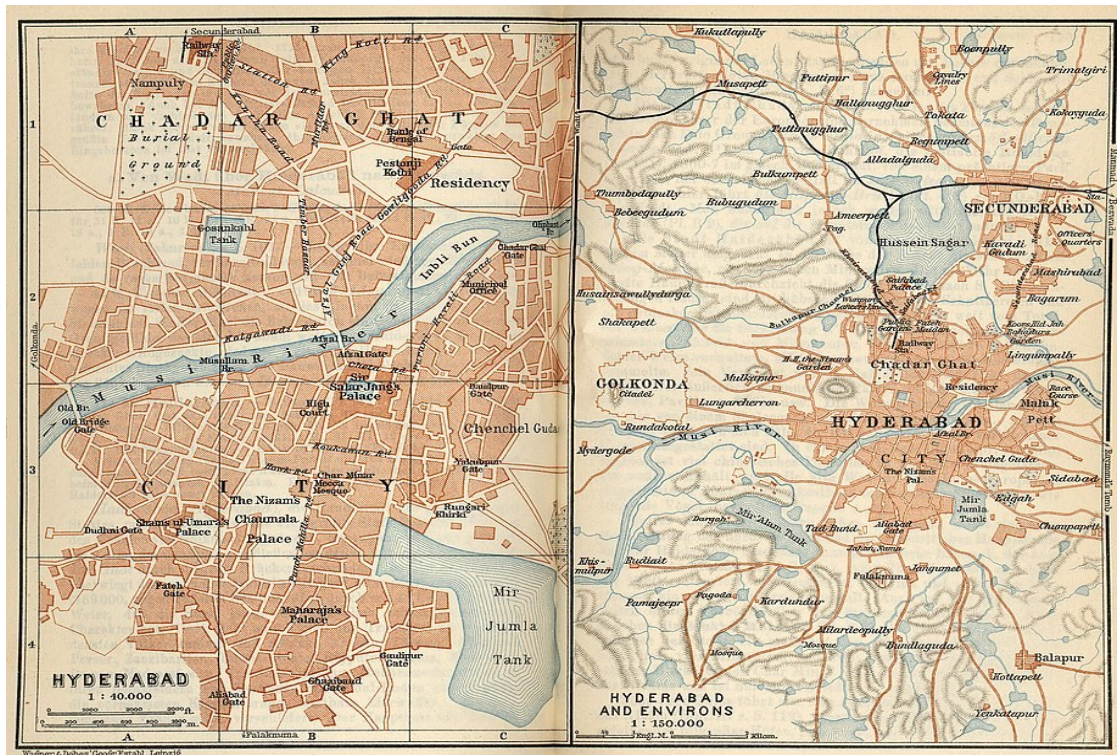


Figure 3. Hyderabad and Environs (1914)

**Table 1. List of gates as mentioned by Bilgrami**

S.no	List of gates	Status
1.	Purana Pul Darwaza	Surviving (State Protected)
2.	Dabeerpura Darwaza	Surviving (State Protected)
3.	Chaderghat Darwaza	Demolished
4.	Yakutpura Darwaza	Demolished
5.	Aliabad Darwaza	Demolished
6.	Champa Darwaza	Demolished
7.	Lal Darwaza	Demolished
8.	Gowlipura Darwaza	Demolished
9.	Fateh Darwaza	Demolished
10.	Doodhbowli Darwaza	Demolished
11.	Dilli Darwaza	Demolished
12.	Mir Jumla Darwaza	Demolished
13	Afzal Darwaza	Demolished

### 3.3. 1914 Hyderabad map

The map (Figure 3) gives a clear demarcation of the fort wall. This map is georeferenced to identify the exact extent and layout of the fort wall. A major chunk of the north fort was destroyed by the Musi River flood in 1908, yet this map shows the boundary wall of the north portion also. There are two additions (two bridges) in the connectivity of the city with the other side of the River Musi: Mussallam Bridge and Afzal Bridge.

### 4. Geospatial analysis and field survey

The Google earth imagery of the fort (Figure 4) is compared with Corona satellite image of 1979 (Figure 5). The comparison shows that adjacent to river Musi, there was a part of the fort that existed in 1979, whereas the same area in Google Earth shows localized development leading to encroachment of the fort as well as a thick growth of vegetation. Our field survey in 2021 showed that there are only ruins of the fort in that area. There are other areas that show that urbanization has led to a loss of fort extent. The image also shows that the Mir Jumla tank was composed of agricultural parcels in 1979, hence urbanization has happened subsequently. The image shows a palaeochannel surrounding the south of the fort connecting Mir Jumla tank in the east to the point in the west where drainage from Mir Alam enters the river; this channel may have also served as a moat as an extra line of defense for the new

capital. A paleochannel that drains water from Saroornagar Lake to the river is also identified. Figure 6 is an FCC (False color composition) Multispectral image (IRS-P6-LIS4) dated December 2008. It also shows that Mir Jumla tank had natural drainage toward the river Musi, while two other lakes; (Mir Alam and Saroornagar lake built in 1806 and 1624, respectively) also have natural drainage channels suggesting the role of such tanks in the development of Hyderabad. Such distinction can also be seen in IRS-1D-LIS3 dated November 2002. Figure 7 Shows a digital elevation model of the landscape of the fort and its environs (Cartosat 10m DEM from <https://bhoonidhi.nrsc.gov.in/bhoonidhi/>). This was generated to study the landform on which the fort was built. The fort was on the south of the river Musi, the northern boundary of which spreads between two streams that enter the river, therefore the fort was wedged in between these two streams. The elevation also shows that a strategic location surrounded by a river in the north, two drains in the east and west, and an elevated area in the south was selected for laying out the new city of Hyderabad. It also shows that the Mir Jumla tank was created by building a bund capturing the drainage from the higher elevation in the south towards the river in the north. A slight elevation of the bund is also detectable in the DEM. The drainage channel coming from Mir Jumla Tank to Musi River can be traced in the elevation profile north of the tank, which is also marked in the Pharaoh Map of Hyderabad, 1854.

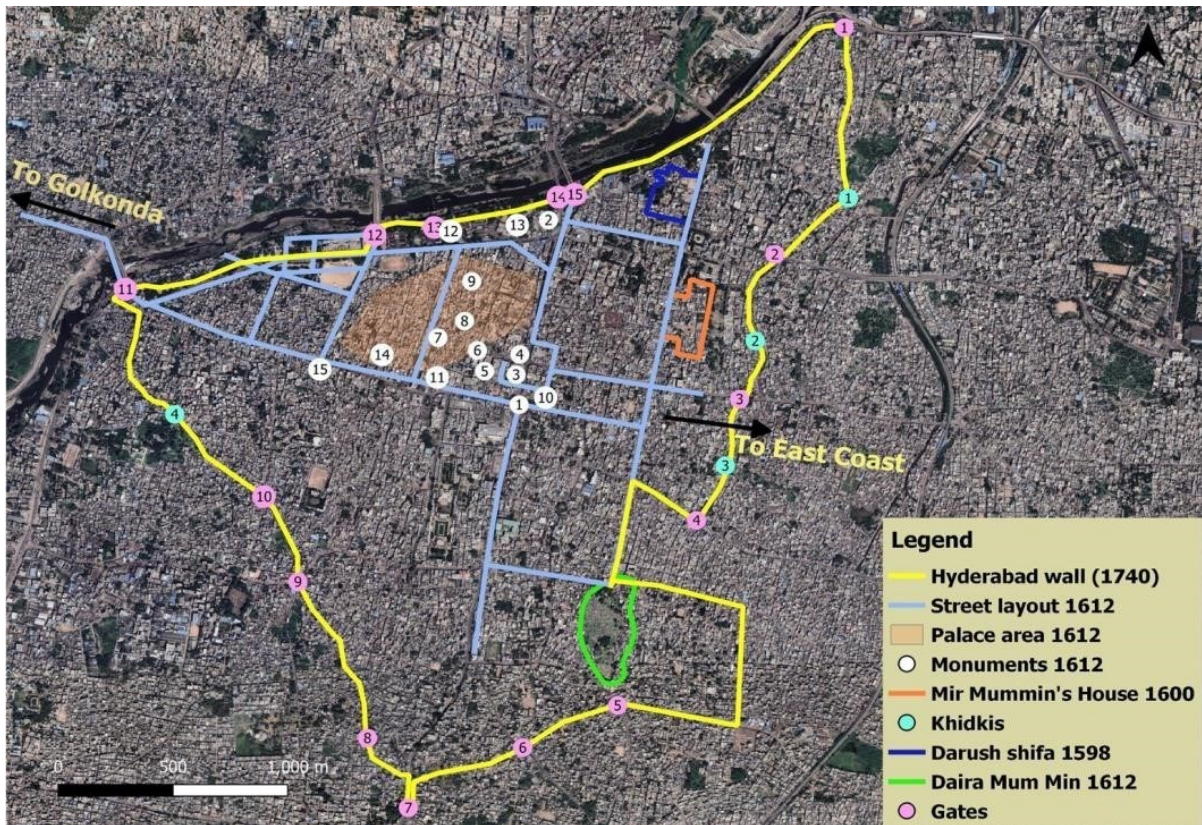


Figure 4. Historical features of fortified Hyderabad georeferenced and presented on Google Earth imagery

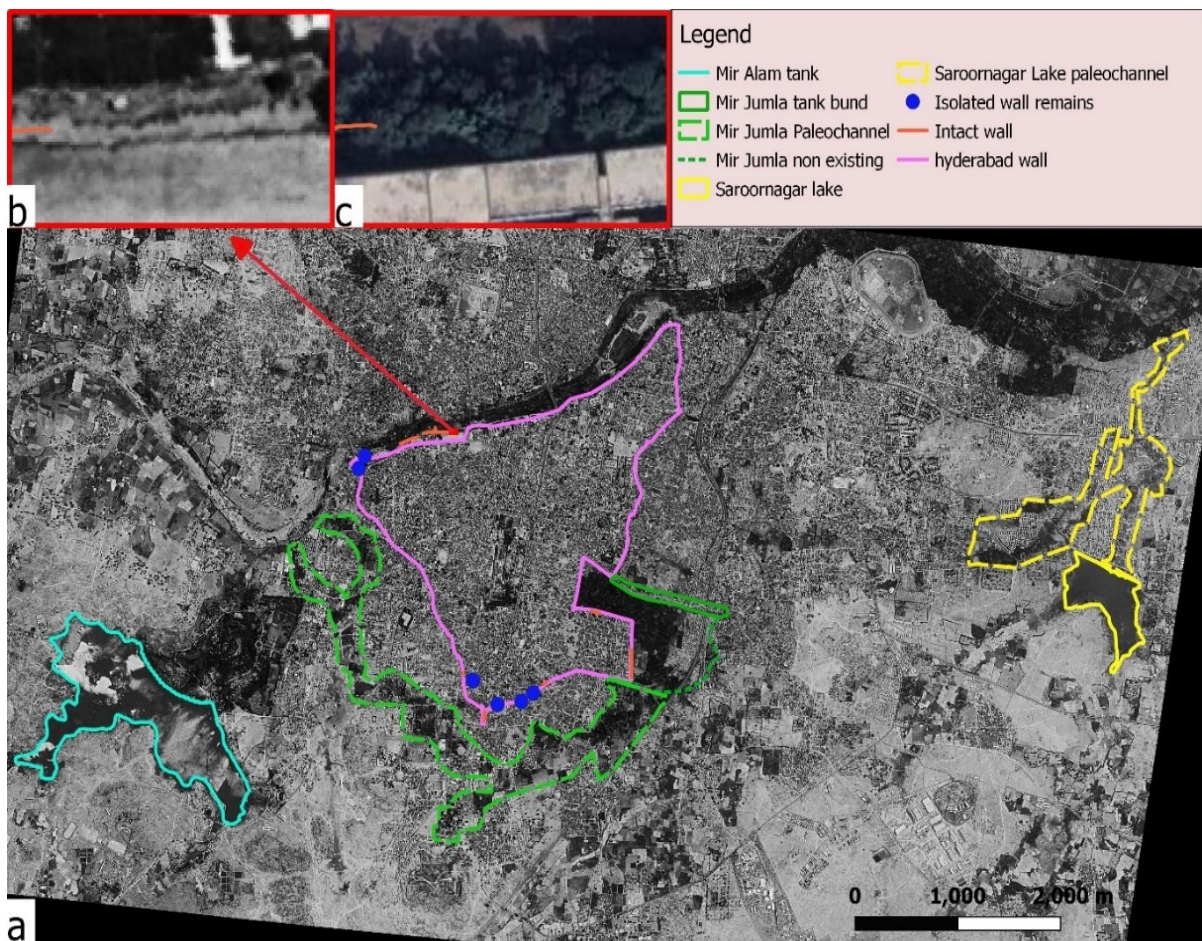


Figure 5. Change in landscape seen through Corona satellite image (1979/05/08): a) Corona satellite image of Hyderabad; b) remains of fort in 1979; c) Broken and encroached wall (of same area as in b) in Google Earth.

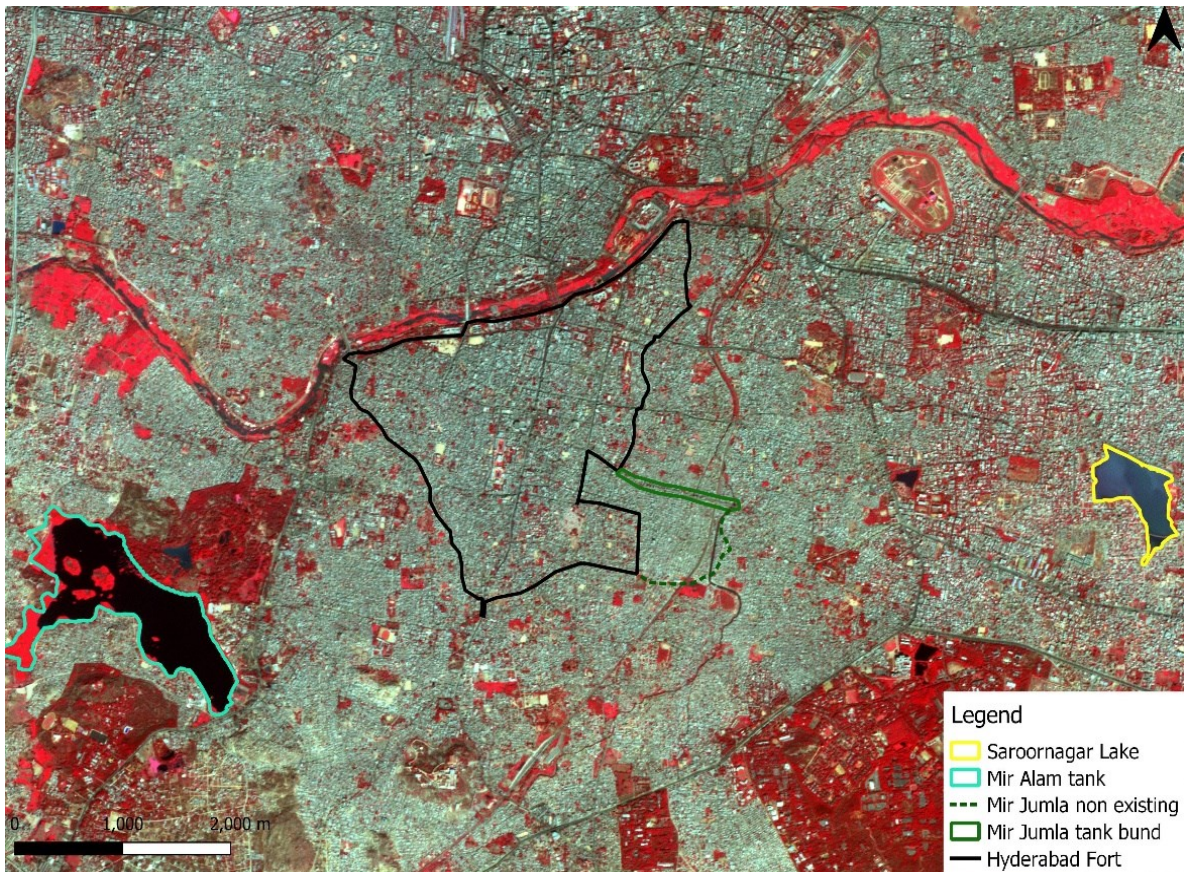


Figure 6. False Color Composite (FCC) from the Multispectral image (IRS P6/LISS IV) dated December, 2008 showing the extent of Hyderabad

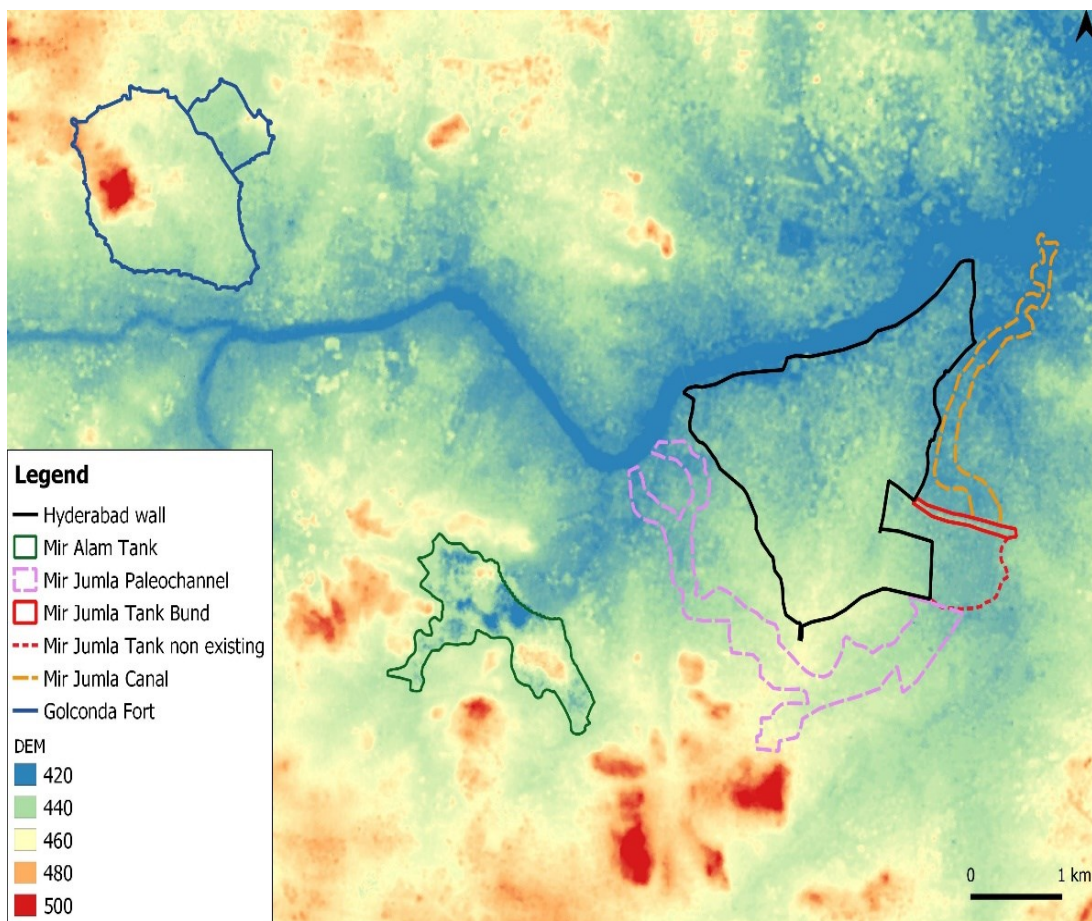


Figure 7. Terrain comparison of Golconda Fort and Hyderabad

It is used to draw a comparison between the terrain in the vicinity of Golconda Fort and Hyderabad Fort. The landscape of Hyderabad provided several advantages: proximity to the river, drainage, and water supply, and well-protected strategic location. These formed a perfect blend of multiple elements to shift the capital to this new location.

Map of 1914 was used to georeference the Hyderabad Fort in order to identify the present locations of the wall. As the perimeter of the fort covers an approximate length of 12 km, it covers grounds where rampant urbanization can be observed which have impacted the heritage value of the fort (Figure 8). Following the georeferenced locations of the fort, the Northern stretch of the fort can be seen going adjacent to the River Musi from Muslim Jung Bridge to Chaderghat road. On ground construction of this wall looks very different compared to other remnants of the fort as it appears relatively recent, therefore it can be deduced that this portion was rebuilt after the Musi flood of 1908. The entire fort portion along the river is intact and adds to the cultural value of the city. As we go clockwise the next noticeable remnant of the wall is found at the southeast part of the fort near Daira Mun Mumin. Almost one kilometre stretch of the fort is present in the underdeveloped dwelling of Gowlipura. The wall is used as part of houses in a few cases, whereas some portions of

the wall stand intact with minimum disturbances (Figure 9). Going further south, the wall continues with scattered smaller remains at Sardar Patel Road, and often become part of many houses. One of the prominent bastions of the wall remains adjacent to a residential complex (Figure 10 (D)). Moving further south towards Aliabad, a notable stretch of approx. 90 meters of wall length is found just near the main market. Aliabad market shops are reused spaces, which originally were parts of entry of the forts or archways having 12-15 ft. width. These were khidkis and major entry points for the cavalry.

There are no parts of the wall as we go further from southwest towards north as built up residential spaces have left no marks of the old city wall. Between Purana Pul and Muslim Jung Pul, in the north of the fort near the ghat area, a major chunk of the wall remains are still present. These remains are reused by the inhabitants, mostly unaware of the structure's historical significance. The wall covers compounds of the Police Transportation Organisation and Modern Government Maternity Hospital as well. The identifiable length of the wall remains in different forms such as completely intact, broken, and renovated, adding up to 3-3.5 km which amounts to a lot of urban heritage space given that Hyderabad is one of the major cities of the country.

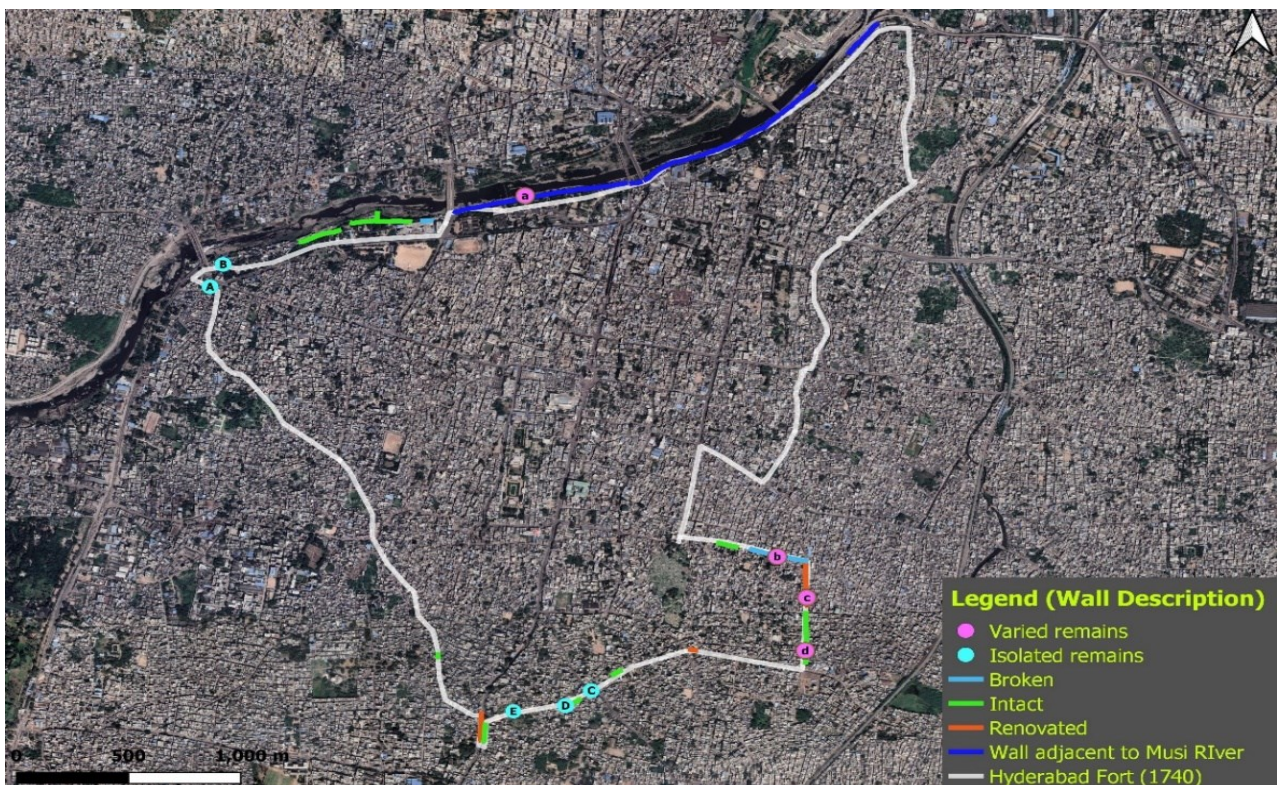


Figure 8. Documented field survey of Hyderabad Fort of 1740



Figure 9. Varied wall remains a) Wall adjacent to Musi River b) Renovated c) Broken and renovated d) Intact



Figure 10. Isolated wall remains in different parts of Hyderabad. (A) Deteriorated portion inside a warehouse. (B) Fort found at the back of a residential quarter (C) Broken wall leading to a main road intersection (D) Intact bastion, part of wall. (E) Part of wall going through a cemetery

**4. Conclusions**

The three maps that have been compared here show the different approaches of map making with varying accuracies. The information obtained from these maps and spatial analysis by georeferencing them gives a clear idea as to where the erstwhile fort wall lay. Geospatial analyses using Corona Satellite imagery, IRS-LIS IV and DEM shows the importance of the landscape for which the new capital of the State of Hyderabad was selected. It also

shows a depiction of tanks that were associated with the construction of the new fort area in Hyderabad.

The present record says that the remaining part of the fort wall was brought down post-independence for development due to the growing population, undermining the importance of this centuries-old structure. The field survey conducted in the present study documents the remaining portions of the fort in accordance with its remaining features. It follows the common scenario of least developed areas having the most prominent remnants

of the fort, thereby suggesting that infrastructural development and urbanization have caused a great deal of damage to this heritage structure. The finding of features such as bastion in a residential space with no protection either by the state department or the ASI shows the gap in the protection measures taken for heritage structures. Since at present the remnants are not in one stretch but in scattered bits in a dense urban setting, it would be challenging to create a heritage management plan based only on the protection status of the scattered physical remains. However, the evidence on the ground suggests that the identification and recognition of these heritage spaces can foster a sustainable form of urban planning and development.

### **Acknowledgments**

The research reported in this paper was conducted as part of a project funded by the Indian Space Research Organization, Department of Space, Government of India, under RESPOND Scheme. The authors thank ISRO for the same. The authors also thank Shubhi Mishra, Project

Associate in the project for her contributions to the field survey

### **References**

- Bilgrami and A. S. Syed. (1992) Landmarks of the Deccan. Hyderabad-Deccan, 1927, p. 94 6 Ibid. pp. 95 Ibid. pp. 95
- Jadunath S. (1963). Hyderabad and Golkonda in 1750 as seen through the French Eyes. Islamic Culture. pp.234-47 (p.239)
- Nayeem M. A. (1987) The Splendour of Hyderabad. Bombay, p. 76
- Shorey S. P., (1983) "Eighteenth Century Hyderabad: Anatomy of an Old Map." In Environmental Design: Journal of the Islamic Environmental Design Research Centre 1-2, edited by Attilo Petruccioli, 180-85. Rome: Dell'oca Editore,
- Sherwan, H. K. (1967) Muhammad-Quli Qutb Shah Founder of Hyderabad. London, p. 14

# Monitoring Road maintenance using video-geotagging in geographical information system: an innovative approach

Ajay Mathur\*, Nishant Tiwari, Vipin Kumar and Brijendra Pateriya  
Punjab Remote Sensing Center, Ludhiana, India  
\*Email: [mathurajay12@gmail.com](mailto:mathurajay12@gmail.com)

(Received: Dec 28, 2021; in final form: Sep 15, 2022)

**Abstract:** Maintenance of roads is a key concern for smooth flow of traffic and goods for any economy to thrive. The maintenance part has been limited in GIS to information collected through ground-based surveys, GPS location of affected road area, uploading geo-tagged photos shared by public through mobile app on GIS data. The present work focuses on one such innovative approach using geo-tagging of videos of road surface with Road layer in GIS. Stretches of road in and around Ludhiana city of Punjab to reflect different scenarios such as roads located in open village area, highways, and broad and congested city roads have been used for understanding condition of surface of road in a contiguous fashion.

**Keywords:** GIS, Video Geotagging, Infrastructure, Road Maintenance

## 1. Introduction

Transportation System is the key to economic growth of any country. India is no exception and is constructing roads at a record speed 37 km/day to cater to its industrial and socio-economic development. In general, the developed countries are spanned by a very dense transport network, which has driven their economies example abounds such as USA, UK, and China.

GIS has been extensively used in conjunction with remote sensing data such as satellite images and drone data for optimal route planning (Mondal et. al., 2021) design processes, store survey details based on GPS data, field survey, satellite images, monitoring the construction and operational issues (Yunus & Hassan, 2010). In general, road alignment has been mapped in GIS using remote sensing data as base layer generally in all GIS based projects. However, a critical component related to maintenance of the roads has not found many GIS driven applications.

Maintenance of roads is a key concern for smooth flow of traffic and goods for any economy to thrive. The maintenance part has been limited in GIS to information collected through ground-based surveys, GPS location of affected road area, uploading geotagged photos shared by public through mobile app on GIS data or using bump integrator (Dattani et. al., 2018) to check for the unevenness of the roads. Dedicated vehicles equipped with high definition cameras and laser scanners can also be used but the limitation of these vehicles is the high cost of purchase/make and high operating cost (Radopoulou et. al. 2016; Werro, 2013). Other methods for monitoring road condition and road maintenance includes using Laser based system (LiDAR, Mobile Laser Scanning (MLS)) (Li et. al. 2020) but these are too complex, costly and are prone to various errors. AI and machine learning has proven to be quite useful in identifying the road condition but most of these algorithm focus on 2D images (Radopoulou and Brilakis 2015; Jog et. al. 2012; Tsai et. al. 2009; Battiato et al. 2006) and might not be able to give proper road condition. Some AI and ML techniques do focus on videos (Koch et. al. 2012) however, they do not contain the telemetry and geolocation data which are important for

road condition assessment. Moreover, some method using AI and ML on phone sensor data (Basavaraju et. al. 2020) but it depends on vehicle moving directly over the damages across the roads.

Gleave (2014) mentioned the effects of untimely maintenance of roads on environment such as increased CO<sub>2</sub> emissions, fuel consumption, and pollution from difficult rehabilitation works, other impacts can be seen in the increased maintenance cost of the road, increased vehicle operating cost, even including less safety and adverse health impacts. Light vehicles (mostly private users) see 34% increase in fuel consumption, while 12% fuel increase is noted in heavy vehicles, furthermore poor road condition can increase maintenance cost for heavy and light vehicles by 129% and 185% respectively (Chatterjee et. al. 2018, Gleave 2014). This brings out the urgency of maintenance of road and the approach in the present work helps in monitoring the condition of the road and in verifying if the said road has been repaired or not after maintenance work has been carried and thus, brings in the transparency factor.

Accurate, timely and cost-effective information about road condition is a key for repair and maintenance of road infrastructure (Nodrat et. al., 2018). The present paper focuses on one such innovative approach using geotagging of videos of road surface with Road layer in GIS with a case study devoted to a small stretch of Ludhiana city in Punjab. Geotagging is the process of adding geographical identification metadata to various media such as a photograph or video and is a form of geospatial metadata (Luo et. al., 2011).

## 2. Objectives

One of the concerns of the govt. is to bring transparency in maintenance of road and also to aid the engineers involved in identifying the stretches of road which needs to be fixed.

The above twin objectives can be met very efficiently by making use of geotagged videos of road surface (videos of road surface linked with location of road on Earth) which provides details of road condition in a contiguous fashion

unlike geotagged photos, which are linked only to a particular point in the long stretch of the road.

The geotagged videos provides information of inventory of road surface in a visual format along with date and time – a big evidence of road surface condition unlike the current trend of paper record which may be prepared for vested interest. Likewise, geotagged videos of road surface condition after said repairs would be evidence enough if the road has been repaired or not. Thus, the objectives of the present work are:

- Make use of Geo-Tagged Videos showing road condition in conjunction with GIS road layer or on top of satellite image in GIS.
- Make database of status of road condition before and after repairs for inventory of repair works.
- Make use of free ware/open-source software for limiting expenses for database generation.

### 3. Study area

Stretches of road in and around Ludhiana city of Punjab to reflect different scenarios such as roads located in open village area, highway, broad and congested roads in the city.

### 4. Methodology

The work involves (Figure 1) taking videos of road surface in a vehicle along with GPS readings. The GPS readings can be taken using a GPS device or equally accurate available mobile apps now-a-days such as GPS tracker, Avenza or many other apps which can be downloaded free of cost on any smartphone generally available with public. This in turn saves on finances for procuring any GPS device. The videos can also be taken through another mobile rather than investing in acquiring costly video camera. Both video and GPS activity should begin at the same time for proper geotagging as common thing to marry both datasets (video and GPS readings) called as video geotagging is the time.

Video geotagging in general sense is the video having location data in its metadata, but in the present work it has been utilized to next level where each frame is associated with location data (taken from GPS track). Since, the location data cannot be put into metadata, therefore, another file format can be created (as UAV tracker of QGIS). For this type of geotagging, it is imperative that the video length and GPS track length (in terms of time) are equal. Speed of vehicle plays an important role in assessing road condition as the general mobile camera can only capture videos at 60 frames per second (FPS), moving too fast would result in some smaller potholes to be missed or video to be blurry. Therefore, the vehicle speed should be kept around 40Kmph (11.11mps, meaning 60 frames are assigned for 11meters), or slower. For present study, the camera settings were 1080p at 60 FPS, with 48MP resolution (mobile camera). GPS track points were taken at every second. Once, the data (video and GPS tracks) are synchronized, the frame at the beginning of the video will have the first GPS coordinate and after video runs for a

second, the second GPS coordinate is assigned and so on resulting in geotagged video.

The twin data of video focused on road surface and its accompanying GPS coordinates can be geotagged in Commercial of the shelf (COTS) software or using free and open source software such as QGIS. However, in the present work video UAV tracker of QGIS, a free option was exercised. Thus, expenses are generally limited to vehicle and manual cost.

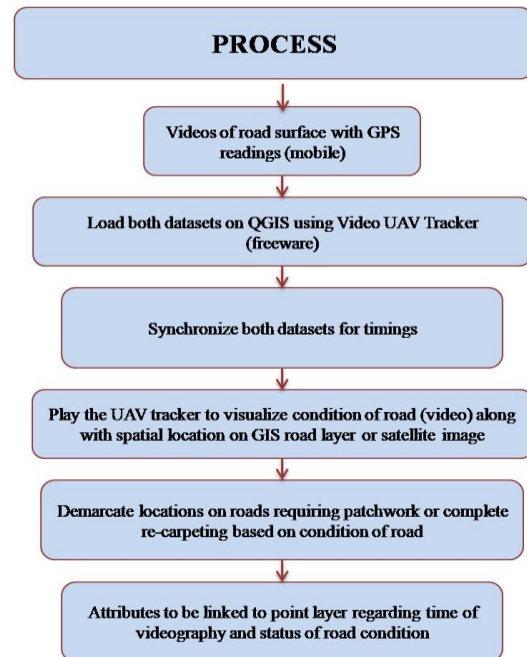


Figure 1. Methodology Flowchart

The workflow (Figure 1) involves loading video and corresponding GPS file in the video UAV tracker of QGIS with GIS vector file of roads if available otherwise Web Map Services available free of cost can be called in the background in QGIS requiring only internet connection, a facility available under “Base Map” option of QGIS. At times, the road layer generated may not be accurate or updated but satellite image would be accurate in terms of geolocation and updated as well. Thus, satellite image available free of cost may be the proper choice.

Both video and GPS must be synchronized in the module. Once synchronized GPS track layer is made available with a pointer. The pointer moves on road GIS layer or georeferenced satellite image in sync with video of the same location on the road. The GIS analyst can then run the video with the pointer highlighting the location of the road. The GIS analyst can infer from video the type of maintenance required (patchwork or complete road to be carpeted) based on condition of road surface made apparent from video. Based on observation of the video geotagged, GIS analyst can demarcate on the GIS layer, the condition of road and suggest the type of maintenance required, such as patchwork or complete road carpeting. The Video part also gives the date and time of acquisition which can be added as attribute at the specified locations where road requires maintenance. If road is repaired, details of repair carried can also be part of attributes giving

complete information of road maintenance which can come handy in future maintenance work also.

**5. Results and discussions**

**5.1 Scenario: Urban road (pre-repair)**

The video clip (Figure 2) taken on an urban road in Ludhiana on 06 October 2021 shows that there are broken patches.

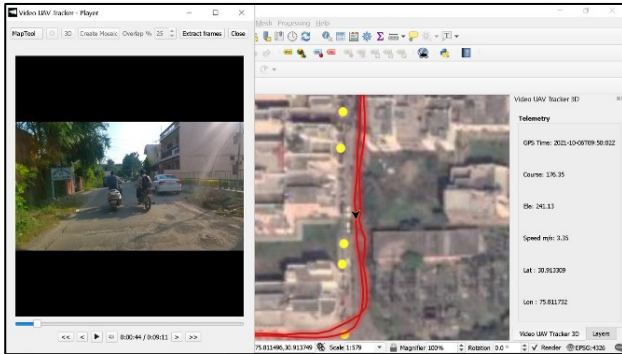


**Figure 2. Urban Road (Pre-Repair)**

The red line is the GPS track, which helps to relate location of Earth with video of road surface.



**Figure 3. Locations of potholes in Urban Road**

On closer inspection, Figure 3 shows the locations of the potholes that were identified using video geotagging. Over 20 potholes as highlighted by yellow points in Figure 3 with extreme damages were identified on less than 500m length of road as such complete carpeting of road is suggested over patchwork

**5.2 Scenario: Urban road (post-repair)**

The video clip (Figure 4) taken on 09 December 2021 shows that the road as shown in Figure 2 has been repaired.

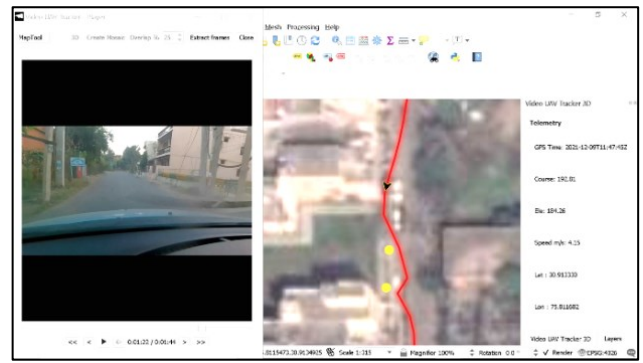


**Figure 4. Urban Road (Post-Repair)**

The red line is the GPS track helps to relate location of Earth with video of road surface. Thus, the process helps to understand condition of road at various times, before and after repair.

Figure 5 shows that the whole stretch of road has been carpeted; the damage of road visible in Figure 3 has been fixed. In addition, the telemetry data (Figure 4) reflects date and time of video acquisition and helps in verifying if the road has been repaired or not as on date thus providing transparency to the work.



**Figure 5. Location of Potholes and road condition after repairs (complete carpeting)**

**5.3 Scenario: Village road**

The video clip (Figure 6) taken on 07 December 2021 of a village road which is exposed to sky and therefore, GPS readings are accurate as the red line in Figure 4 showing GPS track is almost straight and located on road itself.

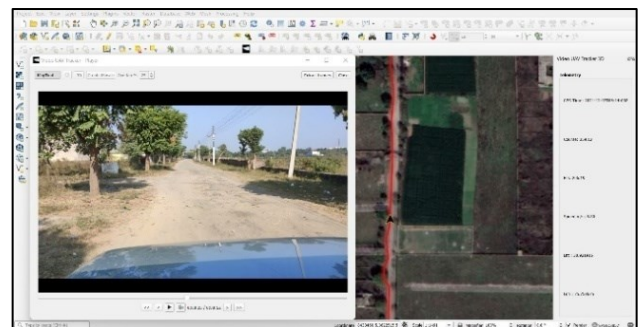


**Figure 6. Village Road**

The road connecting the village to the highway/city was remarkably well maintained however, once inside the village it was clear that the road condition was not up to the mark.

In the 500m (village road) stretch undertaken in the study 90m road required complete carpeting, and in 120m 4 major potholes were present. The two points labeled ‘5’ and ‘6’ in Figure 7 shows the extent up to which carpeting is required



Figure 7. Location of potholes on Village Roads

5.4 Scenario: State highway

The video clip (Figure 8) taken on 07 December 2021 of state highway called as Humbran road in Ludhiana which is broad and therefore, exposed to sky results in accurate GPS readings as the red line (GPS track) in Figure 8 is straight representing GPS track is almost straight and located on road itself. The video snap of road surface shows a very smooth road surface devoid of any potholes and, therefore, needs no repair.

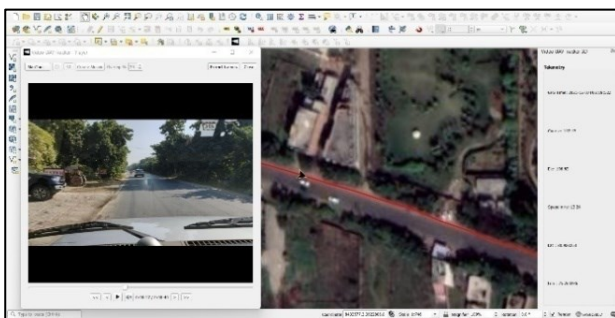


Figure 8. State Highway

5.5 Scenario: Urban Road (Congested)

The video clip (Figure 9) taken on 03 December 2021 a very congested part of Ludhiana city and therefore, not very exposed to sky results in inaccurate GPS readings as the red line (GPS track) in Figure 9 is not located on the road but crosses over the nearby buildings and therefore, would be difficult to relate video (ground condition of road surface from video) with location on ground as GPS track is in error. Thus, in congested areas such methodology may not work efficiently as getting accurate GPS readings may not be possible. However, Figure 10, a zoomed version of the road surface highlighted in Figure 9 with some

intelligence can aid to interpret various stretches of road which shows mixed road surface conditions such as pot holes around point 1,2,3 and 4 which needs patchwork but around pt 0, there is continuous distressed road and needs complete carpeting.

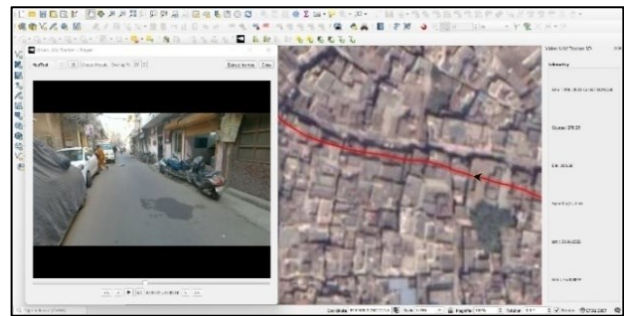


Figure 9. Urban Road (Congested)



Figure 10. Location of potholes in Urban Congested Road

6. Conclusions

It can be concluded from the work that the condition of the road can be had in a contiguous fashion using videos, which can be geotagged with GIS road layer, or georeferenced satellite image for quick assessment of road surface to help relevant authorities plan for repair work as needed. In addition, the process is economical, based on free and open source GIS software, free GPS apps and mobile for videos over costly video cameras. Limitations of the technique may be due to ground conditions such as flooding, traffic jams, or public unrest, which may not permit the vehicle mounted with cameras to record videos, and other limitations may be due to weather problems, or high electrical/magnetic disturbances affecting the functioning of GPS. In addition, the approach can be used where roads are broad and GPS readings can be obtained accurately. The work is likely to bring transparency and help many departments.

The present work gives a visual technique for understanding road conditions by geotagging videos of roads with corresponding road GIS layers. However, to aid the various officials involved in maintenance of road, in interpreting the road conditions such as potholes or completely distressed road, AI classification techniques should be tried in future to classify the video to highlight

potholes or distressed parts of the road. This will not only help in automation and fast work, but it might also help in creation of a decentralized system which can provide road condition over regular period using public/private vehicles, which will further cut down costs and increase transparency significantly.

## References

- Basavaraju A., J. Du, F. Zhou and J. Ji (2020). A Machine Learning Approach to Road Surface Anomaly Assessment Using Smartphone Sensors. *IEEE Sensors Journal*, 20(5), pp. 2635-2647.
- Battiato S., S. Cafiso, G. A. Di, L. Rizzo and F. Stanco (2006). Pavement Surface Distress by Using Non-linear Image Analysis Techniques. *Communications to SIMAI Congress*. 1. 1-9.
- Chatterjee S., P. Saeed, S. Tofangchi and L. M. Kolbe (2018). Intelligent Road Maintenance: A Machine Learning Approach For Surface Defect Detection. *Twenty-Sixth European Conference on Information Systems (ECIS2018)*, Portsmouth, UK, 2018
- Dattani D., M. Vala, D. Sondarva and Y. Dasani (2018). Determination of Pavement Bump-Integrator: State-of-the-Art- Review. *International Journal of Advance Research And Innovative Ideas in Education*, 1, pp. 411-415.
- Gleave S. D. (2014). EU Road Surfaces: Economic and Safety Impact of the lack of Regular Road Maintenance-Study. Report- Policy Department Structural and Cohesion Policies. European Parliament.
- Jog G. M., C. Koch, M. Golparvar-Fard and I. Brilakis (2012). Pothole Properties Measurement through Visual 2D Recognition and 3D Reconstruction. *Computing in Civil Engineering* (2012), pp. 553-560.
- Koch C., G. M. Jog and I. Brilakis (2012). Automated Pothole Distress Assessment Using Asphalt Pavement Video Data. *Journal of Computing in Civil Engineering*, 27(4), pp. 370-378.
- Li W., M. Burrow, N. Metje and G. Ghataora (2020). Automatic Road Survey by Using Vehicle Mounted Laser for Road Asset Management. *IEEE Access*, 8, pp. 94643-94653.
- Luo J., D. Joshi, J. Yu and A. Gallagher (2011). Geotagging in multimedia and computer vision-a survey. *Multimedia Tools and Applications*, 51(1), pp. 187-211.
- Mondal M. S., R. D. Garg, V. Pandey and M. Kappas (2021). Route alignment planning for a new highway between two cities using Geoinformatics techniques. *Egyptian Journal of Remote Sensing and Space Science*.
- Nodrat F. and D. Kang (2018). Prioritizing road maintenance activities using GIS platform and Vb.net. *International Journal of Advanced Computer Science and Applications*, 9(2), pp. 34-41.
- Radopoulou S., I. Brilakis, and C. Koch (2016). A Framework for Automated Condition Monitoring. *Proceedings of Construction Research Progress*. Puerto Rico: San Juan.
- Radopoulou S. and I. Brilakis. (2015). Patch detection for pavement assessment. *Automation in Construction*, 53, pp. 95-104.
- Tsai Y.C., V. Kaul and R. M. Mersereau (2009). Critical assessment of pavement distress segmentation methods. *Journal of Transportation Engineering*, 136(1), pp. 11-19.
- Werro P. (2013). "SCANNER surveys."
- Yunus M. and H. Hassan (2010). Managing Road Maintenance Using Geographic Information System Application. *Journal of Geographic Information System*, 02(04), pp. 215-218

# Paleo-topographic Reconstruction of Cultural Landscapes using Remote Sensing and GIS: A case study of the ancient port of Tamralipti

Arya S Pradeep and M B Rajani  
National Institute of Advanced Studies, Bengaluru  
\*Email: [aryap@nias.res.in](mailto:aryap@nias.res.in)

(Received: Dec 29, 2021; in final form Sep 13, 2022)

**Abstract:** Human interaction with the landscape they inhabit leaves imprints that are largely inconspicuous on the ground. Yet, these remain the most thought provoking among the sets of clues available to us in fuelling the quest to understand our past. Spatial view provided by satellite imagery plays a pivotal part in enabling us to identify these imprints in the form of patterns. In this study, a paleo-environmental reconstruction of a particular cultural landscape using geo-spatial tools has been attempted. A range of historical documents (textual records such as traveller's accounts dating to 5<sup>th</sup> and 7<sup>th</sup> centuries CE, maps of the Indian sub-continent published in the 18<sup>th</sup> and 19<sup>th</sup> centuries) and satellite imagery of the last 50 years (CORONA, Google Earth Digital Globe ) are used to identify and analyse the distribution of cultural sites that are hitherto unexplored to understand the impact of past changes to the landscape of these ancient sites located along one of the most dynamic regions of the Indian subcontinent: the Gangetic Delta. The identification of numerous sites of a distinct pattern and their distribution, analysed along with the morphological signature of the landscape on which they remain almost undetected has led to certain inferences on the possible location and extents of the ancient port of Tamralipti. The study also reveals the coastal and deltaic changes in the vicinity of the ancient port.

**Keywords:** Geo-spatial analysis of Cultural Landscapes, Gangetic Delta, Tamralipti, Google Earth imagery, CORONA imagery.

## 1. Introduction

The delta of the Gangetic river system, where the river and its distributaries debouch into the Bay of Bengal is particularly interesting in a number of ways. Apart from being home to one of world's most intense ecosystems and largest fertile agrarian landscapes, it bears vestiges of an ancient legacy that is veiled in mysteries of a dynamic landscape and fleeting narratives of a bygone past.

According to archaeological and literary sources, Tamralipta/Tamralipti (henceforth, Tamralipti) is believed to have existed between 3<sup>rd</sup> century BCE and 8<sup>th</sup> century CE. The port of Tamralipti served as a major centre for the exchange of commerce and culture. Apart from maritime ties, Tamralipti was well-connected with major inland towns such as Pataliputra (currently identified with Patna). Based on the records left by visiting Chinese monks in the 5<sup>th</sup> and 7<sup>th</sup> centuries CE, it was also a major centre for learning, with strong links to Buddhism. Its significance as a major point of disembarkation on the East Indian coast linking the subcontinent to China, Ceylon and the South East Asia would have attracted a strong current of people and ideas from far and near making the region a melting pot for cultural exchanges.

The present study focuses on areas within the southern region of the Indian state of West Bengal and borderlands of Odisha to look for possible locations for the ancient port of Tamralipti. Although the larger historical, geo-political context would have been under the influence of this site and may have encompassed an even larger extent including parts of Bangladesh.

## 2. The Objective

The main objective of the paper is to explore the region with geospatial data and analysis to identify and locate the

ancient port of Tamralipti and its probable geo-political extents by correlating descriptions of it in historical literature and cartographic records along with archaeological and geomorphological signatures visible in satellite imagery.

## 3. The Methodology

### 3.1 Study of ancient literature

The study began with the analysis of the descriptions left by Chinese monks such as Faxian (5<sup>th</sup> century CE) and Xuanzang (7<sup>th</sup> century CE) of the ancient port town of Tamralipti. Based on excavations in the past decades, the city of Tamluk has been identified with this ancient port.

### 3.2 Analysis of satellite imagery for features suggestive of past settlements

The book *Patterns in Past Settlements: Geospatial Analysis of Imprints of Cultural Heritage on Landscapes* (Rajani, 2021) discusses how satellite imagery reveals clues of past occupations on particular landscapes. For identifying geomorphological features such as paleochannels and coastal strandlines (past coastlines) coarser resolution imagery offers better visibility in contrast to cases where one is looking for buried remains of built features which require higher resolution imagery. These are visible as cropmarks exhibited through a distinct variation of ground surface vegetation tone and texture (Rajani 2021). These are also highly dependent on the season during which the imagery was captured by the satellite.

Analysis of Google Earth imagery in the vicinity of the excavated sites revealed sites that followed a particular arrangement of square shaped concentric enclosures resembling forts and moats, predominantly aligned along cardinal directions. Most of them remain largely

inconspicuous following subsequent land cover developments, both anthropogenic and otherwise.

### 3.3 Study of historical maps and records and location of historical sites

Identification of numerous sites of a particular layout led us to study historical maps of the region and it was found that maps prepared and published in the 18<sup>th</sup> and 19<sup>th</sup> centuries by British cartographers such as James Rennell and Aaron Arrowsmith marked several sites in the region as forts.

Attempts were made to identify these sites (mostly spelt using old British names in the aforementioned maps) based on the closeness in the names provided in these maps and current place names along with their geographic location and with reference to other physiographic features. Subsequently, Google Earth imagery and CORONA satellite imagery was analysed and we observed the same concentric arrangements (both square and rectangular) in the vicinity of the identified locations, some intact, others altered to varying degrees of transformation. This has been elucidated in the respective section later in this paper.

### 3.4 Linking the distribution of sites and the geomorphological signature of the study region

Finally, these sites were plotted and analysed against the geographical character and physiography of the region to derive certain conclusions about the possible location and extents of the ancient port of Tamralipti.

This involved identifying the geographic coordinates of the sites from multiple sources (such as place descriptions in historical records, web portal of protected monuments and sites at both national and state levels) and plotted on Google Earth. These points were then transferred as vector data to Q-GIS to be analysed with multiple imagery such as CORONA, DEM etc.

Further, the pattern of site distribution was analysed with respect to the geographic arrangement (such as proximity to active or paleo water features, ancient shorelines, site elevation etc.). Based on this, inferences were formulated. This has been explained further in the section on Observation and Inferences. The following flow chart (Figure 1) elucidates the methodology.

## 4. Results and discussions

The geographic arrangement of the region has a unique composition. It is edged by the Bay of Bengal to the south, the east is bordered by the river Hooghly and its western fringe is occupied by the river Subarnarekha beyond which are rocky outcrops. The presence of numerous paleo-channels suggests that the rivers channels have changed their course several times in the past. The shoreline has also undergone changes as we observe paleo-strandlines running almost parallel to the current coastal edge.

It is beyond doubt that inland navigation was one of the most common means of transport and commerce in the region by observing the character of its landscape. Apart from natural features like the active and inactive water channels and strandlines, a cultural feature that is the most curious of all in this region is the presence of numerous square and rectangular layouts of similar proportions and alignment. A detailed study of the region using Google Earth and CORONA satellite imagery led us to identify several such layouts forming certain recurrent patterns. In the following sections, the observations and doubts are discussed.

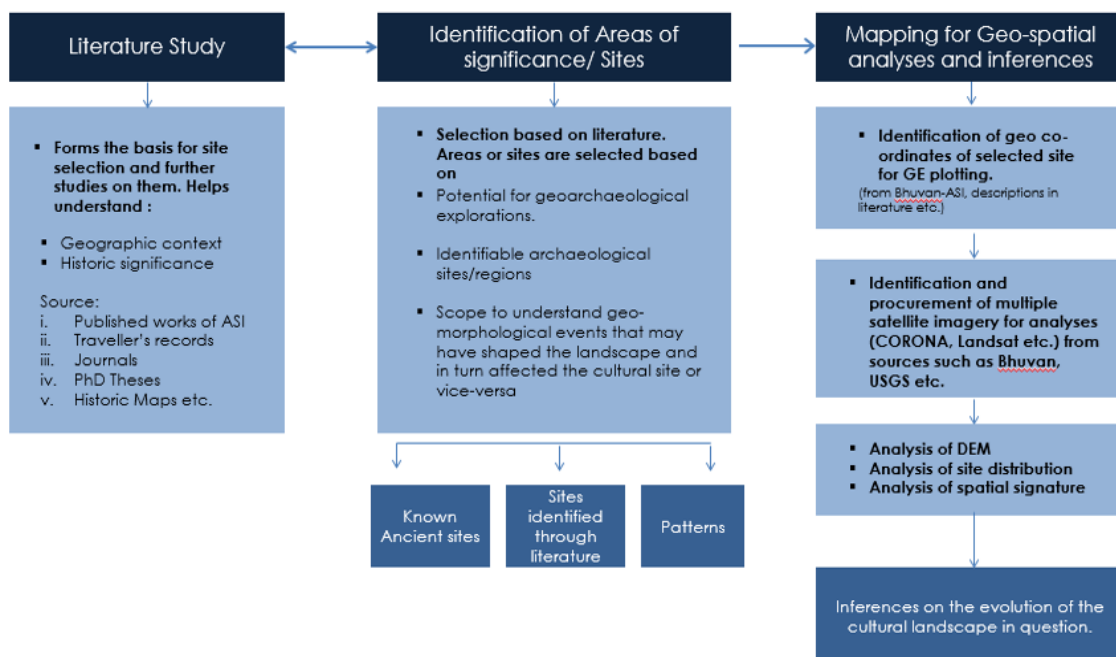


Figure 1. Flow chart explaining the sequence and inter-relation of methods adopted in this study.

#### 4.1. The port of Tamralipti in Ancient Literature

The only literary references so far commonly adopted for its identification with the city of Tamluk in West Bengal, India, are from Chinese records dated to the 4<sup>th</sup> and 7<sup>th</sup> centuries CE (the translations of which have been used for this study).

##### i. Faxian (visited India in early 5<sup>th</sup> century)

An excerpt from 'A Record of Buddhist Kingdoms' as translated by James Legge. (Legge, 1877)

"...Continuing his journey east for nearly 50 yojanas (from the ancient kingdom of Champa), he came to the country of Tamralipti (the capital of which is) a seaport. In the country there are twenty-two monasteries at all of which there are monks residing."

##### ii. Xuanzang (visited India in 7<sup>th</sup> century)

An excerpt from 'Si-Yu-Ki, Buddhist Records of the Western World', as translated by Samuel Beal (Beal, 1884).

"...From Samatat going west 900li (A Chinese unit of distance, equal to about 0.5 km) or so, we reach the country of Tan-mo-li-ti (Tamralipti). This country is 1400 or 1500li in circuit, the capital about 10li. It borders the sea. There are about ten sangharamas (A Buddhist monastery) with about 1000 priests. **The coast of the country is formed by a recess by (or in) the sea, water and land embracing each other.** By the side of the city is a stupa built by Asoka Raja."

##### iii. Alexander Cunningham

An excerpt from *Ancient Geography of India* (Cunningham, 1871) (based on *Histoire de la vie de Hiouen Tshang et de ses Voyage dans l'Inde* by Stanislas Julien) (Julien, 1853)

"The kingdom of Tan-mo-li-ti or Tamralipti is described as 1400 or 1500 li, about 250 miles, in circuit. It was situated on the shoreline, and the surface of the country was low and wet. **The capital was in a bay and was accessible from both land and water.**"

Apart from this, in the original French translation, Julien mentions the presence of a stupa about 200ft high near the capital.

#### 4.2. The geo-spatial Analysis of the Deltaic region: The concentric layouts

Most of these layouts resemble tiers of embankments and may have been part of ancient fortifications and/or part of a larger network of traditional water systems. The architectural character and nature of usage will only be understood through detailed investigations. In order to trace the origins of these recurring layouts, a study of historical maps of the region was done which revealed some interesting information.

While studying the region, a recurrent pattern of concentric layouts, mostly square or rectangular was observed. It is curious to note that some sites of the Archaeological Survey of India (ASI) and a few sites where excavations have been made in the past also form a part of such a concentric arrangement of squares and rectangles (Figure 2).

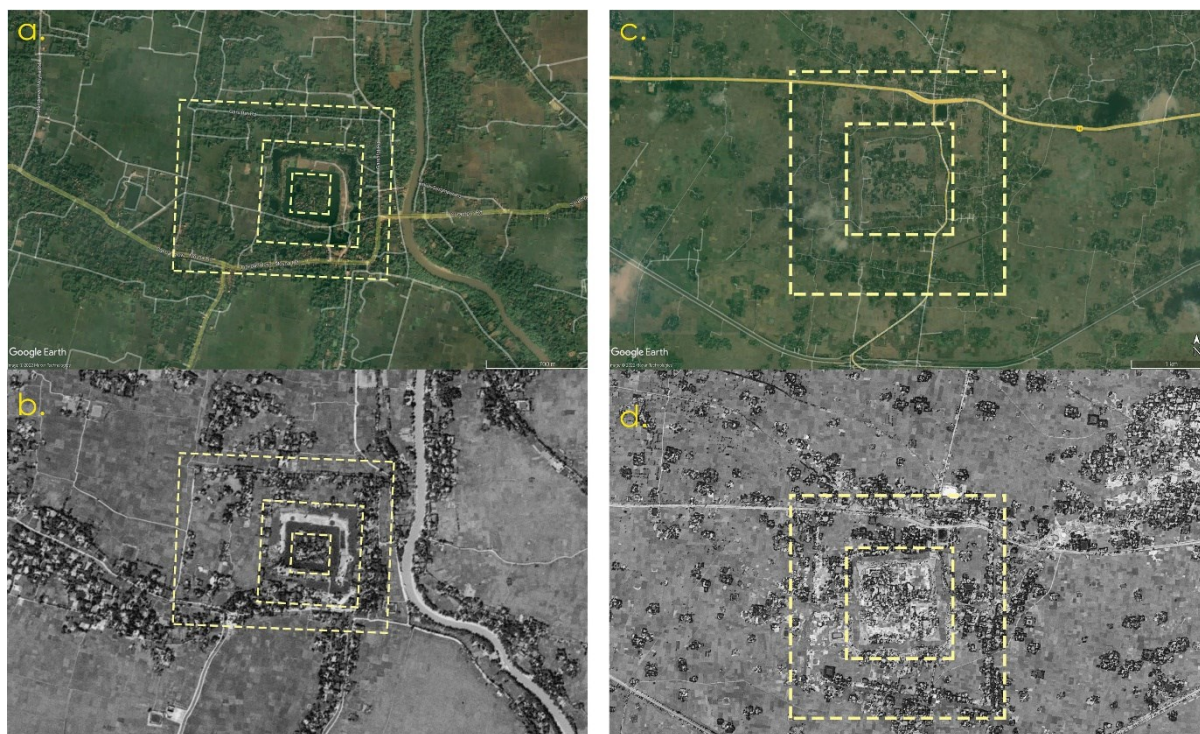


Figure 2. a. The example of Moynagur in West Bengal where the concentric tiers are visible in Google Earth imagery of 1/2010; b. CORONA declassified imagery from USGS portal; c. Two tiered arrangement in site within the study region in Google earth 1/2001

### 4.3 Information in 18<sup>th</sup> and 19<sup>th</sup> century British Maps

#### Aaron Arrowsmith's Map (1816/21)

A map compiled by Aaron Arrowsmith, an English cartographer and published in the early 19<sup>th</sup> century identifies about 9 sites marked as 'forts' within the deltaic region (see Figure 3). An excerpt from the description provided for the map in David Rumsey's online portal:

*"Rare (unrecorded?) 1821 state of Aaron Arrowsmith's massive nine-sheet map of India first published in London in 1816. Arrowsmith's improved Map of India was the greatest map of India published from information*

*predating the Great Trigonometrical survey (1802-1921)."*

Though the names of most sites have been rendered with old British spellings, an attempt was made to identify the places with reference to known places and the comparison of natural features in the vicinity as marked in Arrowsmith's map of 1816. A table including place names as given in the 1816 map of Arrowsmith and their current names, as identified in this study (Table 1.), have been listed below. The accuracy of this identification requires further substantiation.

**Table 1. Place names from Arrowsmith's map and their current identification**

Sl. No	Name in Arrowsmith's Map (sites in the vicinity of which concentric layouts have been observed are marked in <b><i>bold-italics</i></b> )	Current name (conclusion based on similarity in names and identification w.r.t to natural features shown in map)	Co-ordinates (Latitude, Longitude)
1	<b><i>Tamlook</i></b>	TAMLUK	22.292145°, 87.921833°
2	<b><i>Myrahgur</i></b>	MOYNAGUR/ MOYNACHOURA	22.249307°, 87.793615°
3	<b><i>Markondeah</i></b>	MARKUNDA	22.175130°, 87.297317°
4	Buckerabad	BAKHRABAD	22.146032°, 87.387620°
5	Narangur	NARAYANGARH	22.163204°, 87.388194°
6	Turkoah	TUTRANGA	22.043784°, 87.385028°
7	Belarry	BELDA	22.076320°, 87.339798°
8	Balleah	BORAH/BAHALIA	21.732685°, 87.515875°
9	<b><i>Depah</i></b>	DIPA	21.732685°, 87.515875°
10	Ammersee	AMARSAI	22.058949°, 87.602871°
11	Palaspoor	PATASHPUR	22.019910°, 87.540672°
12	<b><i>Kolander</i></b>	KOLANDA	22.092006°, 87.526535°
13	Badercally	BHADRAKALI	22.223808°, 87.427629°
14	Sillee	SALUA	22.266595°, 87.285232°
15	<b><i>Adjudagur</i></b>	AJODHYAGAR	22.283195°, 87.324880°
16	Bansah	BANSAPATRI	22.641392°, 86.654635°
17	<b><i>Doudpoor</i></b>	DAUDPUR	22.274042°, 88.830951°
18	Taujepoor	TAJPUR	21.657832°, 87.626387°
19	Bazdebpoor	BASUDEBPUR	21.824053°, 87.622215°
20	Jargong	JHARGRAM/JAARGO	22.455122°, 86.997770°



Geo-Archaeology of  
**GANGETIC DELTA**

 Fortification

From Aron Arrowsmith's Map published in 1821

**Figure 3. Arrowsmith's map marking forts within the study area. The map is a part of a larger 1816 map of India from David Rumsey's portal.** <sup>7</sup>

It is interesting that out of the patterns identified in this study, some are in close proximity to the sites of Arrowsmith's Map. It will not be possible to ascertain the character or condition of these sites in the 19<sup>th</sup> century, i.e., if they were physically intact, or were present as ruins or mounds, as the map was a compilation of several documents present before the Great Trigonometrical Survey was carried out. We are not certain if ground validation was made for any of these in the 19<sup>th</sup> century. It is crucial to identify historical documents of the region that could have recorded these sites.

*The Journals of Major James Rennell during the surveys of the Ganges and Brahmaputra between 1764 and 1767 as compiled by T.H.D La Touche for the Geological Survey of India (1910) (Touche, 1910)*

*"Major James Rennell was first employed on the survey of the Ganges delta with the special object in view of finding a shorter passage suitable for large vessels from the Ganges to Calcutta, than that through the Sunderbans and the [river] Meghna. The Journal gives a detailed account of this voyage and of three subsequent expeditions, during which he surveyed a great part of Northern and Eastern Bengal. "*

Though a lot of disparities will occur with the course of the rivers and water features as these underwent tremendous changes over the centuries that have passed, Rennell's volume is an irreplaceable resource for the data on the region's historical landscape. He identifies several historical and cultural landmarks of the period; some of these have been marked on his final maps, others in his description. It is of interest, that while trying to identify the buildings or landmarks that he describes in his journal, we came across certain sites, (some of which are identified by him, others in the vicinity of important places that he mentions) follow the patterns that have been observed in the lower reaches of the deltaic region (Figure 4).

**The sites within the larger deltaic landscape**

The distribution of the sites (ASI, other excavated sites, sites from Arrowsmith's and Rennell's Maps and sites identified in this study) and the geomorphological character of the deltaic region render the possibility of the identification of the ancient port of Tamralipti and/or its larger geo-political extents. The following Table 2 and the associated Figure 3 has been used to elucidate the observations.

**Table 2. Details of sites that are identified in this study**

SITE No	Current Name	Latitude	Longitude	Tiers visible / Condition in most recent imagery	Other features (all units in km)	Cardinal alignment
T01	Mahishadal	22.183597°	87.986284°	2 / fragmented	0.5 x 0.8	Clock-wise tilt
T01 A	Ranthala Bagan	22.181453°	88.005363°	1/ fragmented moat like feature	0.2 x 0.4	Clock-wise tilt
T02	Noorpur	22.212509°	88.071201°	1 / fragmented	0.24 x 0.24	Clock-wise tilt
T03	Tamluk hospital	22.287071°	87.919830°	1/ fragmented	0.34 x 0.5	Near perfect N-S alignment
T04_a	Gurudasapur	21.841645°	87.215358°	1/ vegetation cover reveals a square profile with a mound till 2015.	0.4 x 0.4	Clock-wise tilt
T04_b	Chaulia				Linear arrangement of water tanks	Clock-wise tilt
T06	Jallabhaj	22.238978°	88.021936°	1/ rectangular crop mark	0.22 x 0.32	Clock-wise tilt
T09	Falta fort	22.290197°	88.105429°	1/ oval in profile		NA
T12	Bhaua	22.389651°	87.054830°	1/ negative cropmark reveals a square profile with a mound	0.2 x 0.24	Clock-wise tilt
T27	Chandrarekharh	21.963867°	87.058937°	1/ moat clearly visible in the form of cropmark	0.88 x 0.6	N-S
T28	Dhobani sol	21.915828°	87.061476°	1/ square moat clearly distinguishable from cropmark	0.5 x 0.5	N-S
T29	Bedjharia	21.964430°	87.081665°	1/square profile visible from soil mark	0.35 x 0.35	Clock-wise tilt
T30	Unknown	21.946710°	87.072255°		Cropmark with significant elevation in close proximity to an inactive tributary	
T31	Changaul	22.316865°	87.383286°	2/ the configuration is largely altered but connections can be deciphered from the presence and arrangement of linear water features that form the edges	1 x 1.17	N-S
T 33	Kasba Narayngarh	22.156125°	87.390461°	Multiple tiers visible but have been cut across by roads		Near perfect N-S alignment
T 34	Gar Arara	22.623466°	87.372342°	Very significant in terms of the layout which is a single tier square with protrusions on all sides except the eastern end.	0.18 x 0.2 excluding protrusions	N-S
T35	Payrachali	22.049072°	87.603924°	2/ positive cropmark reveals the outer square where the inner	0.24 x 0.24	N-S

				one is seen as a depression.		
T 38	Alisagar	22.385031°	87.555805°	3 / Moat like arrangements are clearly discernible through ground texture differences in satellite imagery	2.28 x 2.28 (outer tier), 1.1 x 1.1 (second tier)	Counter-clockwise tilt
T41	Panchetgarh rajbari	21.955891°	87.560057°	1/ square moat like feature visible	0.45 x 0.45	N-S
T42	IIM	22.444718°	88.299799°	Site records prior to construction of the institution needs to be verified to check if the square water body surrounding it is part of an older site.		Counter-clockwise tilt
T44	Unknown	21.988670°	87.514896°	Linear water feature	1.15 km long	
T 45	Unknown	22.042487°	87.549214°	Linear water feature	0.8 km long	
T 47	Khagra beri	22.118078°	87.455913°		Positive cropmarks, presence of moat like arrangements and elevation profile are significant	
T 49	Unknown	21.797193°	87.323349°	Outer edge of the square profile is raised with settlement on them, the inner tier is presently a tank	0.2 x 0.2	Counter clockwise
T54	Unknown	22.352393°	87.849107°	Comprises of an outer enclosure within which are seen a pair of sites with concentric profile with bastion like features visible in 2007 imagery.	Each site is 0.4 x 0.4	clockwise tilt
T 55	Unknown	22.376802°	87.846778°	A smaller fort which is rectangular with basitons	0.17 x 0.24	N-S

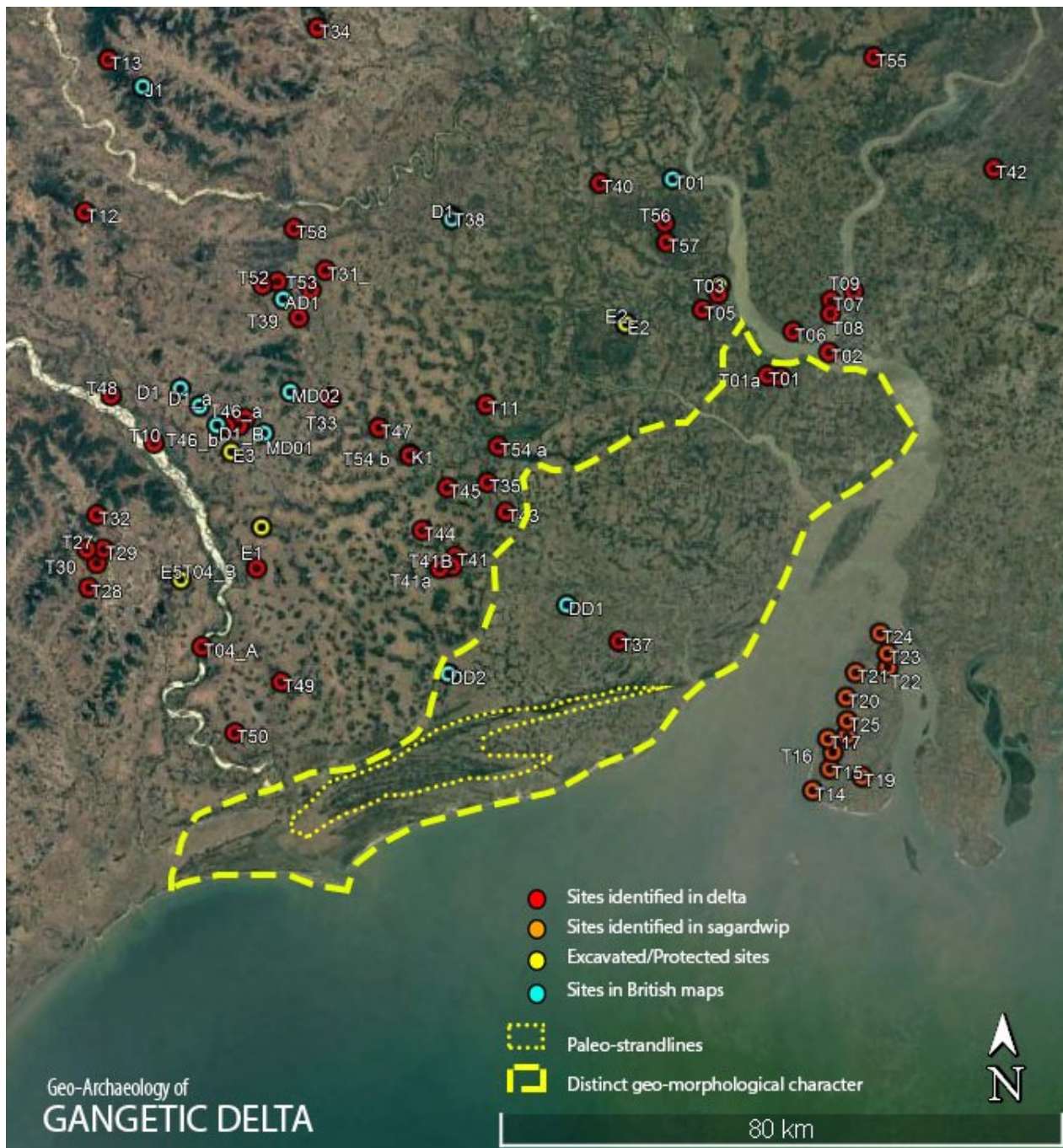


Figure 4. The study area showing the distribution of sites and the geomorphological character of the landscape. Google Earth image 12/1984

**5. Observations and inferences**

With the exception of two, the sites are restricted to the areas north of the region highlighted in yellow in Figure 3. Geological literature also identifies a few strandlines in the region, with the youngest one forming the current shoreline (Pravin 2005). Closer observation of Google Earth imagery reveals a distinct texture in this highlighted region when compared to the areas to its vicinity. The arrangement of paleo-strandlines (Figure 5), paleo and active channels within the highlighted region brings forward several questions on its possible historical character.

**5.1 Presence of strandlines**

The strandlines could be indicative of ancient coastlines that were much inland as compared to the present coast. These however, are not entirely parallel to the current coastline.

**5.2 Network of paleo-channels and active river channels**

A map published in 1740 (Figure 6) (although the information depicted could be much earlier) represents the current deltaic region as several smaller landmasses. Closer observation of Arrowsmith’s map also reveals to us water channels that encircle several regions within the delta. It could well be possible that over time, the fragmented land masses under combined actions of sedimentation from the river and sea coast dynamics

transformed into what is observed at present. Also, from the historical descriptions mentioned in the earlier section of this paper, the capital, Tamralipti, is said to have been located along the bay, accessible by means of land and water.

Thus, this arrangement of paleo-channels and active channels could mean that historically, the region consisted of several smaller islands or fragmented landforms as we

observe in the present day Sundarban. Had this been the case, by observing the arrangement of the strandlines and the concentration of the identified sites, the port of Tamralipti could have been situated in the region that is immediately north to the highlighted region (Figure 3) (which may have been the bay in the historical descriptions along which the capital was situated) as this part could have been easily navigable by water and also accessible through land transport



Figure 5. The arrangement of strandlines is indicative that the coast was much inland in the past. Google Earth image 12/1984



Figure 6. a. The current deltaic region being fragmented by water channels, from the 1740 Seutter Map of India. b. Deltaic region with water channels encircling those (blue dotted lines) as shown in Arrowsmith's Map

A curvilinear feature (Figure 7 inset) at the edge separating the two contrasting geomorphological signatures at some point could either have been a major water channel or the coastal fringe. Had the ancient coastal edge been where the yellow highlight begins, then it is possible that the port of Tamralipti was located within one of the three highlighted regions as we observe vegetation patterns that are typical patterns of archaeological interest and a distinct landscape signature (encircled in red in the Figure 6).

### 5.3 Analysis of digital elevation model and multispectral imagery

Analysis of Digital Elevation Model (Figure 8) for the region strengthens the observations made on the basis of

signatures observed in satellite imageries of various dates. We observed that the three possible locations (highlighted in dashed rectangle in black) are worthy of detailed investigations as they are at a significantly lower elevation compared to areas to its north and south which indicate that this stretch may have been submerged or was separated from the land to its south at some point in history.

Similarly, a distinct vegetation texture is observed along the region which we conclude to have been a former shoreline (refer to Figure 6b.) in LANDSAT imagery of 1973 (Figure 8.b).

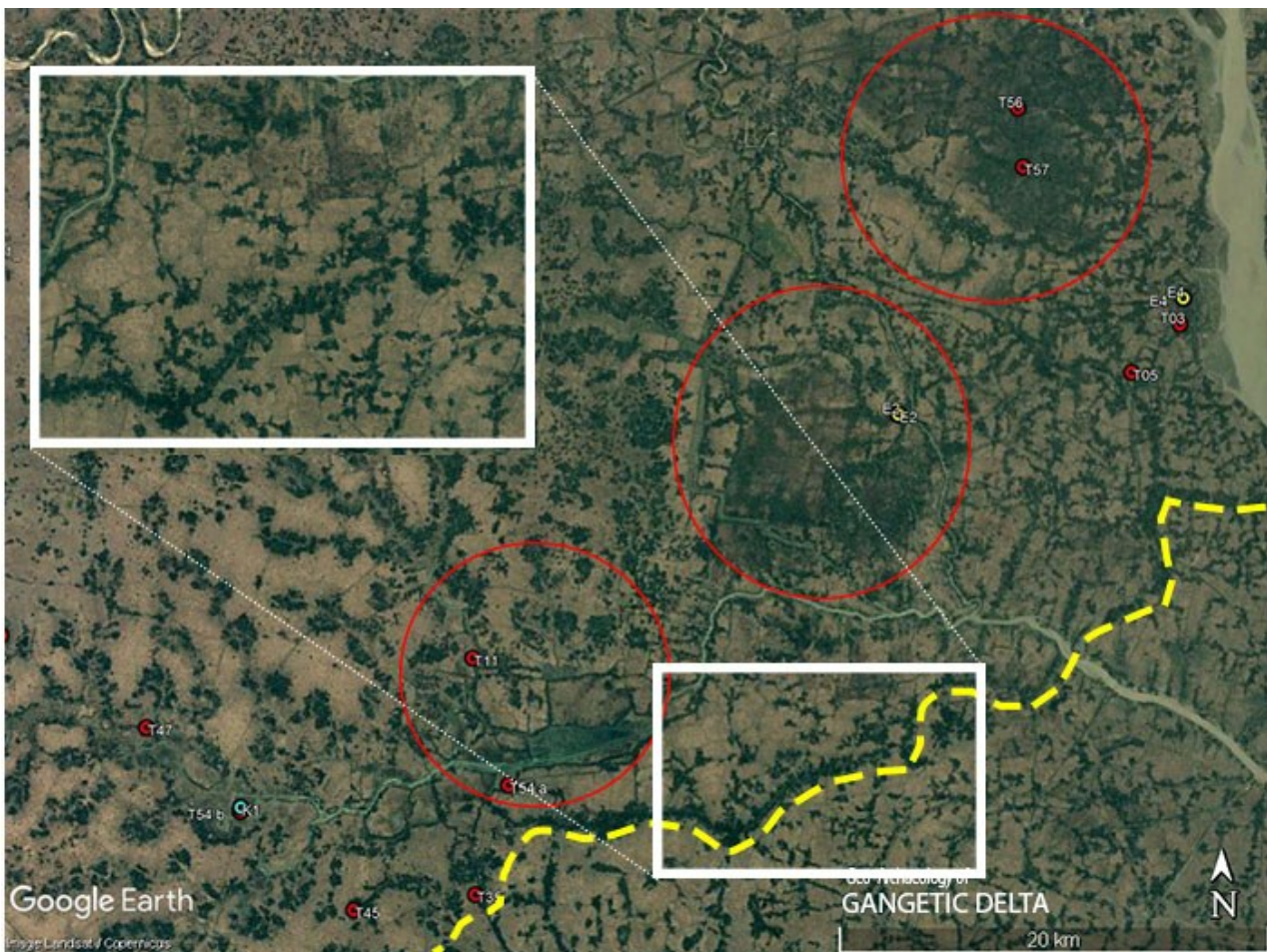


**Figure 7. Areas with a conspicuous distinction in texture located along the probable edge of the ancient coastline. The concentric layouts are also observed within the three areas highlighted in red. Google Earth image 12/1984**

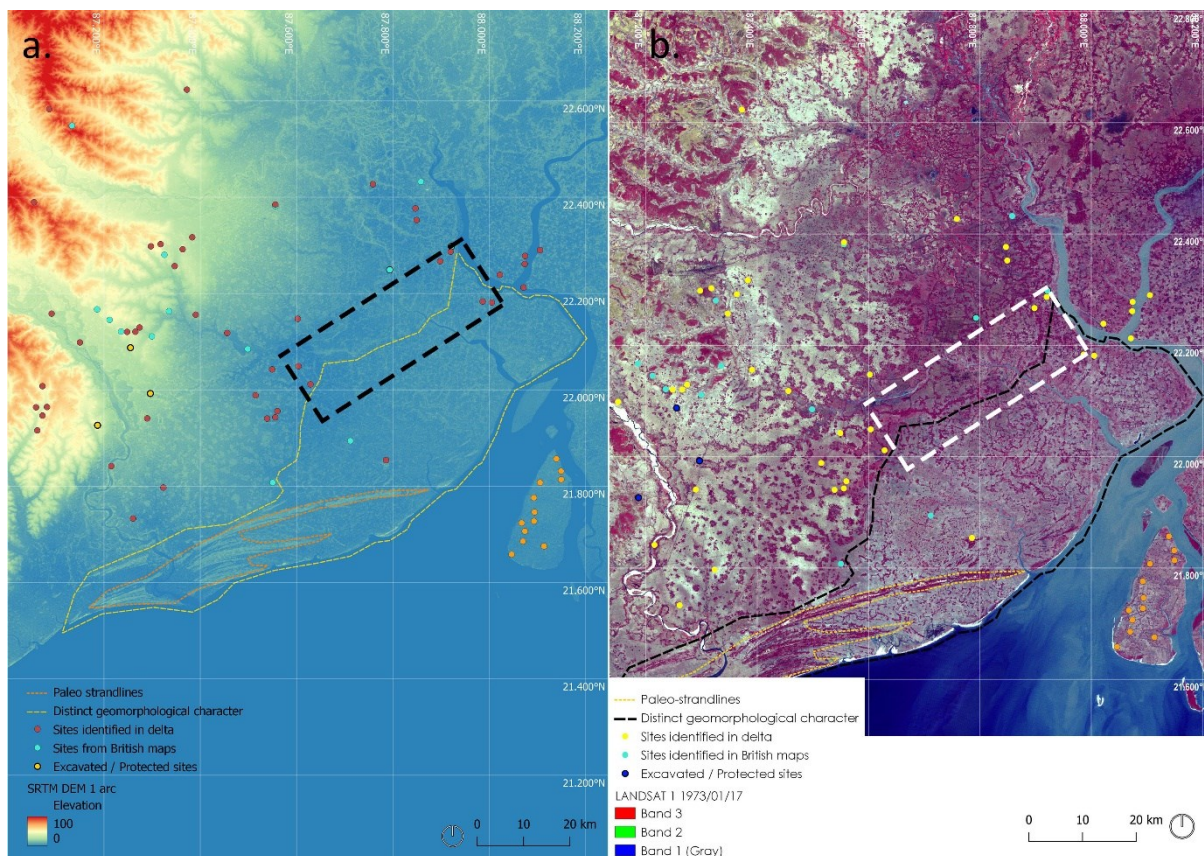


**Figure 8. a. The sites overlaid on SRTM DEM 1 arc data stretched in single band pseudo-colour between 0 and 100 and b. overlaid on LANDSAT 1 imagery dated 1973/01/17.**

## 6. Concluding remarks and future directions

The region that included Bengal and its neighbouring areas were historically under the political and economic control of numerous dynasties. However, despite the identification of potential locations, the current stage of this study does not grant the liberty to place our observations (the concentric layouts in particular) within any chronological framework as this would require intensive research and field investigations. As our primary references are of traveller's records between the 5<sup>th</sup> and 7<sup>th</sup> centuries and European maps published in the 18<sup>th</sup> and 19<sup>th</sup> centuries, the time-frame under consideration spans a few centuries. The geo-spatial patterns observed in the sites that have so far been identified within this region suggest that it was of immense significance in the past. Having been located in a very dynamic landscape, the sites underwent certain degrees of transformation, yet there are strong clues in the form of spatial layouts and other patterns that provide clues to the region's historical character, both architectural and geomorphological. Based on the character of the layouts that have been observed in all the sites that have been identified in this study, it is assumed that their inception would not have been widely separated and that they must have been products of the same socio-cultural context. What constituted this socio-cultural context and what were the regional and cross-cultural contributions that established them would be an interesting research problem to explore as this might shed more light into the illustrious yet eclipsed past of the ancient port in question.

The observations in this paper are based on spatial patterns and can be explored further with field investigations and calls for the need of a multi-disciplinary approach.

Identification of cultural heritage resources are a key component in sustainable city planning. This holds importance in multiple ways, the foremost of which is to empower communities to embrace their cultural heritage through well thought out strategies of city planning by acknowledging these diminishing cultural vestiges. Traditional knowledge systems embodied by these historic built resources, if incorporated appropriately to meet the demands of modern times, will help resolve a majority of the issues arising from human-environment interactions in ecologically sensitive areas such as the study region. Thus, the role played by remote sensing and GIS is vital in the on-going efforts for the conservation of cultural heritage resources.

## Acknowledgements

The work reported in this paper forms a part of the Geo-archaeology project funded by the Space Applications Centre (SAC), Ahmedabad, under the GAP scheme. We thank SAC for supporting and collaborating in this work. We thank Geographicus Rare Antique Maps and Mr David Rumsey Collection for permissions to use the maps from their collection in this work. We thank the anonymous reviewers for their feedback.

**References**

- Beal S. (1884). *The Life of Hiuen-Tsiang by the Shaman Hwui Li, with an Introduction Containing an Account of the Works of I-Tsing*. London: Kegan Paul, Trench, Trubner & Co.
- Cunningham A. (1871). *Ancient Geography of India*. London: Trubner & Co.
- Julien S. (1853). *Histoire de la vie de Hiouen-Tsang et de ses voyages dans l'Inde : depuis l'an 629 jusqu'en 645 / par Hoeï-li et Yen-thsong ; suivi de documents et d'éclaircissements géographiques tirés de la relation originale de Hiouen-Tsang*. Paris.
- Legge J. (1877). *A record of Buddhist kingdoms; being an account by the Chinese monk Fa-Hien of his travels in India and Ceylon, A.D. 399-414, in search of the Buddhist books of discipline*. Oxford.
- Pravin D and B. G. Kunte (2005). *Beach Ridges of India*. *Journal of Coastal Research*.
- Rajani M. B. (2021). *Patterns in Past Settlements: Geospatial Analysis of Imprints of Cultural Heritage on Landscapes*. Springer.
- Touche T. H. (1910). *The Journals of Major James Rennell during the surveys of the Ganges and Brahmaputra between 1764 and 1767*. Geological Survey of India.

## Analysis of Urban Growth and Its Impact on Agriculture Land around the Chalisgaon City in Jalgaon District of Maharashtra, India: A Remote Sensing and GIS Based Approach

Patil Nilesh<sup>1,\*</sup>, Patil Vilas<sup>2</sup>, Patil Sanjaykumar<sup>1</sup>, Patil Bhavesh<sup>1</sup>, Suryawanshi Arvind<sup>3</sup> and Jadhav Kavita<sup>2</sup>

<sup>1</sup> School of Environmental and Earth Sciences, Kavayitri Bahinabai Chaudhari North Maharashtra University, Jalgaon, India

<sup>2</sup> Annasaheb G. D. Bendale Mahila Mahavidyalaya, Jalgaon, India

<sup>3</sup> Nanasaheb Yashwantrao Narayan Chavhan Arts, Science, and Commerce College, Chalisgaon, India

\* E-mail: patilnileshd94@gmail.com

(Received: Feb 3, 2022; in final form: Sep 20, 2022)

**Abstract:** In India, the agricultural land has tremendously disintegrated which changed the land-use patterns. The agricultural land has declined continuously due to rapid urbanization in the country. In India, nearly 45% of the land cover comes under agriculture area, and 22% is under forest land, whereas this land was drastically decreasing day by day. The main aim of the study is to identify the urban growth along with the land use pattern of Chalisgaon city, situated in the Jalgaon district, of Maharashtra state. This is a comparative study from early 1990 to late 2020. The Landsat images have been used for the years 1990, 2000, 2010, and 2020 to identify the change in land use and land cover pattern. These images are processed and analyzed under GIS and maximum likelihood classification method. The Chalisgaon city covers a total of 1850 hectares area. In the last three decades, the total built-up area has increased from 556 hectares to 920 hectares. It is observed that, the urban expansion of the city is a major factor behind the declination the cultivational land area under study. In 1990 the agriculture area was about 1095 hectares that have been reduced to 730 hectares in 2020. This study reveals the agricultural land gradually decreased due to encroachment of urban areas i.e., infrastructural, connectivity, population, and other related facilities.

**Keywords:** Urban Expansion; Agriculture; Land use pattern; Landsat Images; GIS.

### 1. Introduction

Development has played a major role within city limits in the constant evolution of land use, accommodating new infrastructure and projects while displacing conventional land-use patterns (Gumma et al., 2017). Assessment of land use and land cover pattern can be done through remote sensing technology (Hasan et al., 2021). Many academicians and scholars have successfully contributed to urban growth studies based on spatial and temporal patterns (Liu et al., 2019, Zhong et al., 2020, Meng et al., 2020), growth approaches (Liu et al., 2010, Kantakumar et al., 2016), driving processes (Zhong et al., 2020), and development forecast (Zhang et al., 2018). Several researchers have previously analysed metropolitan built-up land development and explained its operating methods for various cities and localities at the national (Sharma et al., 2022, Vani et al., 2020, Saini et al., 2020, Tripathy et al., 2019, Duijine et al., 2019, Salem et al., 2021,) and global (Dadashpoor and Ahani, 2019, Gong et al., 2018, Meng et al., 2020, Ma et al., 2016, Jia et al., 2020,) scales. Expansion of urban land the process of creating an environment conducive to urban populations and their activities is an integral part of urbanization. The inner-city land expansion changes the balance of habitats, geography, hydrology, land cover pattern, and surface energy (Grimm et al., 2008). Towns have occupied a negligible amount of the earth's surface still most urban problems have a profound effect on the environment and global change (Vellinga & Herb, 1999). The entire world is experiencing rapid expansion due to technological enhancement and changes in the lifestyle of human beings living in different localities around the world. (Tewelde & Cabral, 2011). Human geography is an integral part of the change in land utilization. The land is needed for non-agricultural use such as building roads, marketplaces, shopping centres, industries, etc. due to the rising urban population. As a

result, neighbouring agricultural land diminishes. (Songsore, 1977; Mishra, 2002). Numerous factors have impacted food production as urban landscapes have grown. Traditional farming practices used by farmers and family farms have declined due to the replacement of old farming land and migration to urban regions. (Roca, 1993). According to the Indian census published in year 2011, there are 1210.2 million people overall, with 377.1 million living in metropolitan areas. Over the past ten years, metropolitan regions have added 91.0 million people to their population. In relation to the nation's overall population, urban residents make up 31.8% of the population. (Census of India, 2011). Lopez has clearly indicated that such rapid population changes significantly affect the environment, resulting in the loss of farmed land. (Lopez et al., 2001). People move in higher proportions from rural to urban and from small to large urban areas, such as India's urban centres, in rapidly developing nations like India. Following the Industrial Revolution in the 1970s, there was globalization in the 1990s. In the past, forests have been cut down, meadows have been ploughed under or destroyed, marshes have been drained, and fields have been taken over by growing towns, but never at such a rapid rate. (Rahman, 2007).

In specially, information from RS-based multi-dimensional land use data can be used to evaluate structural differences in the LULC pattern. Furthermore, precise and thorough land-use information is important for creating environmentally and urban-friendly planning approaches. Utilizing spatial data, the current study is visualized to evaluate the effects of urban growth on agricultural land. (Alphan, 2003). The present study is visualized to assess the impact of urban expansion on agricultural land using spatial data.

## 2. Materials and methods

### 2.1 Study area

Chalisgaon City lies in Maharashtra's Jalgaon district, in the southwest corner. The Chalisgaon tehsil's administrative center is situated in Chalisgaon city. It is positioned in  $20^{\circ} 26' 20''$  North to  $20^{\circ} 29' 03''$  North latitude and  $74^{\circ} 58' 40''$  East to  $75^{\circ} 02' 13''$  East longitude (Toposheet No. 46 P/3) and is 344 meters above mean sea level. The Tittur river flow through the center of Chalisgaon city (Figure 1). According to the census, the city has a population of 108181 and a total area of 18.50 km<sup>2</sup>. State highways and railroads provide excellent access between Chalisgaon city and other cities. Since it is the only urban center of Chalisgaon tehsil, so the population of the surrounding villages also depends on it for goods and administrative services. Therefore, the surrounding population migrates to Chalisgaon city for a better lifestyle, medical facilities, educational facilities, and happiness, etc. The immigrant population and natural development population have been responsible for the

expansion of the city. Chalisgaon is very developed in terms of agriculture so many agro-based industries are established in Chalisgaon such as Textile Mills, Belganga Sugar Factory, and Oil and Vidya Factory.

The combined primary and secondary data are used to support the current investigation. For the investigation of land use patterns, Landsat data from four decades (1990, 2000, 2010, and 2020) is examined. The USGS Earth Explorer website has been used to download Landsat data for the last four decades. ERDAS envision version 2015 and ArcGIS version 10.2 were also used to analyze the primary data, which included radiometric and geometric adjustments as well as registered to Universal Transverse Mercator projection (UTM-Zone 43 North) in the World Geodetic System (WGS84) datum. The municipal corporation Chalisgaon, the district statistics office of Jalgaon, the census handbook, etc. all have exposure to secondary data. Table 1 displays the specifics of the satellite data that have been gathered.

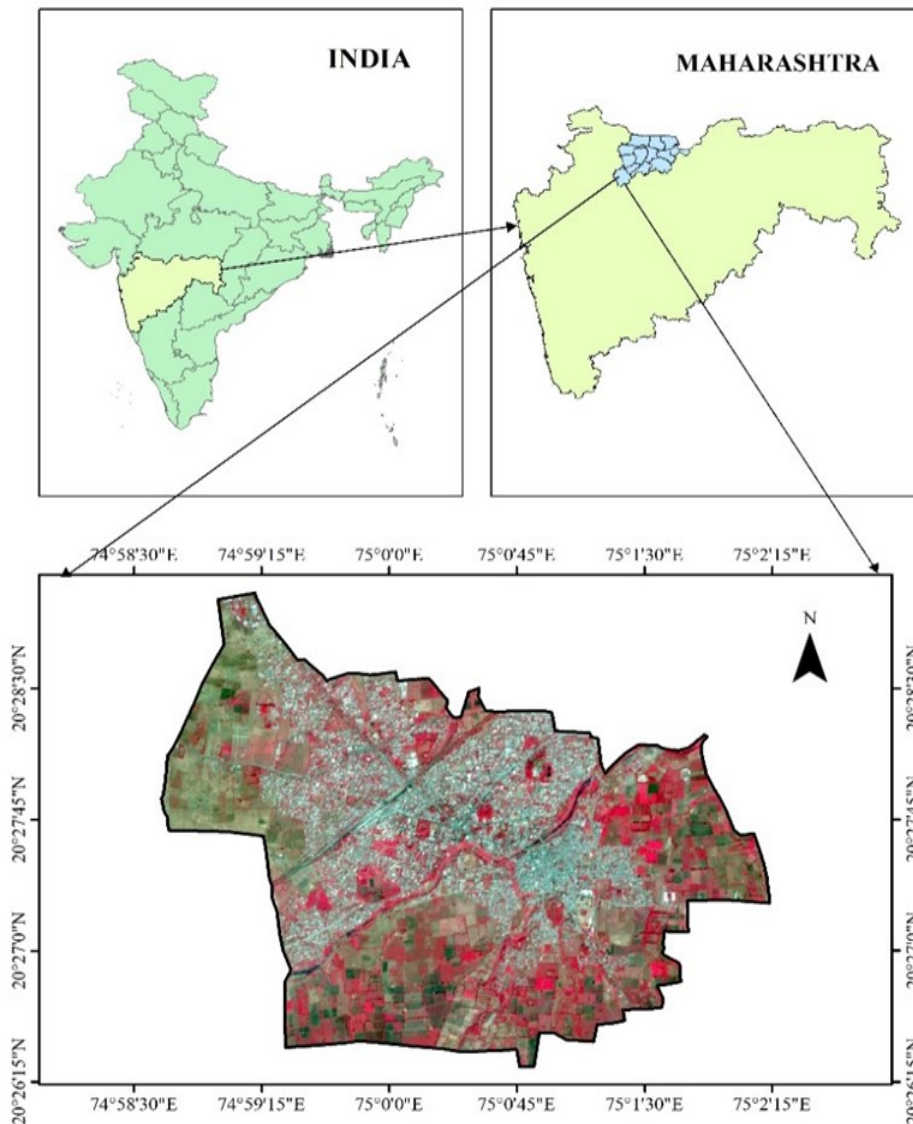


Figure 1. Location map and satellite image of the Chalisgaon city

**Table 1. Specifications of Landsat data.**

Data	Year of acquisition	Path/Row	Bands	Resolution
Landsat 5 TM imagery	01/02/1990	147/46	4,3,2	30m
Landsat 5 TM imagery	20/02/2000	147/46	4,3,2	30m
Landsat 7 ETM+ imagery	31/01/2010	147/46	4,3,2	30m
Landsat 7 ETM+ imagery	18/01/2020	147/46	4,3,2	30m

Source: USGS Earth Explorer website

**2.2 Data processing and classification**

False Colour Composite is also known as FCC generation: The multi-spectral (multi-band) composite image is generated with the ERDAS imagine software utilized to download Landsat images and the layer stacking function to generate seven distinct bands images of Landsat. From this, a standardized FCC is created using the fourth, third, and second bands, from which the LULC scheme was extracted. From the reference data and Google Earth imagery, training sites are selected. The training sites are used by the ERDAS image classification software to determine the various land cover classes in the entire image of the study area. In general, a total of eighty training sites have been used to train the Landsat images. Maximum likelihood classification determines the likelihood that a given pixel belongs to a certain class by assuming that the statistics for each class in each band are normally distributed. All pixels are categorized unless a probability threshold is chosen.

Each pixel is categorized into the class with the highest likelihood (that is, the maximum likelihood). The pixel remains unclassified if the highest likelihood is below a threshold you specify. Size, shape, location, number of pixels, number of training sites for a particular class, placement, and uniformity were some of the features that were considered when assigning training sites. The maximum likelihood algorithm and minimum-distance classification are utilized in this study's supervised classification. Five major LULC classes are chosen for mapping the entire study region such as agricultural land; barren land; built-up land; vegetation land and water bodies.

ENVI implements maximum likelihood classification by calculating the following discriminant functions for each pixel in the image (Richards, 1999):

$$g_i(x) = \ln p(\omega_i) - \frac{1}{2} \ln |\Sigma_i| - \frac{1}{2}(x - m_i)^T \Sigma_i^{-1} (x - m_i)$$

where:

i = class

x = n-dimensional data (where n is the number of bands)

p(ωi) = probability that class ωi occurs in the image and is assumed the same for all classes

|\Sigma\_i| = determinant of the covariance matrix of the data in class ωi

\Sigma\_i^{-1} = its inverse matrix

m\_i = mean vector

**2.3 Accuracy assessment**

The error matrix is calculated for the assessment of the correctness of classified land use land cover images. It noted that, when linked with an identical site in the field, the matrix verified that the pixel had appropriately identified a certain feature type. The calculation of overall accuracy, user's accuracy (UA), producer's accuracy (PA), and Kappa coefficient provides an accurate result for classified images. In this entire process, we randomly selected 250 sample points (reference data) from the various sites of the study by ground authentication of GPS survey and Google Earth engine for appropriate calculation.

$$\text{Overall accuracy (OA)} = \frac{\text{Total number of correct sample points}}{100\% \text{ total number of sample points}} \tag{1}$$

$$\text{Producer's accuracy (PA)} = 100\% - \text{error of commission (\%)} \tag{2}$$

$$\text{User's accuracy (UA)} = 100\% - \text{error of commission (\%)} \tag{3}$$

$$\text{Commission error} = \frac{\text{(off diagonal row elements)}}{\text{(total number of row)}} \tag{4}$$

$$\text{Omission error} = \frac{\text{(off diagonal column elements)}}{\text{(total number of column)}} \tag{5}$$

$$\text{Kappa coefficient (K)} = \frac{N * \sum a - \sum ef}{N^2 - \sum ef} \tag{6}$$

where a diagonal frequency, N denotes total frequency, ef denotes expected frequency.

**3. Materials and methods**

**3.1 Population growth and urban expansion**

In the last three decades, Chalisgaon city's population along with population density have been constantly increased due to natural population growth and immigration from the surrounding villages which resulted into urban expansion of the city. Its observed that, the total population of Chalisgaon city was 77,420 in year 1991 that had increased to 1,08,181 in year 2011. The growth rate percentage is an important parameter to understand the change in land use and land cover pattern of the area under study. While comparing the growth rate for the years 1991-2001 with years 2001-2011, significant increase was observed from 17.68% to 18.73% respectively. The constant increase in population density is also noted from year 2011 to year 1991 (Table 2). The geographical factor, employment opportunity, infrastructural facilities, availability of good educational institutions, commercial activities, and industrial development in Chalisgaon city

are favourable for the dwelling of the citizen. All the above mentioned factors are favourable for the migration of people from other areas toward Chalisgaon city. It's observed that natural population growth and immigration played a significant part in the amplification of urban area in the study region which ultimately resulted into declination of agricultural land.

**Table 2. Chalisgaon city population growth, 1991-2011**

Year	Population	Increased	Density	Growth rate in %
1991	77420	18078	4164	----
2001	91110	13690	4901	<b>17.68</b>
2011	108181	17071	5819	<b>18.73</b>

Source: Census report, Government of India

**3.2 Land use land cover changes and loss of Agriculture land**

A total of five land cover categories were identified and classified in the study. These were Built-up, Barren, Agriculture, Vegetation, and water bodies areas as shown in figure 2. There are significant Spatio-temporal changes in the pattern of land use land cover in the city of Chalisgaon as shown in table 3. The continuously positive changes were observed in the classes; built-up land and barren land, whereas barren land has negative change between 1990 to 2000. The negative changes were observed in Agriculture, vegetation, and waterbodies. However, but waterbodies have positive changes between 2010 to 2020. The built-up land has increased from 556 hectares to 920 hectares from 1990 to 2020 (table 3) with a percentage change of 19.64 (Table 3 and Figure2 & Figure 5). The study shows that there is a remarkable increase in the urban area between 1990 to 2020 (of 82 percent) while a total of 375 hectares of fertile agricultural land were lost due to the city's expansion. The main reason behind the increase in housing (i.e., settlements) and the development of infrastructures such as health, education, and other socio-economic factors.

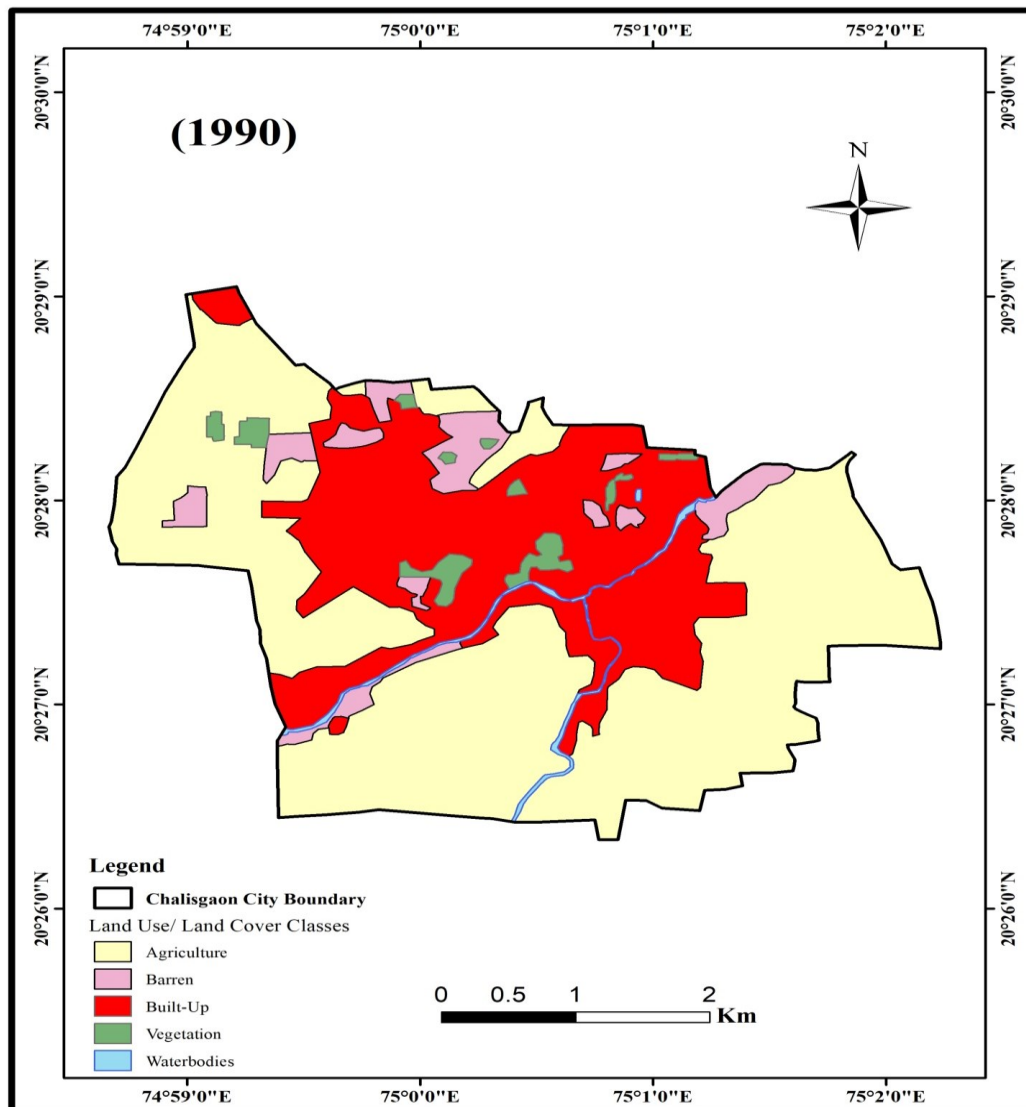


**Figure 1. Land use/ land cover map of Chalisgaon city for the year 1990**

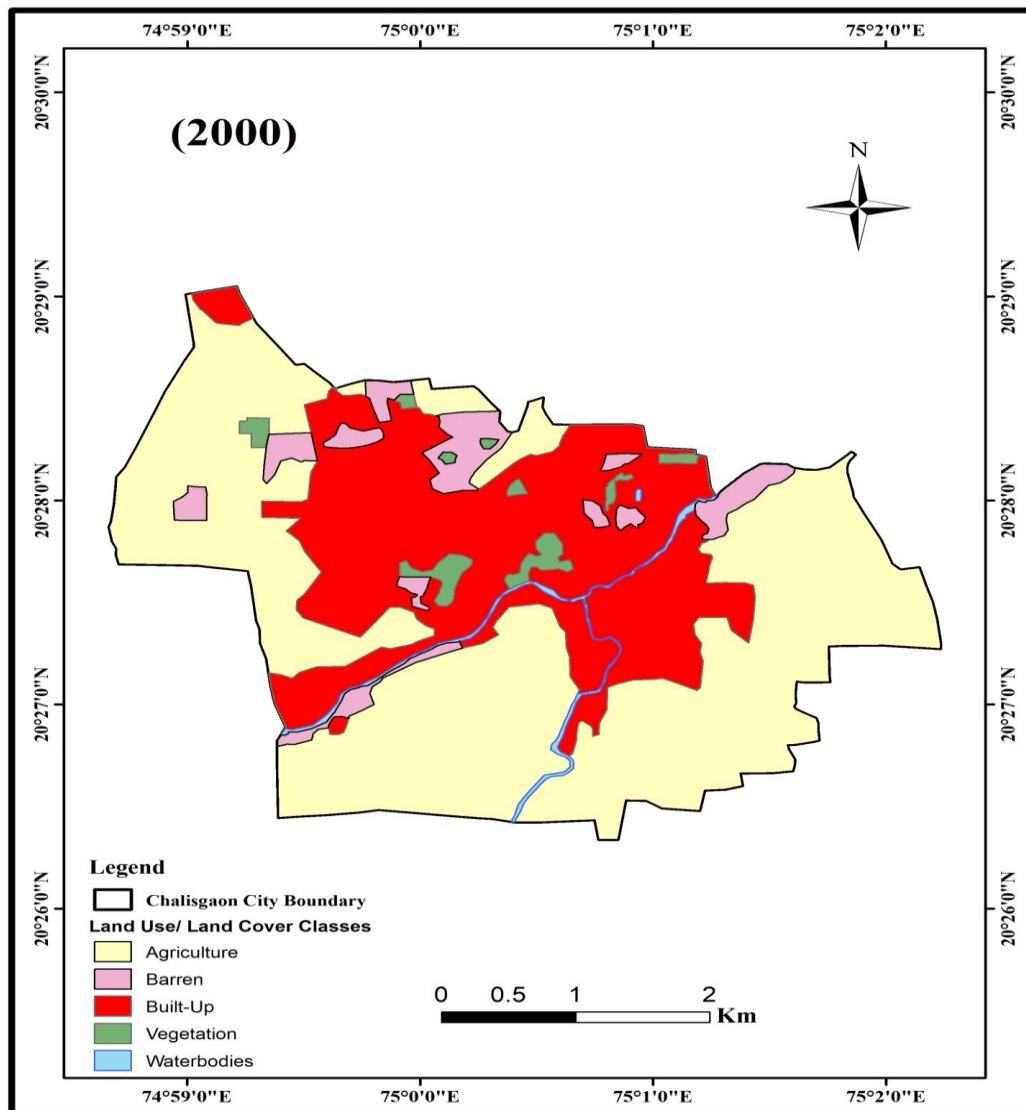


Figure 3. Land use/ land cover map of Chalisgaon city for the year 2000

Table 3: Land use land cover change from 1990 to 2020 (in Hectares)

Sr. No.	LULC		1990	2000	2010	2020	Changes (1990-2020)
1	Built up	Ha.	556	640	760	920	364
		%	30.05	34.59	41.09	49.69	19.64
2	Barren	Ha.	121	118	129	141	20
		%	6.54	6.38	6.97	7.61	1.07
3	Agriculture	Ha.	1095	1021	919	730	-365
		%	59.19	55.19	49.67	39.46	-19.73
4	Vegetation	Ha.	57	52	25	32	-25
		%	3.08	2.81	1.37	1.74	-1.34
5	Water bodies	Ha.	21	19	17	28	7
		%	1.14	1.03	0.91	1.50	0.36
	Total	Ha.	1850	1850	1850	1850	00
		%	100	100	100	100	00

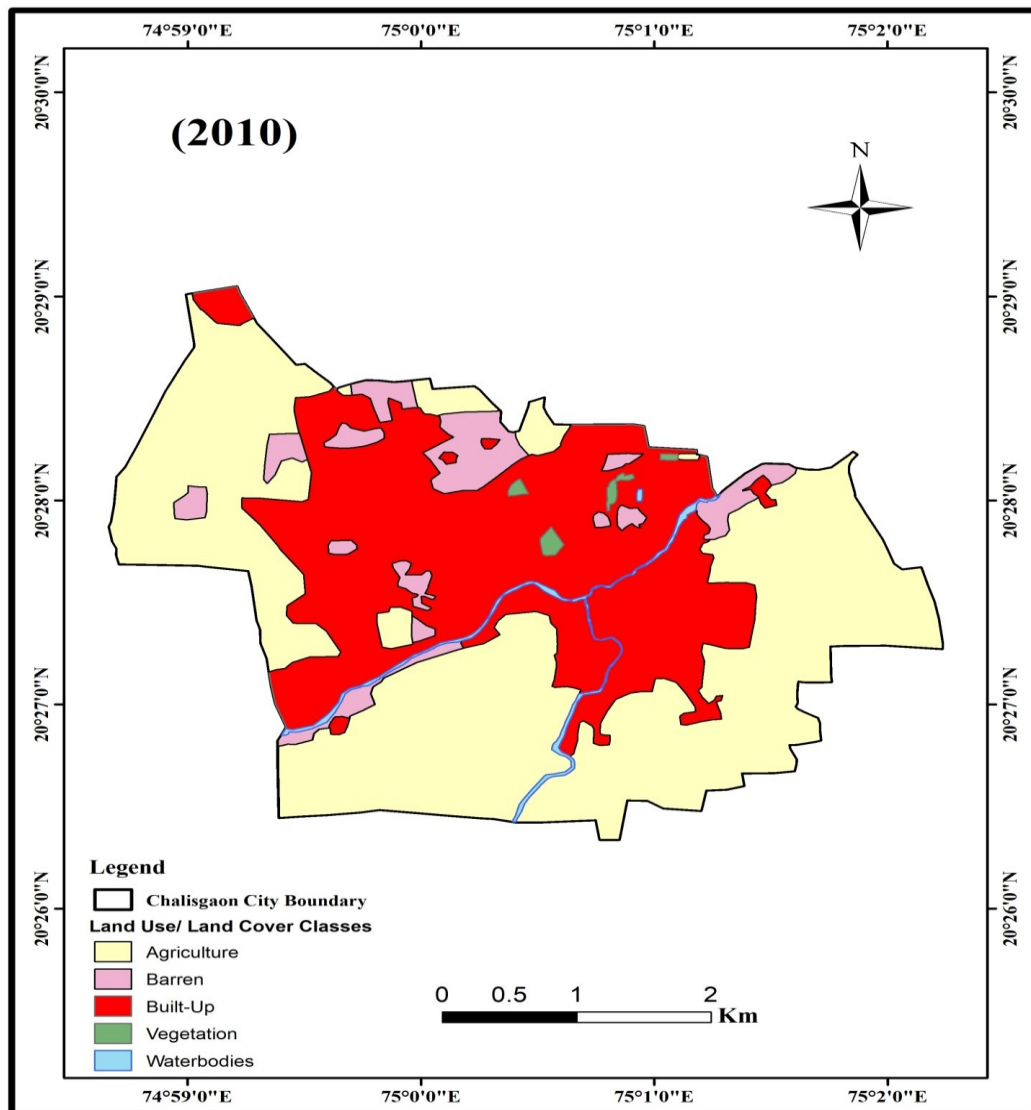


Figure 4. Land use/ land cover map of Chalisgaon city for the year 2010

Table 4. Accuracy Assessment of Land use /land cover classification

LULC Classes	1990		2000		2010		2020	
	PA (%)	UA (%)						
Built up	90.00	81.82	90.92	83.33	88.87	80.12	91.60	84.61
Barren	77.78	87.50	77.91	77.78	88.98	88.83	80.12	88.86
Agriculture	100.00	91.67	81.88	90.01	86.67	92.85	86.64	92.13
Vegetation	80.12	100.00	67.42	66.67	100.00	85.71	100.00	100.00
Waterbody	100.00	100.00	84.75	83.76	83.33	100.00	100.00	100.00
Overall accuracy	90.00%		81.45%		88.82%		91.48	
Kappa coefficient	0.87		0.78		0.85		0.87	

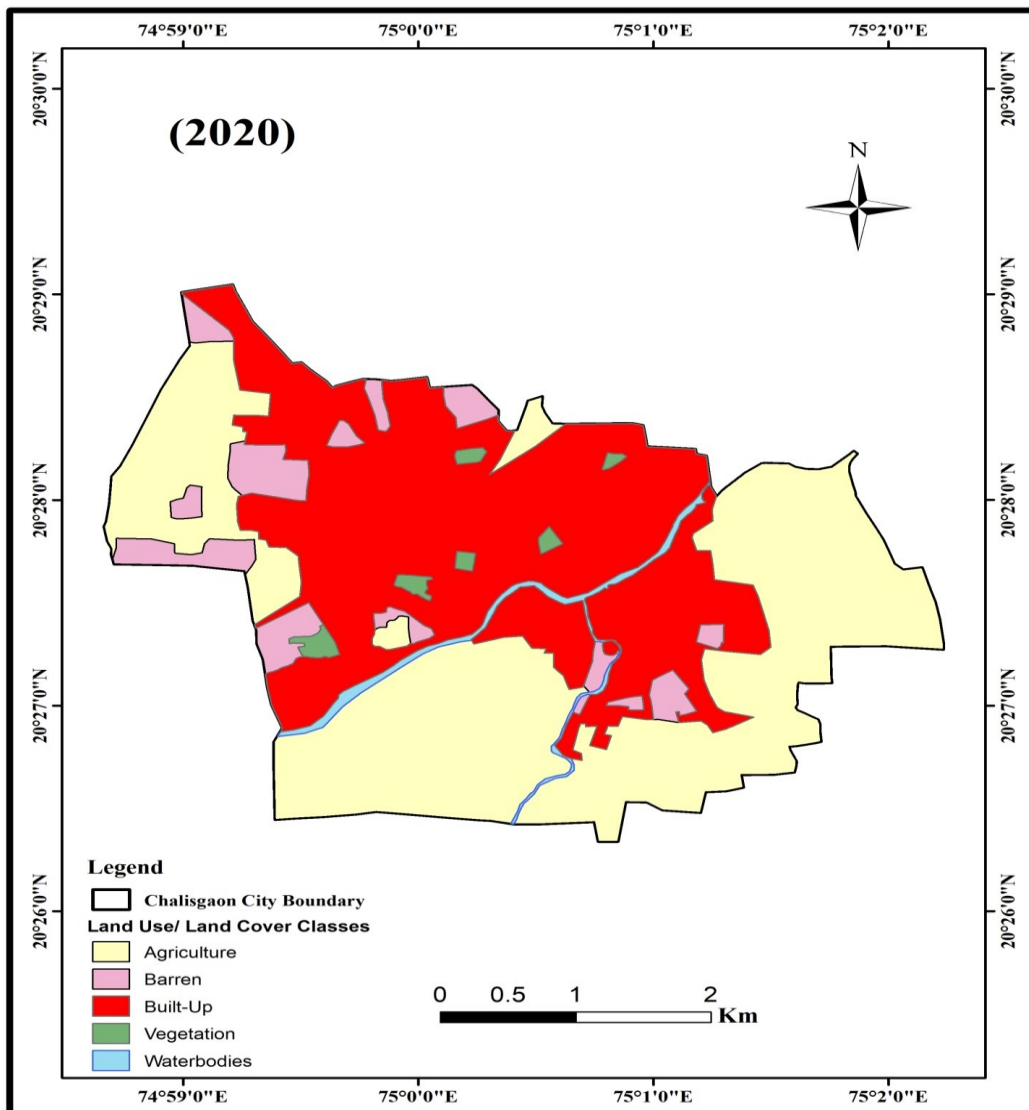


Figure 5. Land use/ land cover map of Chalisgaon city for the year 2020

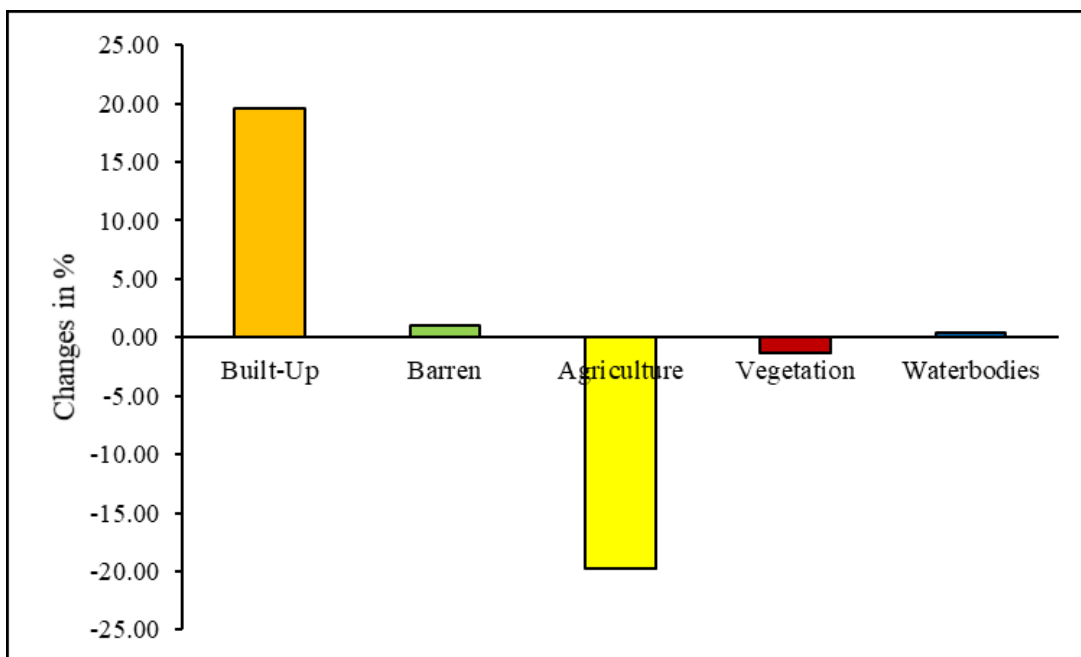


Figure 6. Changes of different land use land cover from 1990 and 2020 for Chalisgaon city

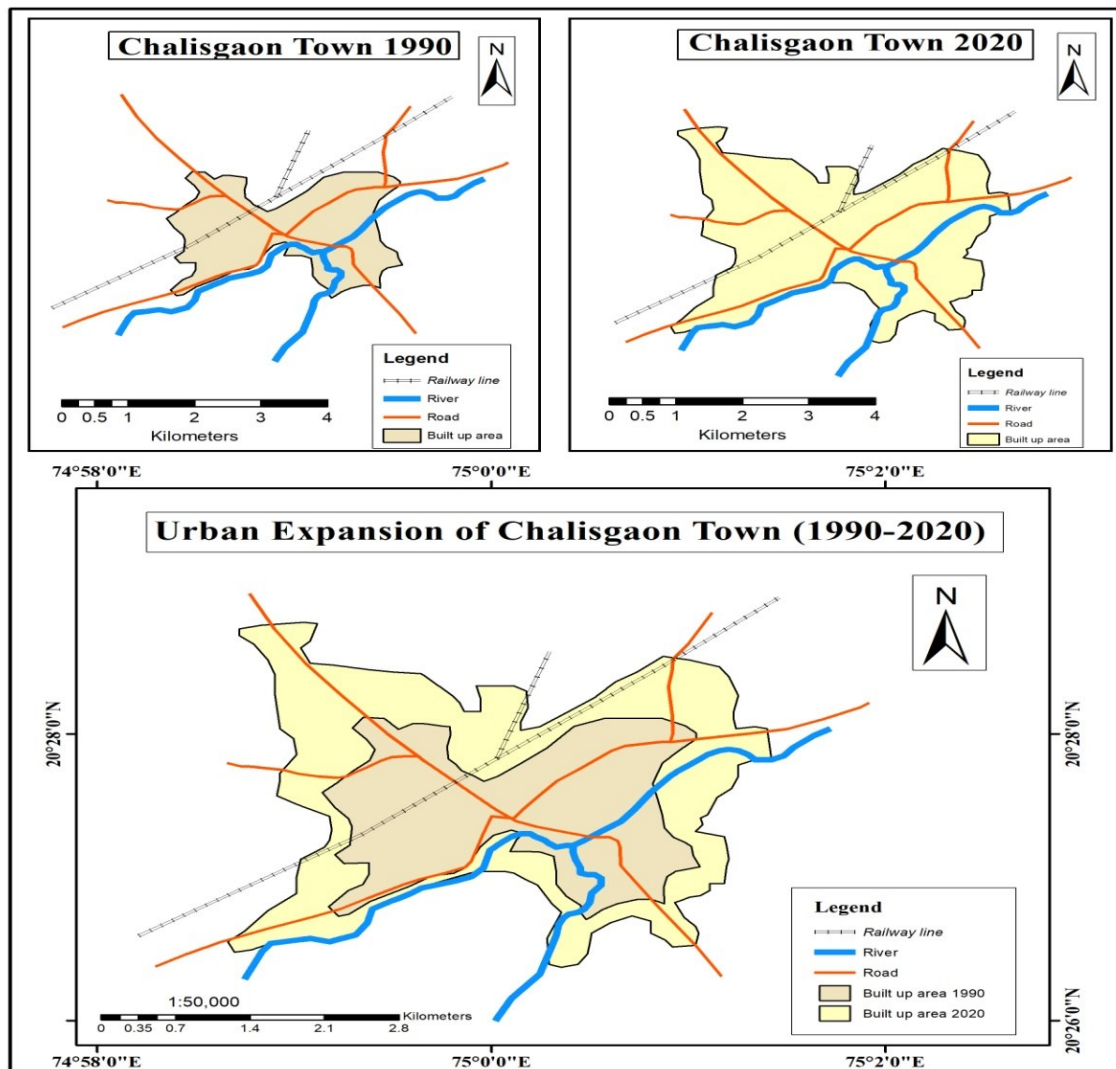


Figure 7. Map showing urban expansion since the year 1990 till 2020 in Chalisgaon city

### 3.3 Accuracy measurement of classification

Utilizing 150 control points from the LULC classified images for each year, the accuracy evaluation was utilized to validate the identification. The overall accuracy, producer's accuracy, and user's accuracy were computed separately. The condensed results of the assessment were plotted in Table 4. The matrix's diagonal elements are the only ones considered for overall accuracy. The overall accuracies were determined to be 90.00, 81.45, 88.82, and 91.48 for 1990, 2000, 2010, and 2020, respectively. The kappa coefficient values for the grouped images are 0.87, 0.78, 0.85, and 0.87 respectively. The accuracy result indicates that there is a strong association between digital classifications and ground reality (reference points) (Congalton, 1991). This sensible overall accuracy satisfied the change detection analysis criteria and was acceptable (Anderson et al., 1976; Lea and Curtis, 2010).

## 4. Conclusions

Agricultural The loss of agricultural land due to urban expansion and the urban lean in public funding for infrastructure, services, and subsidies are just illustrations of how modernization is frequently seen as having adverse effects on agriculture. The study shows that the impact of urban expansion of degradation of agricultural land in the

study area was investigated the year 1990 to 2020. The land use/land cover study of the area under investigation was prepared using Landsat imageries. The maximum likelihood classification and minimum distance classification methods were used for thematic mapping of Landsat images. The results showed that land use land cover classes of Chalisgaon city have experienced rapid changes, particularly in built-up and agricultural land. Urbanization is the main cause for development in the region, and a huge area of cultivated land has been converted into a built-up land. Population explosion and changing land-use patterns are core responsible factors of urbanization. Built-up area of Chalisgaon city observed a general increment of 19.64% of the total area i.e., from 556 hectares to 920 hectares and the study area has lost about 365 hectares of fertile agriculture land during the study period 1990 to 2020. The accuracy assessment of the has been done by using Kappa coefficient, results shows that good accuracy for the study area. The overall accuracy is varies from 81.45% to 91.487%, while kappa coefficient is more 0.78 refers good accuracy. The result of this study can serve as basic information for policymakers and planners at the local level of administration to ensure that urban expansion information in the Chalisgaon city is smart and sustainable.

## References

- Alphan H. (2003). Land- use change and urbanization of Adana Turkey, *Land degradation and development* 14(6), pp. 575-586.
- Anderson J. R., E. E. Hardy, J. T. Roach and R. E. Witmer (1976). A Land Use and Land Cover Classification System for Use with Remote Sensor Data. Us Geological Survey Professional Paper 964, A Revision of the Land Use Classification System as Presented in U.S. Geological Survey Circular 671, United States Government Printing Office, Washington DC.pp.20357
- Congalton R. (1991). A review of assessing the accuracy of classification of remotely sensed data. *Remote Sensing Environment Elsevier Publishing*, 37(1), pp. 35-46.
- Duijine V., R. J., & Nijman, J. (2019). India's emergent urban formations. *Annals of the American Association of Geographers*, 109(6), pp.1978-1998
- Dadashpoor H. and S. Ahani (2019). Land tenure-related conflicts in peri-urban areas: A review. *Land Use Policy*, 85, pp.218-229.
- Gong J., Z. Hu, W. Chen, Y. Liu and J. Wang (2018). Urban expansion dynamics and modes in metropolitan Guangzhou, China. *Land Use Policy*, 72, pp.100-109.
- Grimm N. B., S. H. Faeth, N. E. Golubiewski, C. L. Redman, J. Wu, X. Bai and J. M. Briggs (2008). Global change and the ecology of cities. *science*, 319 (5864), pp.756-760.
- Gumma M. K., I. Mohammad, S. Nedumaran, A. Whitbread and C. J. Lagerkvist (2017). Urban sprawl and adverse impacts on agricultural land: A case study on Hyderabad, India. *Remote sensing*, 9(11), pp.1136.
- Hasan, M. M., R. Islam and M. S. Rahman (2021). Analysis of land use and land cover changing patterns of Bangladesh using remote sensing technology. *American Journal of Environmental Sciences*, 17(3), pp.71-81.
- Jia M., Y. Liu, S. N. Lieske and T. Chen (2020). Public policy change and its impact on urban expansion: An evaluation of 265 cities in China. *Land Use Policy*, 97, pp.104754.
- Kantakumar L. N., S. Kumar and K. Schneider (2016). Spatiotemporal urban expansion in Pune metropolis, India using remote sensing. *Habitat International*, 51, pp.11-22.
- Lea C. and A. Curtis (2010). Thematic accuracy assessment procedures: National Park Service Vegetation Inventory, version 2.0. National Park Service, Fort Collins, Colorado: Natural resource report NPS/2010/NRP-2010/204.
- Liu F., Z. Zhang and X. Wang (2019). Urban expansion in Xiongan New Area since 1975. *Geocarto International*, 34(14), pp.1568-1583.
- Liu X., X. Li, Y. Chen, Z. Tan, S. Li and B. Ai (2010). A new landscape index for quantifying urban expansion using multi-temporal remotely sensed data. *Landscape ecology*, 25(5), pp.671-682.
- López E., G. Bocco, M. Mendoza and E. Duhau (2001). Predicting land-cover and land-use change in the urban fringe: A case in Morelia city, Mexico., *Landscape and urban planning* 55(4), pp.271-285.
- Ma Q., C. He, and J. Wu (2016). Behind the rapid expansion of urban impervious surfaces in China: Major influencing factors revealed by a hierarchical multiscale analysis. *Land Use Policy*, 59, pp.434-445.
- Meng L., Y. Sun and S. Zhao (2020). Comparing the spatial and temporal dynamics of urban expansion in Guangzhou and Shenzhen from 1975 to 2015: A case study of pioneer cities in China's rapid urbanization. *Land Use Policy*, 97, pp.104753.
- Mishra V. (2002). Population growth and intensification of land use in India, *International Journal of Population Geography* 8(5), pp.365-383.
- Rahman A. (2007). Application of remote sensing and GIS technique for urban environmental management and sustainable development of Delhi, India., In *Applied remote sensing for urban planning, governance and sustainability*, pp.165-197.
- Richards J. (1999), *Remote Sensing Digital Image Analysis*, Berlin: Springer-Verlag, 240 pp.31-49
- Roca Z. (1993). Urbanization and rural women: Impact of rural-to-urban migration. Rome, United Nations Food and Agriculture Organization, pp.1-10.
- Saini V. and R. K. Tiwari (2020). A systematic review of urban sprawl studies in India: a geospatial data perspective. *Arabian Journal of Geosciences*, 13(17), pp.1-21.
- Salem M., A. Bose, B. Bashir, D. Basak, S. Roy, I.R. Chowdhury, ... and N. Tsurusaki (2021). Urban expansion simulation based on various driving factors using a logistic regression model: Delhi as a case study. *Sustainability*, 13(19), pp.10805.
- Sharma M. and R. K. Abhay (2022). Urban growth and quality of life: inter-district and intra-district analysis of housing in NCT-Delhi, 2001–2011–2020. *GeoJournal*, pp.1-23.
- Songsore J. (1977). Towards building a model of urban growth dynamics: the case of large northern Ghanaian towns. *Universitas (Legon)* 6, pp.1-17.

Tewolde M. G. and P. Cabral (2011). Urban sprawl analysis and modeling in Asmara, Eritrea. *Remote Sensing* 3(10), pp. 2148-2165.

Tripathy P. and A. Kumar (2019). Monitoring and modelling spatio-temporal urban growth of Delhi using Cellular Automata and geoinformatics., *Cities*, 90, pp.52-63.

Vani M. and P. Prasad (2020). Assessment of spatio-temporal changes in land use and land cover, urban sprawl, and land surface temperature in and around Vijayawada city, India. *Environment, Development and Sustainability*, 22(4), pp.3079-3095.

Vellinga P. and N. Herb (1999). *Industrial Transformation Science Plan*, IHDP Report 12 Bonn, Germany., pp.12-29

Zhang Z, F. Liu, X. Zhao, X. Wang, L. Shi, J. Xu, S. Yu, Q. Wen, L. Zuo, L. Yi, S. Hu and B. Liu (2018), Urban expansion in China based on remote sensing technology: a review *Chin. Geogr. Sci.*, 28 (5), pp.727-743

Zhong Y., A. Lin, L. He, Z. Zhou and M. Yuan (2020). Spatiotemporal dynamics and driving forces of urban land-use expansion: a case study of the Yangtze River economic belt, China. *Remote Sensing*, 12(2), pp.287.

## A spatio-temporal analysis of changing trends in rainfall pattern: A case study of Kutch District

Lakhan Jain\* and Bindu Bhatt  
The Maharaja Sayajirao University of Baroda, Vadodara  
\*Email: [igeographers@gmail.com](mailto:igeographers@gmail.com)

(Received: Dec 30, 2021; in final form: Sep 21, 2022)

**Abstract:** Changing trends captivate millions of analytical minds. It grabs much when the impact on human lives and properties is involved. The utmost concern is changing weather patterns, which led to a worse impact on the amount and distribution of the precipitation. Essentially, the challenge in several nations is to reach the whole population with adequate water per day. Even a country like India, which has thousands of rivers, streams, lakes, ponds, etc. unable to reach the whole population, as it depends on the uneven event, the Monsoon for its >80% annual rain during monsoon months (June-September). The Nation's westernmost district, Kutch, which holds the title for the largest area-wise district in India, has been bearing from changing trends in rainfall for a long time. The rainfall distribution within the district is uneven and has experienced contrasting extreme events like drought and flood within consecutive years. The present study attempts to analyse the Spatio-temporal rainfall pattern for 58 years from 1961 to 2018 for the Kutch district using the IMD4 long-term daily gridded (High Spatial Resolution,  $0.25^\circ \times 0.25^\circ$ ) rainfall dataset. In addition, the Mann-Kendall (MK) test and Sen's slope method were performed to detect the trends and the magnitude of change over the studied period, respectively. The results indicate high rainfall variability during monsoon months in the north and northwest, while relatively moderate and low in the south and west parts of the district, respectively, and show an upward trend in monsoon rainfall at a 5% significance level in all the Taluka of the Kutch district.

**Keywords:** Rainfall Variability, Trend, Mann-Kendall, Sen's Slope, IMD

### 1. Introduction

Studies to detect climate change and its impact on the various sectors deserve urgent attention in light of the impact of climate change on agriculture, increased risk of hunger (Solomon, S. et al., 2007), water scarcity, rapid melting of glaciers, and decreased river flows (Jain et al., 2013). Climate may vary in different ways over different time scales and geographical scales (Mehta & Yadav, 2021; Zarch et al., 2011). Many researchers have been focusing on rainfall and temperature trend and forecasting future values and changes in climate all over the world to understand the effects of climate change (Deoli & Rana, 2019). Climate variability in the arid parts of India poses a great risk to the people and resources of these regions (Attri & Tyagi, 2010; Narayanan et al., 2013) as the smallest fluctuations of weather parameters like precipitation, not only damage the agriculture and economy of the region but disturb the overall water cycle (Krishna Kumar et al., 2004; Narayanan et al., 2013; Zhang et al., 2011).

Although climate change is a broad area of research, the changing pattern of precipitation deserves urgent and systematic attention as it will affect the availability of food supply (Jain et al., 2013). Rainfall contributes significantly to the hydrological cycle, and the Spatio-temporal rainfall variability is crucial from both a scientific and a socioeconomic standpoint (Mehta & Yadav, 2021; Ramkar & Yadav, 2019). Precipitation changes used to have a substantial impact on society, and thus it's necessary to have up-to-date data to predict where precipitation is occurring and how much it varies (Gajbhiye et al., 2016; Yaduvanshi et al., 2015). Floods and droughts would occur due to the precipitation trend's abrupt change (Edossa et al., 2010; Gajbhiye et al., 2016). Long-term rainfall pattern detection is required to understand the problems associated with flooding, droughts, and various uses of water (Mehta

& Yadav, 2021). It will improve the outcome of future climatic scenarios (Edossa et al., 2010). Therefore, regular precipitation monitoring is necessary for better analysis and forecasting (Mehta & Yadav, 2021).

Understanding and quantifying long-term rainfall variability at the regional scale is crucial for a country like India, where economic growth is much dependent on agricultural production, which is linked closely to rainfall distribution (Mohapatra et al., 2021). In the past, several attempts have been made to identify national and regional rainfall trends in India (Gajbhiye et al., 2016). The ability to predict potential future changes using trend analysis has shown to be a beneficial tool (Islam et al., 2014; Yue & Hashino, 2003). Even before the 17th century, researchers in India began to study the rainy season, and since then, scientific research has advanced due to improved knowledge and forecasting tools. India's economy is heavily dependent on agriculture. Hence research into the space-time variability of rainfall assumes enormous significance (Davey & Pielke, 2005). As per estimates, India experiences large spatial variations in annual precipitation, with a lower value of 35% in Tamilnadu and Pondicherry, while in contrast, Gujarat experiences maximum variations (95%). Therefore, studying rainfall variability in Gujarat is of the utmost. The findings may be applicable at the micro-level only because rainfall in the State varies from less than 500 mm in the arid Kutch regions to more than 2500 mm in the South Gujarat region (Priyan, 2015).

The present study attempts to understand the Spatio-temporal variability of monsoon rainfall from 1961 to 2018 in the Kutch district of Gujarat. In addition, the study involves a monotonic trend analysis of rainfall data for the Kutch district. Although the trend assessment can be done using several methods, The Mann-Kendall (MK) test and the Sen's slope estimator have been used in the present

study and are the most widely employed methods for hydrological trend analysis. The handling of missing data, the requirement for a few assumptions, the independence of the data distribution (Ali et al., 2019; Dabanlı et al., 2016), and searching for a trend in a time series without specifying whether the trend is linear or non-linear are one of the few benefits of these non-parametric methods and are known to be more resistant to outliers than other analysis techniques (Luo et al., 2020).

**2. Materials and methods**

**2.1 Study area**

Being the largest and westernmost district of the Nation, Kutch (Kachchh) has covered about 45,674 sq. km. of area. The district lies between latitudes 22°44'11 to 24°42'25 and longitudes 68°09'46 to 71°55'47. The district is bounded on the north and northwest by Pakistan, northeast by the state of Rajasthan, east by districts of Banaskantha and Patan, South-east by Surendranagar and Morbi districts, South by the Gulf of Kutch, and South-west by the Arabian Sea (<https://kachchh.nic.in/about-district/>). The district has 10 Taluka viz. Abdasa, Anjar, Bhachau, Bhuj, Gandhidham, Lakhpat, Mandvi, Mundra, Nakhatrana, and Rapar (<https://www.census2011.co.in/data/district/182-kachchh-gujarat.html>).

**2.2 Data source**

The India Meteorological Department (IMD) maintains weather observatories in India; they calibrate all instruments and check the quality of all observed data (Dave & James, 2017). Long-term daily gridded (High spatial Resolution, 0.25 x 0.25) rainfall data over India for the year 1961-2018 has been collected from the Indian Meteorological Department Library. The unit of rainfall is in millimetres (mm). The yearly data file consists of 365/366 records corresponding to non-leap/ leap years (Pai et al., 2014). For operational convenience, the Indian land area is divided into 36 meteorological subdivisions by the IMD. Primarily, such a classification is meant for generating weather forecasts over political boundaries like states (Mohapatra et al., 2021; Saikranthi et al., 2013).

The present study is based on a newly developed high spatial resolution IMD4 dataset that was interpolated at fixed spatial grid points of 0.25° x 0.25° resolution nationwide (Pai et al., 2014) for the Kutch district (Figure 1). The distribution of 60 grid points containing the rainfall data over the Kutch district is shown in Table 1.

**Table 1. Distribution of grid points Taluka-wise.**

Taluka	Grid points
Abdasa	3
Anjar	1
Bhachau	3
Bhuj	8
Gandhidham	2
Lakhpat	4
Mandvi	2
Mundra	1
Nakhatrana	3
Rapar	4
Rann*	29

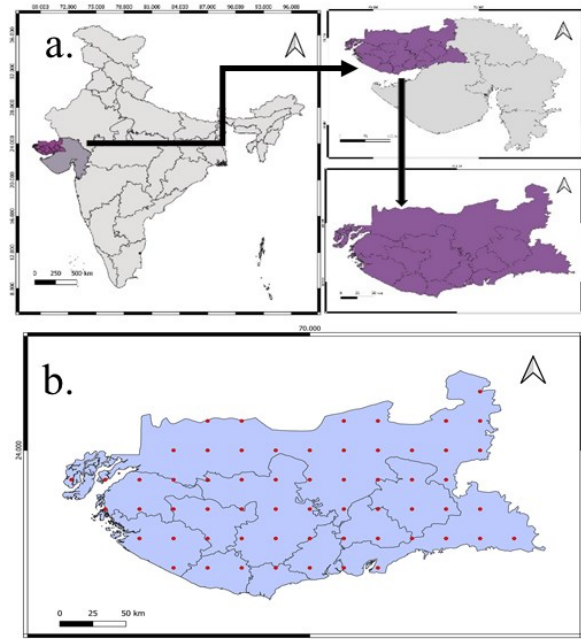


**Figure 1. a: Location of Kutch in Gujarat and India, 1b: Distribution of grid points over the Kutch district.**

Stations are separated as per IMD criteria:

1. Winter season (January- February),
2. Pre-monsoon season (March-May),
3. Monsoon season (June-September),
4. Post-monsoon season (October- December).

**2.3 Methods**

The flowchart in Figure 2 illustrates the methods used in the study. At first, the Python console (plugin to QGIS) has used to collect grid points containing the rainfall data for the Kutch district from IMD Library.

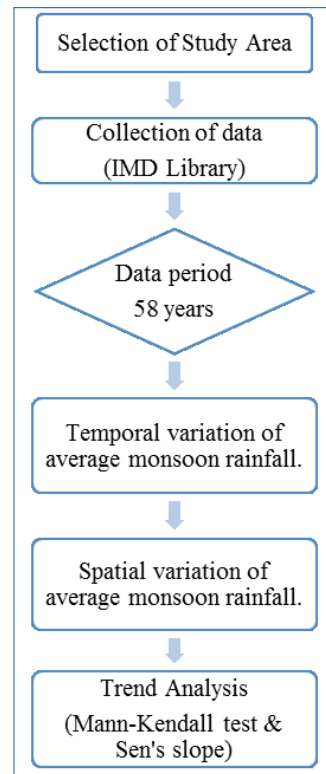


**Figure 2. Flowchart of the methodology adopted**

Later, an intersection algorithm has performed to extract the overlapping portions of features in the input data (Study area) and overlay layers (grid points). The intersection algorithm is applied separately for each taluka of the Kutch district to extract the overlapping grid points. Basic statistical parameters, including mean, standard deviation (SD), and coefficient of variation, have been determined as part of the analysis's initial stage using rainfall data for each Taluka in the Kutch district.

2.3.1 Spatio-temporal Rainfall Variability

Rainfall variability and probability trends were determined using IMD4 daily gridded rainfall data. The coefficient of variation (CV), derived from the mean and standard deviation (Sample), has been calculated as follows:

$$\text{Coefficient of variation} = \frac{\text{Standard deviation}}{\text{Mean}} \times 100 \quad (1)$$

The CV is a standardization of the standard deviation, allowing for comparison of variability estimates regardless of the magnitude of analyte concentration, at least for the majority of the assay's working range (Reed et al., 2002). Whereas, Standard deviation is calculated by

$$SD = \frac{\sqrt{1}}{n-1} \sum (x_i - \bar{x})^2 \quad (2)$$

Here,  $\bar{x}$  is the Arithmetic mean of the observations, and SD is the Sample standard deviation.

A 5-years moving average was applied to smoothen out the variability in the monsoon rainfall over 58 years (1961-2018) at 10 Taluka of the Kutch district.

2.3.2 Trend Analysis

**Mann-Kendall Test**

A rank-based non-parametric Mann-Kendall (MK) test has been used in this study and is considered the most popular test used for trend analysis of hydro meteorological data (Yue & Hashino, 2003). (Mann, 1945) primarily used this test, and (Kendall, 1975) subsequently derived the test statistic distribution. The Mann-Kendall test performs well with skewed variables, can manage missing values, and is resistant to the impact of extremes (Deni et al., 2010; Mishra et al., 2009). Furthermore, other researchers have primarily employed this approach to detect rainfall trends in their studies and got reliable results (Basistha et al., 2009; CHEN et al., 2007; Dufek & Ambrizzi, 2008; Goswami et al., 2006; Patra et al., 2012; Rio et al., 2011; Rose, 2009)

For a series  $X_1, X_2, \dots, X_n$  (Sharma & Singh, 2017), S statistics can be given by:

$$S = \sum_{i=1}^{n-1} \sum_{j=i+1}^n \text{sgn}(X_j - X_i) \quad (3)$$

where  $X_i$  is ranked from  $i = 1, 2, \dots, n - 1$  and  $X_j$  is ranked from  $j = i + 1$  and  $n$  is the length of the data set.

$$\text{sgn}(\theta) = \begin{cases} 1 & \dots \text{if } \theta > 0 \\ 0 & \dots \text{if } \theta = 0 \\ -1 & \dots \text{if } \theta < 0 \end{cases} \quad (4)$$

The test statistics S's positive/negative signs imply an upward/ downward trend in the data. The Mann-Kendall statistics' variance for a sample size of  $n = 8$  is given by (Patra et al., 2012; Sharma & Singh, 2017):

$$\text{Var}(S) = \frac{[n(n-1)(2n+1) - \sum_t t(t-1)(2t+5)]}{18} \quad (5)$$

where  $t_i$  is the number of ties present up to sample  $i$  (Sharma & Saha, 2017).

The following formula has been used to estimate the standardised MK test statistics (Z) (Sharma & Singh, 2017):

$$Z = \begin{cases} \frac{s-1}{\sqrt{V(s)}} & \text{if } S > 0 \\ 0 & \text{if } S = 0 \\ \frac{s+1}{\sqrt{V(s)}} & \text{if } S < 0 \end{cases} \quad (6)$$

The Z follows a standard normal distribution with zero mean and unit variance, where the positive value indicates an upward trend while a negative value indicates a downward trend. If the value of Z is greater than  $Z_{\alpha/2}$ , then it is considered a significant trend (where  $\alpha$  is the significance level) (Sharma & Singh, 2017; Yao et al., 2018). In this study, significance level  $\alpha = 0.05$  has used.

**Sen's slope**

Theil-Sen's estimator calculates the magnitude of the rainfall trend (Sen, 1968; Theil, 1950). Sen's nonparametric approach have used to calculate the true slope of an existing trend (as a change annually) and is also used in cases where the trend is linear (Thenmozhi & Kottiswaran, 2016). The slope estimates of N pairs of data are primarily calculated by

$$\beta = \left[ \frac{X_i - X_j}{i - j} \right] \text{ for } i = 1, n \quad (7)$$

Here  $X_i$  and  $X_j$  are data values at the time  $i$  and  $k$ , respectively, where ( $i > j$ ). The median of the N values of  $\beta$  is Sen's estimator slope (Narayanan et al., 2013), which is calculated as

$$N = (n(n-1))/2 \quad (8)$$

The practical significance of a trend was assessed using Theil and Sen's median slope and evaluating the percentage change over the mean for the relevant period because statistically significant trends might not have practical significance and vice versa (Narayanan et al., 2013). The monotonic trend is measured using  $\beta$  (Kundu et al., 2015; Xu et al., 2003). When  $\beta > 0$ , the time series indicates an upward trend; otherwise, a downward trend prevails (Luo et al., 2020).

**3. Results and discussion**

Monsoon Months (June-September) receive about 94% of annual rain in the Kutch district. The uneven phenomenon,

Monsoon generally arrives at the end of June over the Kachchh district, while it withdraws to mid-September. Figure 3. indicates a high variation in monsoon rainfall in the Kutch district, which has experienced deficit, and surplus rain years often and within consecutive years and showed a long-term increasing trend in monsoon rainfall, while an insignificant decline trend was found between 2009 to 2018 for monsoon rain showed in Figure 4.

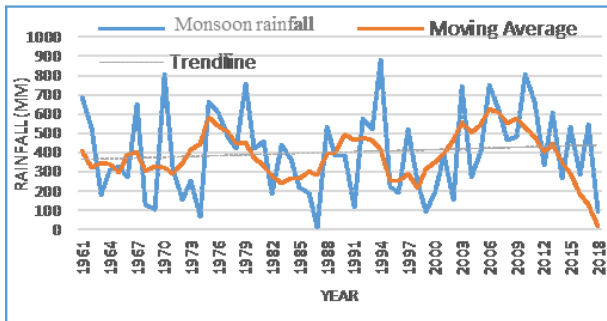


**Figure 3. Monsoon rainfall for the Kutch district (1961-2018) with a 5-years Moving average.**

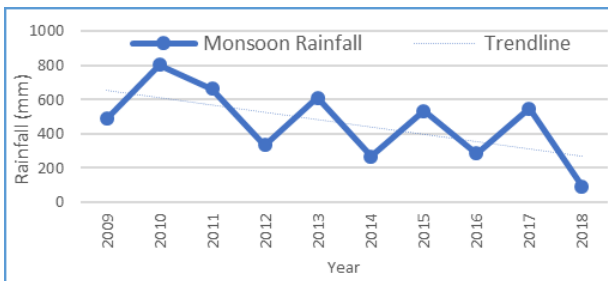


**Figure 4. Variation in monsoon rainfall of the Kutch district, 2009-2018.**

**Criteria analysis**

The annual rainfall during the studied period has been classified (Table 2.) as a deficit, below normal, normal, above average, and surplus based on Central Arid Zone Research Institute report, which has prepared by R. S. Singh (Lakhia, 2016).

**Table 2. Criteria to classify the annual rain years.**

Type	Definition
<b>Deficit years</b>	A year receiving the rainfall less than 50% to the normal annual rainfall.
<b>Below Normal years</b>	A year receiving the rainfall between 50 to 75% of the normal annual rainfall.
<b>Normal Years</b>	A year receiving the rainfall between 75 to 125% of the normal annual rainfall
<b>Above Normal years</b>	A year receiving rainfall between 125% to 150% of the normal annual rainfall.
<b>Surplus years</b>	A year receiving a rainfall of 150 % or more to the normal annual rainfall.

According to the analysis (Table 3), Kutch has experienced 11 (18.96%) deficit years, 10 (17.24%) years with below-

normal rainfall, 19 (32.75%) years with normal rainfall, 8 (13.79%) years with above-average rainfall, and 10 (17.24%) years with surplus rainfall over the studied period of 58 years.

**Table 3. Distribution of Rainfall for the Kutch District.**

Deficit years <215m m	Below Normal years 215-324m m	Normal years 324-540mm	Above Normal years 540-646m m	Surplus years >646m m	
1968	1963	1962	1998	1976	1961
1969	1964	1965	1999	1980	1967
1972	1966	1977	2001	1981	1970
1974	1971	1978	2005	1992	1975
1986	1973	1983	2008	2007	1979
1987	1982	1984	2009	2013	1994
1991	1985	1988	2012	2015	2003
1996	1995	1989	2016	2017	2006
2000	2004	1990			2010
2002	2014	1993			2011
2018		1997			
<b>Total 11 years</b>	<b>Total 10 years</b>	<b>Total 19 years</b>	<b>Total 8 years</b>	<b>Total 10 years</b>	

**Seasonal distribution**

Kutch receives its maximum rain during the monsoon months between June to September, followed by Post-monsoon, Pre-monsoon, and least rain during the winters. Non-Monsoon months contribute nearly 6% to the average annual rainfall. Post-monsoon months (October-December) contribute maximum rain among the non-monsoon months, i.e., ≤4% of annual rainfall, while October receives the highest rain during the Post-monsoon months. One of the vital causes of heavy rainfall during the Post-monsoon months is the occurrence of a cyclone or late withdrawal of monsoon. Whereas, Pre-monsoon and winter seasons contribute less precipitation and receive rain due to the occurrence of local events and western disturbances. While examining the trend of rainfall in the Kutch district, monsoon rain has been considered and taken into account. The temporal variation of the monsoon rainfall at 10 Taluka was examined individually from 1961 to 2018 (Figure 5).

The mean monsoon rainfall for the Kutch district is 402.28 mm over the studied period of 58 years (Table 4). The Coefficient of variation and probability of monsoon rainfall is 54.34% and 45.65%, respectively. Table 5. highlights the mean, CV, and monsoon rainfall probability for all the Taluka of the Kutch district, including Rann.

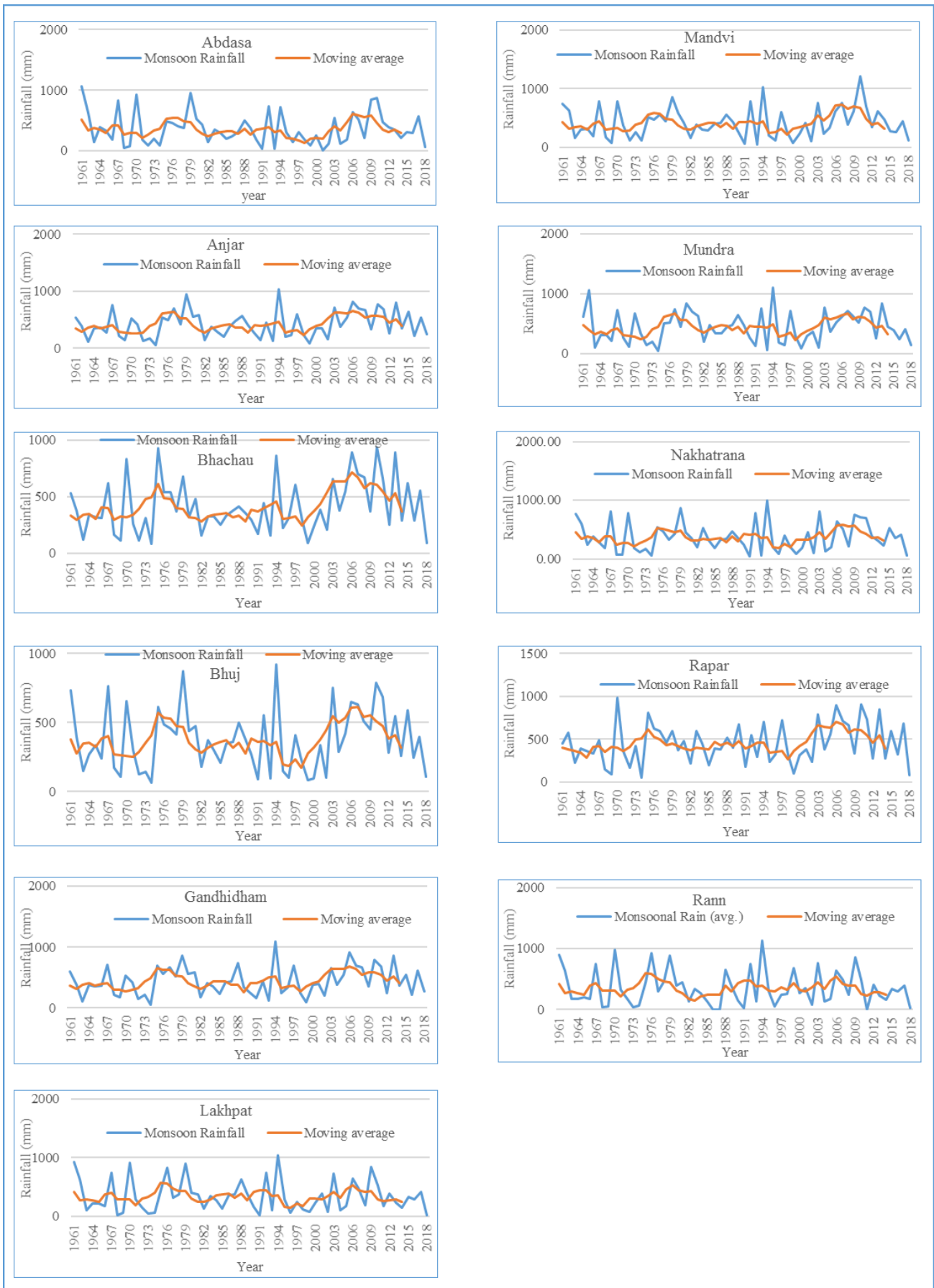


**Figure 5. Temporal variations of average monsoon rainfall for the Taluka of Kutch district (1961-2018) with a 5 years moving average.**

**Table 4. Monsoon Rainfall Statistics for the Kutch district.**

District	Mean (mm)	Standard deviation (mm)	Coefficient of Variation (%)	Rainfall Probability (%)
Kutch	402.28	218.62	54.34	45.65

**Table 5. Monsoon Rainfall Statistics for the Taluka of Kutch district. \*Not included as Taluka.**

Taluka	Mean (mm)	Standard deviation (mm)	Coefficient of Variation (%)	Rainfall Probability (%)
Abdasa	394.72	271.74	68.84	31.16
Anjar	441.24	243.50	55.18	44.82
Bhachau	427.55	262.67	61.43	38.57
Bhuj	388.56	244.21	62.85	37.15
Gandhidham	465.39	254.11	54.60	45.40
Lakhpat	367.00	275.78	75.14	24.86
Mandvi	439.50	271.72	61.82	38.18
Mundra	452.84	272.82	60.24	39.76
Nakhatrana	389.74	258.80	66.40	33.6
Rapar	499.91	237.68	47.54	52.46
Rann*	353.50	288.47	81.60	18.40

According to (Arnhold & Milani, 2011) criteria to classify the Coefficient of variation depends on the mean and standard deviation of CVs. The calculated mean and standard deviation of CV is 63.24 and 9.59, respectively.

The CVs were ranked as low [ $CV \leq (m - 1 SD)$ ], moderate [ $(m - 1 SD) < CV \leq (m + 1 SD)$ ], high [ $(m + 1 SD) < CV \leq (m + 2 SD)$ ] and very high [ $CV \geq (m + 2 SD)$ ], whereas, m is the mean of the CV, while SD is standard deviation (Arnhold & Milani, 2011).

Accordingly, values of  $CV \leq 53.64\%$  are low,  $53.64\% < CV < 72.83\%$  are moderate,  $72.83\% < CV < 82.42\%$  are high, and  $CV \geq 82.42\%$  are very high. Table 6 shows the maximum number of Taluka fallen in moderate CV class (i.e., 8 Taluka), followed by high (2, including Rann) and low (1). Rapar has the least CV among all the Taluka, while Rann, followed by Lakhpat, has the highest CV (Figure 6).

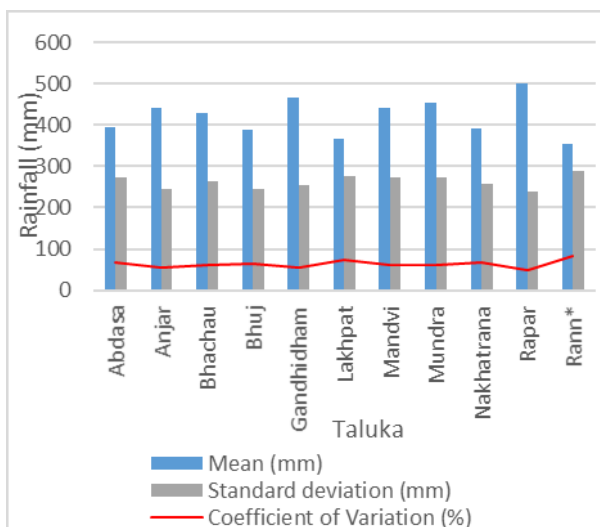


**Figure 6. Taluka-wise monsoon rainfall statistics.**

**Table 6. Classification of Coefficient of variation.**

Range	Value	Number of Taluka (Incl. Rann)
$\leq 53.64$	Low	1
53.64-72.83	Moderate	8
72.83-82.42	High	2
$\geq 82.42$	very high	-

The probability of monsoon rain is high in Rapar (52.46%), followed by Gandhidham and Anjar (45.40% and 44.82%, respectively). While in contrast, a low probability of monsoon rain has been found in Rann (18.40%), followed by Lakhpat (24.86%) (Figure 7).

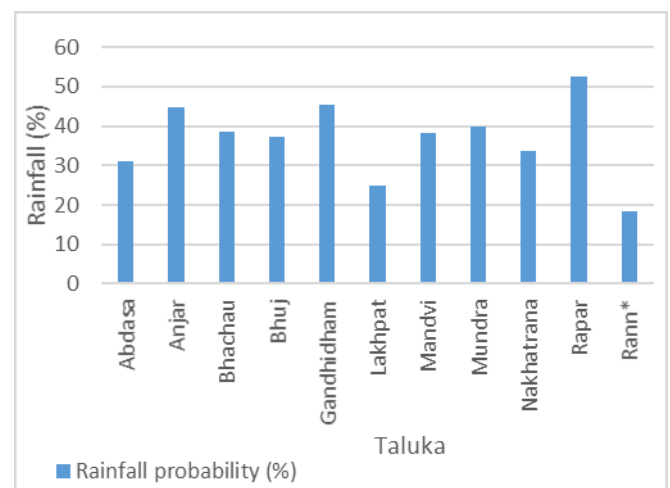


**Figure 7. Taluka-wise monsoon rainfall probability.**

The north and northwest part of the district has high monsoon rain variability which indicates a higher probability of extreme events occurring, while the south and south-central parts have relatively moderate rainfall variability, followed by the west having the lowest rainfall variability among all (Figure 8).

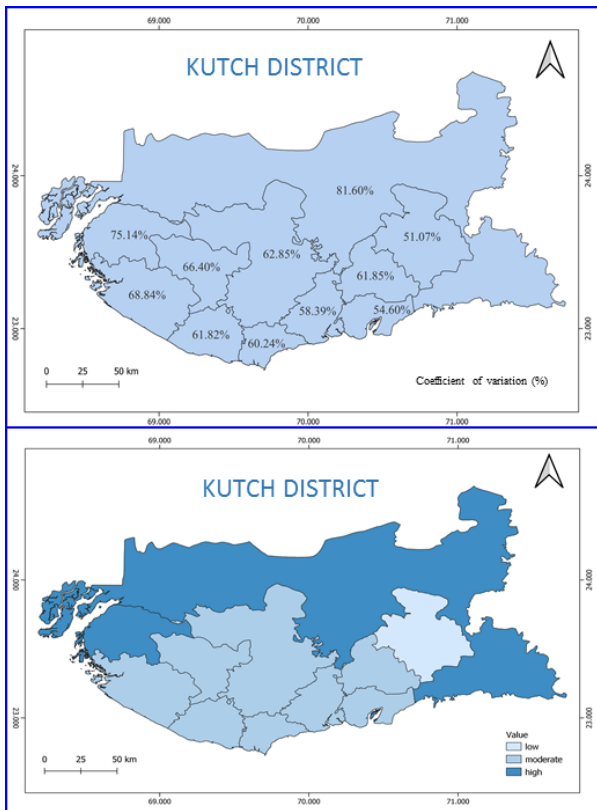


**Figure 8. Rainfall Variability for the Kutch district, 1961-2018.**

Although, the present study demands criteria that classify the Coefficient of variation with its mean and SD i.e., (Arnhold & Milani, 2011), otherwise, the CV above 40% assumes high (Asif et al., 2015), and indicates the higher risk of extreme events occurring.

**Trend analysis**

Table 7. shows a monotonic upward trend in monsoon rainfall for the Kutch district as  $Z > 0$ , i.e., 2.50. at a 5% significance level. The value of  $\beta$  is 2.578, i.e.,  $\beta > 0$ . The positive value of  $\beta$  shows an upward trend in Figure 10.

**Table 7. MK and Sen’s slope statistics for the Kutch district.**

	p-value	Sen’s slope ( $\beta$ )	Alpha ( $\alpha$ )	S	Z
Kutch	0.012	2.578	0.05	33700	2.50

The positive  $\beta$  value ( $\beta > 0$ ) indicates an upward trend in monsoon rainfall over the studied period of 58 years (Figure 9).

The  $\beta$  value for all the Taluka of the Kutch district, including Rann, is  $> 0$  at a 5% significance level. This indicates an upward trend in monsoon rain at all the Taluka (Table 8).

The upward trend has been found ( $Z > 0$ ) in all the Taluka (Figure 10) and Rann of the Kutch district at a 5% significance level (Table 9).

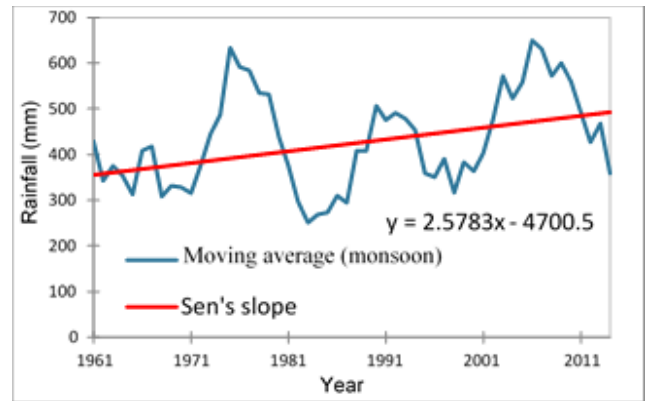


**Figure 9. Trend of Monsoon rainfall for the Kutch district.**

**Table 8. MK and Sen’s slope statistics for the Taluka of Kutch district.**

Taluka	p-value	Sen’s slope ( $\beta$ )	Alpha ( $\alpha$ )	S	p-value < 0.05
Abdasa	0.238	1.270	0.05	158.00	False
Anjar	0.004	3.220	0.05	388.00	True
Bhachau	0.004	4.100	0.05	381.00	True
Bhuj	0.041	2.200	0.05	274.00	True
Gandhidham	0.001	3.754	0.05	432.00	True
Lakhat	0.704	0.376	0.05	051.00	False
Mandvi	0.033	2.425	0.05	286.00	True
Mundra	0.029	2.514	0.05	293.00	True
Nakhatrana	0.063	2.111	0.05	249.00	False
Rapar	0.010	2.304	0.05	347.00	True
Rann*	0.041	2.200	0.05	274.00	True

**Table 9. Z Statistics and trend for the Taluka of Kutch district.**

Taluka	Z	Trend
Abdasa	1.17	Upward
Anjar	2.88	Upward
Bhachau	2.83	Upward
Bhuj	2.03	Upward
Gandhidham	3.21	Upward
Lakhat	0.37	Upward
Mandvi	2.12	Upward
Mundra	2.17	Upward
Nakhatrana	1.85	Upward
Rapar	2.58	Upward
Rann*	2.03	Upward



Figure 10. Trend of Monsoon Rainfall for each Taluka of the Kutch district, 1961-2018

#### 4. Conclusions

The present study involves the observation of rainfall trends using 60 grid points (IMD4 rainfall dataset,  $0.25^\circ \times 0.25^\circ$ ) having the daily gridded rain data over the Kutch district from 1961 to 2018 for 58 years. The observed high rainfall variability in monsoon months during the studied period indicates a higher probability of extreme events occurring in the north and northwest part of the district, while relatively moderate in the south and central Kutch and least among all in Rapar (west). There have been 11 (18.96%) deficit years, 10 (17.24%) years with below-normal rainfall, 19 (32.75%) years with normal rainfall, 8 (13.79%) years with above-average rainfall, and 10 (17.24%) years with surplus rainfall over the studied period of 58 years. The non-parametric Mann-Kendall (MK) test have used to quantify the significance of the rainfall trend, which shows an upward trend for all the Taluka of Kutch district ( $Z > 0$ ) at a significance level of 5%. The Sen's slope shows the trend's magnitude, which results in an upward trend ( $\beta > 0$ ). This study would help us to forecast future rainfall, which is beneficial to prevent extreme events and their consequences.

#### Acknowledgments

The authors acknowledge the Indian Meteorological Department Library for providing rainfall data and the University Grants Commission (UGC) for financial support.

#### References

- Ali R., A. Kuriqi, S. Abubaker and Kisi, O. (2019). Long-term trends and seasonality detection of the observed flow in Yangtze River using Mann-Kendall and Sen's innovative trend method. *Water (Switzerland)*, 11(9). <https://doi.org/10.3390/w11091855>
- Arnhold E. and K. F. Milani (2011). Rank-ordering coefficients of variation for popping expansion. *Acta Scientiarum. Agronomy*, 33(3). <https://doi.org/10.4025/actasciagron.v33i3.11911>
- Asif M., C. Islam-ul-haq, A. G. Mangrio, N. Mustafa and B. Iqbal (2015). Analysis of application uniformity and pressure variation of microtube emitter of trickle irrigation system. *Net Journal of Agricultural Science*, 3(1).
- Attri S. D. and A. Tyagi (2010). Climate profile of India. *Environment Meteorology, India Meteorological Department*.
- Basistha A., D. S. Arya and N. K. Goel (2009). Analysis of historical changes in rainfall in the Indian Himalayas. *International Journal of Climatology*, 29(4). <https://doi.org/10.1002/joc.1706>
- CHEN Y., W. LI Ning, X.U. Hong, C. chun and X. HAO (2007). Effects of climate change on water resources in Tarim River Basin, Northwest China. *Journal of Environmental Sciences*, 19(4). [https://doi.org/10.1016/S1001-0742\(07\)60082-5](https://doi.org/10.1016/S1001-0742(07)60082-5)
- Dabanlı İ., Z. Şen, M. O. Yeleğen, E. Şişman, B. Selek and Y. S. Güçlü (2016). Trend Assessment by the Innovative-Şen Method. *Water Resources Management*, 30(14). <https://doi.org/10.1007/s11269-016-1478-4>
- Dave H. and M. E. James (2017). Characteristics of intense rainfall over Gujarat State (India) based on percentile criteria. *Hydrological Sciences Journal*, 62(12). <https://doi.org/10.1080/02626667.2017.1357818>
- Davey C. A. and R. A. Pielke. (2005). Microclimate exposures of surface-based weather stations: Implications for the assessment of long-term temperature trends. *Bulletin of the American Meteorological Society*, 86(4).
- Deni S. M., J. Suhaila, W. Z. Wan zin and A. A. Jemain (2010). Spatial trends of dry spells over Peninsular Malaysia during monsoon seasons. *Theoretical and Applied Climatology*, 99(3-4). <https://doi.org/10.1007/s00704-009-0147-4>
- Deoli V. and S. Rana (2019). Seasonal Trend Analysis in Rainfall and Temperature for Udaipur District of Rajasthan. *Current World Environment*, 14(2). <https://doi.org/10.12944/cwe.14.2.15>
- Dufek A. S. and T. Ambrizzi (2008). Precipitation variability in São Paulo State, Brazil. *Theoretical and Applied Climatology*, 93(3-4). <https://doi.org/10.1007/s00704-007-0348-7>
- Edossa D. C., M. S. Babel and A. D. Gupta (2010). Drought analysis in the Awash River Basin, Ethiopia. *Water Resources Management*, 24(7). <https://doi.org/10.1007/s11269-009-9508-0>
- Gajbhiye S., C. Meshram, S. K. Singh, P. K. Srivastava and T. Islam (2016). Precipitation trend analysis of Sindh River basin, India, from 102-year record (1901-2002). *Atmospheric Science Letters*, 17(1). <https://doi.org/10.1002/asl.602>
- Goswami B. N., V. Venugopal, D. Sangupta, M. S. Madhusoodanan and P. K. Xavier (2006). Increasing trend of extreme rain events over India in a warming environment. *Science*, 314(5804). <https://doi.org/10.1126/science.1132027>
- Islam T., M. Gupta, S. Mukherjee, P. K. Srivastava and X. Zhu (2014). Computational intelligence techniques in earth and environmental sciences. In *Computational Intelligence Techniques in Earth and Environmental Sciences* (Vol. 9789401786423). <https://doi.org/10.1007/978-94-017-8642-3>
- Jain S. K., V. Kumar and M. Saharia (2013). Analysis of rainfall and temperature trends in northeast India. *International Journal of Climatology*, 33(4). <https://doi.org/10.1002/joc.3483>
- Kendall M. G. (1975). *Rank Correlation Methods* (4th edn.) Charles Griffin. San Francisco, CA.
- Krishna K. K., K. Rupa, R. G. Ashrit, N. R. Deshpande and J. W. Hansen (2004). Climate impacts on Indian agriculture. *International Journal of Climatology*, 24(11). <https://doi.org/10.1002/joc.1081>

- Kundu S., D. Khare, A. Mondal and P. K. Mishra (2015). Analysis of spatial and temporal variation in rainfall trend of Madhya Pradesh, India (1901–2011). *Environmental Earth Sciences*, 73(12). <https://doi.org/10.1007/s12665-014-3978-y>
- Lakhia N. A. (2016). A remote sensing and gis based hydro geomorphic approach for identification of site specific groundwater artificial recharge techniques a study of sakar and sang river basin [The Maharaja Sayajirao University of Baroda]. <http://hdl.handle.net/10603/183039>
- Luo N., D. Mao, B. Wen and X. Liu (2020). Climate change affected vegetation dynamics in the northern Xinjiang of China: Evaluation by SPEI and NDVI. *Land*, 9(3). <https://doi.org/10.3390/land9030090>
- Mann H. B. (1945). Nonparametric Tests Against Trend. *Econometrica*, 13(3). <https://doi.org/10.2307/1907187>
- Mehta D. and S. M. Yadav (2021). An analysis of rainfall variability and drought over Barmer District of Rajasthan, Northwest India. *Water Supply*, 21(5). <https://doi.org/10.2166/ws.2021.053>
- Mishra A. K., M. Özger and V. P. Singh (2009). Trend and persistence of precipitation under climate change scenarios for Kansabati basin, India. *Hydrological Processes*, 23(16). <https://doi.org/10.1002/hyp.7342>
- Mohapatra G., V. Rakesh, S. Purwar and A. P. Dimri (2021). Spatio-temporal rainfall variability over different meteorological subdivisions in India: analysis using different machine learning techniques. *Theoretical and Applied Climatology*, 145(1–2). <https://doi.org/10.1007/s00704-021-03644-7>
- Narayanan P., A. Basistha, S. Sarkar and S. Kamna (2013). Trend analysis and ARIMA modelling of pre-monsoon rainfall data for western India. *Comptes Rendus - Geoscience*, 345(1). <https://doi.org/10.1016/j.crte.2012.12.001>
- Pai D. S., L. Sridhar, M. Rajeevan, O. P. Sreejith, N. S. Satbhai and B. Mukhopadhyay (2014). Development of a new high spatial resolution (0.25° × 0.25°) long period (1901-2010) daily gridded rainfall data set over India and its comparison with existing data sets over the region. *Mausam*, 65(1). <https://doi.org/10.54302/mausam.v65i1.851>
- Patra J. P., A. Mishra, R. Singh and N. S. Raghuwanshi (2012). Detecting rainfall trends in twentieth century (1871-2006) over Orissa State, India. *Climatic Change*, 111(3). <https://doi.org/10.1007/s10584-011-0215-5>
- Priyan K. (2015). Spatial and Temporal Variability of Rainfall in Anand District of Gujarat State. *Aquatic Procedia*, 4. <https://doi.org/10.1016/j.aqpro.2015.02.092>
- Ramkar P. and S. M. Yadav (2019). Rainfall Trend Analysis Using Nonparametric Test: A Case Study of Malegaon City. In *Water Resources and Environmental Engineering II*. [https://doi.org/10.1007/978-981-13-2038-5\\_3](https://doi.org/10.1007/978-981-13-2038-5_3)
- Reed G. F., F. Lynn and B. D. Meade (2002). Use of coefficient of variation in assessing variability of quantitative assays. *Clinical and Diagnostic Laboratory Immunology*, 9(6). <https://doi.org/10.1128/CDLI.9.6.1235-1239.2002>
- Río S. D., L. Herrero, R. Fraile and A. Penas (2011). Spatial distribution of recent rainfall trends in Spain (1961-2006). *International Journal of Climatology*, 31(5). <https://doi.org/10.1002/joc.2111>
- Rose S. (2009). Rainfall-runoff trends in the south-eastern USA: 1938-2005. *Hydrological Processes*, 23(8). <https://doi.org/10.1002/hyp.7177>
- Saikranthi K., T. Narayana Rao, M. Rajeevan and S. Vijaya Bhaskara Rao (2013). Identification and validation of homogeneous rainfall zones in India using correlation analysis. *Journal of Hydrometeorology*, 14(1). <https://doi.org/10.1175/JHM-D-12-071.1>
- Sen P. K. (1968). Estimates of the Regression Coefficient Based on Kendall's Tau. *Journal of the American Statistical Association*, 63(324). <https://doi.org/10.1080/01621459.1968.10480934>
- Sharma S. and A. K. Saha. (2017). Statistical analysis of rainfall trends over Damodar River basin, India. *Arabian Journal of Geosciences*, 10(15). <https://doi.org/10.1007/s12517-017-3096-8>
- Sharma S. and P. K. Singh (2017). Long term spatiotemporal variability in rainfall trends over the state of Jharkhand, India. *Climate*, 5(1). <https://doi.org/10.3390/cli5010018>
- Solomon S., M. Qin, Z. Manning, M. Chen, K. B. Marquis, M. T. Averyt, H. L. Miller, S. Solomon, D. Qin, M. Manning, Z. Chen, M. Marquis, K. B. Averyt, M. Tignor and H. L. Miller (2007). Summary for Policymakers. In: *Climate Change 2007: The Physical Science Basis. Contribution of Working Group I to the Fourth Assessment Report of the Intergovernmental Panel on Climate Change*. D Qin M Manning Z Chen M Marquis K Averyt M Tignor and HL Miller New York Cambridge University Press Pp, Geneva. <https://doi.org/10.1038/446727a>
- Theil H. (1950). A rank-invariant method of linear and polynomial regression analysis, 3; confidence regions for the parameters of polynomial regression equations. *Indagationes Mathematicae*, 1(2).
- Thenmozhi M. and S. V. Kottiswaran (2016). Analysis of Rainfall Trend Using Mann– Kendall Test and the Sen's Slope Estimator in Udumalpet of Tirupur District in Tamil Nadu. *International Journal of Agricultural Science and Research (IJASR)*, 6(2).
- Xu, Z. X., K. Takeuchi and H. Ishidaira (2003). Monotonic trend and step changes in Japanese precipitation. *Journal of Hydrology*, 279(1–4). [https://doi.org/10.1016/S0022-1694\(03\)00178-1](https://doi.org/10.1016/S0022-1694(03)00178-1)
- Yaduvanshi A., P. K. Srivastava and A. C. Pandey (2015). Integrating TRMM and MODIS satellite with socio-economic vulnerability for monitoring drought risk over a tropical region of India. *Physics and Chemistry of the Earth*, 83–84. <https://doi.org/10.1016/j.pce.2015.01.006>
- Yao, F. Z., E. Reynard, I. Ouattara, Y. A. N'go, J. M. Fallot and I. Savané. (2018). A New Statistical Approach to

Assess Climate Variability in the White Bandama Watershed, Northern Côte d'Ivoire. *Atmospheric and Climate Sciences*, 08(04). <https://doi.org/10.4236/acs.2018.84027>

Yue S. and M. Hashino (2003). Long term trends of annual and monthly precipitation in Japan. *Journal of the American Water Resources Association*, 39(3). <https://doi.org/10.1111/j.1752-1688.2003.tb03677.x>

Zarch M. A. A., H. Malekinezhad, M. H. Mobin, M. T. Dastorani and M. R. Kousari (2011). Drought Monitoring

by Reconnaissance Drought Index (RDI) in Iran. *Water Resources Management*, 25(13). <https://doi.org/10.1007/s11269-011-9867-1>

Zhang Q., C. Y. Xu, X. Chen and Z. Zhang (2011). Statistical behaviours of precipitation regimes China and their links with atmospheric circulation 1960-2005. *International Journal of Climatology*, 31(11). <https://doi.org/10.1002/joc.2193>

## Understanding the Vegetation Dynamics of NCT- Delhi Using Remote Sensing

Parul Singh<sup>\*1</sup>, Sudha Ravindranath<sup>2</sup>, Vidya A<sup>2</sup>, K Ganesha Raj<sup>2</sup>

<sup>1</sup> GIS Cell, Motilal Nehru National Institute of Technology, Prayagraj, 211004

<sup>2</sup>Regional Remote Sensing Centre - South, Bengaluru, Karnataka, 560037

\*Email: parul.2021rg102@mnnit.ac.in

(Received: Jan 11, 2022; in final form: Sep 29, 2022)

**Abstract:** Urban vegetation is a crucial ecosystem component that keeps the environment in check. The existence of a well-distributed vegetation cover helps to ensure the city's long-term sustainability and aesthetic appeal. Rapid urban expansion has direct and indirect effects on vegetation growth and its distribution. This paper studied the vegetation cover dynamics using remotely sensed Landsat series datasets in the National Capital Territory (NCT) of Delhi. The study examined the vegetation change over 28 years and observed a reduction of about 15% due to rapid urbanization. This work studied the prominent Green Spaces (GS) in NCT- Delhi and highlighted their significance. The study also investigated the district-wise change in the vegetation cover. The vegetation mapping of the region can be utilized as a tool for integrated spatial planning to address urban challenges like air pollution, reducing the effects of urban heat islands, and public health improvement.

**Keywords:** Vegetation cover, ecosystem, vegetation index, urban spread, Green Space (GS)

### 1. Introduction

Cities are growing, causing global climate change, which needs effective, and sustainable urban development. Urbanization swift imposes much pressure on land and drainage channels, subsequently putting pressure on floodplains, low-lying areas, green spaces, recreational areas, and heritage sites. Cities are marked by tremendous population growth; industries deteriorate air and water quality. The rapid increase in urban infrastructure transformed the green city into concrete space. Urban areas are complex organizations consisting of diverse elements that evolve over contrasting spatio-temporal scales (Blaschke et al., 2011). Human prosperity depends on infrastructure, defined as the interconnected systems supporting and supplying essential living conditions for humans to facilitate, sustain, or enhance society's living status. The ecological infrastructures are defined as the structural landscape network that constitutes the essential landscape elements and spatial patterns that are vital for preserving the integrity and identity of the natural and cultural landscapes, as well as ensuring sustainable ecosystem services, cultural heritage protection, and recreational events (Yu, 2012). These include water and vegetation near the built environment, which delivers ecosystem services at different spatial scales. The ecological infrastructure comprises all 'green and blue spaces' that may be settled in urban and peri-urban areas. The ramification of urbanization on biodiversity and ecosystems, as well as the potential benefits from urban ecosystem restoration, are still inadequately understood (McDonald and Marcotullio 2011). Green spaces are an intrinsic component of the urban landscape, demonstrate essential functions like urban heat island mitigation (Susca et al., 2011; Yuan and Bauer, 2007), reducing carbon emissions (Nowak and Dwyer, 2007; Seto et al., 2012), reducing air pollution (Nowak et al., 1998) and promoting general human health (Tzoulas et al., 2007).

The term 'urban vegetation' represents the total assemblage of plants (including urban forests) within and on the periphery of cities and towns. It comprises a diversity of

plants in a wide range of habitats. They are set up and managed for various reasons and exhibit economic, social, aesthetic, and ecological value (Carne 1994). Urban vegetation cover is a critical component in mitigating climate change impacts (Cadenasso et al., 2006). It maintains environmental sustainability and helps in various ecosystem services, including air purification, water infiltration, noise reduction, and carbon sequestration (Elmqvist et al., 2013). The planting habitats consist of sidewalks and highways, urban squares and plazas, parks, institutional grounds, industrial and residential areas. The urban environment provides opportunities for conservation outside natural habitats, necessary in protecting biodiversity, for instance, botanic gardens.

The quantification and mapping of the vegetation cover in the urban area play an essential role in assessing urban structural changes and achieving a sustainable environment (Chikr El-Mezour et al., 2010). Vegetation cover mapping is imperative for urban planning, natural resource management, ecological studies, and hydrological modelling (Su et al., 2016). Thus, the identification, evaluation, and characterization of urban vegetation remain a high priority for environmental research policy.

Remote sensing is the study of acquiring information, used to gather information about any feature without coming into physical contact (Joseph 2005). Multispectral remote sensing imageries are valuable for better understanding the earth's environment (Ahmadi et al., 2010). These data have been widely used as a cost-effective tool in mapping and monitoring large areas (Gould, 2000; Freeman et al., 2002). The application and scope of remote sensing are comprehensive (Shimoda 2013). Integrating remotely sensed data and ancillary data has many applications, including land cover classification, forest classification, soil moisture measurement, snow mapping, sea ice type classification, etc. Remote sensing is widely used in land cover classification, including vegetation mapping (Abd Latif et al., 2011). The application of satellite data to

monitor vegetation dynamics was an excellent achievement for vegetation studies in the 20th century. The spectral characteristics of vegetation reflectance can indicate the strength of vegetation activity. Thus, vegetation indices are extensively used in agriculture, biology, geography, urban planning, hydrology, and forestry research (Zhao et al., 2012).

Urban areas have evolved as the focal point of the environment involving large consumers and acting as distributors of various services. The poor urban ecosystem caused local and broader environmental degradation, social problems, economic decline, human health issue, and further disconnection from nature (Teodorescu, 2010). Delhi is one of the megacities globally, combating rapid haphazard urban development and exhibiting massive pollution levels from industries, residential complexes, and transportation systems (Singh 2015). With the rapid growth of the population in Delhi, the region is facing many problems associated with housing, waste disposal, air pollution, traffic congestion, shortage of electric power, and security (Singh et al., 2020). According to a United Nations report, Delhi will replace Tokyo and become the world's biggest megacity by 2030 (UN, 2018). Delhi is a significant attraction for migrants from all over the country due to its flourishing service economy, other opportunities, and infrastructure. The neighboring cities of Delhi, like Gurugram, Noida, Ghaziabad, Faridabad, Sonipat, and Bahadurgarh, have also experienced urban growth over the past three decades. The region spread in the fertile Indo-Gangetic plain, having a variety of vegetation covers, including forests, ridge vegetation, and many ecologically sensitive areas.

Considering urbanization and its negative impact on vegetation, it is imperative to protect, promote and enhance the existing vegetation cover of the city. This study aims to provide the spatio-temporal perspective on urban vegetation cover that has taken place in the last 28 years in NCT- Delhi, and examine the importance of green spaces in NCT-Delhi. The study also put forward several suggestions and recommendations based on temporal vegetation cover analysis.

## 2. Study area and data

### 2.1. Study area

The study covers the National Capital Territory (NCT)-Delhi region, which is located between the 28°24'17"N and 28°53'00"N latitudes and 76°45'30"E and 77°21'30"E longitudes with a geographical area of 1,490 km<sup>2</sup> (Figure 1). It is part of the Indo-Gangetic alluvial plains, at an elevation of 198 - 220m above mean sea level (Bidhuri & Khan, 2020). The region's climate is semi-arid; both summer and winter are severe. The climate in NCT- Delhi is influenced by its location and the air prevailing throughout the year. The average daily temperature is 40.9° C in summer, whereas, in the winter, it is only 8 °C (Tiwari et al., 2009). The topography of Delhi is divided into the Ridge, the Yamuna floodplain, and the plain. The ridge region is the most dominating physiographic feature

and provides suitable factors that facilitate the growth of acacias and other cacti. During the monsoon season, herbaceous plants grow in abundance in the ridge region. Shisham trees are found in the plains region of Delhi (Gosain et al., 2009). The Yamuna Floodplains are low-laying and sandy. The floodplain region is subject to frequent floods during the monsoon season. The region is drowning in floodwater after the flood subsides, leaving moisture in the soil, making the land rich in fertility. The vegetation of Delhi mainly consists of medium-sized trees and herbs (Khera et al., 2009). The region is also known for its diverse flowering plants. According to Census 2011, 16.7 million population live in Delhi (Census of India, 2011).

### 2.2. Data

In this research work, medium-resolution multispectral Landsat satellite datasets were used, including Landsat 5 for 1992 and Landsat 8 for 2020. The satellite datasets have been acquired from <https://earthexplorer.usgs.gov/>. While downloading the satellite images for monitoring the vegetation, it was kept in mind to acquire images of same time periods when vegetation cover was at its peak. Generally, the best month to map vegetation cover on satellite imagery are October-November and February-March. Due to availability of cloud free data of Landsat imagery, March month has been acquired for assessing the vegetation cover of NCT- Delhi. The details of satellite datasets have been given in Table 1.

**Table 1. Satellite dataset**

Satellite images	Sensor	Date	Spatial resolution
Landsat 5	Thematic Mapper (TM)	16 March 1992	30m
Landsat 8	Operational Land Imager (OLI)	18 March, 2020	30m

## 3. Methodology

Figure 2 summarizes the methodology adopted for the study. In the present study, 'urban' refers to the central urban area and outlying suburban. Thus, it incorporates commercial and industrial, residential areas, transportation corridors, and peripheral areas, which serve as the interface between the suburbs and hinterlands.

### 3.1. Data processing

The remotely sensed Landsat series datasets were used in the study. The images are cloud-free and belong to the same period. QGIS open software has been used to carry out satellite image processing. The preprocessing involved the radiometric calibration and clipping of datasets as per area of interest.

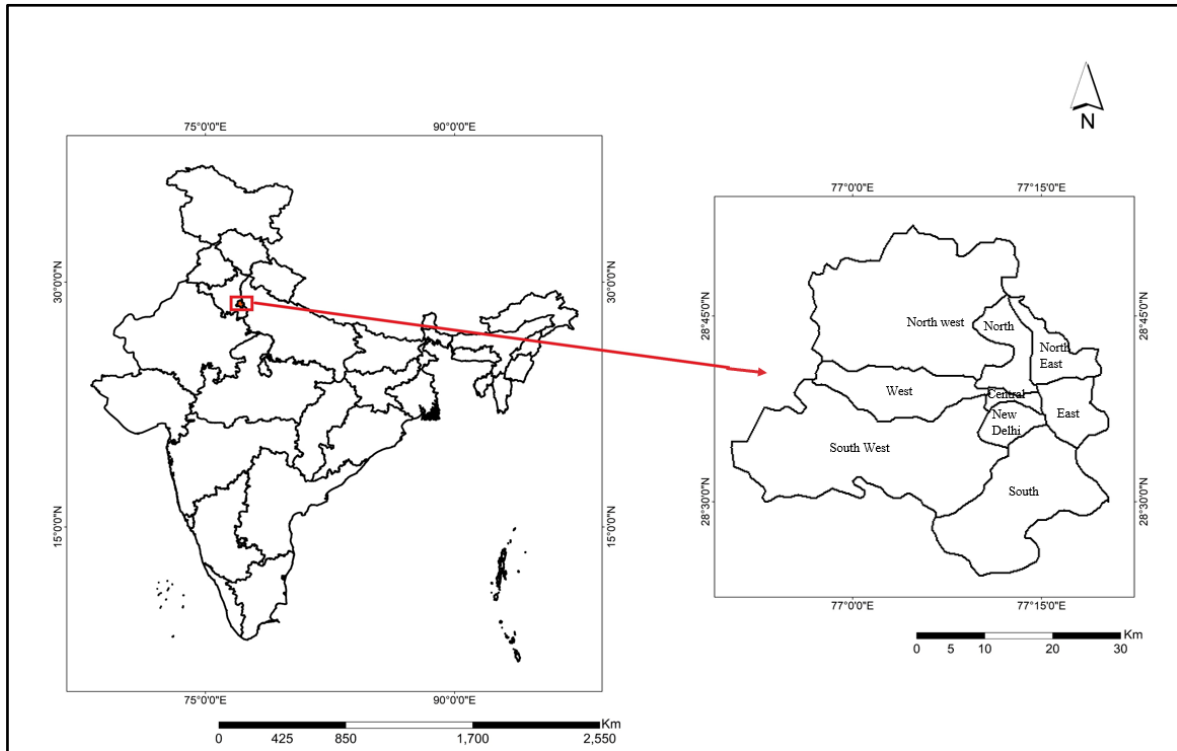


Figure 1. Location of the study area

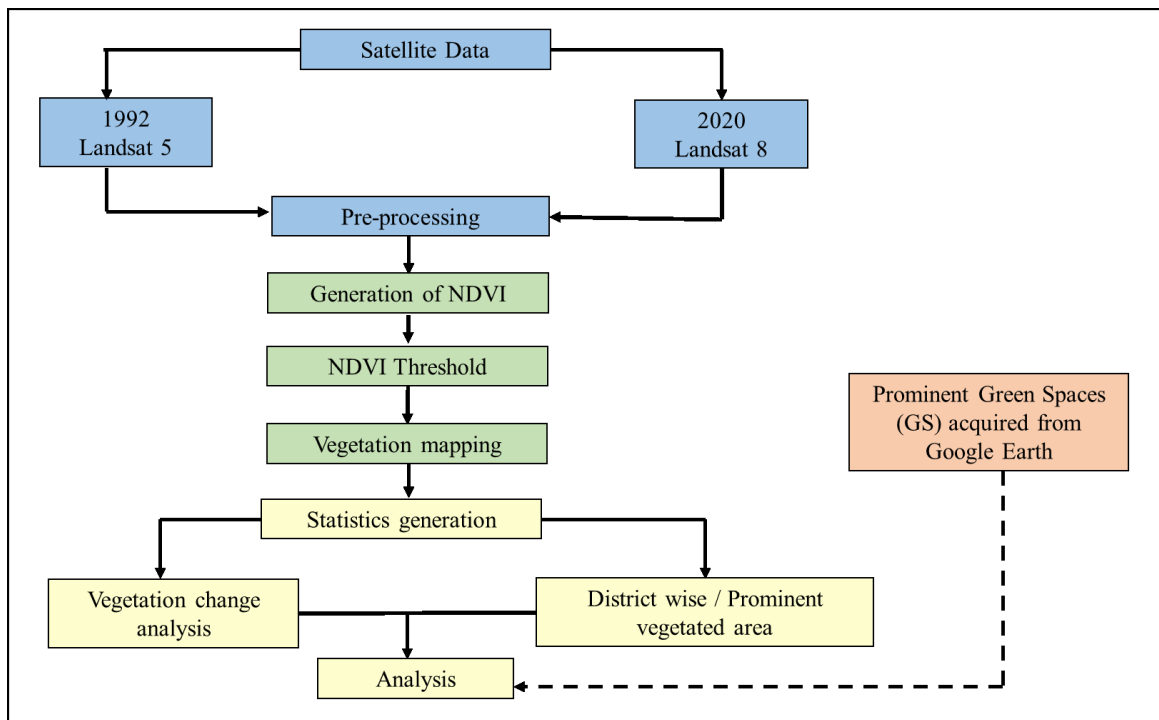


Figure 2. Methodology workflow

**3.2. Calculation of Normalized Difference Vegetation Index (NDVI)**

The Normalized Difference Vegetation Index (NDVI) is the most widely used vegetation index, developed by Rouse et al. (1974) from the Remote Sensing Centre of Texas University. It is the NIR and Red band ratio, ranging between -1 to 1.

$$NDVI = (NIR - RED) / (NIR + RED)$$

The NDVI is capable of detecting changes in land cover caused by human activities such as construction and other developments. The negative NDVI values (values approaching -1) indicate water. NDVI values near zero (-0.1 to 0.1) are typically associated with barren land and sand. Low, positive values depict the little green cover region such as grassland and the scrub (approximately 0.2 to 0.4), while high NDVI ranges (values approaching 1)

correspond to lush and healthy vegetation. The NDVI values adopted for mapping vegetation in the region are presented in Table 2. The present study calculates NDVI on temporal Landsat series datasets to analyze the spatio-temporal vegetation cover over 28 years period in NCT-Delhi.

### 3.3. Vegetation Change and Green Spaces (GS)

In the present study, the classification was primarily aimed at assessing the vegetation cover change in NCT Delhi. The spatio-temporal transformation in the vegetation category has been detected using NDVI threshold values. "NDVI values were implemented to reclassify NDVI output with reference to the land cover based on its spectral properties; earlier similar method was employed by

The different landcover categories were identified using the spectral property of the features with their respective NDVI values. The concept of Green Spaces (GS) has been discussed in the study with reference to NCT-Delhi. The GS locations were obtained from Google Earth. Assessing the GS contributes to a more holistic explanation of the significance of the urban vegetation in the region

## 4. Results and discussion

### 4.1 NDVI generation

In this study, vegetation is defined as the area under scrub, cultivated land, and vegetation inside the city. Vegetation inside the city means the plantation along the roads, urban green spaces, gardens, parks, etc. As the temporal datasets belong to the same month, so it is considered that there should be minimal difference in cultivated land.

The NDVI output of 1992 was between -0.355 to 0.644, and NDVI values for 2020 lie between -0.109 to 0.52 (Figure 3 (a)). It was observed that the area under cultivation (cropland) showed higher NDVI values; simultaneously, the region under water and built-up showed lesser NDVI values.

The NDVI outputs generated vegetation cover maps by assigning the NDVI threshold values. This approach efficiently differentiates the vegetation class from the other classes. This method provides powerful insights and makes visualizing the vegetation cover and its health easier. Three land cover classes have been made for vegetation analysis, namely, tree/scrubs, crops/plantation, and others (Figure 3 (b)). The tree/scrub category represents the low and sparse vegetation, including the city vegetation (gardens, parks, urban green spaces, etc.) and scrubland. The crops/plantation landcover category indicates the dense vegetation cover, mainly seen in agricultural land. The other class represents the built-up, fallow/open land, and water. It was observed that in 1992 vegetation cover was evenly distributed. The built-up is concentrated in the city's core, and the peripheral region showed dense vegetation indicating agricultural land. In 2020, there was a huge loss in vegetation cover in North West, West, and South West districts due to the

Bharathkumar and Mohammed-Aslam (2015) while performing crop pattern mapping of Tumkur taluk.

**Table 2. Vegetation classes and NDVI value**

Classes	Description	NDVI values
Other	Built-up, road network, fallow and barren land	-1 to 0.19
Scrub/ Tree	Scrub, urban green spaces	0.2 to 0.5
Crop/ plantation	Dense vegetation region	0.5 to 1

transformation of agricultural lands into residential layouts and commercial complexes.

The New Delhi district accounts for less vegetation loss because its infrastructure was mainly occupied by the government headquarters, offices, and government residential complexes developed since the British period. The British Architect Edwin Lutyens and Herbert Baker planned and constructed several buildings in New Delhi, such as Rashtrapati Bhavan, Parliament House, the Secretariat building, and many other administrative blocks built by these two architects. These buildings are still in their earlier form, with a vast area covered by greenery is still present there. The vegetation cover area derived from the vegetation maps is given in Table 3. In 1992, 56% area was under vegetation, which reduced to 41% in 2020.

**Table 3. Vegetation cover statistics**

Landcover	1992 Area in km2	1992 Area in %	2020 Area in km2	2020 Area in %
Tree/ scrub	468	31%	331	22%
Crops/ plantation	371	25%	276	19%
Others	651	44%	883	59%

### 4.2 Urban vegetation cover district-wise analysis

Vegetation cover change is determined as the changes in the vegetation-cover area and mean NDVI per unit area in the region. The change in vegetation cover is the direct response to anthropogenic activity, which leads to climate change. Based on the spatio-temporal vegetation cover study, a vegetation change map highlighting the positive change, negative change, and the areas with no changes was presented (Figure 4). Positive changes indicated the densification and spread of vegetation, which is seen as the change in other classes of vegetation category (including sparse and dense vegetation), negative changes show the land transformation of vegetation class to other class, primarily attributed to the establishment of new residential layouts, development, and construction of commercial infrastructure. The no-change category represents the areas having no changes in land cover.

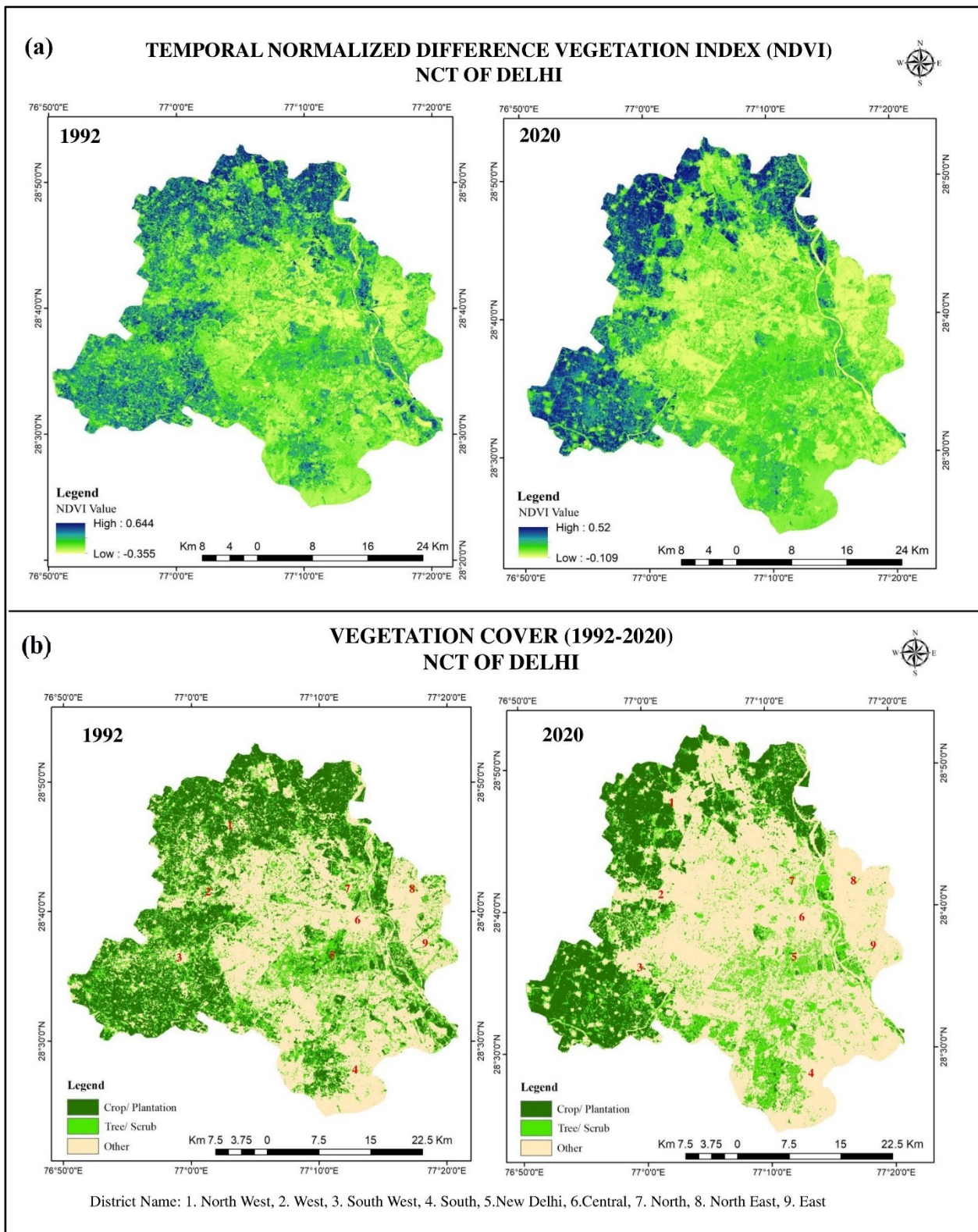


**Figure 3. (a) NDVI maps derived from Landsat 5 (1992), and Landsat 8 (2020), Figure 3(b): Temporal vegetation cover of NCT- Delhi (1992-2020)**

It was observed that the core of the city has permanent vegetation covers in government offices, education institutions, and research centers premises, cantonment areas having a large patch of greenery, and a Ridge. The city core has a vegetation spread varied from small patches to large adjoining vegetation patches. Vegetation cover exists in a linear pattern along the roads. The city is

extending in a radial pattern and multi-nuclei form and experiencing horizontal and vertical urban spread.

From the district-wise comparative analysis, it was observed that the North East and East district of Delhi, which was already occupied by dense settlement, represented the least greenery in the entire region and showed less reduction in the vegetation cover (Figure 5).

The vegetation greenness was almost balanced in New Delhi and Central Delhi due to administrative units like the central secretariat (north and south block), Rashtrapati Bhavan, Rajpath, and India Gate, reflecting healthy tree cover. The NDVI values of these areas range from 0.4 to 0.6. Along the Yamuna river, the floodplain, which is the

most fertile part of the region, also shows relatively higher NDVI values because of the presence of agricultural land.

Substantial changes of around 188km<sup>2</sup> in the vegetation cover have been seen in the North West and South West Delhi due to the development of residential layouts like Rohini, Janakpuri, Dwarka, and Najafgarh.

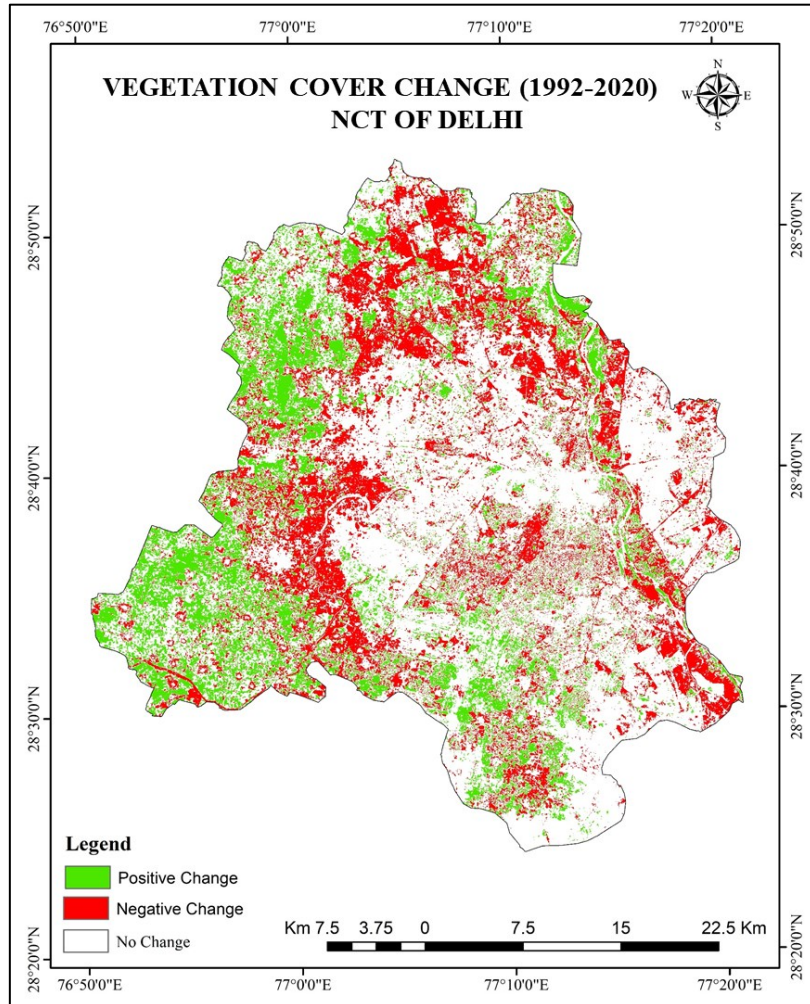


Figure 4. Vegetation cover change of NCT- Delhi

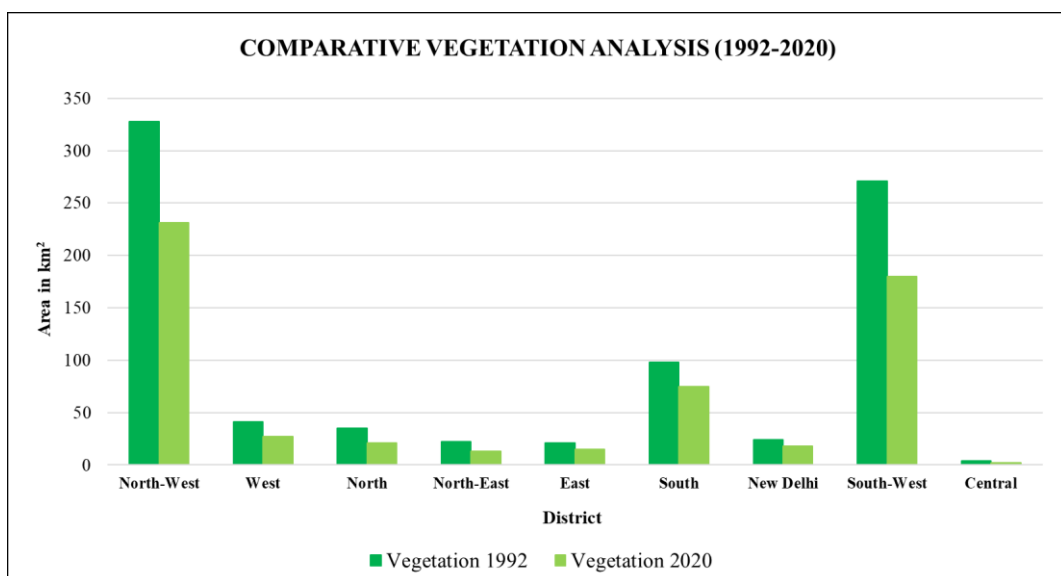


Figure 5. Comparative district-wise vegetation cover change of NCT- Delhi (1992-2020)

From the vegetation change analysis, it is evident that in 28 years, the region experiences a considerable reduction of about 15% in vegetation cover, primarily due to an increase in residential layout and rampant infrastructural development.

### 4.3 Green spaces and their importance

Green spaces are the essential component of green infrastructure, immensely vital for developing countries like India and China (Turaga et al., 2020). Green spaces and recreational or open spaces consist of community parks, gardens, schoolyards, playgrounds, cemeteries, etc. These areas are wholly or partially covered with trees, shrubs, grass, and other vegetation types. In India, the concept of 'urban green spaces' is comprehensively used for trees in urban parks, forests, and canopy cover along roads, which positively contribute to the city's greenery, human health, and biodiversity conservation (Bhalla & Bhattacharya, 2015). Green spaces are providing a new concept that is an intelligent method for natural preservation and urban planning. Green infrastructure planning is an approach that advocates an equal role for ecological resources within a human-centered understanding of how landscape and other built infrastructures interact (Elliott et al., 2020).

Delhi primarily has two prominent natural features, the Yamuna River floodplain, and the Delhi Ridge (Kumar et al., 2011). The Ridge is the remnant of Aravalli Hills in NCT- Delhi, which functions as a lung for the city. Delhi, the greenest city, despite all the unprecedented and rapid urbanization in Delhi, led to extensive pressure on the physical environment with a high pollution level. Significant urban green spaces of NCT- Delhi are depicted in Figure 6. Delhi Ridge is considered the lungs of the city. The Ridge has been divided into four fragmented zones: Northern Ridge, Central Ridge, South Central Ridge, and Southern Ridge. Typically, the ridge forests are covered with thorny scrubs adding little greenery and having native vegetation species. But due to increasing urbanization pressure on the land, a considerable portion of the Ridge was converted to new residential spaces and business complexes. Some part of the Ridge was given legal rights for protection, but further Ridges areas, unfortunately, did not hold such protection and faced a continuous reduction in green cover (Sinha, 2014). From the study, it was observed that the major significant green spaces lie around the Ridge and Yamuna Flood Plain.

Delhi has six biodiversity parks that are extremely prosperous in flora and fauna species (Koul, 2017). The biodiversity parks are distinct landscape that functions as the habitat of native flora, fauna, and microbial species.

They provide various ecological functions like recharging the groundwater, sinking the CO<sub>2</sub>, conserving the natural heritage, including native species of plants and animals, and serving as a recreational activity (Dhote and Mukherjee, 2018). These parks have been developed by Delhi Development Authority. Yamuna biodiversity park, situated on the Yamuna Riverfront, is a habitat of migratory and resident birds (Saxena et al., 2021). It enhances groundwater recharge and conserves the wild genetic resources of crops. Aravalli biodiversity park is situated northwest of Vasant Vihar. The park suffers from mining, and overexploitation of medicinal plants and is near to its extinction. The prime motive of this biodiversity park is to promote environmental awareness among the public. Neela Hauz Biodiversity park lies in South Central Ridge, next to Sanjay Van (Sonowal et al., 2019). This is mini biodiversity having a wetland area along the Aruna Asaf Ali Road. The park has around 90 native plant species and 70 bird species, including migratory birds. The Northern Ridge, also known as Kamla Nehru Ridge, is situated near Delhi University. The Ridge has various recharging depressions to activate the aquifers. Tughlaqabad Biodiversity Park resides on the Southern Ridge, including the Tughlaqabad Fort (Panwar & Dhote, 2022). Tilpath Valley biodiversity park is spread over Southern Ridge, well connected to valleys of Asola and Bhatti Wildlife Sanctuaries. This valley received drainage from all nearby hill ranges, facilitating recharge of the aquifer network.

Significant and crucial changes were observed around the Delhi Ridges, the dense urban growth and scale down of vegetation in and around Delhi Ridge have been considered as the loss of biodiversity and cause instability in the urban environment. There are indicative substantial changes that have been seen in Northern Ridge due to the extension of various educational institutions, like the University of Delhi and Indraprastha college. The Central Ridge is enclosed by New Delhi in its East, residential areas such as Kirti Nagar and Patel Nagar, and industrial locality like Mayapuri, which is a major hub of heavy metal and small-scale industries, facing dense urban growth and loss of vegetation in the nearby areas. Likewise, South Central Ridge and Southern Ridge also possess a huge reduction and variation in the densification of vegetation cover due to new infrastructural development and expansion of residential layout. In the study, the Delhi Ridge vegetation comes under the category of Tree/Scrub, showing 31% vegetation cover in 1992, which reduced to 22% in 2020. The overall 9% loss of greenery has been seen due to the rapid urban growth, which resulted in the transformation and distribution of vegetation cover in and around Delhi Ridge.

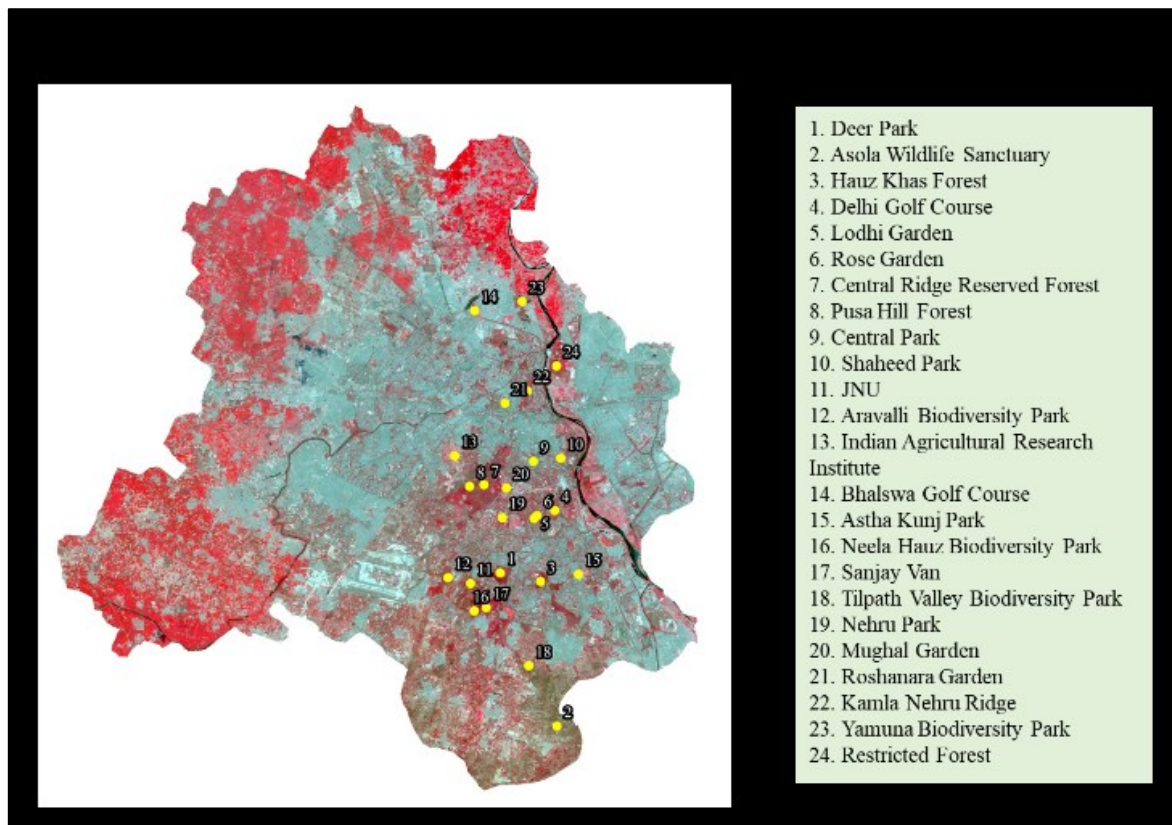


Figure 6. Major green spaces of NCT- Delhi

## 5. Conclusions

Cities are complex places, continuously undergoing structural changes, growth, and renovation (Rydin et al., 2012). They are engines of economic and cultural growth, as well as change drivers (Vliet et al., 2002). The NCT of Delhi's rise as a leading center, owing to its administrative importance, location, infrastructure, and other amenities have resulted in rapid population growth. The city's rampant expansion and sprawling emphasize sustainable, affordable, and environment-befitting planning and development. The study attempts to evaluate vegetation cover dynamics over 28 years in the NCT of Delhi and examines the region facing a reduction in overall vegetation cover.

The result showed a considerable loss in vegetation cover due to the extensive conversion of agricultural lands to the built-up category, encroachment, and densification in and around Delhi Ridge.

The harsh reality of the 21st century is climate change and environmental pollution, and cities all over the world are battling to deal with the new environmental issues. Nature-based solutions have a crucial role in achieving a future compact city that is liveable and sustainable. The concept of green buildings, eco-roofs, and vertical gardens need to be promoted. Native indigenous vegetation, which serves as an ecologically beneficial aspect of biodiversity conservation, can help improve vegetation density in parks and forests.

The Government of India, along with the state governments, have taken several initiatives, such as management of solid and liquid waste, protection,

preservation, rejuvenation, and management of lakes, ponds, rivers, wetlands, and forests. Swachh Bharat Mission-Urban (SBM-Urban) is a flagship initiative of the Government of India; it aims to keep Indian cities clean by setting up 100% door-to-door waste collection and working toward making cities garbage-free. Recently, SBM-Urban 2.0 was introduced to maintain the sanitation and solid waste management results attained and accelerate the momentum generated. To promote healthy cities and provide universal access to safe, inclusive and accessible green and public spaces, the Atal Mission for Rejuvenation and Urban Transformation (AMRUT) mission is promoting green and open spaces in cities.

This study can contribute to the conservation of the region's green areas and the sustainability of the urban environment. Mapping vegetation cover is vital for spatial planning to conquer urban challenges. Further research can illustrate the fine-scale changes in vegetation cover by using sub-pixel analysis using high-resolution multitemporal remotely sensed datasets.

## References

- Abd Latif Z., S. N. A. Aman and R. Ghazali (2011). Delineation of tree crown and canopy height using airborne LiDAR and aerial photo. 2011 IEEE 7th International Colloquium on Signal Processing and Its Applications. doi:10.1109/cspa.2011.5759902
- Ahmadi H. and A. Nusrath (2010). Vegetation change detection of Neka River in Iran by using remote-sensing and GIS. *Journal of geography and geology*, 2(1), 58. <http://www.ccsenet.org/journal/index.php/jgg/article/download/5107/5765>

- Bhalla P. and P. Bhattacharya (2015). Urban Biodiversity and Green Spaces in Delhi: a case study of new settlement and Lutyens' Delhi. *Journal of Human Ecology*, 52(1-2), 83-96.
- Bharathkumar L. and M. A. Mohammed-Aslam (2015). Crop pattern mapping of tumkur taluk using NDVI technique: a remote sensing and GIS approach. *Aquatic Procedia*, 4, 1397-1404. doi: 10.1016/j.aqpro.2015.02.181
- Bidhuri S. and M. M. A. Khan (2020). Assessment of ground water quality of central and southeast districts of NCT of Delhi. *Journal of the Geological Society of India*, 95(1), 95-103.
- Blaschke T., G. J. Hay, Q. Weng and B. Resch. (2011). Collective sensing: Integrating geospatial technologies to understand urban systems—An overview. *Remote Sensing*, 3(8), 1743-1776.
- Cadenasso M. L., S. T. A. Pickett and J. M. Grove (2006). Integrative approaches to investigating human-natural systems: The Baltimore ecosystem study. *Natures Sciences Sociétés*, 14,4–14.
- Carne J. (1994, October). Urban vegetation: ecological and social value. In *Proceedings of the 1994 national greening Australia conference, October* (pp. 4-6).
- Chikr El-Mezouar, M., N. Taleb, K. Kpalma K. and J. Ronsin, 2010. A high-resolution index for vegetation extraction in IKONOS images. *Remote Sensing for Agriculture, Ecosystems, and Hydrology XII*. doi:10.1117/12.866187
- Dhote M. and D. Mukherjee (2018). Co-benefits of urban biodiversity. In *Mainstreaming Climate Co-Benefits in Indian Cities* (pp. 211-241). Springer, Singapore.
- Elliott H., C. Eon and J. K. Breadsell (2020). Improving City vitality through urban heat reduction with green infrastructure and design solutions: A systematic literature review. *Buildings*, 10(12), 219.
- Elmqvist T., M. Fragkias, J. Goodness, B. Güneralp, P. J. Marcotullio, R. L. McDonald, ... & C. Wilkinson. (2013). *Urbanization, biodiversity and ecosystem services: challenges and opportunities: a global assessment* (p. 755). Springer Nature. doi.org/10.1007/978-94-007-7088-1
- Freeman A., B. Chapman and P. Siqueira (2002). The JERS-1 Amazon Multi-season Mapping Study (JAMMS): Science objectives and implications for future missions. *International Journal of Remote Sensing*, 23(7), 1447-1460.
- Gosain A. K., P. K. Khandelwal and S. Kulshrestha (2009). Urban floods: Case study of Delhi. *Disaster Dev*, 3, 15.
- Gould W. (2000). Remote sensing of vegetation, plant species richness, and regional biodiversity hotspots. *Ecological Applications*, 10(6), 1861-1870.
- INDIA P. (2011). Census of India 2011 provisional population totals. *New Delhi: Office of the Registrar General and Census Commissioner*. <http://censusindia.gov.in/>
- Joseph G. (2005). *Fundamentals of remote sensing*. Universities Press.
- Khera N., V. Mehta and B. C. Sabata (2009). Interrelationship of birds and habitat features in urban greenspaces in Delhi, India. *Urban Forestry & urban greening*, 8(3), 187-196.
- Koul M. (2017). *Biodiversity Parks—Restoring Degraded Environments*.
- Kumar M., M. S. Rao, B. Kumar and A. Ramanathan (2011). Identification of aquifer-recharge zones and sources in an urban development area (Delhi, India), by correlating isotopic tracers with hydrological features. *Hydrogeology journal*, 19(2), 463-474.
- McDonald R. and P. Marcotullio (2011). Global effects of urbanization on ecosystem services. *Handbook of urban ecology*, 193-205.
- Nowak D. J. and J. F. Dwyer (2007). Understanding the benefits and costs of urban forest ecosystems. In *Urban and community forestry in the northeast* (pp. 25-46). Springer, Dordrecht. doi.org/10.1007/978-1-4020-4289-8\_2
- Nowak D. J., P. J. McHale, M. Ibarra, D. Crane, J. C. Stevens and C.J. Luley (1998). Modeling the effects of urban vegetation on air pollution. In *Air pollution modeling and its application XII* (pp. 399-407). Springer, Boston, MA. doi.org/10.1007/978-1-4757-9128-0\_41
- Panwar H. and M. Dhote (2022). Degraded Land Management in Urban Areas: The Case of Biodiversity Parks in Delhi. In *Sustainable Urbanism in Developing Countries* (pp. 291-304). CRC Press.
- Rouse J. W., R. H. Haas, J. A. Schell and D. W. Deering (1974). Monitoring vegetation systems in the Great Plains with ERTS. *NASA special publication*, 351(1974), 309.
- Rydin Y., A. Bleahu, M. Davies, J.D. Dávila, S. Friel, G. De Grandis, N. Groce, P. C. Hallal, I. Hamilton, P. Howden-Chapman, K. M. Lai, C. J. Lim, J. Martins, D. Osrin, I. Ridley, I. Scott, M. Taylor, P. Wilkinson and J. Wilson (2012). Shaping cities for health: complexity and the planning of urban environments in the 21st century. *Lancet (London, England)*, 379(9831), 2079–2108. doi.org/10.1016/S0140-6736(12)60435-8
- Saxena R., R. Rath, S. Gupta and N. Sood (2021). A review on ecological degradation, its causes and sustainable development in Delhi, India. *Journal of Applied and Natural Science*, 13(4), 1294-1304.
- Seto K. C., B. Güneralp and L. R. Hutyrá (2012). Global forecasts of urban expansion to 2030 and direct impacts on biodiversity and carbon pools. *Proceedings of the National Academy of Sciences*, 109(40), 16083-16088. doi.org/10.1073/pnas.1211658109
- Shimoda H. (2013) Remote Sensing Data Applications. In: Pelton J.N., Madry S., Camacho-Lara S. (eds) *Handbook of Satellite Applications*. Springer, New York, NY. doi.org/10.1007/978-1-4419-7671-0\_47

- Singh P., S. Ravindranath, A. Vidya and K. G. Raj (2020). An assessment of urban growth of Delhi using geospatial techniques. *Journal of Geomatics*, 14(2), 171–177.
- Singh R. B. (Ed.). (2015). *Urban development challenges, risks and resilience in Asian mega cities*. Tokyo: Springer. doi.org/10.1007/978-4-431-55043-3
- Sinha G.N. (Ed.) (2014). *An Introduction to the Delhi Ridge*. Department of Forests & Wildlife, Govt. of NCT of Delhi, New Delhi. xxiv+154 pp.
- Sonowal K., P. Kumar, N. Dwivedi, P. Kumar and R. Mondal (2019). The Dying Wetlands of Delhi: An Overview on the Threats and Conservation Strategies of Wetlands. *G-Journal of Environmental Science and Technology*, 7(1), 1-5.
- Su Y., Q. Guo, D. L. Fry, B. M. Collins, M. Kelly, J. P. Flanagan and J. J. Battles (2016). A vegetation mapping strategy for conifer forests by combining airborne LiDAR data and aerial imagery. *Canadian Journal of Remote Sensing*, 42(1), 1-15.
- Susca T., S. R. Gaffin and G. R. Dell'Osso (2011). Positive effects of vegetation: Urban heat island and green roofs. *Environmental pollution*, 159(8-9), 2119-2126. doi.org/10.1016/j.envpol.2011.03.007
- Teodorescu G. (2010). Climate change impact on urban ecosystems and sustainable development of cities in Romania. *WSEAS Transactions on Environment and Development*, 2(6), 103-112.
- Tiwari S., A. K. Srivastava, D. S. Bisht, T. Bano, S. Singh, S. Behura, ... and B. Padmanabhamurty (2009). Black carbon and chemical characteristics of PM10 and PM2.5 at an urban site of North India. *Journal of Atmospheric Chemistry*, 62(3), 193-209.
- Turaga R. M. R., U. Jha-Thakur, S. Chakrabarti and D. Hossain (2020). Exploring the role of Urban Green Spaces in smartening cities in India. *Impact assessment and project appraisal*, 38(6), 479-490.
- Tzoulas K., K. Korpela, S. Venn, V. Yli-Pelkonen, A. Kaźmierczak, J. Niemela and P. James (2007). Promoting ecosystem and human health in urban areas using Green Infrastructure: A literature review. *Landscape and urban planning*, 81(3), 167-178. doi.org/10.1016/j.landurbplan.2007.02.001
- UN (2018). The World's Cities in 2018: Data Booklet, Statistical Papers - United Nations (Ser. A), Population and Vital Statistics Report, UN, New York doi.org/10.18356/c93f4dc6-en
- Vliet W. V. (2002). Cities in a globalizing world: from engines of growth to agents of change. *Environment and Urbanization*, 14(1), 31-40. doi.org/10.1177%2F095624780201400103
- Yu K., (2012). Ecological infrastructure leads the way: the negative approach and landscape urbanism for smart preservation and smart growth. In: Richter, M., Weiland, U. (Eds.), *Applied Urban Ecology: A Global Framework*. Blackwell Publishing Ltd, Oxford, pp. 152–169
- Yuan F. and M. E. Bauer. (2007). Comparison of impervious surface area and normalized difference vegetation index as indicators of surface urban heat island effects in Landsat imagery. *Remote Sensing of Environment*, 106(3), 375–386. doi.org/10.1016/j.rse.2006.09.003
- Zhao X., D. Zhou and J. Fang (2012). Satellite-based Studies on Large-Scale Vegetation Changes in China F. *Journal of integrative plant biology*, 54(10), 713-728. doi.org/10.1111/j.1744-7909.2012.01167.x

**Author Index (Vol. 16)**

Abhinav Mehta		2	146
Abubakar, A.Z	(see Azua, S)	2	103
Afabor I	(see Omogunloye O.G)	1	81
Ahmadu, A.A	(see Azua, S)	2	103
Ajay Mathur		2	196
Akomolafe, E.A	(see Azua, S)	2	103
Alabi A.O	(see Omogunloye O.G)	1	81
Aliyu, Y.A	(see Azua, S)	2	103
Amadi U	(see Omogunloye O.G)	1	81
Amanpreet Kaur Benipal	(see Kusum Lata)	2	134
Anam Sabir		1	45
Anil Kumar	(see Anam Sabir and Mragank Snighal)	1 2	45 167
Anil Sood	(see Kusum Lata)	2	134
Arya S Pradeep		2	201
Ashish Payal	(see Mragank Snighal)	2	167
Azua, S		2	103
Ben U. Ngene	(see Ojo, S. Aderemi)	1	14
Bharath, H.A	(see Madhumita, D)	1	1
Bhaskar Ramchandra Nikam	(see Manaruchi Mohapatra)	1	33
Bindu Bhatt	(see Lakhan Jain)	2	223
Brijendra Pateriya	(see Kusum Lata and Ajay Mathur)	2	134 196
Cole O. A	(see Omogunloye O.G)	1	81
Devendra Singh Chouhan	(see Seema Jalan)	2	176
Dipanwita Haldar	(see Steena Stephen)	2	159
Enilolobo A	(see Omogunloye O.G)	1	81
Ganesha Raj	(see Parul Singh)	2	234
Garg, P.K		2	152
Garuba S	(see Omogunloye O.G)	1	81
Gaurav Kumar Pal		2	187
Gupta K.K	(see Mohan R. Zade)	1	66
Hiremath, S.K		1	94
Ibitoye J.A	(see Omogunloye O.G)	1	81
Jadhav Kavita	(see Patil Nilesh)	2	213
Jai Gopal Singla		1	23
Joseph O. Olusina	(see Ojo, S. Aderemi)	1	14
Kawaldeep Kaur	(see Kusum Lata)	2	134
Kulkarni, P.T	(see Hiremath, S.K)	1	94
Kusum Lata		2	134
Lakhan Jain		2	223
Madhumita, D		1	1
Majekodunmi, Q.O	(see Azua, S)	2	103
Manaruchi Mohapatra		1	33
Mayank Sharma		2	114
Mehak Jindal		1	55
Mohan R. Zade		1	66
Mragank Snighal		2	167
Nishant Tiwari	(see Ajay Mathur)	2	196

Ojo, S. Aderemi		1	14
Okonufua E	(see Omogunloye O.G)	1	81
Omogunloye O.G		1	81
Pankaj Bodani	(see Ujjwal K. Gupta)	1	6
Parul Singh		2	234
Patel, N.R	(see Steena Stephen)	2	159
Patil Bhavesh	(see Patil Nilesh)	2	213
Patil Nilesh		2	213
Patil Sanjaykumar	(see Patil Nilesh)	2	213
Patil Vilas	(see Patil Nilesh)	2	213
Prasun Kumar Gupta	(see Manaruchi Mohapatra and Mehak Jindal)	1	33 55
Praveen Kumar Thakur	(see Manaruchi Mohapatra)	1	33
Raaed Mohamed Kamel Hassouna		2	123
Raghavendra Sara	(see Mayank Sharma)	2	114
Rajani M.B	(see Gaurav Kumar Pal and Arya S Pradeep)	2	187 201
Salami T.J	(see Omogunloye O.G)	1	81
Seema Jalan		2	176
Shailesh Chaure	(see Seema Jalan)	2	176
Shashikant A. Sharma	(see Ujjwal K. Gupta)	1	6
Shefali Agrawal	(see Mayank Sharma)	2	114
Shital Shukla	(see Abhinav Mehta)	2	146
Shrey Rakholia	(see Abhinav Mehta)	2	146
Soni G.P	(see Mohan R. Zade)	1	66
Steena Stephen		2	159
Sudha Ravindranath	(see Parul Singh)	2	234
Sunanda Trivedi	(see Jai Gopal Singla)	1	23
Suryawanshi Arvind	(see Patil Nilesh)	2	213
Ujjwal K. Gupta		1	6
Vidya A	(see Parul Singh)	2	234
Vipan Kumar	(see Ajay Mathur)	2	196
Youngu, T.T	(see Azua, S)	2	103

## INDIAN SOCIETY OF GEOMATICS: AWARDS

### National Geomatics Award for Excellence

This award has been instituted to recognize outstanding and conspicuously important contribution in promoting geomatics technology and applications at the country level. The contributions should have made major impact on the use of this technology for national development.

Areas of contribution considered for the award are:

1. Geographical Information System
2. Global Positioning System
3. Photogrammetry
4. Digital Cartography
5. Applications of Geomatics

The award shall consist of Rs. 50,000/- in cash, a medal and citation.

#### Eligibility

Any citizen of India, engaged in activities related to geomatics technology and its applications is eligible for this award. The prize is awarded on the basis of work primarily done in India.

The age limit for awardees is 45 years or above as on June 30 of the year of award.

#### Selection

A duly constituted Award Committee will evaluate all nominations received. The committee shall consist of eminent experts in the field of geo-spatial technology, to be identified by the Executive Council, ISG. The committee shall forward selected name/s to ISG – EC for approval and announcement. Apart from those persons, whose nominations have been received, the Committee may consider any person or persons who, in their opinion, have made outstanding contributions to development of geo-spatial technology and applications.

The award can be withheld in any year if, in the opinion of the committee, no candidate is found suitable in that particular year.

#### Presentation of the Award

The award shall be presented during the Annual Convention of ISG. Local Hospitality shall be taken care by ISG & Air fare (low cost) may be reimbursed if awardees request for it.

#### How to make Nomination

The nominations can be proposed by Head of a major research institute/ centre; Vice-Chancellor of a university; Secretary of Government Scientific Departments; President of a National Academy, President, Indian Society of Geomatics / Indian Society of Remote Sensing / Indian National Cartographic Association / ISG fellow or two life members of the society with more than 10 year old membership.

A candidate once nominated would be considered for a total period of two years. Nomination should be sent in the prescribed format to Secretary, ISG.

The last date for receiving nominations shall be September 30 or otherwise extended.

### **Format for nomination of Geomatics Award for Excellence**

1. Name of the Nominee
2. Postal Address
3. Academic Background (Bachelor degree onwards)
4. Field of Specialisation
5. Important positions held (in chronological order)
6. Professional Experience including foreign assignments.
7. Important Awards / Honours
8. Important Publications/Patents: (A set of ten most important publications to be enclosed with this form)
9. Contributions of Nominee based on which the nomination is sent (in 1000 words, also provide a statement  
in 50 words which may be used for citation.):
10. Other Relevant Information:

Proposer:

Signature  
Name  
Address  
Phone/ Fax  
E-mail  
Life Membership No. (in case of ISG Member):

Place & Date

Endorsed by (in case nomination is by 2 ISG Life members)

Signature  
Name  
Address  
Phone/ Fax  
E-mail  
Life Membership No. (in case of ISG Member):

Place & Date

(The proposer should give a brief citation of the nominee's work)

### **National Geomatics Award**

**National Geomatics Award** to be given each year: a) for original and significant contribution in Geomatics technology, b) for innovative applications in the field of Geomatics. Each award comprises a medal, a citation and a sum of Rs 25,000/- The guidelines for these awards are available on ISG website.

### **ISG Chapter Award for Best Performance**

The best chapter award will be given to an active chapter of Indian Society of Geomatics, which has made significant contribution to further the mandate and goal of the society. The award consists of a citation and medal

### **President's Appreciation Medal for Contribution to the ISG**

This award will be given to a member of the society, who has made noteworthy contribution to the growth of the ISG (its main body or any chapter). The Award consists of a Medal and a Citation.

### **Prof. Kakani Nageswara Rao Endowment Young Achiever Award**

Indian Society of Geomatics instituted a new award from year 2013 named "Prof. Kakani Nageswara Rao Endowment Young Achiever Award", to encourage young researchers/scientists/academicians pursuing research in the field of geospatial technology/applications. The award carries a cash prize of Rs. 10,000/- along with a citation.

## NATIONAL GEOMATICS AWARD

Indian Society of Geomatics has instituted two National Geomatics Awards to be given each year for (a) Original and significant contribution in Geomatics technology, (b) Innovative application(s) in the field of Geomatics. Each award comprises a medal, a citation and a sum of Rs. 25,000/-.

### The guidelines for the award are as under

Areas of contribution considered for the award (both technology and applications)

1. Geographical Information System
2. Global Positioning System
3. Photogrammetry
4. Digital Cartography
5. Remote Sensing

### Eligibility

Any citizen of India engaged in scientific work in any of the above-mentioned areas of research is eligible for the award.

The awards are to be given for the work largely carried out in India.

- First award will be given for original contribution in the field of Geomatics technology supported by publications in a refereed journal of repute.
- Second award will be given for carrying out innovative application(s). Supported by publications in rear reviewed Journals of repute.
- The contribution for the first award should have been accepted by peers through citation of the work.
- Work based on the applications of existing technologies will not be considered for the first award.
- The work should have made impact on the overall development of Geomatics.

### How to Send Nomination

Nominations should be sent in the prescribed format, completed in all aspects to the Secretary, Indian Society of Geomatics, Space Applications Centre Campus, Ahmedabad 380 015 by August 31 of the year of award.

### Selection Process

An expert committee, consisting of at least three members, constituted by the Executive Council of the Indian Society of Geomatics, will scrutinize the nominations and recommend the awardees' names to the Executive Council. The Council will decide on the award based on the recommendations.

## FORMAT FOR AWARD NOMINATION

1. Name of the Candidate:
2. Present Position:
3. Positions held earlier (chronological order):
4. Academic qualifications (Bachelor's degree onwards):
5. Names of at least three Indian Scientists/Technologist in the area as possible referees \*:
6. Brief write up on the work (500 words) for which award is claimed:
7. Publication(s) on the above work (reprint(s) to be enclosed):
8. List of other publications of the candidate:
9. Citation of the work for which award is claimed:
10. Impact of the work (for which award is claimed) on the development in the field of Geomatics (500 words):
11. Whether the work has already won any award? If so, give details:

The Applications in the above format (five copies) should be submitted (by Registered Post or Speed Post) to

The Secretary, Indian Society of Geomatics,  
Space Applications Centre Campus,  
Ahmedabad-380015

so as to reach by September 30 of the year of award

\*ISG is, however, not bound to accept these names and can refer the nomination to other experts/peers

**INDIAN SOCIETY OF GEOMATICS: FELLOWS**

Shri Pramod P. Kale, Pune  
 Dr George Joseph, Ahmedabad  
 Dr A.K.S. Gopalan, Hyderabad  
 Dr Prithvish Nag, Varanasi  
 Dr Baldev Sahai, Ahmedabad  
 Shri A.R. Dasgupta, Ahmedabad  
 Dr R.R. Navalgund, Bengaluru  
 Shri Rajesh Mathur, New Delhi  
 Dr Ajai, Ahmedabad  
 Prof P. Venkatachalam, Mumbai  
 Dr Shailesh Nayak  
 Prof I.V. Murlu Krishna  
 Prof SM Ramasamy, Tiruchirapalli  
 Dr Ashok Kaushal, Pune  
 Shri A.S. Kiran Kumar, Bengaluru  
 Prof. P.K. Verma, Bhopal  
 Maj. Gen. Siva Kumar, Hyderabad  
 Dr A S Rajawat, Ahmedabad  
 Dr Shakil Romshoo, Srinagar

**INDIAN SOCIETY OF GEOMATICS: PATRON MEMBERS**

- P-1 Director, Space Applications Centre (ISRO), Jodhpur Tekra Satellite Road, Ahmedabad - 380 015  
 P-2 Settlement Commissioner, The Settlement Commissioner & Director of Land Records-Gujarat, Block No. 13, Floor 2, Old Sachivalay, Sector-10, Gandhinagar - 382 010  
 P-3 Commissioner, Mumbai Metropolitan Region Development Authority, Bandra-Kurla Complex, Bandra East, Mumbai - 400 051  
 P-4 Commissioner, land Records & Settlements Office, MP, Gwalior - 474 007  
 P-5 Director General, Centre for Development of Advanced Computing (C-DAC), Pune University Campus, Ganesh Khind, Pune - 411 007  
 P-6 Chairman, Indian Space Research Organization (ISRO), ISRO H.Q., Antariksha Bhavan, New BEL Road, Bengaluru 560 231  
 P-7 Director General, Forest Survey of India, Kaulagarh Road, P.O. I.P.E., Dehra Dun - 248 195  
 P-8 Commissioner, Vadodara Municipal Corporation, M.S. University, Vadodara - 390 002  
 P-9 Director, Centre for Environmental Planning and Technology (CEPT), Navarangpura, Ahmedabad - 380 009  
 P-10 Managing Director, ESRI INDIA, NIIT GIS Ltd., 8, Balaji Estate, Sudarshan Munjal Marg, Kalkaji, New Delhi - 110 019  
 P-11 Director, Gujarat Water Supply and Sewerage Board (GWSSB), Jalseva Bhavan, Sector - 10A, Gandhinagar - 382 010  
 P-12 Director, National Atlas & Thematic Mapping Organization (NATMO), Salt Lake, Kolkata - 700 064  
 P-13 Director of Operations, GIS Services, Genesys International Corporation Ltd., 73-A, SDF-III, SEEPZ, Andheri (E), Mumbai - 400 096  
 P-14 Managing Director, Speck Systems Limited, B-49, Electronics Complex, Kushiaguda, Hyderabad - 500 062  
 P-15 Director, Institute of Remote Sensing (IRS), Anna University, Sardar Patel Road, Chennai - 600 025  
 P-16 Managing Director, Tri-Geo Image Systems Ltd., 813 Nagarjuna Hills, PunjaGutta, Hyderabad - 500 082  
 P-17 Managing Director, Scanpoint Graphics Ltd., B/h Town Hall, Ashram Road, Ahmedabad - 380 006  
 P-18 Secretary General, Institute for Sustainable Development Research Studies (ISDRS), 7, Manav Ashram Colony, Goplapura Mod, Tonk Road, Jaipur - 302 018  
 P-19 Commandant, Defense institute for GeoSpatial Information & Training (DIGIT), Nr. Army HQs Camp, Rao Tula Ram Marg, Cantt., New Delhi - 110 010  
 P-20 Vice President, New Rolta India Ltd., Rolta Bhavan, 22nd Street, MIDC-Marol, Andheri East, Mumbai - 400 093  
 P-21 Director, National Remote Sensing Centre (NRSC), Deptt. of Space, Govt. of India, Balanagar, Hyderabad - 500 037  
 P-22 Managing Director, ERDAS India Ltd., Plot No. 7, Type-I, IE Kukatpalli, Hyderabad - 500 072  
 P-23 Senior Manager, Larsen & Toubro Limited, Library and Documentation Centre ECC Constr. Gp., P.B. No. 979, Mount Poonamallee Road, Manapakkam, Chennai - 600 089.  
 P-24 Director, North Eastern Space Applications Centre (NE-SAC), Department of Space, Umiam, Meghalaya 793 103  
 P-25 Programme Coordinator, GSDG, Centre for Development of Advanced Computing (C-DAC), Pune University Campus, Pune - 411 007  
 P-26 Chief Executive, Jishnu Ocean Technologies, PL-6A, Bldg. No. 6/15, Sector - 1, Khanda Colony, New Panvel (W), Navi Mumbai - 410 206  
 P-27 Director General, A.P. State Remote Sensing Applications Centre (APSRAC), 8th Floor, "B" Block, Swarnajayanthi Complex, Ameerpet, Hyderabad- 500 038  
 P-28 Director, Advanced Data Processing Res. Institute (ADRIN), 203, Akbar Road, Tarbund, Manovikas Nagar P.O., Secunderabad -500 009  
 P-29 Managing Director, LEICA Geosystems Geospatial Imaging Pvt. (I) Ltd., 3, Enkay Square, 448a Udyog Vihar, Phase-5, Gurgaon- 122 016  
 P-30 Director, Defense Terrain Research Limited (DTRL), Ministry of Defense, Govt. of India, Defense Research & Development Organisation, Metacafe House, New Delhi - 110 054  
 P-31 Chairman, OGC India Forum, E/701, Gokul Residency, Thakur Village, Kandivali (E), Mumbai - 400 101  
 P-32 Managing Director, ML Infomap Pvt. Ltd., 124-A, Katwaria Sarai, New Delhi - 110 016  
 P-33 Director, Rolta India Limited, Rolta Tower, "A", Rolta Technology Park, MIDC, Andheri (E), Mumbai - 400 093  
 P-34 Director, State Remote Sensing Applications Centre, Aizawl - 796 012, Mizoram

## Instructions for Authors

The journal covers all aspects of Geomatics – geodata acquisition, pre-processing, processing, analysis and publishing. Broadly this implies inclusion of areas like GIS, GPS, Photogrammetry, Cartography, Remote Sensing, Surveying, Spatial Data Infrastructure and Technology including hardware, software, algorithm, model and applications. It endeavors to provide an international forum for rapid publication of developments in the field – both in technology and applications.

A manuscript for publication must be based on original research work done by the author(s). It should not have been published in part or full in any type of publication nor should it be under consideration for publication in any periodical. Unsolicited review papers will not be published.

The Editorial Board or the Indian Society of Geomatics is not responsible for the opinions expressed by the authors.

### Language

The language of the Journal will be English (Indian). However, manuscripts in English (US) and English (British) are also acceptable from authors from countries located outside India.

### Manuscript Format

Each paper should have a title, name(s) of author(s), and affiliation of each of the authors with complete mailing address, e-mail address, an abstract, four to six keywords, and the text. The text should include introduction/background, research method, results, discussion, followed by acknowledgements and references. The main text should be divided in sections. Section headings should be concise and numbered in sequence, using a decimal system for subsections. Figures, images and their captions should be inserted at appropriate points of the text. Figures, images and tables should fit in two column format of the journal. If absolutely necessary, figures, images and tables can spread across the two columns. Figures and images, however, should not exceed half a page in height. A title should be provided for each Table, Image and Figure. All figures and images should be in 600 dpi resolution and sized as per column/margin width. Authors must ensure that diagrams/figures should not lose easy readability upon reduction to column size. The SI (metric) units and international quantities should be used throughout the paper. In case measurements are given in any other system, equivalent measurements in SI (metric) units should be indicated in brackets.

Use MS Word with English (UK/US) or English (Indian) dictionary. The page size should be A4 paper, with 2 cm margin on all sides. Title, authors and affiliation should be centred. Abstract should be justified across margins. The manuscript text should be in two columns of 8.2 cm each with a gutter of 6mm between them. Use only Times New Roman fonts. Title should be 12 points bold. Authors and affiliation should be 9 points. All other text including headings should be 10 points. Heading numbering scheme should be decimal e.g. 1, 1.1, 1.2.3, etc. Headings should be in bold.

Normally length of a published paper should be about 6-10 pages in A4 size including figures. Use of illustrations in colour should be restricted and resorted to only where it is absolutely necessary and not for enhancing the look of the paper. If the number of colour illustrations exceeds five, authors' institution may be asked to reimburse the extra cost involved, which at current rates is about Rs. 2500 per coloured figure/diagram/plate/illustration.

### Submission of Manuscript

Submissions should be in electronic form via email. The manuscript may be sent by email to [editorjogisg@gmail.com](mailto:editorjogisg@gmail.com). In exceptional cases hard copy submission in camera ready form may be allowed with the prior permission of the Chief Editor. Submission in any other form will be returned to the author. To speed up the review process, authors are advised to provide a list of three probable reviewers with their institutional address and e-mail IDs.

### Guidelines for Citing References

Names of all cited publications should be given in full. No abbreviations should be used. Following procedure is to be adopted.

### Journal Publications

Bahuguna, I.M. and A.V. Kulkarni (2005). Application of digital elevation model and orthoimages derived from IRS-1C Pan stereo data in monitoring variations in glacial dimensions, *Journal of the Indian Society of Remote Sensing*, 33(1), 107- 112. (to be referred to in the text as Bahuguna and Kulkarni (2005) or if more than two sets of authors are to be referred to, as (Bahuguna and Kulkarni, 2005; Jain et al., 1994)) When more than two authors are to be referred to, use Jain et al. (1994). However, in References, all authors are to be mentioned.

### Publication in a Book

Misra, V.N. (1984). *Climate, a factor in the rise and fall of the Indus Civilization – Evidence from Rajasthan and Beyond* in *Frontiers of the Indus Civilization* (B.B. Lal and S.P. Gupta: Chief Editors) Books and Books, New Delhi, pp. 461-489

### Papers Published in Seminar/ Symposium Proceedings

Jain, A., A.R. Shirish, M. Das, K. Das, M.C. Porwal, and P.S. Roy (1994). *Remote Sensing and Geographic Information System – An approach for the assessment of biotic interference in the forest ecosystem*. Proceedings. 15th Asian Conference on Remote Sensing, Bangalore, November 17-23, 1994, pp. 65-72.

### Books

Possehl, Gregory L. (1999). *Indus Age: The beginnings*. Oxford and IBH Publishing Corporation, New Delhi.

**Reviewing**

Each paper will be reviewed by three peers. Papers forwarded by members of the Editorial or Advisory Boards along with their comments would get processed faster and may be reviewed by two referees only.

Sample format for Authors is available in downloadable form at ISG website: [www.isgindia.org/JOG/Sample\\_format.doc](http://www.isgindia.org/JOG/Sample_format.doc)

**Copyright**

The copyright of the paper selected for publication will rest with the Indian Society of Geomatics. Corresponding author shall be required to sign a copyright assignment form, on behalf of all authors, once the paper is selected for publication. Authors are, however, at liberty to use this material elsewhere after obtaining permission from the Indian Society of Geomatics.

If the authors have used any copyright material in their manuscript, it is understood that they have obtained permission from the owner of the copyright material and they should convey the same along with the manuscript to the Chief Editor.

**Certificate of Original Work**

The authors will also provide a certificate that the paper is an original work, not published or being considered for publication elsewhere.

In the event the certificate turns out to be false, the Journal shall ban the author(s) from publishing in the Journal for a period of five years and inform the same to all other related publications.

**Reprints**

Authors will be allowed to download the (PDF) of their paper from ISG Website [www.isgindia.org](http://www.isgindia.org), No hard copy reprints will be provided.

<b>Journal of Geomatics</b>		
<b>Advertisement Rates</b>		
	<b>1 Issue</b>	<b>4 Issues</b>
<b>Back Cover Page in colour</b>	<b>Rs. 25,000</b>	<b>Rs. 80,000</b>
<b>Inside Cover Page in colour</b>	<b>Rs. 20,000</b>	<b>Rs. 64,000</b>
<b>Full Page inside in colour</b>	<b>Rs. 15,000</b>	<b>Rs. 48,000</b>
<b>Full Page inside in B/W</b>	<b>Rs. 10,000</b>	<b>Rs. 32,000</b>

### **Advertisement Details**

<b>Mechanical Details</b>
<b>Double Spread/Center Spread (42 x 29.7) cm</b>
<b>Full page bleed (21 x 29.7) cm</b>
<b>Full page non-bleed (19 x 27.7) cm</b>

### **Art Requirements**

**Negatives:** Art must be right reading, emulsion, down. Film must be supplied in one piece per color, each identified by color. Camera-ready art is accepted for black & White adds; however, film is preferred. Electronic Files are also accepted.

**Electronic File Requirements:** All material must be received before ad close dates.

**Software:** Adobe illustrator 9.0 (saved as EPS). Adobe Photoshop CS (saved as EPS or TIFF). Please convert higher versions down. If you can only supply an IBM format, the file must be in viewable EPS or TIFF format with fonts embedded as that format.

**Colour Ads:** Colour separations must be provided, right reading, emulsion down. Please note that files using RGB or Pantone colours (PMS) must be converted to CMYK before we receive files.



# ISG

To,  
The Secretary, Indian Society of Geomatics  
6202, Space Applications Centre (ISRO)  
AHMEDABAD – 380 015. INDIA

Sir,  
I want to become a Member/ Life Member/ Sustaining Member/ Patron Member/Foreign Member/Student Member of the Indian Society of Geomatics, Ahmedabad for the year \_\_\_\_\_. Membership fee of Rs.\_\_\_\_/- is being sent to you by Cash/DD/Cheque. (In case of DD/Cheque No.\_\_\_\_dated\_\_\_\_\_drawn on Bank.

\_\_\_\_\_. I agree to abide by the Constitution of the Society.

**Date:**

**Place:**

**Signature**

• Name: Mr/Ms/Mrs/Dr \_\_\_\_\_  
• Address: \_\_\_\_\_  
\_\_\_\_\_ PIN: \_\_\_\_\_

• Phone: \_\_\_\_\_ Fax: \_\_\_\_\_ Email: \_\_\_\_\_  
• Date of Birth \_\_\_\_\_  
• Qualifications \_\_\_\_\_  
• Specialisation: \_\_\_\_\_  
• Designation: \_\_\_\_\_ Organisation. \_\_\_\_\_  
• Membership in other Societies: \_\_\_\_\_  
• Mailing Address: \_\_\_\_\_  
\_\_\_\_\_ PIN: \_\_\_\_\_

Proposed by:  
(Member's Name and No)  
Signature of Proposer

For Office Use: A/P/L Member No.		Receipt No.		Date:	
-------------------------------------	--	-------------	--	-------	--

**Indian Society of Geomatics (ISG), Room No. 6202 Space Applications Centre (ISRO),  
Ahmedabad-380015, Gujarat. Url: [www.isgindia.org](http://www.isgindia.org) Phone: +91-79 26916202  
Email: [secretary@isgindia.org](mailto:secretary@isgindia.org) or [sasharma@sac.isro.gov.in](mailto:sasharma@sac.isro.gov.in) Fax +91-79-26916287**

## MEMBERSHIP FEES

Sr. No.	Membership Category	Life/Patron Membership fees		Annual Subscription
		₹ Indian	US \$ Foreign	₹ Indian
1.	Annual Member	10	---	300
2.	Life Member			
	a) Admitted below 45 years of age	2500	250	
	b) Admitted after 45 years of age	2000	200	
3.	Sustaining Member	---	---	2000
4.	Patron Member	50000	3000	---
5.	Student Member	10	---	100

## MEMBERSHIP GUIDELINES

- Subscription for Life Membership is also accepted in two equal instalments payable within duration of three months, if so desired by the applicant. In such a case, please specify that payment will be in instalments and also the probable date for the second instalment (within three months of the first instalment).
- A Member of the Society should countersign application of membership as proposer.
- Subscription in DD or Cheque should be made out in the name of '**Indian Society of Geomatics**' and payable at Ahmedabad.
- Direct deposit in ISG A/Cs must include bank fee RS. 25/- for cash payment.
- Financial year of the Society is from April 1 to March 31.
- For further details, contact Secretary, Indian Society of Geomatics at the address given above.
- ISG has chapters already established at the following places. Ahmedabad, Ajmer, Bhagalpur, Bhopal, Chennai, Dehradun, Delhi, Hissar, Hyderabad, Jaipur, Ludhiana, Mangalore, Mumbai, Mysore, Pune, Shillong, Trichi, Srinagar, Vadodara, Vallabh Vidya Nagar, Visakhapatnam and Trivandrum. Applicants for membership have the option to contact Secretary/Chairman of the local chapter for enrolment. Details can be found at the website of the Society: [www.isgindia.org](http://www.isgindia.org).
- Journal of the Society will be sent to Life Members by softcopy only.

**Indian Society of Geomatics (ISG), Room No. 6202 Space Applications Centre (ISRO),**

**Ahmedabad-380015, Gujarat.** Url: [www.isgindia.org](http://www.isgindia.org) Phone: +91-79 26916202

Email: [secretary@isgindia.org](mailto:secretary@isgindia.org) or [sasharma@sac.isro.gov.in](mailto:sasharma@sac.isro.gov.in) Fax +91-79-26916287

Geomatics Revealed

# IGiS

Integrated GIS & IP Software

VERSION 2.0



MAKE IN INDIA



**National Awards on Technology**  
By The Former President of India,  
Dr. A. P. J. Abdul Kalam



**Launch of IGiS Version 2.0**  
By Padam Shri AS Kiran Kumar, Chairman, ISRO and  
Shri Tapan Mishra, DIRECTOR, SAC, ISRO.

## What's new in IGiS

IGiS Version 2.0 is full of enhancements which you'll appreciate every day. New advanced GIS/IP and SAR modules are vital now a days. New COM Based Architecture makes you even more productive. The more you do with IGiS Version 2.0, the more you'll wonder how you ever did without it.

## Enhancements in IGiS Version 2.0

- Advanced GIS / Image Processing
- Microwave SAR Analysis
- Meteorological Analysis
- COM Based Scalable Architecture
- New Ribbon Bar GUI
- Python Customization
- OGC Standards



Product Development Partner



Government of India | Department of Space  
Indian Space Research Organisation - (ISRO)



Scanpoint Geomatics Ltd.

[www.scanpointgeomatics.com](http://www.scanpointgeomatics.com)

**Scanpoint Geomatics Ltd.**

Corporate Office : 12, Abhishree Corporate Park, Iskcon - Ambli Road, Ahmedabad - 380 058. Gujrat (India)  
[P] +91 2717 297096-98 [F] +91 2717 297039 [E] [info@scanpointgeomatics.com](mailto:info@scanpointgeomatics.com) [W] [www.scanpointgeomatics.com](http://www.scanpointgeomatics.com)

INDIAN SPACE RESEARCH ORGANISATION  
GOVERNMENT OF INDIA

# A Smart Destination For Geospatial Solutions

National Remote Sensing Centre  
Hyderabad, India  
[www.nrsc.gov.in](http://www.nrsc.gov.in)  
[www.bhuvan.nrsc.gov.in](http://www.bhuvan.nrsc.gov.in)  
[data@nrsc.gov.in](mailto:data@nrsc.gov.in)

nrsc



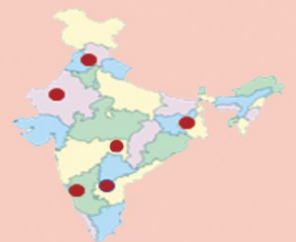
Only Organization in the Country  
to Acquire & Supply  
Satellite Data to Users



Aerial Acquisition for Specific  
User Demands &  
Disaster Management Support



Open Data & Value Added  
Products Dissemination  
Through Bhuvan



Region Specific Solutions



Capacity Building in  
Remote Sensing Applications